Fall 12-18-2015

A Simulation of the Mississippi River Salt Wedge Estuary Using a Three-Dimensional Cartesian Z Coordinate Model

Steven K. Ayres
University of New Orleans, alatar@att.net

A Simulation of the Mississippi River Salt Wedge Estuary Using a Three-Dimensional Cartesian *Z* Coordinate Model

A Dissertation

Submitted to the Graduate Faculty of the
University of New Orleans
in partial fulfillment of the
requirements for the degree of

Doctor of Philosophy
in
Engineering and Applied Science
Civil and Environmental Engineering

by

Steven Kyle Ayres

B.S. Texas Tech University, 1986
M.S. Texas Tech University, 1991

December, 2015

ACKNOWLEDGEMENTS

This dissertation would not have been possible without the guidance and help of several individuals who in one way or another contributed and extended their valuable assistance in the preparation and completion of this study.

First and foremost, I would like to extend my sincerest gratitude to my advisor, Dr. John A. McCorquodale, who exhibited extreme patience and wisdom throughout years of study and research which included several initial ideas, numerous failures, a few successes, and final results. Dr. McCorquodale's Sediment Transport class was the first course I took at the University of New Orleans in 2007. His passion for the subject was contagious and inspired me to pursue this achievement.

I would also like to thank Dr. Barbara A. Kleiss for recognizing the value of the research early in the study process and providing the management framework and support which allowed uninterrupted research.

The staff of the Department of Defense High Performance Computing Center was invaluable with the tasks of code compilation and debugging. I would also like to acknowledge the assistance of the Deltares open source support staff and the Delft3D open source community who provided assistance and ideas during the model development phase.

Mr. Gary L. Brown of the U. S. Army Corps of Engineers, Engineer Research and Development Center provided assistance in the early stages of model development by helping to overcome some of the technical hurdles.

Last but not least, I dedicate this work to my wife, son, and daughter. I would especially like to thank my wife, Aniko, for continuously providing encouragement even when I thought giving up was the sanest course of action.

Table of Contents

LIST OF FIGURES

LIST OF TABLES

ABSTRACT

The stratified flow of the lower Mississippi River due to density gradients is a well-documented phenomenon. This stratification of fresh and saline water manifests itself as a heavier wedge of saline water that extends upriver and a buoyant fresh water plume extending into the Gulf of Mexico past the Southwest Pass jetties. The maximum absolute distance of saltwater intrusion observed anywhere in the world occurred on the Mississippi River in 1939 and 1940 when saltwater was observed approximately 225 km upstream from the mouth of Southwest Pass. The U. S. Army Corps of Engineers now prevents the wedge from migrating upstream by constructing a subaqueous barrier in the river channel. A curvilinear grid was constructed representative of the modern Mississippi River delta. Boundary conditions were developed for the drought year of 2012 and the grid was tested in order to evaluate the salinity intrusion and sediment transport abilities of the Cartesian *Z*-coordinate Delft3D code. The *Z*-model proved to have the ability to propagate the saline density current as observed in the prototype. The effect of salinity on fine sediment transport is evaluated by manipulation of the settling velocity through a cosine function provided in the model code. Manipulation of the fine sediment fall velocity through the cosine function was an effective means to simulate the re-circulation of flocculated sediments in the saline wedge turbidity maxima. In addition, the *Z*-model capably reproduced the fine sediment concentration profiles in a fully turbulent shear flow environment. With the ability to reproduce the seasonal saline density current and its effect on sedimentation within the turbidity maxima as well as sedimentation characteristics in a fully turbulent shear flow, a model capable of analyzing all of the major processes affecting fine sediment transport within the Mississippi River salt wedge estuary has been developed.

Keywords: Mississippi River delta, Delft3D, stratification, flocculation, salt wedge estuary, turbidity maxima

1 INTRODUCTION

1.1 Background

The Mississippi River system, the largest on the North American continent, drains an area of 3,344,560 sq km and has been active since at least Late Jurassic times, approximately 145 million years ago (Figure 1-1). The system carries an estimated 6.21 x 10^{11} kg of sediment load annually to the delta and northern Gulf of Mexico, the receiving basin for the Mississippi River system. The Gulf of Mexico is characterized as a microtidal environment with a tidal range averaging around 0.43 m with low wave energy. The delivery of this high sediment load to a low energy environment results in build-up of a thick sequence of alluvial, shelf, slope, and basinal deposits, which has prograded the coastal-plain shoreline seaward (Coleman, 1988).

Figure 1-1 The Mississippi River drainage basin. (modified from http://www2.epa.gov/ms-htf/mississippiatchafalaya-river-basin-marb)

Since the Cretaceous times (145 to 66 million years ago), the sites of maximum deposition have shifted within the Gulf coastal plain. The Modern Plaquemines-Balize delta of the Mississippi River began progradation 1000-800 years ago, only shortly after the Lafourche delta and the two operated simultaneously for a period of time (Figure 1-2).

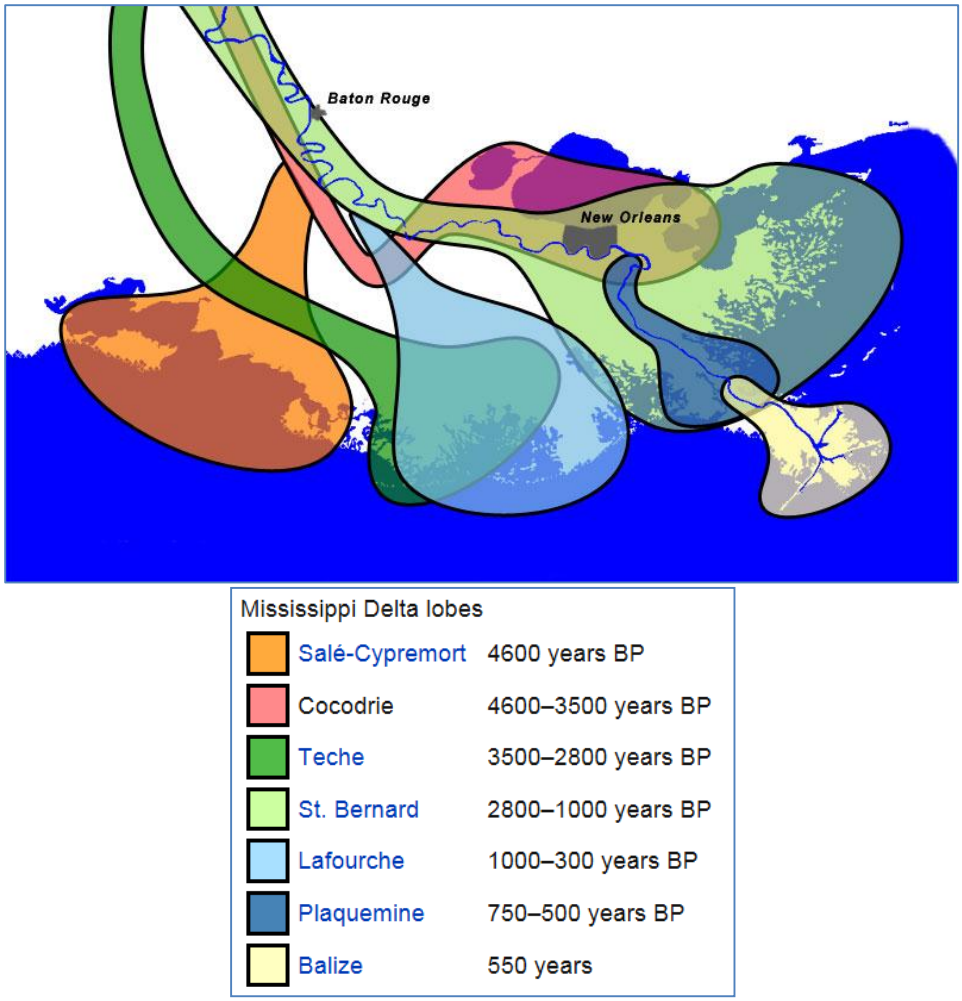

Figure 1-2 The chronology of the major delta lobes of the Mississippi delta (based on Kolb and Van Lopik, 1958)

The Modern Plaquemines-Balize delta is considered a digitate or birdsfoot delta in contrast to previous lobe configurations and consists of a number of natural levee flanked distributaries (Figure 1-3). The delta is also classified as a hypopycnal delta due to the buoyant flow, resulting from fresh river water entering a denser saline environment. This buoyant flow condition causes the formation of a salt wedge allowing the river water to flow over the heavier Gulf water. This allows the distibutary mouth bars to be deposited further into the receiving basin than if friction or inertia were dominant (Wright, 1985).

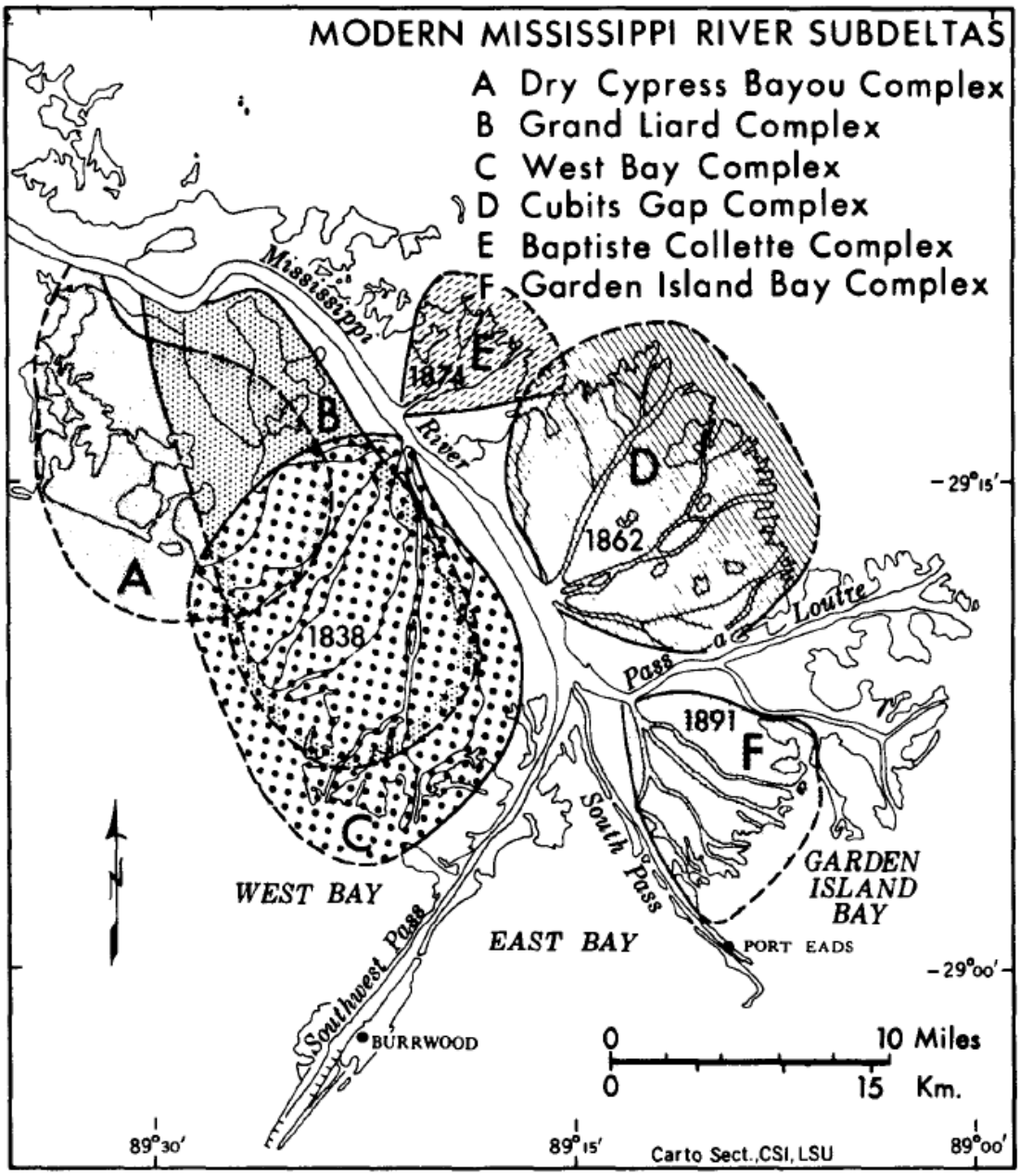

Figure 1-3 Bay fills of the modern Balize delta, Mississippi River. Filling episodes A and B occurred prior to historic maps in the delta. Filling episodes C-F occurred during the period 1838 to present, and the dates indicated are the period of the break (Coleman, 1988).

The delta has been heavily engineered to its present form chiefly for navigation and flood control purposes. Anthropogenic shaping of the delta began as early as 1726 when the French began using harrows to break up the bar at the mouth of Southwest Pass (Cowdrey, 1977). The main navigation route today is through Southwest Pass and is

maintained at a navigable depth of 13.7 meters. The channel had been maintained to a depth of 12.2 meters prior to congressional authorization in 1985 of the deeper channel. A navigable depth of 16.8 meters is currently authorized by Congress but has not been constructed to this date due to a lack of a cost share agreement between government agencies.

Rock lining now protects the banks of Southwest Pass from erosion and timber pile dikes line the Southwest Pass channel and parts of the lower river to help guide sediment laden waters through the channels (as seen in Figure 1-4). Rock jetties define the entrance to Southwest Pass from the Gulf of Mexico as seen in Figure 1-5. These structures are subject to damage from Hurricanes and are periodically re-built by the U. S. Army Corps of Engineers (USACE); reference Figure 1-6, Figure 1-7, Figure 1-8, Figure 1-9, Figure 1-10, and Figure 1-11 for pictures of before and after repairs of typical structures.

Figure 1-4 Foreshore rock protection and timber piling dikes can be seen in this picture circa June 2012 (source: U. S. Army Corps of Engineers, New Orleans District)

Figure 1-5 Southwest Pass Entrance showing rock jetties and timber pile dikes, date unknown (source: U. S. Army Corps of Engineers, New Orleans District)

Figure 1-6 Southwest Pass jetty before repair (source: U. S. Army Corps of Engineers, New Orleans District)

Figure 1-7 Southwest Pass jetty after repair, circa May 2009 – Sep 2010 (source: U. S. Army Corps of Engineers, New Orleans District)

Figure 1-8 A typical timber pile dike before repair (source: U. S. Army Corps of Engineers, New Orleans District)

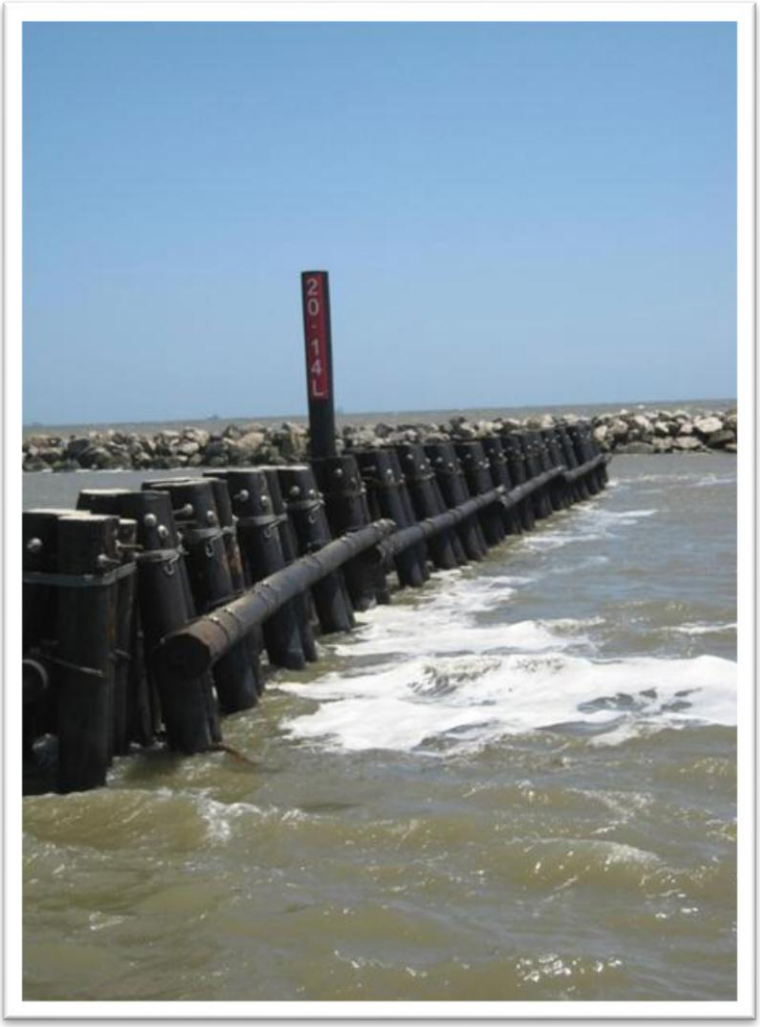

Figure 1-9 Timber pile dike after repair, circa Sep 2009 – Mar 2011 (source: U. S. Army Corps of Engineers, New Orleans District)

Figure 1-10 Foreshore rock protection damage (source: U. S. Army Corps of Engineers, New Orleans District)

Figure 1-11 Foreshore rock protection after repair (source: U. S. Army Corps of Engineers, New Orleans District)

Currently the Baptiste Collette Bayou and Grand/Tiger Pass navigation channels are maintained at a minimum navigable depth of 4.3 meters. A rock jetty defines the entrance to the Baptiste Collette Bayou channel from the Gulf of Mexico. South Pass had been regularly maintained as a navigable channel in the past, but efforts have largely shifted to maintaining Southwest Pass as the primary navigation route, however South Pass sees intermittent maintenance efforts as funding constraints dictate. Figure 1-12 displays geographic features of the modern Mississippi delta.

Figure 1-12 Features of the modern Mississippi River Delta

The average expenditure of the U. S. Government on Southwest Pass and the lower Mississippi River dredging has been around $55 million/year for the period from 2008-2012 with a corresponding 13.3 million cubic meters average annual volume of dredged material (Figure 1-13). This includes the reach from River Kilometer (RK) 35 Below Head of Passes (BHP) to RK 16 Above Head of Passes (AHP).

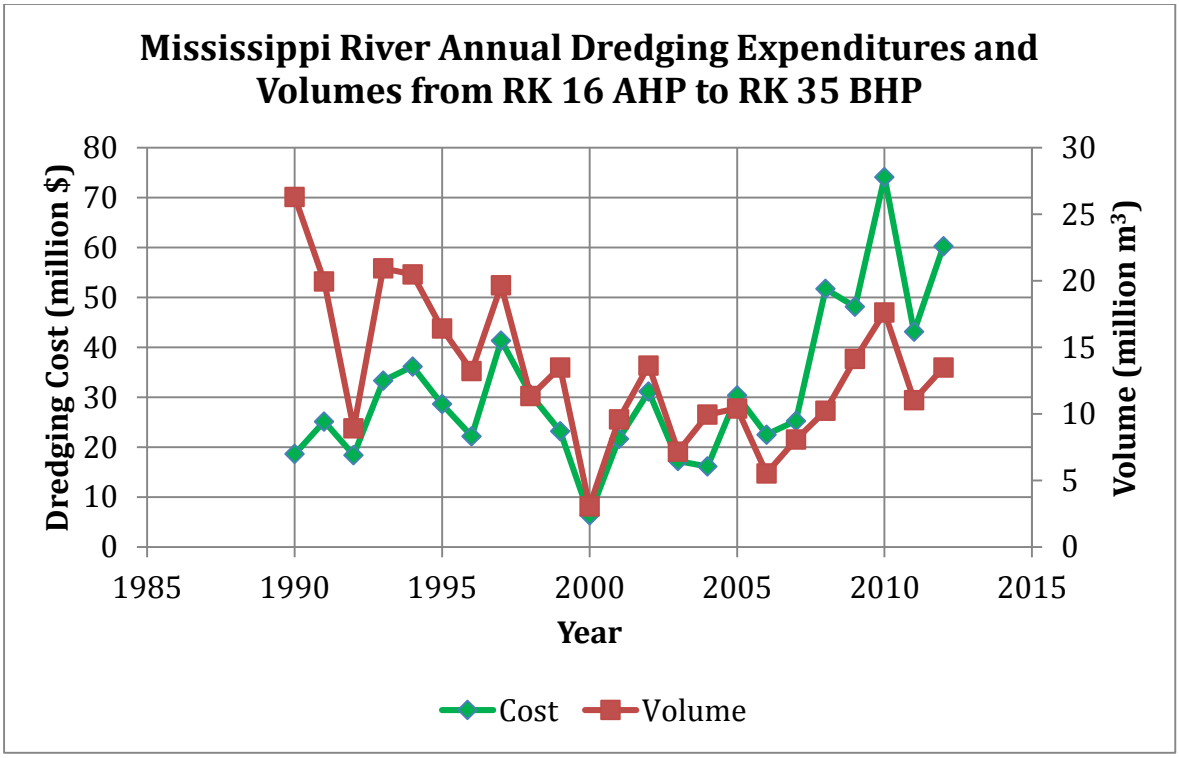

Figure 1-13 Lower Mississippi River and Southwest Pass Dredging Expenditures.

A deeper navigation channel has been proposed and is currently under consideration that will accommodate larger ships traversing an expanded Panama Canal. The proposed deeper navigation channel through Southwest Pass has the potential to increase the upriver progression of the saline wedge. The Corps of Engineers constructs a subaqueous barrier sill at around RK 102 to prevent wedge progression past that point but the deeper navigation channel may increase the frequency of the need for the sill construction. The sill has been constructed previously in the years 1988, 1999, and 2012. Channel maintenance to the previously authorized 16.8 meters would only exacerbate salinity intrusion issues and may increase the frequency of the need for saltwater intrusion remediation measures.

Other capital improvement projects such as river diversions for marsh restoration purposes necessitate a better understanding of the factors affecting sedimentation

processes and salinity intrusion in the Mississippi delta in order to predict the impact of future projects on maintenance needs and resultant expenditures.

1.2 Statement of the Problem

The desire to understand the ramifications of proposed modifications to the physical environment of the Mississippi delta estuary requires that some form of predictive tool be created that accounts for the major physical processes affecting sedimentation and salinity intrusion in the estuary. Historically, empirical relationships were developed to aid in prediction of resultant impacts to changes in a system. Physical models have also been utilized to assist in the design of physical features in the delta. However, even scale physical models would be incapable of reproducing the flow stratification and resultant shoaling impacts in the prototype. Today, advances in numerical modeling techniques have reached a point where it is possible to reproduce the necessary processes to develop a predictive tool capable of providing insight to possible impacts of these proposed physical changes.

Stratification of flow in the lower Mississippi River and Southwest Pass necessitates a three- dimensional (3D) or two-dimensional (2D) laterally averaged approach to properly capture the flow dynamics and sedimentation processes in the delta. However, the 2D laterally averaged approach would only be applicable in the channel and not be useful for the estuary. Therefore a full 3D approach is sought after.

Flocculation effects on fine sediment settling characteristics due to salinity intrusion cannot be ignored if all major processes affecting sedimentation in the delta are to be accounted for. A full 3D model of the delta that accounts for a detailed representation of flow distribution in the passes and stratification of flow would require a very powerful computing platform. Sufficient data are needed to understand the impact of the various processes on sedimentation patterns in the delta. Currently such data are limited to the areas that are monitored at any given time.

An understanding of the water sediment ratios at the passes needed for long term modeling has been lacking. Available data are limited to only the discharge and concentration conditions that existed at the time of collection. Therefore, a fully 3D model that accounts for all major processes affecting water/sediment exchange through the major passes is desired.

1.3 Objectives

The main objective of this study is to develop a comprehensive delta model that includes flow stratification and resultant impacts on fine sediment processes.

The specific objectives of the study are:

1) Develop a model of the delta capable of replicating the flow stratification observed in the lower river channel and Southwest Pass.
2) Develop a model capable of quantitatively accounting for flocculation of fine particles due to salinity.
3) Develop a model capable of accurately simulating the water and sediment distribution through the major distributaries of the delta.
4) Develop a 3D model of the delta that includes the effect of structures on flow dynamics including the jetties and timber pile dikes.
5) Develop a modeling tool capable of quantifying the water/sediment ratios of the major distributaries for a range of flows.
6) Assess the influence of flow stratification on fine sediment transport characteristics in the lower river channel during drought conditions.

1.4 General Methodology

The following methodology was followed during the course of research:

1) A literature review was conducted.
2) A 3D model code was selected.
3) A determination of 3D code capabilities was conducted.

4) A representative grid was constructed of the lower Mississippi River and delta.
5) Suitable boundary conditions were developed to test the models capability to reproduce observed data.
6) The model was calibrated to match observed data.
7) Recommendations of the model's suitability for future alternative analysis were summarized.

2 PHYSICAL PROCESSES OF A SALT WEDGE ESTUARY

2.1 General

Estuaries may be classified based on the arrangement of the salinity isoconcentrations pictured in a cross section profile of the estuary. In this manner, estuaries may be classified based on water circulation and include salt wedge estuaries, partially-mixed estuaries, well-mixed estuaries and fjord-type estuaries (Figure 2-1). The salinity in an estuary may range from near sea water levels to nearly fresh. Since the river water is fresh, it floats on top of the dense saltwater and the level of mixing occurs based on numerous factors including geography, tidal forces, river flow, and wind. Stronger tidal forces typically form partially mixed and well mixed estuaries (Figure 2-1).

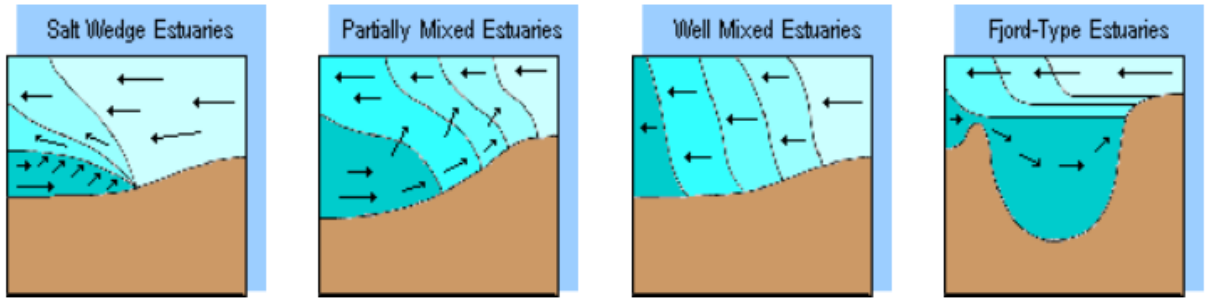

Figure 2-1 Estuary classification based on water circulation (Courtesy of Barataria-Terrebonne National Estauary Program, http://www.btnep.org)

During low flows, the Mississippi River estuary is a highly stratified estuary or salt wedge estuary. In this type of estuary, river discharge exceeds marine input and tidal effects have a secondary influence. The seaward bound fresh river water floats on top of the more dense saline seawater. At the same time, the heavier seawater travels inland under the fresh river water. The seawater layer thins as it moves inland, forming a "wedge", (Figure 2-2). Velocity differences between the two layers generate internal waves at the interface or pycnocline, mixing the seawater upward into the freshwater layer.

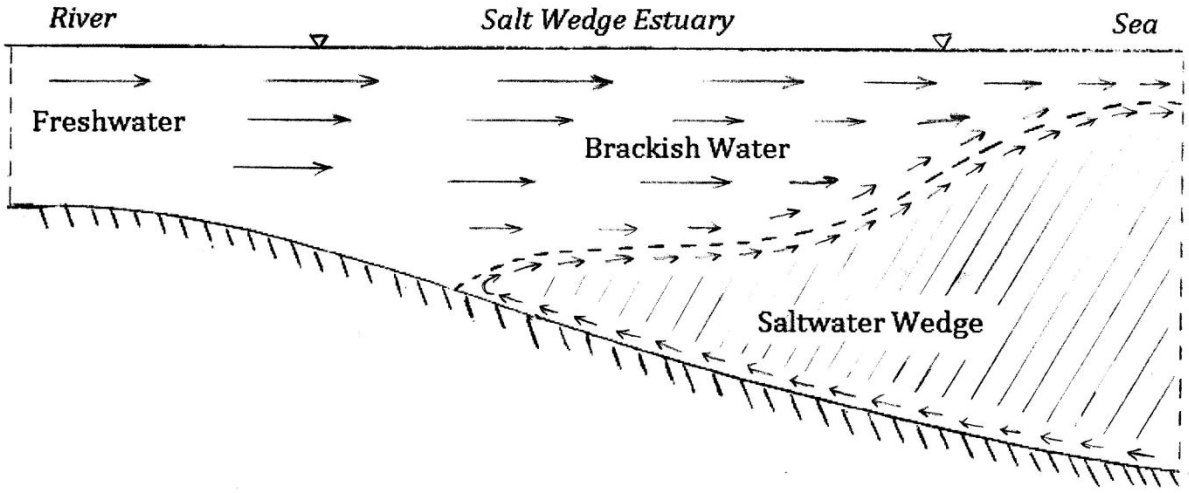

Figure 2-2 Saltwater wedge estuary schematic

A zone of turbidity maxima occurs in the tip of the wedge and has been observed in many river mouths. It was once thought that this high turbidity area was due to flocculation processes, it is however due to hydrodynamic estuarine re-circulation. The retention time of an individual particle is increased in the salt wedge estuary due to this re-circulation. Postma (1967) described the process in this way; a sediment particle carried downstream with river water may sink into the lower water layer. Since residual water movement in this layer is directed upstream, the particle will now move in the opposite direction. Vertical mixing may eventually bring the particle back into the upper water layer, so that it is again carried seaward. The process may be repeated, or the particle may be carried to the sea. Theoretically, a particle may be carried back and forth a number of times before it finally escapes the system. Similarly, suspended matter of marine origin is carried upstream in the salt wedge. The stratified region therefore acts as a sediment trap in which sedimentary material of either freshwater or marine origin may be circulated many times. Thus high concentrations of suspended matter may be accumulated (Postma, 1967).

Although re-circulation is considered the primary contributor to the retention time of the particles in the turbidity maxima, flocculation is also an important contributor to the

processes increasing the retention time of the individual particles and the concentration of the resultant turbidity maxima. The presence of electrolytes such as sodium chloride in the suspending fluid (salt wedge) is a contributor to flocculation but double valence calcium and magnesium ions are the main contributors to coagulation and hence flocculation. Saline solutions are ionic and the ions neutralize the charges on the particles thus reducing the normally repelling forces of the clay particles (Ippen, 1966, Graf 1971).

Simmons (1966) described the shoaling magnitude resulting from this zone of turbidity maxima at the location of the jetty in Southwest Pass. For river stages of less than 3.0 meters (10 feet) on the Carrollton Gage at New Orleans, the saltwater wedge tip is located well upstream from the entrance to Southwest Pass (the wedge moves upstream as much as 217 km for minimum stage), and for such conditions no significant shoaling takes place in the jetty and bar channel. For stages in excess of about 3.0 meters (10 feet), up to the maximum of about 6.1 meters (20 feet), the wedge tip is located within the jetty and bar channel, and very rapid shoaling occurs in and adjacent to the wedge tip. Figure 2-3 shows the magnitude of shoaling which occurred in a 2-week period during which dredges could not operate in the area because of a navigation hazard. The river stage during this period was very stable at about 5.0 to 5.3 meters (16.5 feet to 17.5 feet), and it will be noted that filling of the channel amounted to as much as 8.5 meters (28 feet) in one area, with an average fill over the entire area of about 1.8 or 2.1 meters (6 or 7 feet). Dredging operations in this area are required on an around-the-clock basis during river stages in excess of about 3.0 meters (10 feet) in order to permit uninterrupted navigation of this channel (Simmons, 1966).

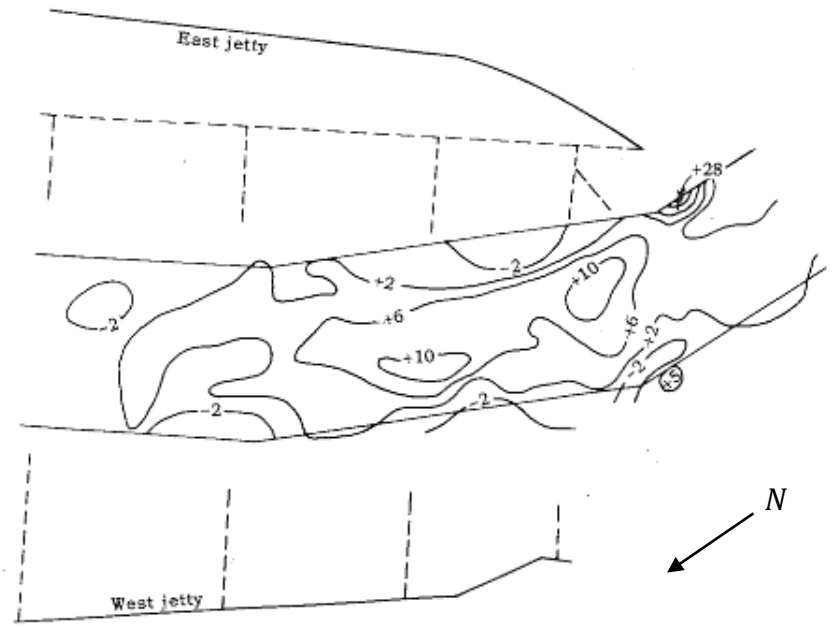

Figure 2-3 Shoaling for 2-week period in the Southwest Pass Jetty in March 1948, contours are in feet (based on Simmons, 1966)

2.2 Saline Wedge Mechanics

In order to model the major processes inherent in a salt wedge estuary with+ a numerical model, an understanding of the flow mechanics of a stratified flow system are necessary. Perhaps one of the earliest attempts to describe the mechanics of an arrested saline wedge was by Schijf and Schönfeld in 1953 (Schijf and Schönfeld, 1953). A two-layer theory was applied to develop a predictive model of the wedge intrusion length.

A system of two homogeneous layers of liquids (salt and fresh water) separated by a sharp interface is considered. The density difference between the two liquids is assumed to be small compared to the density itself, or $\epsilon = (\rho_2 - \rho_1): \rho_2 \approx (\rho_2 + \rho_1)/2 \approx \rho_1$

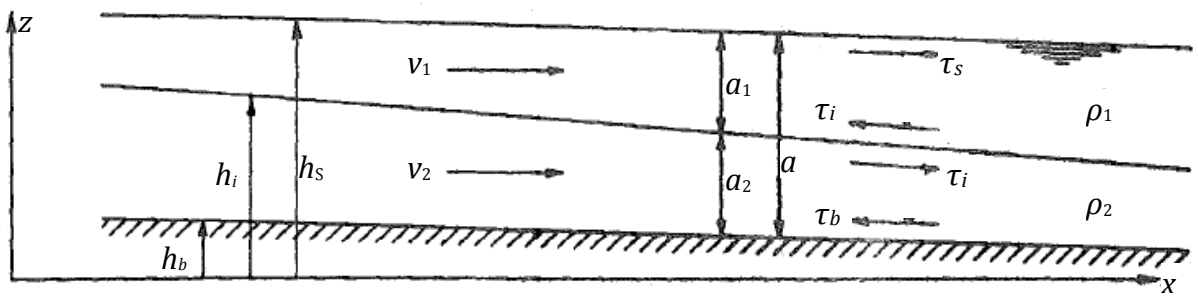

Figure 2-4 Two layer system, based on Schijf and Schönfeld, 1953

Neglecting vertical accelerations, the dynamical and continuity equations may be written as:

$$\frac{\partial a_1}{\partial t} + v_1 \frac{\partial a_1}{\partial x} + a_1 \frac{\partial v_1}{\partial x} = 0 \tag{2-1}$$

$$\frac{\partial a_2}{\partial t} + v_2 \frac{\partial a_2}{\partial x} + a_2 \frac{\partial v_2}{\partial x} = 0 \tag{2-2}$$

$$\frac{\partial v_1}{\partial t} + g\frac{\partial a_1}{\partial x} + g\frac{\partial a_2}{\partial x} + v_1 \frac{\partial v_1}{\partial x} + g(i_1 - i_b) = 0 \tag{2-3}$$

$$\frac{\partial v_2}{\partial t} + (1-\epsilon)g\frac{\partial a_1}{\partial x} + g\frac{\partial a_2}{\partial x} + v_2 \frac{\partial v_2}{\partial x} + g(i_2 - i_b) = 0 \tag{2-4}$$

The shear stresses of the layers are set to $\tau_{i_1} = \frac{\tau_i - \tau_s}{g\rho_1 a_1}$ and $\tau_{i_2} = \frac{\tau_b - \tau_i}{g\rho_2 a_2}$, where τ_s, τ_i, and τ_b are the respective shear stresses along the surface, the interface, and the bottom. The bottom slope is denoted by i_b, where $i_b = -dh_b/dx$. For the no wind and no ice cover situation, the surface stress may be assumed to be zero. Furthermore, turbulent flow is assumed, therefore:

$$\tau_i = \frac{\rho g |v_1 - v_2|(v_1 - v_2)}{4Ci^2} \tag{2-5}$$

$$\tau_b = \frac{\rho g |v_2| v_2}{C_b^2} \tag{2-6}$$

where C_b is the coefficient of flow for the bottom, and C_i for the interface. ρ_1 and ρ_2 are approximated by $\rho = \frac{1}{2}(\rho_1 + \rho_2)$.

For rivers entering a salt water body with a small tidal range, such as the Mississippi River, the fresh river water discharges over a stagnant salt water body which has penetrated upstream along the river bottom, see Figure 2-5.

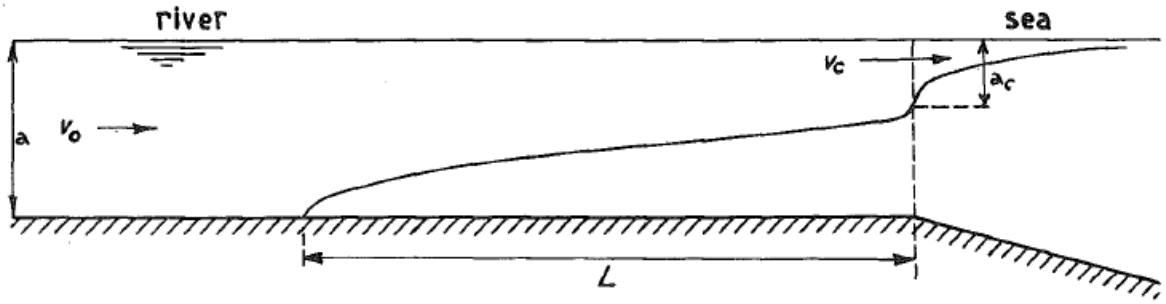

Figure 2-5 Arrested wedge figure from Schijf and Schonfeld (1953).

The flow of the upper layer is critical at the mouth, thus an equation describing the behavior of the interface may be obtained by combining the dynamical equations of the two layers:

$$\epsilon g \frac{da_1}{dx} + v_1 \frac{dv_1}{dx} + \frac{v_1^2 a}{4C_i^2 a_1 (a - a_1)} = 0 \qquad (2\text{-}7)$$

where C_i is the coefficient of friction along the interface, ϵ is the difference in density between the two layers, a is the upstream freshwater river depth, and v_0 is the average upstream river velocity.

Integration of the interface equation yields:

$$L = \frac{C_i^2}{g} a \left[\frac{1}{5} \frac{\epsilon g a}{v_0^2} - 2 + 3 \sqrt[3]{\frac{v_0^2}{\epsilon g a}} - \frac{6}{5} \sqrt[3]{\frac{v_0^2}{\epsilon g a}}^2 \right] \qquad (2\text{-}8)$$

When v_0 increases, the thickness of the upper layer at the river mouth, $a_c = \frac{v_0^2}{\epsilon g}$, increases as well as the friction at the interface and slope. Therefore, the length of the wedge decreases for these reasons. When the river velocity, v_0, becomes greater than the double-critical velocity, v_{cc}, the wedge is wholly expelled from the river.

Keulegan also developed length relationships for arrested saline wedges (Keulegan 1966). If ρ is the density of fresh water, $\rho + \Delta\rho$ the density of sea water and ρ_m is the density of the two liquids, Keulegan noted that a densimetric velocity may be defined by:

$$V_\Delta = \sqrt{\frac{\Delta\rho}{\rho_m} gH} \tag{2-9}$$

where g is the acceleration due to gravity and H is the depth of the river. In a similar vein, the densimetric Reynolds number is defined by:

$$R_e = V_\Delta \frac{H}{\nu} \tag{2-10}$$

where ν is the kinematic viscosity of water. Noting that the surface gradient of water in the channel plays only a secondary role in an arrested wedge, from dimensional reasoning the relation between the velocity of the saline front, V and the travel distance, L has the form:

$$\frac{V}{V_\Delta} = f_0\left(\frac{L}{H}, \frac{V_r}{V_\Delta}, \frac{V_\Delta H}{\nu}, \frac{H}{B}\right) \tag{2-11}$$

where V_r is the velocity of the river opposing the advancing wedge. It follows that the relationship for the length of an arrested saline wedge, L_0 takes the form:

$$\frac{L_0}{H} = f\left(\frac{V_r}{V_\Delta}, \frac{V_\Delta H}{\nu}, \frac{H}{B}\right) \tag{2-12}$$

From flume data, Keulegan established the law of the length as:

$$\frac{L_0}{H} = A\left(\frac{V_r}{V_\Delta}\right)^{-5/2} \tag{2-13}$$

with a variable A. For a constant channel width to water depth ratio, equation 2-12 suggests that the variable A depends on the densimetric Reynolds number, $V_\Delta H/\nu$. Natural water courses with Reynolds numbers on the order of 10^7 or greater were shown to follow the relationship:

$$\frac{L_0}{H} = 6.0\left(\frac{V_\Delta H}{\nu}\right)^{1/4}\left(\frac{2V_r}{V_\Delta}\right)^{-5/2} \tag{2-14}$$

Keulegan demonstrated the validity of this relationship with example data from South Pass. It was observed that the length of the arrested wedge in South Pass was 22.5 km with a corresponding Mississippi River discharge of 2,830 m^3/s. With a river width of 460 meters, a depth of 13.7 meters, a water Temperature of 20° C, and $\Delta\rho/\rho_m$ as 0.02, V_r is estimated to be 0.45 m/s and V_Δ as 1.64 m/s, therefore $2V_r/V_\Delta = 0.55$. The densimetric Reynolds number equals 2.25 X 10^7. With these values placed in equation 2-14, a wedge length of 24.9 miles is determined.

In addition to the assumption of steady state conditions, the other important assumptions that allow a solution for the arrested wedge shape are a tideless sea, a uniform rectangular channel cross section with a horizontal bottom and constant water depth, no mixing along the interface, and a constant friction coefficient along the saltwater and freshwater interface (Harleman, 1990).

With these assumptions, Harleman showed that the theoretical shape of the arrested saline wedge could be presented in a dimensionless manner as a function of the densimetric Froude number, $\mathbf{F}_0$, based on the mean freshwater river velocity U_0 and depth h_0 upstream of the arrested wedge where:

$$\mathbf{F}_0 = \frac{U_0}{\sqrt{g'h_0}}, \text{with } g' = g\frac{(\rho_2 - \rho_1)}{\rho_2} \tag{2-15}$$

For an arrested wedge with no entrainment, the mean velocity in the lower layer is zero. At the junction between the river channel and the ocean, the relative depths of the two layers are such that the local densimetric Froude number of the upper layer is equal to unity. Therefore, the upper-layer flow is critical and the depth ratio at the entrance is:

$$\frac{h_{ic}}{h_0} = (\mathbf{F}_0)^{2/3} \tag{2-16}$$

When $h_{ic} = h_0$, the wedge is expelled from the river channel and $\mathbf{F}_0 = 1$ (Harleman, 1961).

Arita and Jirka extended the two-layer theory by including a formulation based on the zero velocity line (ZVL) as an alternative to the density interface as shown in Figure 2-6. Mixing and entrainment across the interface were neglected but circulation dynamics within the lower layer were included (Arita and Jirka, 1987).

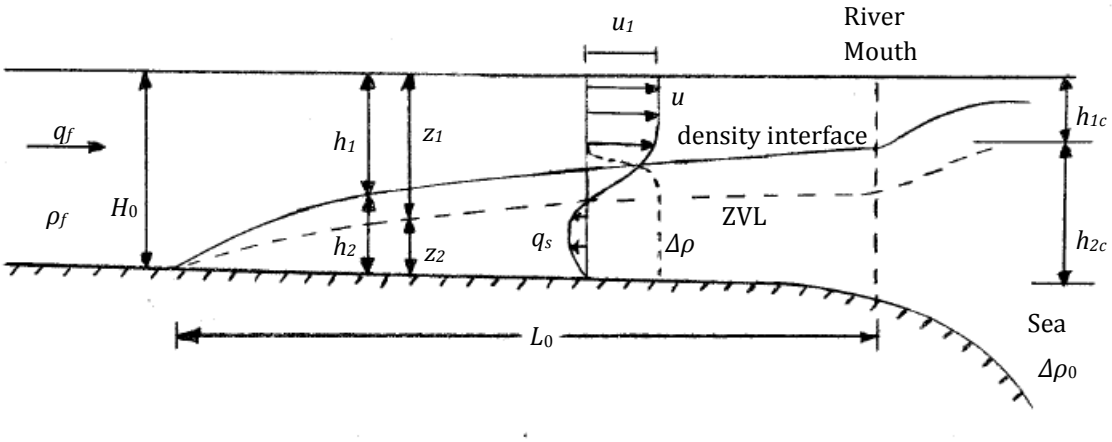

Figure 2-6 Salt Wedge Geometry and Internal Structure

The two-layer equations were solved numerically and the predicted wedge length as a function of the Reynolds number was plotted as shown in Figure 2-7. The Reynolds number was corrected for the different width-depth ratios used in the various experiments using the following:

$$R = \frac{\frac{q_f}{\nu}}{\left(2\frac{\bar{h}_1}{B} + 1\right)} \tag{2-17}$$

in which $\bar{h}_1 = \frac{(H_0 + h_{1c})}{2}$ and B is the flume width. This figure demonstrates the significance of the effect of large Reynolds numbers on wedge length and the limitation of physical models. The role of physical models in the study of salinity intrusion is limited to qualitative insights due to this Reynolds number effect.

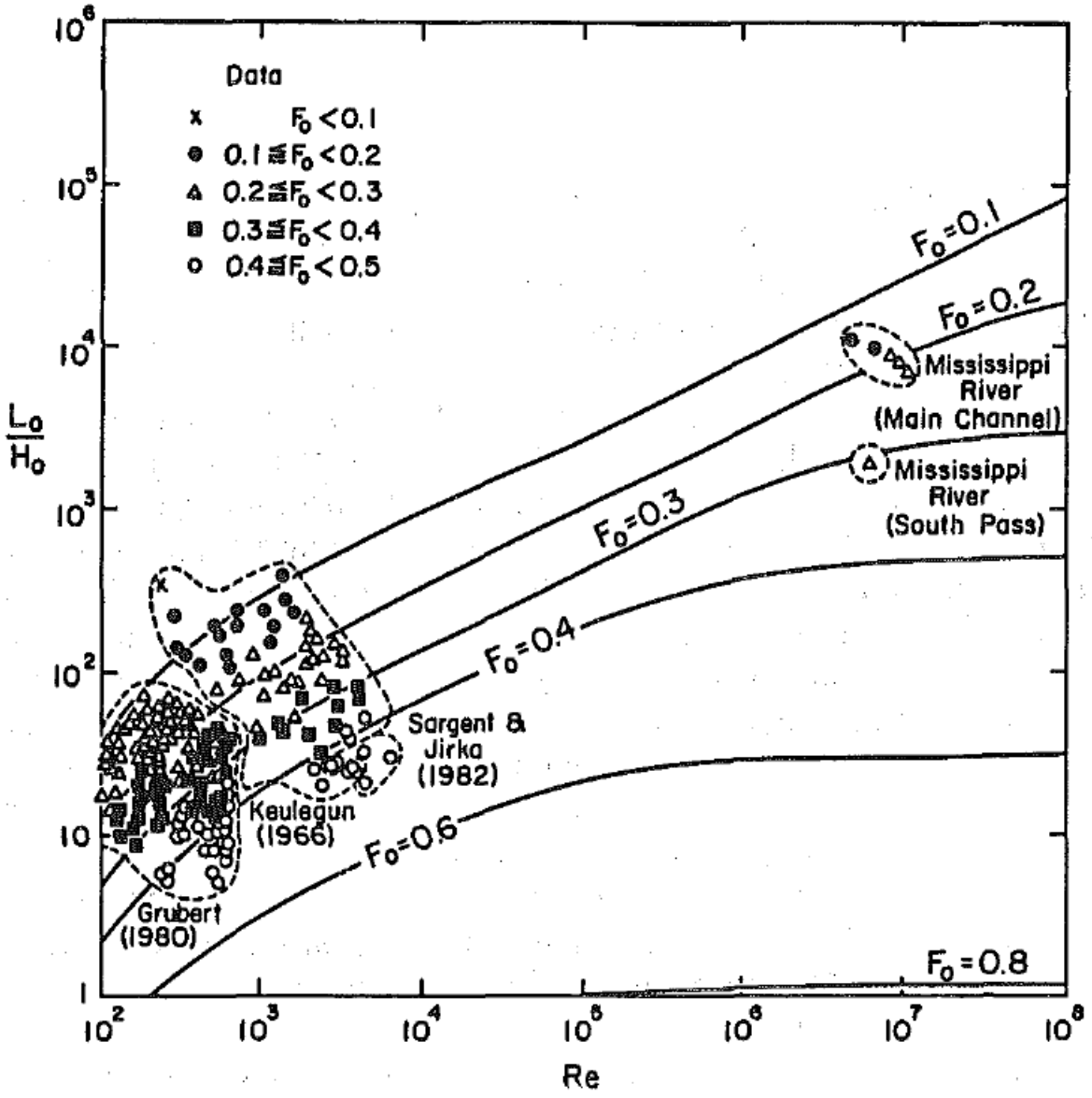

Figure 2-7 Comparison of Predicted Wedge Length L_0/H_0 and Observations in Field and Laboratory as Function of Reynolds Number R and Froude Number F_0; Horizontal Bottom, S_b=0 (from Arita and Jirka 1987, with permission from ASCE)

An inherent difficulty in the application of empirical methods to the case of the Mississippi River channel is the inability to account for the way in which salinity progresses and regresses in the channel. As shown in Figure 2-8 the salinity wedge progresses in a step-wise manner as it fills deep pools in the river channel. Examination of the measurements, reveals that the wedge needed several weeks to reach equilibrium due to the river bottom topography with a relatively constant discharge in October 1939.

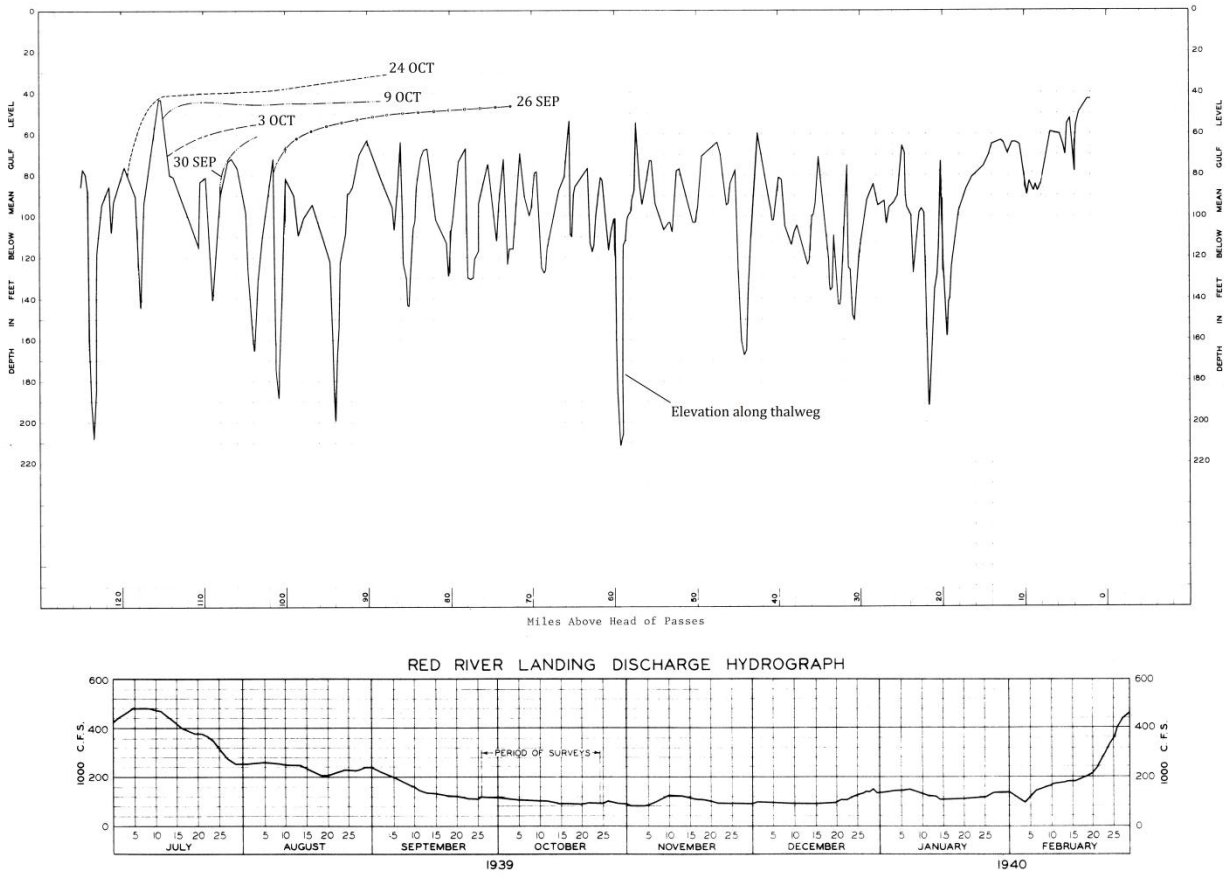

Figure 2-8 Observations on progression of the salinity interface (defined as the 5000 ppm chloride radical) in the Mississippi River during 1939

Balloffet and Borah applied the two-layer theory of Schijf and Schönfeld and Keulegan's concepts to simulate salinity intrusion in the Mississippi River. A model based on arrested salinity wedge theory was developed applicable to quasi-steady-state flow conditions. The model simulated Keulegan's experimental results well. It also simulated position of the salt wedge tips and interfaces in the Mississippi River with adjustment of the interfacial friction factor. The friction factor had to be over adjusted to compensate for the effects of the lag produced from progressively filled thalweg reservoirs (Balloffet and Borah, 1985).

A laterally averaged two-dimensional model was used by Johnson, Boyd, and Keulegan to evaluate the effectiveness of a submerged sill to stop upstream movement of the salt wedge and resultant contamination of water treatment supply intakes situated along the river. The results of this model study provided the basis for the sill that was

constructed by the USACE during the 1988, 1999, and 2012 droughts (Johnson, Boyd, and Keulegan, 1987 and Johnson, Boyd, and Copeland, 1987).

2.3 Stratified Flow Mixing Processes

When a freshwater source such as a river enters a saltwater body, mixing between the two water sources creates brackish water. There are unique mixing processes involved in generation of the brackish water that occur at different spatial scales.

At the smallest scale, on the order of 10^{-11}m, diffusion occurs at the molecular level. Molecular diffusion is simply due to the thermal motion of particles at temperatures above absolute zero. The rate of movement depends on temperature, viscosity of the entraining fluid and mass of the particles. Molecular diffusion is responsible for the net flux of molecules from a region of higher concentration to one of lower concentration, but diffusion can also occur without an initial concentration gradient. In time the diffusion process will eventually result in complete mixing.

At the largest scale, average flow brings two discrete bodies of differing salinity levels together to allow the intermediate scale of mixing to occur, also referred to as turbulence. In a stratified flow system, turbulent mixing occurs across the interface of the two fluid bodies whereby salt is carried in the overlying fresh water by the mechanism of breaking internal waves, also referred to as Kelvin-Helmholtz instabilities. Turbulence along the interface greatly increases the surface area of the interface, allowing increased rates of molecular diffusion, which is the only mixing process that ultimately generates brackish water.

Limitation of the length scale of turbulence by stratification has profound effects on the ability of the flow to diffuse momentum, density, suspended particulate matter (Kay et al, 2003). Three important turbulence length scales exist in a stratified flow. The Ozmidov scale, $L_{OZ} = (\varepsilon/N^3)^{\frac{1}{2}}$, is the largest scale of vertical overturns in which the potential energy results from utilization of all of the turbulent kinetic energy (TKE) available in the

turbulence (Ozmidov, 1965). The Ellison scale, $L_T = -\rho'_{rms}/\rho_Z$, represents the typical vertical displacement of fluid, where ρ'_{rms} is the root mean squared variance of density as measured by a density sensor recording at a fixed position in the flow (Ellison, 1957). The Kolmogorov microscale, $L_K = (\nu^3/\varepsilon)^{\frac{1}{4}}$, where ν is the kinematic viscosity, is the scale at which viscous effects become important, or a fraction of a millimeter or less in estuarine mixing.

In the definition of the Ozmidov scale, *N* is the Brunt–Väisälä buoyancy frequency or tendency of a fluid parcel to oscillate:

$$N = \left(\frac{-g}{\rho_0}\frac{\partial \rho}{\partial z}\right)^{\frac{1}{2}} \tag{2-18}$$

The condition for stable stratification exists when $N^2 > 0$ and unstable stratification exists when $N^2 < 0$.

High velocity gradients increase turbulent mixing and weaken stratification. However, in flows with strong vertical density gradients, turbulent mixing is limited by the buoyancy forces. The stability of the stratification may be characterized by the interaction between buoyancy forces and turbulent shear production through the Richardson number:

$$Ri = \frac{N^2}{\left(\frac{du}{dz}\right)^2} \tag{2-19}$$

where *N* is the Brunt–Väisälä frequency. Velocity shear is considered to overcome the tendency of a stratified fluid to remain stratified for $Ri < 0.25$ and turbulent mixing will occur. Turbulent mixing is generally suppressed for large values of *Ri* (Richardson, 1920).

2.4 Salt Wedge Estuary Sedimentation Processes

In estuaries, a large portion of the sediment load consists of fine grained clay and silt particles. This is especially the case for salt wedge estuaries where flow conditions in the freshwater source are low enough to allow progression of a salinity wedge. Flocculation of clay and fine silt particles, as well as erosion and deposition of cohesive sediment between

the bed and the water column are the primary drivers of sedimentation processes within a salt wedge estuary.

2.4.1 Flocculation of fine sediments

Electrostatic forces created by the surface ionic charges of the clay particles (and to a lesser degree, very fine silt particles) cause the particles to flocculate. Salinity modifies the charges by adsorption of cations and formation of an electrical double layer. Flocculation potential is dependent on their concentration and turbulent shearing within the fluid. At low concentrations, a small amount of shearing enhances the collision potential of the particles, but a higher shearing collision will tend to disrupt flocs rather than promote their growth. Therefore, floc size, density, and strength are all functions of salinity, concentration and turbulent shearing (van Leussen, 1988, Graf, 1971).

Chien and Zhaohui described the changes that occur to the fine particles during the flocculation process in this way:

1) In homogeneous suspensions of fine sediment particles in water, a film of bound water adheres to the surface of every particle.

2) If several fine particles form a floc, in addition to the bound water film on the particle surface, some free water is confined within the floc. This confined water cannot be separated from the floc by gravitational force. Therefore the effective diameter of the sediment particles is larger. At this stage, the flocs are suspended in water homogeneously.

3) A network structure is formed by the connection of flocs. At first, the structure is loose and the spaces within the structure are relatively large. These spaces are filled with free water that can be squeezed out by gravitational force (called gravitational free water).

4) If the structure is dense and the flocs are close to each other, the spaces within the structure and the corresponding amount of gravitational free water are less. If the spaces are small enough, the gravitational free water within the spaces may change to confined free water.

Factors affecting degree of flocculation include mineral composition of sediment particles, quality of the water and particle size. The finer the particle is, the stronger the physico-chemical effect on a particle surface, and hence the stronger the flocculation (Chien and Zhaohui, 1999).

Migniot studied the various factors affecting the flocculation process including size distribution, mineral composition, salinity, etc…, defining a flocculation factor F to indicate the magnitude of the flocculation effect:

$$F = \omega_{F50}/\omega_{D50} \tag{2-20}$$

in which ω_{F50} and ω_{D50} are the mean settling velocities of a floc and a basic sediment particle. From experiments, Migniot obtained a relationship between flocculation factor F and the size of a basic particle, as shown in Figure 2-9.

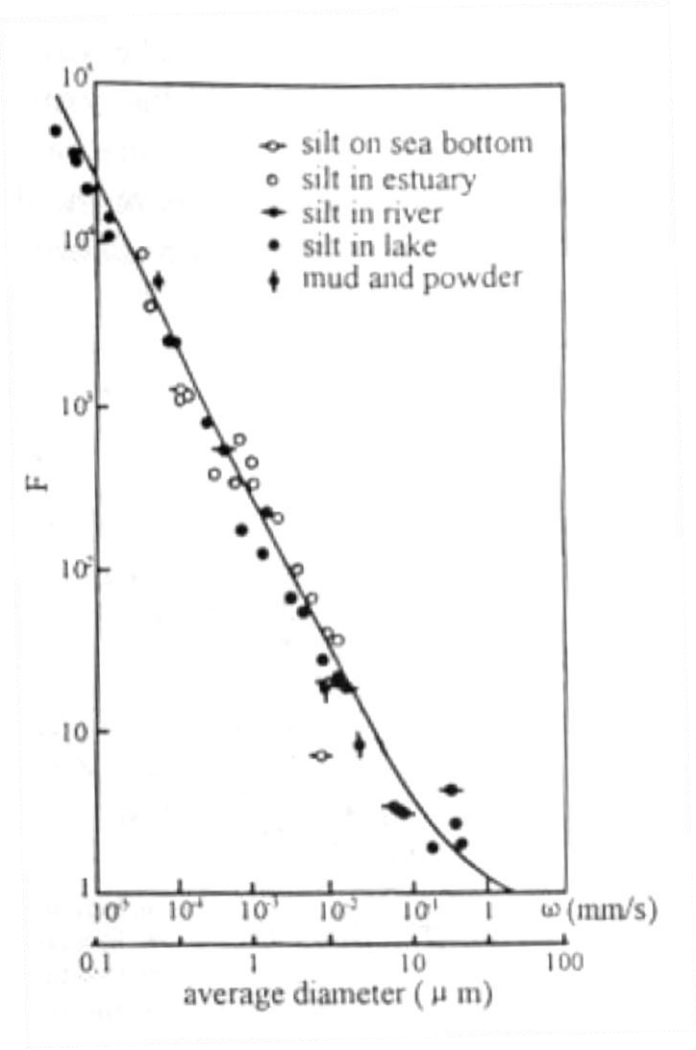

Figure 2-9 F vs. size of a basic particle (based on a figure from Migniot, 1968)

The figure shows that the settling velocity of flocs can be a thousand or more times that of a single particle and the effect of flocculation is less for larger particles. If the particle size is greater than 0.03 mm, flocculation has no effect and the effect of flocculation is small if the particle size is between 0.01 mm and 0.03 mm. A practical upper limit for a particle size to be affected by flocculation may be considered to be approximately 0.01 mm.

The finer the sediment, the larger the flocculation factor and the larger the settling velocity of a floc is compared to the basic particle. This means that the settling velocities of

flocs are much less variable than the fall velocities of basic particles. Migniot found that for silt suspensions with flocs, the mean settling velocity was within the range of 0.15 and 0.6 mm/s, independent of the size of the basic particles (Migniot, 1968).

Migniot summarized the effect of salinity on floc settling velocity with a family of curves representing several different concentrations of fine sediment. For each curve, the fall velocity increases rapidly as the salinity increases from a low concentration. At a certain salinity threshold, the fall velocity no longer increases as the salinity increases. For higher sediment concentrations, the maximum fall velocity is reached at lower salinity values. For very high sediment concentrations (10 kg/m^3 or higher), the fall velocity may decrease at higher salinity concentrations (Migniot, 1968). This is due to the flocs connecting to each other and forming a skeleton microstructure which tends to decrease settling velocity, however, this phenomenon is not a concern with the Mississippi estuary due to the lower in-situ fine sediment concentration range.

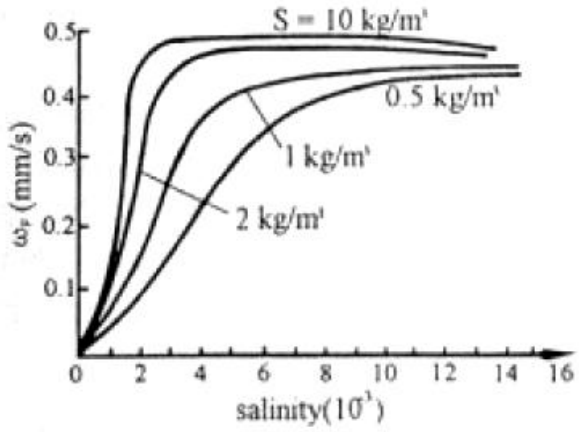

Figure 2-10 Effect of salinity on floc settling velocity (based on a figure from Migniot, 1968)

Mehta and Li gave a general expression for aggregate settling velocity which divided the settling range into four zones – free settling, flocculation settling, hindered settling and negligible settling which are expressed as:

$$\bar{W}_s(C) = \begin{cases} W_{s50}, C < C_1; \text{Free settling} \\ a_w \dfrac{C^{n_w}}{(C^2 + b_w^2)^{m_w}}; \text{Flocculation and Hindered settling} \\ C_3 < C; \text{ Negligible settling} \end{cases} \quad (2\text{-}21)$$

where C = total fine sediment concentration, W_{s50}=free settling velocity, a_w, n_w, b_w, and m_w=empirical settling coefficients, C_1=0.1-0.3 kg/m^3, and C_3=2-5 kg/m^3. Hindered settling occurs when the suspended sediment concentration increases and inhibits consolidation (Mehta and Li, 1996).

Portela, Ramos, and Trigo-Teixeira confirmed the effect of salinity on settling velocity of flocs by examining sediment samples from the Tagus estuary in Portugal using a settling column apparatus. The sediment samples consisted of mixtures with 63% clay and 37% non-clay minerals. The D_{10}, D_{50}, and D_{90} diameters were 2, 9, and 37 microns respectively. Figure 2-11 displays the experiment results as a plot of observed settling velocity as a function of salinity. In addition to the median settling velocity, the mass weighted velocities were evaluated, which is thought to be a more accurate representation of the sediment fluxes to the bed. The observed floc settling velocities are not inconsistent with Stoke's law for freshwater conditions given the grain size distribution of the sediment (Portela Ramos, and Trigo-Teixeira, 2013).

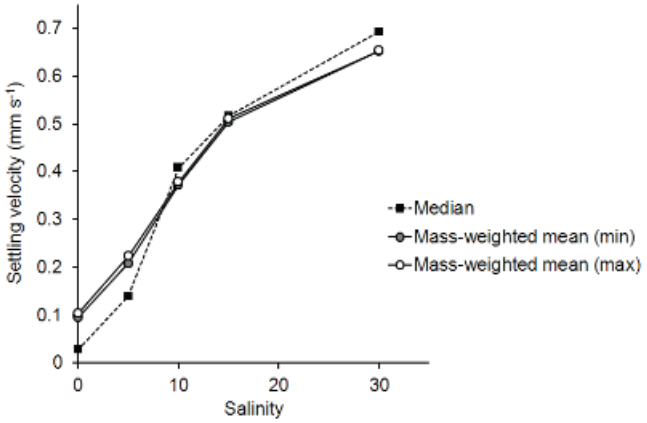

Figure 2-11 Floc settling velocities under the influence of salinity for Tagus estuary samples (from Portela et al., 2013)

2.4.2 Fine sediment deposition and erosion

Krone investigated San Francisco Bay sediments and found salinity triggers floc formations at concentrations as low as 1 g/L salinity for which the attractive forces begin to overcome the repulsive forces between particles. The median settling velocity was found to attain a maximum from a salinity of 5 g/L for 120 ppm sediment concentration to 15 g/L ppm for a sediment concentration of 1,000 ppm. For unhindered settling, Krone found that the median settling velocity of fines follows the 4/3 law:

$$w_s = \alpha_8 C^{4/3} \tag{2-22}$$

where α_8 is a dimensional constant.

According to Krone, hindered settling occurs starting at about 10 g/L and his experiments followed the equation:

$$\frac{V_{ft}}{V_{f\infty}} - 1 = \frac{k_f}{t} \tag{2-23}$$

where V_{ft} is the flocculent volume in time t, $V_{f\infty}$ is the flocculent volume at an infinite time and k_f is a constant with dimensions of time given as 0.95 of the time required for the flocculent volume to become equal to $2V_{f\infty}$.

Using flume experimentation with a fine sediment bed and the sediment continuity principle, Krone developed the following theory for deposition of cohesive sediments below sediment concentrations of 0.3 g/L:

$$\frac{dC}{dt} = -C v_s \frac{P_r}{y_0} \tag{2-24}$$

where P_r is the probability of a settling unit to stick to the bed, y_0 is the depth of the fluid in the flume, C is the sediment concentration at time t and v_s is the settling velocity.

The Krone fine sediment deposition formulation is easily adapted to numerical models and is widely used today in numerous 1D and multi-dimensional model codes to

compute the deposition flux of cohesive sediment fractions between the water column and the bed (Krone, 1972).

$$D = w_s C_b \left(1 - \frac{\tau_b}{\tau_d}\right) \tag{2-25}$$

Partheniades conducted flume studies to evaluate erosion characteristics of fine sediment beds (Partheniades, 1965). Using a stochastic process similar to that employed by Krone for deposition processes and Einstein for coarse grain transport (Einstein, 1950), a formula was developed relating erosion rate to the bed shear stress:

$$E = \frac{AD_S\gamma_S}{t^{(\tau_0)}}P \tag{2-26}$$

where A is a shape factor, D is the average diameter of a clay particle or clay cluster, γ_s is the unit weight of solids, $t^{(\tau 0)}$ is the time required for the breaking of a particle acted on by a shear stress, τ_0 and P is the probability of a particle being eroded during the unit time.

Ariathurai would later linearize Partheniade's non-linear erosion relationship leading to the empirical relationship:

$$E = M\left(\frac{\tau_b}{\tau_{cr}} - 1\right) \tag{2-27}$$

where M is an erosion parameter, τ_b is the bed shear stress, and τ_{cr} is the bed shear stress with respect to erosion. This erosion relationship is referred to as the "Ariathurai-Partheniades" formula. Collectively with the deposition relationship developed by Krone, the formulas are knows as the Partheniades-Krone formulations for determination of the cohesive sediment fraction flux between the water column and sediment bed (Partheniades, 2007).

3 GOVERNING EQUATIONS FOR A 3D ESTUARY MODEL

3.1 Conservation Laws of Physics

The governing equations of fluid flow as it pertains to macro-scale applications such as an estuary stem from mathematical statements of the conservation laws of physics, principally the conservation of mass and momentum. Molecular motions are generally ignored in these macro-scale applications and the behavior of the fluid may be described in terms of its macroscopic properties such as velocity, pressure, density and temperature, and their space and time derivatives. These properties are regarded as averages defining a fluid particle and are not influenced by individual molecules.

The conservation of mass for a fluid particle may be stated as: the rate of increase or decrease of mass in a fluid particle is equal to the net rate of flow of mass into or out of the fluid particle. For an incompressible fluid such as water, in which case the density, ρ, is assumed to be constant, the equation for conservation of mass becomes:

$$\frac{\partial u}{\partial x}+\frac{\partial v}{\partial y}+\frac{\partial w}{\partial z}=0 \tag{3-1}$$

where $u(x,y,z,t)$, $v(x,y,z,t)$, and $w(x,y,z,t)$ are the time-dependent Reynolds-averaged velocities in the x,y, and z Cartesian directions (x and y in the horizontal direction and z in the vertical), and t is the time.

Newton's second law of motion (conservation of momentum) states that the vector sum of the forces on an object is equal to the total mass of that object multiplied by the acceleration of the object. When applying Newton's second law of motion to a fluid particle, the law states that the rate of change of momentum of a fluid particle equals the sum of the forces on the particle or:

$$\frac{D(\rho\vec{u})}{Dt}=\vec{F}_V, \tag{3-2}$$

in which ρ is the fluid density, $\vec{u}$ is the velocity of the fluid element and $\vec{F}_V$ is the resulting volume forces on the fluid element.

3.2 The Navier-Stokes Equations

The Navier-Stokes equation describes the motion of a viscous Newtonian fluid. The equation arises from applying Newton's second law to fluid motion, together with the assumption that the stress in the fluid is the sum of a diffusing viscous term, proportional to the gradient of velocity, and a pressure term. The general form of the equation of fluid motion is:

$$\frac{D(\rho\vec{u})}{Dt} = \rho\vec{F} - \nabla p + \rho\nu\nabla^2\vec{u} \tag{3-3}$$

where $\vec{u}(\vec{x},t)$ is the flow velocity, $\vec{x}$ is the place vector, t is time, $p(\vec{x},t)$ is the pressure, $\vec{F}$ represents body forces (per unit volume) acting on the fluid, and ν is the molecular viscosity.

The full set of Navier-Stokes equations for an incompressible fluid (i.e., water) in Cartesian form is:

$$\frac{\partial u}{\partial t} + u\frac{\partial u}{\partial x} + v\frac{\partial u}{\partial y} + w\frac{\partial u}{\partial z} = -\frac{1}{\rho}\frac{\partial p}{\partial x} - g\frac{\partial \eta}{\partial x} + \nu\left(\frac{\partial^2 u}{\partial x^2} + \frac{\partial^2 u}{\partial y^2} + \frac{\partial^2 u}{\partial z^2}\right) \tag{3-4}$$

$$\frac{\partial v}{\partial t} + u\frac{\partial v}{\partial x} + v\frac{\partial v}{\partial y} + w\frac{\partial v}{\partial z} = -\frac{1}{\rho}\frac{\partial p}{\partial y} - g\frac{\partial \eta}{\partial y} + \nu\left(\frac{\partial^2 v}{\partial x^2} + \frac{\partial^2 v}{\partial y^2} + \frac{\partial^2 v}{\partial z^2}\right) \tag{3-5}$$

$$\frac{\partial w}{\partial t} + u\frac{\partial w}{\partial x} + v\frac{\partial w}{\partial y} + w\frac{\partial w}{\partial z} = -\frac{1}{\rho}\frac{\partial p}{\partial z} - g\frac{\partial \eta}{\partial z} + \nu\left(\frac{\partial^2 w}{\partial x^2} + \frac{\partial^2 w}{\partial y^2} + \frac{\partial^2 w}{\partial z^2}\right) \tag{3-6}$$

where η denotes the vertical direction (Prasuhn, 1980).

3.3 The Boussinesq Approximation for Buoyancy-Driven Flows

The Boussinesq approximation assumes that density differences are sufficiently small ($\frac{\Delta\rho}{\rho_0} \ll 1$, where ρ_0 is a reference density) so as to be neglected, except where they appear in terms multiplied by the acceleration due to gravity. Essentially, the Boussinesq approximation assumes that the difference in inertia is negligible but gravity is sufficiently strong to make the specific weight appreciably different between the two fluids (buoyancy). Applying the Boussinesq approximation, the equation of fluid motion now takes the form:

$$\frac{D\vec{u}}{Dt} = \frac{\rho}{\rho_0}\vec{F} - \frac{1}{\rho_0}\nabla p + \nu\nabla^2\vec{u} \tag{3-7}$$

where $\vec{u}(\vec{x},t)$ is the flow velocity, $\vec{x}$ is the place vector, t is time, $p(\vec{x},t)$ is the pressure, $\vec{F}$ represents body forces (per unit volume) acting on the fluid, and ν is the molecular viscosity.

3.4 The Reynolds Averaged Navier-Stokes Equations

Model codes that solve the Navier-Stokes equations are available but are computationally expensive. The multi-dimensional model codes available for estuary applications are largely based on the Reynolds averaged Navier-Stokes (RANS) Equations. The RANS equations are derived from the Navier-Stokes equations through temporal averaging of instantaneous velocities over an appropriate time scale (Spasojevic and Holly Jr., 2008). This operation results in a shift of the stresses associated with the momentum exchange of correlated fluctuating velocities from the momentum advection terms to Reynolds stress terms. The Reynolds stresses must then be resolved using a turbulence model.

Reynolds proposed splitting the velocity into a mean and fluctuating part, where $u = \bar{u} + u'$, $v = \bar{v} + v'$, and $w = \bar{w} + w'$. This velocity decomposition, together with the definition of the turbulent shear stresses; $\tau_{xx} = -\rho\overline{u'u'}$, $\tau_{yx} = -\rho\overline{v'u'}$, $\tau_{zx} = -\rho\overline{w'u'}$, etc...,

gives rise to the long form of the Reynolds-averaged *u*-, *v*-, and *w*-momentum conservation equations utilizing the Boussinesq approximation:

$$\frac{\partial u}{\partial t}+\frac{\partial (uu)}{\partial x}+\frac{\partial (vu)}{\partial y}+\frac{\partial (wu)}{\partial z} = fv-\frac{1}{\rho_0}\rho g\frac{\partial \eta}{\partial x}-\frac{1}{\rho_0}\frac{\partial p}{\partial x}+\frac{1}{\rho_0}\left(\frac{\partial \tau_{xx}}{\partial x}+\frac{\partial \tau_{yx}}{\partial y}+\frac{\partial \tau_{zx}}{\partial z}\right) \quad (3\text{-}8)$$

$$\frac{\partial v}{\partial t}+\frac{\partial (uv)}{\partial x}+\frac{\partial (vv)}{\partial y}+\frac{\partial (wv)}{\partial z} = -fu-\frac{1}{\rho_0}\rho g\frac{\partial \eta}{\partial y}-\frac{1}{\rho_0}\frac{\partial p}{\partial y}+\frac{1}{\rho_0}\left(\frac{\partial \tau_{xy}}{\partial x}+\frac{\partial \tau_{yy}}{\partial y}+\frac{\partial \tau_{zy}}{\partial z}\right) \quad (3\text{-}9)$$

$$\frac{\partial w}{\partial t}+\frac{\partial (uw)}{\partial x}+\frac{\partial (vw)}{\partial y}+\frac{\partial (ww)}{\partial z} = -\frac{1}{\rho_0}\rho g\frac{\partial \eta}{\partial z}-\frac{1}{\rho_0}\frac{\partial p}{\partial z}+\frac{1}{\rho_0}\left(\frac{\partial \tau_{xz}}{\partial x}+\frac{\partial \tau_{yz}}{\partial y}+\frac{\partial \tau_{zz}}{\partial z}\right) \quad (3\text{-}10)$$

where $\rho(x,y,z,t)$ is the density of the water and sediment mixture, ρ_0 is the reference density, g is the gravitational acceleration constant, η represents the vertical direction, and $p(x,y,z,t)$ is the pressure term. f represents a Coriolis parameter equal to $2\Omega\sin\varphi$, with Ω, the angular rotational velocity and φ the latitude. This parameter is important when modeling large water bodies such as the subject for this study. τ represents the fluid shear tensor, incorporating molecular stresses and those stresses resulting from the Reynolds averaging process. The molecular stresses are much smaller than the Reynolds stresses and are generally neglected in macro-scale model codes. However, the stresses resulting from the Reynolds averaging process cannot be neglected and a separate process is used to compute these stresses and achieve closure of the RANS equation set, this is referred to as a turbulence closure model.

3.5 The Hydrostatic Pressure Assumption (Shallow-Water Equations)

For large scale system models, where the horizontal length scale is much greater than the vertical length scale, it is possible to considerably simplify the RANS equations by assuming that the pressure gradient is hydrostatic in the vertical. In essence, vertical accelerations of the fluid are ignored and the pressure variation is assumed to be linear from the surface to any point below. Therefore:

$$\frac{\partial}{\partial z}\left(z+\frac{p}{\rho g}\right)=0 \tag{3-11}$$

The free surface elevation is represented in the equation as:

$$z+\frac{p}{\rho g}=\zeta(x,y,t) \tag{3-12}$$

The introduction of the hydrostatic pressure assumption into the RANS 3D equation set greatly simplifies the computational requirements by replacing the pressure with the free surface elevation as one of the dependent variables, the resultant horizontal momentum equations are:

$$\frac{\partial u}{\partial t}+\frac{\partial(uu)}{\partial x}+\frac{\partial(vu)}{\partial y}+\frac{\partial(wu)}{\partial z} = fv-g\frac{\partial(z_b+h)}{\partial x}-\frac{g}{\rho_0}(\zeta-z)\frac{\partial\rho}{\partial x}+\frac{1}{\rho_0}\left(\frac{\partial\tau_{xx}}{\partial x}+\frac{\partial\tau_{yx}}{\partial y}+\frac{\partial\tau_{zx}}{\partial z}\right) \tag{3-13}$$

$$\frac{\partial v}{\partial t}+\frac{\partial(uv)}{\partial x}+\frac{\partial(vv)}{\partial y}+\frac{\partial(wv)}{\partial z} = -fu-g\frac{\partial(z_b+h)}{\partial y}-\frac{g}{\rho_0}(\zeta-z)\frac{\partial\rho}{\partial y}+\frac{1}{\rho_0}\left(\frac{\partial\tau_{xy}}{\partial x}+\frac{\partial\tau_{yy}}{\partial y}+\frac{\partial\tau_{zy}}{\partial z}\right) \tag{3-14}$$

where $z_b(x,y)$ is the bed elevation above datum and $h(x,y,t)$ is the flow depth. The flow depth can now be computed by solving the depth-averaged two-dimensional case. The free surface elevation is now a known variable in the remaining 3D equations. The vertical velocity w in a 3D model code may not necessarily be involved in the computation process and may be computed for post-processing needs from the continuity equation.

The density-gradient terms are retained in the shallow water equations to account for changes in density due to salinity, temperature, and constituent concentration. The density-gradient terms are simplified from the RANS equations by replacing p/ρ with $g(\zeta - z)$, combining the hydrostatic-pressure assumption and the Boussinesq approximation. Density can now be evaluated from the state equations for salinity and temperature and/or an empirical sediment transport relationship.

3.6 Equations of State

The density of water ρ_w is a function of its dissolved constituents and temperature. In the case of saline water, the density was determined directly through a series of measurements and follows the relationship (UNESCO, 1981a,b):

$$\rho_w = \rho_0 + AS + BS^{3/2} + CS^2 \tag{3-15}$$

where

$$\rho_0 = 999.842594 + 6.793952 \times 10^{-2}T - 9.095290 \times 10^{-3}T^2 + 1.001685 \times 10^{-4}T^3 - 1.120083 \times 10^{-6}T^4 + 6.536332 \times 10^{-9}T^5$$

$$A = 8.24493 \times 10^{-1} - 4.0899 \times 10^{-3}T + 7.6438 \times 10^{-5}T^2 - 8.2467 \times 10^{-7}T^3 + 5.3875 \times 10^{-9}T^4$$

$$B = -5.72466 \times 10^{-3} + 1.0227 \times 10^{-4}T - 1.6546 \times 10^{-6}T^2$$

$$C = 4.8314 \times 10^{-4}$$

This relationship is valid for temperature T between 0 and 40℃ and salinities S between 0.5 and 43 ppt.

In the case of sediment laden water, the density of the fluid mixture may be adjusted by determination of the volume of the sediment mass and subtraction of the mass of displaced water resulting in a density estimate of the water and sediment mixture:

$$\rho_{mixture} = \rho_w + C\left(1 - \frac{\rho_w}{\rho_s}\right) \tag{3-16}$$

in which ρ_w is the density of fresh or saline water, C is the sediment concentration, and ρ_s is the specific sediment density.

3.7 Convection-Diffusion (Transport) Equation

The convection-diffusion equation (scalar transport equation) describes the transfer of a constituent (heat, salinity, mass particles, etc…) inside a system due to diffusion and convection processes. Therefore, it is a combination of the diffusion and convection equations. The general form of the equation is:

$$\frac{\partial c}{\partial t} = \nabla \cdot (D\nabla c) - \nabla \cdot (\vec{v}c) + R \tag{3-17}$$

In this form of the equation, c is the scalar quantity of interest; D represents diffusivity, and $\vec{v}$ is the average velocity that the quantity is moving. For example, if c represents salt in a river, then $\vec{v}$ would represent the velocity of the river flow. R represents the various sources and sinks of the constituent. ∇ represents gradient and $\nabla \cdot$ represents divergence.

The diffusion process is represented by the $\nabla \cdot (D\nabla c)$ contribution on the right hand side of the transport equation. Using the example of dissolved salt in a river, this process describes the movement of salt concentration from higher concentration areas to lower concentration areas through the diffusion process.

The convection process is represented by the $-\nabla \cdot (\vec{v}c)$ contribution on the right hand side of the equation. Again using a river as an example, this process describes the movement of a higher temperature mass of water released into a river from an industrial facility as it moves downriver with the river flow (advection).

The source and sink term, *R*, may represent the exchange of sediment and organic matter between the bed and the water column in the case of an estuary system. If the system is defined with the bed as a boundary, in the case of sediment particles, the grain settling velocity would govern the removal of particles from the system and the grain slip velocity (onset of incipient motion) would govern the addition of particles to the system.

3.8 Exner Equation

In addition to consideration of transport of matter through the advection process, the exchange of material between the bed and water column may be accounted for in an estuary model. The Exner equation is an intuitive sediment mass-conservation equation (Spasojevic, 2008) and accounts for exchange of material between the bed and the water column as well as the bed load flux:

$$\rho_s(1-p_b)\frac{\partial z_b}{\partial t} + \nabla \cdot \vec{q}_b + E - D = 0 \tag{3-18}$$

ρ_s is the density of sediment assumed to be constant, p_b is the porosity of the bed material, assumed to be constant, z_b represents the bed-surface elevation, $\vec{q}_b$ is the bed-load flux, E is the entrainment flux from the bed to the water column and D is the deposition flux from the water column to the bed. The Exner equation is essentially two-dimensional in the plane parallel with the bed.

4 NUMERICAL MODELING CONCEPTS

4.1 Numerical solution techniques

Numerical models may be classified by the number of dimensions of discretization. For example, a one-dimensional model (1D) scheme would be composed of uniformly or variably spaced cross sections in the horizontal or vertical direction as needed to define the geometry of the prototype. 1D models have been proven to be very useful in river studies where the flow is not stratified and cross channel currents are not a major concern. Erosion and deposition of sediment are generally averaged over the entire submerged portion of the cross section. The application of a1D model in estuary problems would be limited to situations in which the flow direction is predominantly perpendicular to the cross section orientation and constituents are well mixed.

A two-dimensional (2D) model adds an additional computational dimension over the 1D model. Normally, for river and estuary applications, the additional dimension is in the horizontal direction so that velocity may be computed in the horizontal x and y directions. As the velocity over the water column would be necessarily uni-directional, these depth averaged models would be incapable of resolving stratified flow. However, the additional dimension may be in the vertical direction resulting in a laterally averaged scheme. Such laterally averaged 2D models have proven to be useful in modeling stratified flow in rivers and estuaries and have been applied in the Mississippi River estuary to model salinity intrusion (Johnson, 1987). However, as in the 1D model case, sediment erosion and deposition would be averaged over the lateral section. These laterally averaged models would not be capable of resolving sedimentation patterns across the river channel.

Therefore a three-dimensional (3D) model is required to simulate both flow stratification and cross channel sedimentation patterns as exist in the Mississippi River estuary. In general, there are three methods used to solve 3D mobile bed problems. They are the finite-difference, finite-element, and finite-volume approaches. Finite-difference solvers utilize an orthogonal fixed or curvilinear grid, while finite-element and finite-

volume solvers may employ a structured or unstructured grid. The number of 3D (necessary for salinity stratification) mobile bed codes is rather small. Two examples of available mobile bed codes employing the finite-difference solution technique are CH3D-SED (Spasojevic and Holly Jr., 1993), and Delft3D (Putra et. al., 2015). ADH (Savant, Berger, and McAlpin, 2014) is an example of a finite-element flexible mesh solver, however, at the time of this writing, the 3D version of the code is under development and support of sediment transport with the 3D version is still at the research level. Another code under development is a flexible mesh version of the Delft3D code. Since 3D mobile bed codes employing the finite-difference approach are more widely available at this time, the focus of discussion in this study will be the finite-difference scheme.

Finite-difference methods are numerical methods for approximating the solutions to differential equations using finite difference equations to approximate derivatives. This is a fundamental difference to the finite-element and finite-volume methods which are integral based approaches in the sense that they are derived not through approximations of partial derivatives, but rather through consideration of conservation laws applied to volumetric elements and careful evaluation of fluxes across nonparallel faces of the elements (Spasojevic and Holly Jr., 2008).

One considerable disadvantage to the finite-difference scheme is the need to construct grid lines along parallel lines. This means that if refinement in the grid is desired, then the same refinement must be applied in both grid directions whether the refinement is needed in other parts of the grid or not. However, considerable computational efficiency is gained by structuring algorithms along single grid lines in each of the three directions. This grid inflexibility is somewhat overcome by introduction of a curvilinear relaxation aspect to the grid, but finite-difference grids will never be able to achieve the flexibility in grid construction of finite-element approaches.

4.2 Courant-Friedrichs-Lewy condition

The Courant-Friedrichs-Lewy (CFL) time step limitation must be obeyed to achieve numerical stability in finite difference schemes (Courant, Friedrichs, and Lewy, 1967). In principle, if a wave is moving across a discrete spatial grid, then the length between grid points must be less than the time for the wave to travel to the adjacent grid point. In practice, this means that the time step is proportional to the grid point spacing. The general CFL condition for the *n*-dimensional case is:

$$CFL_{wave} = \Delta t \sum_{i=1}^{n} \frac{u_{x_i}}{\Delta x_i} \leq CFL_{max} \tag{4-1}$$

in which u is the magnitude of the velocity, Δt is the time step, and Δx is the length interval. The value of CFL_{max} changes with the method used to solve the discretised equation. If an explicit solver is used then typically, $CFL_{max} = 1$. Implicit solvers are usually less sensitive to numerical instability, so larger values of CFL_{max} are tolerated.

For numerical solvers employing the shallow water equations, the condition takes the form:

$$CFL_{wave} = 2\Delta t\sqrt{gH}\sqrt{\frac{1}{\Delta x^2} + \frac{1}{\Delta y^2}} \tag{4-2}$$

where g is the acceleration due to gravity and H is the total water depth. Δx and Δy represent the smallest grid spaces in both horizontal directions of the physical space.

4.3 The Crank-Nicolson finite-difference solver

Due to the time step limitations imposed on a finite-difference solver by the CFL condition, an implicit method may be employed to keep the time steps as large as possible while still adhering to the CFL condition. Implicit methods solve a set of equations

involving both the current state of the system and a later one, while explicit methods calculate the state of a system at a later time from the state of the system at the current time. If $Y(t)$ is the current system state and $Y(t + \Delta t)$ is the state at the later time, then, for an explicit method:

$$Y(t + \Delta t) = F(Y(t)) \tag{4-3}$$

An implicit solver solves the equation:

$$G\big(Y(t), Y(t + \Delta t)\big) = 0 \tag{4-4}$$

Implicit methods require an extra computation, but this extra computational burden is more than compensated for by the ability to use somewhat larger time steps to achieve the same level of accuracy. Explicit methods typically require very small time steps to keep the error in the result bounded.

One commonly used implicit numerical technique is the Crank-Nicolson method. The method is based on central difference in space and the trapezoidal rule in time, resulting in second-order convergence in time and is unconditionally stable (Crank and Nicolson, 1947).

For example, if the partial differential equation is:

$$\frac{\partial u}{\partial t} = F\left(u, x, t, \frac{\partial u}{\partial x}, \frac{\partial^2 u}{\partial x^2}\right) \tag{4-5}$$

and letting $u(j\Delta x, n\Delta t) = u_j^n$, the Crank-Nicolson method is then a combination of the forward Euler method at n and the backward Euler method at $n + 1$:

$$\frac{u_j^{n+1} + u_j^n}{\Delta t} = F_j^n\left(u, x, t, \frac{\partial u}{\partial x}, \frac{\partial^2 u}{\partial x^2}\right) \quad \text{(forward Euler)} \tag{4-6}$$

$$\frac{u_j^{n+1} + u_j^n}{\Delta t} = F_j^{n+1}\left(u, x, t, \frac{\partial u}{\partial x}, \frac{\partial^2 u}{\partial x^2}\right) \quad \text{(backward Euler)} \tag{4-7}$$

$$\frac{u_j^{n+1} + u_j^n}{\Delta t} = \frac{1}{2}\left[F_j^{n+1}\left(u, x, t, \frac{\partial u}{\partial x}, \frac{\partial^2 y}{\partial x^2}\right) + F_j^n\left(u, x, t, \frac{\partial u}{\partial x}, \frac{\partial^2 y}{\partial x^2}\right)\right] \text{(Crank} - \text{Nicolson)} \tag{4-8}$$

The six grid points utilized in the Crank-Nicolson method are displayed conceptually in Figure 4-1.

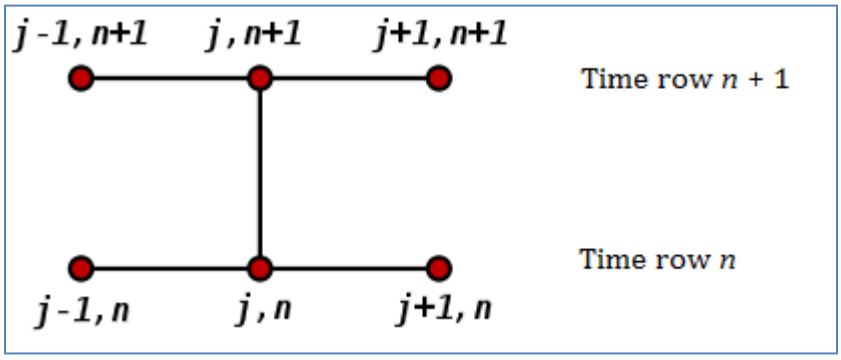

Figure 4-1 The six points in the Crank-Nicolson scheme, "Crank-Nicolson-stencil" by Berland at English Wikipedia - Transferred from en.wikipedia to Commons.. Licensed under Public Domain via Commons - https://commons.wikimedia.org/wiki/File:Crank-Nicolson-stencil.svg#/media/File:Crank-Nicolson-stencil.svg

4.4 The Alternating Direction Implicit time integration method

The Crank-Nicolson method results in a very complicated set of equations in multiple dimensions in which the band width of the resultant matrix created by the method is generally quite large which makes the solution of the system of linear equations computationally demanding to solve. The Alternating Direction Implicit (ADI) method was introduced in 1955 as a technique for the numerical solution of elliptic and parabolic differential equations and has the distinct advantage of generating a tridiagonal matrix which is more efficiently handled by matrix solvers (Peaceman and Rachford, 1955).

For example, consider the linear diffusion equation in two dimensions,

$$\frac{\partial u}{\partial t} = \left(\frac{\partial^2 u}{\partial x^2} + \frac{\partial^2 u}{\partial y^2}\right) = \left(u_{xx} + u_{yy}\right) = \Delta u \tag{4-9}$$

The Crank-Nicolson method produces the following finite difference equation:

$$\frac{u_{ij}^{n+1} - u_{ij}^{n}}{\Delta t} = \frac{1}{2}\left(\delta_x^2 + \delta_y^2\right)\left(u_{ij}^{n+1} + u_{ij}^{n}\right) \tag{4-10}$$

where δ_p is the central difference operator for the p-coordinate. The ADI method splits this finite difference equation into one equation with the x-derivative taken implicitly and one with the y-derivative taken implicitly:

$$\frac{u_{ij}^{n+1/2} - u_{ij}^{n}}{\Delta t/2} = \left(\delta_x^2 u_{ij}^{n+1/2} + \delta_y^2 u_{ij}^{n}\right) \tag{4-11}$$

$$\frac{u_{ij}^{n+1} - u_{ij}^{n+1/2}}{\Delta t/2} = \left(\delta_x^2 u_{ij}^{n+1/2} + \delta_y^2 u_{ij}^{n+1}\right) \tag{4-12}$$

The equations thus produced by the method are symmetric and tridiagonal in nature. Additionally, the method is unconditionally stable and second order in time and space. The computational ADI stencil is displayed in Figure 4-2.

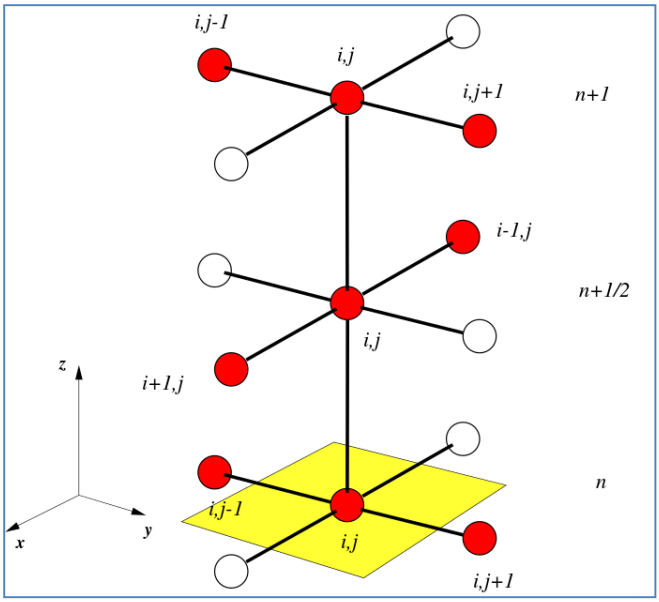

Figure 4-2 ADI stencil "ADI-stencil" by Sidney.hy.li - Own work. Licensed under CC BY-SA 3.0 via Commons - https://commons.wikimedia.org/wiki/File:ADI-stencil.svg#/media/File:ADI-stencil.svg

4.5 Discretisation of the physical space

The physical quantities may be computed by different means in the computational grid. The Arakawa grid system depicts various means of computing orthogonal physical quantities on rectangular grids. These grid systems are commonly used on finite difference grids for earth system models for meteorology and oceanography applications. For examples, the Princeton Ocean Model (Blumberg and Mellor, 1987) and the Weather Research and Forecasting Model use an Arakawa staggered C-grid configuration. The five Arakawa grids are labeled A-E, reference Figure 4-3. (Arakawa and Lamb, 1977).

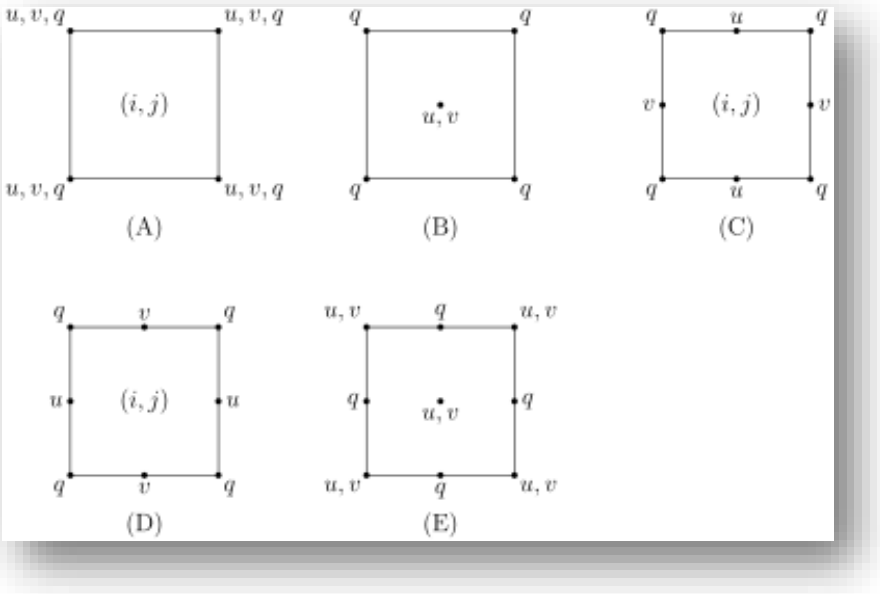

Figure 4-3 Arakawa grid types "Discretization for the different Arakawa grids" by JuliusSimplus - Generated with Asymptote to reproduce Arakawa grid. Licensed under CC BY-SA 3.0 via Commons - https://commons.wikimedia.org/wiki/File:Discretization_for_the_different_Arakawa_grids.svg#/media/File:Discretization_for_the_different_Arakawa_grids.svg

The Arakawa A-grid is the only unstaggered grid type of the five in that all quantities are computed at the same point on each grid cell, at the center or corners. The B-grid separates the two sets of quantities, mass may be computed at the corners and velocity at the center as depicted in Figure 4-3 or vice versa. The C-grid further separates the vector quantities, e. g., the mass may be computed at the corners, and the velocity components along the cell faces. A D-grid is simply a 90 degree rotation of the C-grid. The E-grid is rotated 45 degrees with respect to the other grid orientations. In this way, all quantities are computed along a single face of the cell.

4.6 Vertical discretisation techniques and mathematical diffusion

Because the shallow water equations require the z-direction to be vertical, the options available for the treatment of the vertical layering in a finite difference code solving the shallow water equation set is rather limited. Perhaps the most common and more mature method is to apply the same number of layers and vertical spacing based on percentage of water column, or the so called “sigma stretched” method, originally introduced for atmospheric models (Phillips, 1957). The vertical layering is bounded by

two sigma layers that are boundary fitted to the bottom and free surface as shown in Figure 4-4. The sigma stretched scheme is well suited to mobile bed problems as a smooth representation of the bed is achieved, resulting in accurate shear stress values.

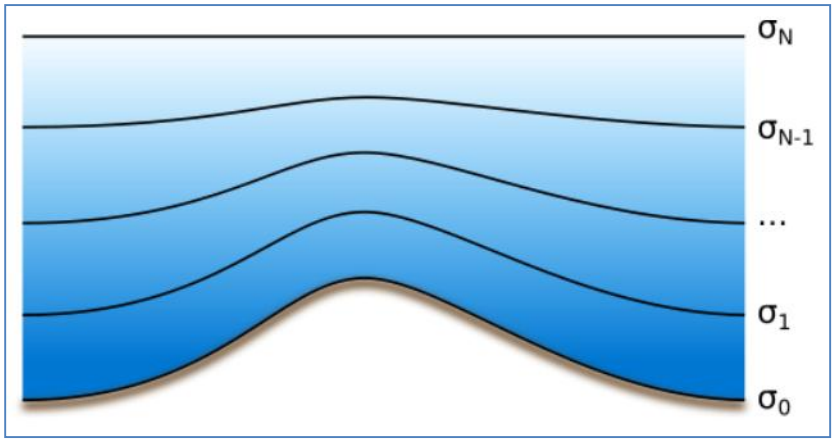

Figure 4-4 The sigma stretched layer concept. "Sigma-z-coordinates" by Titoxd - Own work. Licensed under CC0 via Commons - https://commons.wikimedia.org/wiki/File:Sigma-z-coordinates.svg#/media/File:Sigma-z-coordinates.svg

Drawbacks to the sigma stretched technique include a thinning of the layers as the water level becomes shallower as the number of vertical layers is constant throughout the grid. When modeling highly stratified systems, such as the Mississippi River salt wedge estuary, the introduction of numerical diffusion (aka sigma creep) resultant from the boundary fitted elements can prevent the model from achieving accurate stratification of the salinity.

In order to minimize artificial mathematical diffusion of scalar properties such as salinity and temperature, a Cartesian (Z-level) co-ordinate vertical layering scheme may be used. The Z-level scheme employs a number of horizontal layers to discretize the vertical direction. Therefore, the Z-level grid is not boundary fitted in the vertical and a high vertical resolution may be employed to capture the steep density gradient at the pycnocline in a weakly forced stratified estuary system. Historically, the Z-level layering method has been more commonly utilized in Groundwater modeling systems, for example, MODFLOW

developed in the early 1980's (McDonald, 2003). However, the Z-level layering scheme has more recently been deployed in Surface Water Environmental system models including the EPA's Environmental Fluid Dynamics Code (EFDC) and Deltare's Delft3D modeling system.

Hybrid layering systems have been developed to take advantage of the strengths of both layering schemes such as the contour fitting feature of the sigma method and the ability of the Z-layer scheme to more accurately render density layers. Some atmospheric models employ a hybrid sigma-pressure coordinate scheme, which combines sigma-denominated layers at the bottom following the terrain with isobaric upper layers. Hybrid methods have also been employed in coastal ocean models such as the Princton Ocean Model and the Finite Volume Coastal Ocean Model (FVCOM) to get around the mathematical diffusion problem inherent in sigma layer models, see Figure 4-5 for an example of a hybrid layering scheme.

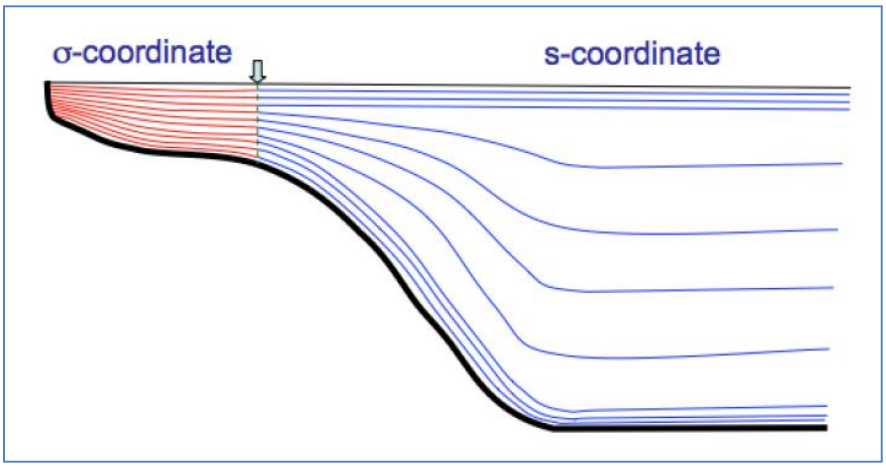

Figure 4-5 FVCOM hybrid layering concept (Chen et al, 2011)

4.7 Model Boundary Conditions

Computational models are necessarily limited in their aerial extent and will always need information at the model boundaries in order to have the ability to accurately predict conditions in the computational domain of the model. Model boundaries may be classified as open water boundaries, free surface boundaries, and bottom surface boundaries. The bottom surface and free water surface are assumed to be impermeable and the velocity

perpendicular to these impermeable boundaries (w) is assumed to be zero (kinematic boundary condition).

The free surface boundary in a shallow water model such as an estuary application can be very important as the wind may influence movement of water through wave set up and can especially influence movement of water and constituents in shallow areas such as marshes. At the free surface, the influence of wind can be defined with a wind shear stress as:

$$\tau_{wind} = \rho_{air} C_D U_h^2 \tag{4-13}$$

where ρ_{air} is the density of air, U_h is the wind speed at some specific height h, and C_D represents a dimensionless wind-drag coefficient that is a repository for all remaining dependencies. The wind shear stress may then be used to determine the surface boundary condition for the momentum equations.

The bottom surface boundary may be fixed or mobile depending on the model application. Shear stresses at the bed may come from flow and waves. For a riverine application that does not consider wave stresses, the bottom shear stress is defined as:

$$\tau_{bed} = \rho_{water} C_f U^2 \tag{4-14}$$

where ρ_{water} is the density of water, U is the depth averaged velocity, and C_f represents a dimensionless friction coefficient that is a repository for all remaining dependencies which may include friction due to vegetation, dunes, grain roughness, and other sources of roughness. A 3D model would typically consider the velocity in the bottom-most layer for shear stress calculations.

Some commonly used applications of this friction coefficient in river and estuary modeling are through the use of Manning's *n* value and the Chézy coefficient to describe bed roughness. Chézy's coefficient C_Z is related to the friction coefficient through:

$$C_Z = \left(\frac{g}{C_f}\right)^{1/2} \tag{4-15}$$

These applications of the friction coefficient are commonly used to calibrate model response to observed prototype performance.

In an estuary model application, the open water or water-to-water boundaries are usually applied as a total river or stream discharge or other inflow source and tidal boundaries at the edges of the receiving waters. Open water tide boundaries may be defined using a water level signal or by definition of the current magnitude and direction. It should be noted that water level alone is insufficient information to fully define the water exchange at tide boundaries and problems such as unrealistic re-circulation patterns may develop at these model boundaries. Sources of freshwater inflow are typically defined with a total discharge record or spatial velocity definition. These water to water boundaries may also be defined using a coarser larger domain model with the more refined local model as an inset to the larger domain model (nested models).

4.8 Turbulence closure

In order to compute turbulent flows with the RANS equations, it is necessary to determine the Reynolds stresses and the scalar transport terms in order to close the system of mean flow equations. Turbulence models are commonly used in practice to achieve this closure. Turbulence models may be classified by the number of additional transport equations that need to be solved along with the RANS equations. In practice, two of the most common closure models are the zero-equation mixing length model and the two-equation *k*-ε model.

Perhaps the first attempt to develop a turbulence model was by Boussinesq in the 1870's. As mentioned at the end of section 3.4, the total shear stress, τ represents the fluid shear tensor, incorporating molecular stresses and those stresses resulting from the Reynolds averaging process. If u represents the horizontal velocity in the stream-wise direction and w in the vertical direction, equilibrium analysis has shown that the total shear stress may be written in the form (Prasuhn, 1980):

$$\tau = \mu \frac{\partial \bar{u}}{\partial z} - \rho \overline{u'w'} \tag{4-16}$$

Boussinesq proposed that the two stress sources were analogous in a fully turbulent flow by introducing an eddy viscosity term, η:

$$-\rho \overline{u'w'} = \eta \frac{\partial \bar{u}}{\partial z} \tag{4-17}$$

The total shear stress may then be written as:

$$\tau = \mu \frac{\partial \bar{u}}{\partial z} + \eta \frac{\partial \bar{u}}{\partial z} \tag{4-18}$$

The turbulent mixing contribution far outweighs the molecular viscosity term in the macro-scale, therefore, the total shear stress for estuary considerations may be written as:

$$\tau = \eta \frac{\partial \bar{u}}{\partial z} = \rho K_m \frac{\partial \bar{u}}{\partial z} \tag{4-19}$$

where K_m represents the kinematic eddy viscosity.

The mixing length model was developed by Ludwig Prandtl in the early 20th century, and is a method that attempts to describe momentum transfer by turbulence Reynolds stresses within a Newtonian fluid boundary by means of an eddy viscosity. Although the model is considered to give a rough approximation of the turbulent Reynolds stress, it is commonly used in practice today due to its low computational overhead.

The mixing length, L, is defined as the distance a fluid parcel can travel while conserving its properties before mixing with the surrounding fluid. Prandtl described that the mixing length: "may be considered as the diameter of the masses of fluid moving as a whole in each individual case, or again, as the distance traversed by a mass of this type before it becomes blended in with neighboring masses…"(Prandtl, 1926). The concept is depicted in Figure 4-6; here a fluid parcel of temperature, T, is seen travelling vertically across a temperature gradient. The fluctuation in temperature that the parcel experienced throughout the process is T'. So T' is the temperature deviation from its surrounding environment after it has moved over the mixing length L'.

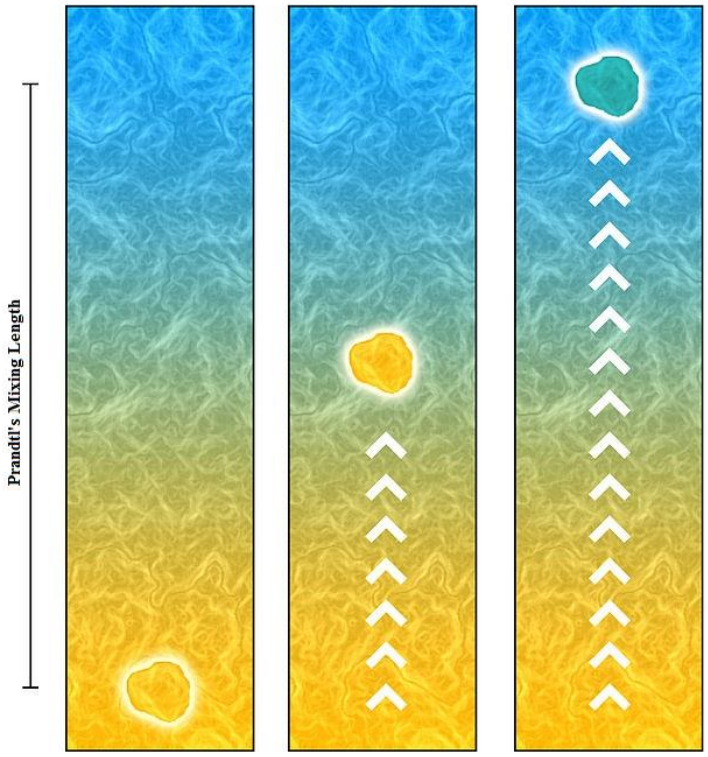

Figure 4-6 Mixing Length concept.

Through Reynolds decomposition, the temperature may be expressed as, $= \bar{T} + T'$, where $\bar{T}$, is the slowly varying component and T' is the fluctuating component. T' can be expressed in terms of the mixing length:

$$T' = -L\frac{\partial \bar{T}}{\partial z} \tag{4-20}$$

Although with a somewhat weaker theoretical justification since the pressure gradient force can alter the fluctuating components, the fluctuating components of velocity, u' and w', can also be expressed in a similar fashion:

$$u' = -L\frac{\partial \bar{u}}{\partial z} \qquad w' = -L\frac{\partial \bar{w}}{\partial z} \tag{4-21}$$

Therefore,

$$\tau = -\rho\overline{u'w'} \approx \rho w' L \frac{\partial \bar{u}}{\partial z} \tag{4-22}$$

In practice, w' is assumed to be roughly equal to u', resulting in:

$$\tau = \rho L^2 \frac{\partial \bar{u}}{\partial z}\left|\frac{\partial \bar{u}}{\partial z}\right| \tag{4-23}$$

A commonly used turbulence closure model in engineering applications is the two-equation k-ε model (Launder, 1974). The model is known as the k-ε because the mixing length L is determined from transport equations for the turbulent kinetic energy, k and the energy dissipation ε:

$$L = C_D \frac{k\sqrt{k}}{\varepsilon} \tag{4-24}$$

In practice, C_D has been determined to be about 0.1925 through calibration
In application of this turbulence model, it is assumed that the horizontal scale is much larger than the vertical one. It is also assumed that the production, buoyancy, and dissipation terms dominate, because of this assumption, conservation of the turbulent quantities is less important and the transport equation is non-conservative.

The exact k-ε equations contain many un-measurable terms and unknowns. The standard k-ε turbulence model, which is based on our best understanding of the relevant processes, minimizes unknowns and is applicable to a wide range of turbulent applications. The model uses two PDE's to describe turbulent kinetic energy and turbulent energy dissipation:

$$\frac{\partial(\rho k)}{\partial t} + \frac{\partial(\rho k u_i)}{\partial x_i} = \frac{\partial}{\partial x_j}\left[\frac{\mu_t}{\sigma_k}\frac{\partial k}{\partial x_j}\right] + 2\mu_t E_{ij}E_{ij} - \rho\varepsilon \tag{4-25}$$

$$\frac{\partial(\rho\varepsilon)}{\partial t}+\frac{\partial(\rho\varepsilon u_i)}{\partial x_i}=\frac{\partial}{\partial x_j}\left[\frac{\mu_t}{\sigma_\varepsilon}\frac{\partial\varepsilon}{\partial x_j}\right]+C_{1\varepsilon}\frac{\varepsilon}{k}2\mu_t E_{ij}E_{ij}-C_{2\varepsilon}\rho\frac{\varepsilon^2}{k} \tag{4-26}$$

where u_i represents the velocity in the corresponding direction, E_{ij} is the component of the rate of deformation, and μ_t represents the eddy viscosity:

$$\mu_t=\rho C_\mu\frac{k^2}{\varepsilon} \tag{4-27}$$

The equations contain some adjustable constants whose values have been determined through data fitting for a wide range of turbulent applications (Rodi, 1984):

$$C_\mu=0.09 \quad \sigma_k=1.00 \quad \sigma_\varepsilon=1.30 \quad C_{1\varepsilon}=1.44 \quad C_{2\varepsilon}=1.92$$

The *k*-ε turbulence model is the most widely used and validated turbulence model and is usually available in computer model codes solving the shallow water equations for estuary and river applications. However, it should be used with caution in stratified flow situations, as the turbulent eddy viscosity at the interface would reduce to zero and vertical mixing due to internal gravity waves (Kelvin-Helmholtz instability) would not be accounted for. Vertical mixing would only occur through molecular diffusion calculations. Therefore, an additional means would be required to account for vertical mixing due to breaking waves along the interface for stratified flow applications.

4.9 Cohesive Sediment Erosion and Deposition

Partheniades developed a non-linear relationship between the erosion rate of mud and the bed shear stress using flume data (Partheniades, 1962). Ariathurai later linearized this relationship, resulting in the empirical Ariathurai-Partheniades formula (Ariathurai, 1974) which is easily adapted for use in computer models:

$$E=M\left(\frac{\tau_b}{\tau_e}-1\right) \tag{4-28}$$

where E is the erosion flux, M is an erosion rate constant which may be used to calibrate the computed rates to observed rates, τ_b is the bed shear stress, and τ_e is the critical shear stress for erosion.

The deposition flux (D) of silt and clay classes of sediment is commonly calculated in numerical models with the relationship attributed to Krone (Krone, 1962):

$$D = w_s C \left(1 - \frac{\tau_b}{\tau_d}\right) \tag{4-29}$$

where w_s is the settling velocity of the grain, C is the near bottom concentration of the grain, τ_b is the bed shear stress, and τ_d is the critical shear stress for deposition.

5 DELFT3D

5.1 Selection of Delft3D

In late 2010, it was announced by Deltares, that their finite difference code, Delft3D would become available as open source code starting in January 2011. Since this code was advertised as supporting the ability to model multiple processes simultaneously such as salinity and cohesive sediment, the Delft3D open source code was selected for this study. Just as important as the code, is the ability to access the code effectively with grid design tools and having the ability to effectively analyze model results. Deltares provides the pre- and post-processing tools upon request to open source users.

The Delft3D suite is composed of several modules, grouped around a mutual interface, with the capability to interact with one another. The Delft3D-FLOW module was used in this study of the Lower Mississippi River. Delft3D-FLOW is a multi-dimensional (2D or 3D) hydrodynamic (and transport) simulation program which calculates non-steady flow and transport phenomena that result from tidal and meteorological forcing on a rectilinear or curvilinear, boundary fitted grid. In 3D simulations, the vertical grid is defined following the σ-layer approach or Cartesian Z-level approach. The initial release of the Delft3D open source code (Version 4.00) did not support sediment transport with the Z-level model, this feature was later added in 2013 (Version 6.01.00) and is used in this model study. Domain decomposition is available as a means to sub-divide the domain into multiple smaller grids for computational efficiency, although this feature was investigated early in the study process, it was abandoned in favor of an automated domain decomposition process using the Message Passing Interface (MPI) method. The MPI version of the Z-level code (Version 6.01.06) was made available in early 2014 by Deltares.

The resources of the U. S. Army Engineer Research and Development Center Department of Defense Supercomputing Resource Center in Vicksburg, Mississippi were available to the author and the direction of this model study eventually migrated to the Cray XE-6 system (Garnet) located there as the PC proved to be impractical for a 3D model with such a large number of active computational nodes and state variables.

5.2 Delft3D *Z*-model Overview

As the σ-layer approach proved to be unsatisfactory for certain flow cases, including weakly forced stratified flow situations, in 2003 (Version 3.12) the Delft3D *Z*-level model was introduced to address these situations. The *Z*-level model provides horizontal co-ordinate lines that are nearly parallel with the pycnocline of a weakly forced stratified system, such as is the case with the Mississippi Delta. These parallel grid lines are not subject to the artificial diffusion that plagues contour following co-ordinate lines such as in the σ-layer model scheme.

Unfortunately, these horizontal co-ordinate lines result in the bottom and free-surface having a stair-case appearance and the thickness of the bottom layer will vary by cell with some thick and some very thin layers at the bottom. This can create problems in the calculation of the bed shear stress which is used as a main driver of many sediment transport formulations. For this reason, the σ-layer model approach is the preferred layering scheme when salinity does not need to be addressed. Since a rigorous reproduction of salinity transport was required for this study, the *Z*-level model is the preferred vertical discretization approach.

The shortcoming of the *Z*-level model approach regarding the shear stress calculation is partially overcome in Delft3D by readjusting the thickness of the two bottommost layers in the water column. The interface between the two bottom layers is shifted up if the bottom layer is thinner than the second most bottom layer to give the two layers equal thickness locally.

The shallow water equations are discretized on a curvilinear grid where orthogonality and a well-structured grid are assumed. The spacing in a well-structured grid varies smoothly over the computational region to minimize inaccuracy in the finite difference operators. The gridlines should also follow land-water boundaries as much as possible to avoid stair-step water edges. The water level and velocity variables are arranged in an Arakawa C-grid configuration. The water level points are defined in the center of a continuity cell and the velocity components are perpendicular to the grid cell

faces where they are situated. The Delft3D code solves the 2D depth averaged (σ-layer model only) or 3D non-linear shallow water equations with the hydrostatic assumption using a finite difference approach.

Methods available in the *Z*-level model to spatially discretize the horizontal advection terms for momentum include explicit and implicit upwind schemes, an explicit flooding scheme and an explicit upwind finite-volume scheme. The van Leer-2 and IUPW schemes are available to discretize the horizontal advection terms for transport. The Alternating Direction Implicit (ADI) method for shallow water equations is used for time integration. Although several turbulence models are available for the σ-layer model, the *k*-ε turbulence model is the only available closure scheme supported for the *Z*-level model.

5.3 Numerical methods used in this study

Although the user may have several options in the selection of numerical solvers in Delft3D, the following discussion is limited to those methods utilized in this study. The reader is referred to the Delft3D Hydro-Morphodynamics user manual (Deltares, 2014) for further details of Delft3D capabilities, including details on the σ-layer model which is considered to be a more mature code than the research *Z*-level model.

5.3.1 Methods for discretization of the 3D shallow water equations

5.3.1.1 Horizontal momentum solver

Several methods are available to solve the horizontal advective momentum terms in the Z-level model including:

- Explicit Multi-Directional Upwind scheme
- Implicit Multi-Directional Upwind scheme
- Implicit (first-order) Upwind scheme
- Explicit Flooding scheme
- Explicit Upwind Finite-Volume scheme

The default method, Explicit Multi-Directional Upwind (MDUE) discretization scheme was used for this study. The MDUE scheme approximates the advection terms along streamlines and is of first order accuracy. The following equations describe the discretization for a flow in Delft3D with positive *U* and *V*-components:

$$\left.\frac{u}{\sqrt{G_{\xi\xi}}}\frac{\partial u}{\partial \xi}\right|_{m,n,k} = \begin{cases} \dfrac{u_{m,n,k}}{\left(\sqrt{G_{\eta\eta}}\right)_{m,n}}\left(\dfrac{u_{m,n-1,k}-u_{m-1,n-1,k}}{\Delta\xi}\right) & \text{if: } v^{-\xi\eta}_{m,n,k} > u_{m,n,k} > 0 \\ \dfrac{u_{m,n,k}}{\left(\sqrt{G_{\eta\eta}}\right)_{m,n}}\left(\dfrac{u_{m,n,k}-u_{m-1,n,k}}{\Delta\xi}\right) & \text{if: } u_{m,n,k} > v^{-\xi\eta}_{m,n,k} > 0 \end{cases} \tag{5-1}$$

and:

$$\left.\frac{v}{\sqrt{G_{\eta\eta}}}\frac{\partial u}{\partial \eta}\right|_{m,n,k} = \begin{cases} \dfrac{v^{-\xi\eta}_{m,n,k}}{\left(\sqrt{G_{\eta\eta}}\right)_{m,n}}\left(\dfrac{u_{m,n,k}-u_{m,n-1,k}}{\Delta\eta}\right) & \text{if: } v^{-\xi\eta}_{m,n,k} > u_{m,n,k} > 0 \\ \dfrac{v^{-\xi\eta}_{m,n,k}}{\left(\sqrt{G_{\eta\eta}}\right)_{m,n}}\left(\dfrac{u_{m-1,n,k}-u_{m-1,n-1,k}}{\Delta\eta}\right) & \text{if: } u_{m,n,k} > v^{-\xi\eta}_{m,n,k} > 0 \end{cases} \tag{5-2}$$

where the $\sqrt{G_{\xi\xi}}$ and $\sqrt{G_{\eta\eta}}$ terms represent the Δx and Δy grid spacing on a curvilinear grid. The discretization at the boundaries is necessarily reduced to a smaller stencil to avoid an artificial boundary layer and instabilities (Deltares, 2014).

5.3.1.2 Vertical momentum solver

Two methods are available to solve the vertical advection momentum terms in the *Z*-model, a central implicit scheme and an upwind explicit scheme. The default central implicit scheme was used for this study. The less stable upwind explicit scheme is only available if the finite volume method is used for the horizontal advection. The second order central difference used for the space discretization is:

$$\left. w\frac{\partial u}{\partial z}\right|_{m,n,k} = w^{-\xi z}_{m,n,k}\left[\frac{u_{m,n,k+1}-u_{m,n,k-1}}{\frac{1}{2}h_{m,n,k-1}+h_{m,n,k}+\frac{1}{2}h_{m,n,k+1}}\right] \tag{5-3}$$

where $h_{m,n,k}$is the thickness of the layer with index k defined by $h_{m,n,k} = z_k - z_{k-1}$ (Deltares, 2014).

5.3.1.3 Horizontal viscosity terms

The horizontal viscosity term, ν_H is integrated explicitly leading to an additional stability condition:

$$\Delta t \leq \frac{1}{2\nu_H}\left(\frac{1}{\Delta x^2} + \frac{1}{\Delta y^x}\right)^{-1}$$

where the$\sqrt{G_{\xi\xi}}$ and $\sqrt{G_{\eta\eta}}$ terms represent the Δx and Δy grid spacing on a curvilinear grid (Deltares, 2014).

5.3.1.4 Vertical viscosity terms

Viscosity terms are approximated by central differences and are computed at the layer interfaces. The vertical viscosity term is discretized as (Deltares, 2014):

$$\frac{\partial}{\partial z}\left(\nu_V \frac{\partial u}{\partial z}\right)\Big|_{m,n,k} = \frac{\nu_V|_{m,n,k+1}}{h_{m,n,k}}\left(\frac{u_{m,n,k+1} - u_{m,n,k}}{\frac{1}{2}(h_{m,n,k+1}+h_{m,n,k})}\right) - \frac{\nu_V|_{m,n,k}}{h_{m,n,k}}\left(\frac{u_{m,n,k} - u_{m,n,k-1}}{\frac{1}{2}(h_{m,n,k}+h_{m,n,k-1})}\right) \quad (5\text{-}6)$$

5.3.2 Methods for solving the transport equation

5.3.2.1 Horizontal transport solver

The horizontal transport terms are approximated with the Van Leer-2 scheme (Van Leer, 1974). The Van Leer-2 scheme is a combination of a first order upwind scheme and a second order upwind scheme. The first order upwind scheme is applied in the case of a local minimum or maximum. Fromm's second order upwind scheme is used in case of a smooth numerical solution. The horizontal fluxes are calculated by (Deltares, 2014):

$$F_{m,n,k} = u_{m,n,k} h_{m,n,k} \Delta y \begin{cases} c_{m,n,k} + \alpha(1 - CFL_{adv-u})(c_{m,n,k} - c_{m-1,n,k}) \dfrac{c_{m+1,n,k} - c_{m,n,k}}{c_{m+1,n,k} - c_{m-1,n,k}} \\ \text{when } u_{m,n,k} \geq 0, \\ c_{m+1,n,k} + \alpha(1 + CFL_{adv-u})(c_{m,n,k} - c_{m-1,n,k}) \dfrac{c_{m+1,n,k} - c_{m+2,n,k}}{c_{m,n,k} - c_{m+2,n,k}} \\ \text{when } u_{m,n,k} < 0, \end{cases} \quad (5\text{-}7)$$

with:

$$CFL_{adv-u} = \frac{\Delta t |u|}{\Delta x} \quad (5\text{-}8)$$

and:

$$\alpha = \begin{cases} 0, \left| \dfrac{c_{m+1,n,k} - 2c_{m,n,k} + c_{m-1,n,k}}{c_{m+1,n,k} - c_{m-1,n,k}} \right| > 1, \begin{pmatrix} \text{local max.} \\ \text{or min.} \end{pmatrix}, \\ 1, \left| \dfrac{c_{m+1,n,k} - 2c_{m,n,k} + c_{m-1,n,k}}{c_{m+1,n,k} - c_{m-1,n,k}} \right| \leq 1, (\text{monotone}). \end{cases} \quad (5\text{-}9)$$

5.3.2.2 Vertical transport solver

Vertical fluxes in Delft3D are discretized with a central scheme where time integration in the vertical is fully implicit which leads to a tri-diagonal system in the vertical (Deltares, 2014):

$$(wc)_{m,n,k} - (wc)_{m,n,k-1} = w_{m,n,k} \left(\frac{c_{m,n,k} + c_{m,n,k+1}}{2} \right) - w_{m,n,k-1} \left(\frac{c_{m,n,k} + c_{m,n,k-1}}{2} \right) \quad (5\text{-}10)$$

5.3.2.3 Forester filter

Central differences in the horizontal and vertical directions may give rise to non-physical spurious oscillations in the solution resulting in negative concentrations. A filter

may be applied to dampen these numerical wiggles. In Delft3D, if concentration $c_{m,n,k}$is negative, then the iterative filtering process in the x-direction is given by (Deltares, 2014):

$$c_{m,n,k}^{p+1} = c_{m,n,k}^{p} + \frac{c_{m+1,n,k}^{p} + 2c_{m,n,k}^{p} + c_{m-1,n,k}^{p}}{4} \tag{5-11}$$

where p denotes the iteration number. A maximum of 100 iterations are performed, and a warning is generated if there is still a grid cell with negative concentration after 100 iterations.

Similarly, a filter may be applied to smooth the vertical density profile to smooth out local maximums and minimums whereby a local maximum satisfies:

$$c_{m,n,k} > \max\left(c_{m,n,k+1}, c_{m,n,k-1}\right) + 0.001 \tag{5-12}$$

Whereas a local minimum satisfies:

$$c_{m,n,k} < \min\left(c_{m,n,k+1}, c_{m,n,k-1}\right) + 0.001 \tag{5-13}$$

For example if salinity $s_{m,n,k} > s_{m,n,k-1} + 0.001$, then the vertical filter is applied such that:

$$s_{m,n,k} = s_{m,n,k} - \min(\Delta z_k, z_{k-1}) \frac{\left(s_{m,n,k} - s_{m,n,k-1}\right)}{2\Delta z_k} \tag{5-14}$$

$$s_{m,n,k-1} = s_{m,n,k-1} + \min(\Delta z_k, z_{k-1}) \frac{\left(s_{m,n,k} - s_{m,n,k-1}\right)}{2\Delta z_{k-1}} \tag{5-15}$$

This filtering process is only applied to the salinity and temperature constituents in Delft3D (Deltares, 2014).

5.3.3 Turbulence closure

The Delft3D *Z*-level model code is limited to the use of the *k*-*ε* method for turbulence closure. The production, buoyancy, and dissipation terms are assumed to be the dominating terms and therefore the conservation of the turbulent quantities is less important and the transport equation is implemented in a non-conservative form.

The eddy viscosity is based on information from the previous half time step and the eddy viscosity and turbulent transport quantities, *k* and *ε* are positioned at the layer interfaces in the center of the computational cell. In this way, the vertical gradients in the production term and buoyancy term are accurately discretized and the vertical boundary conditions at the bed and free surface may be implemented. Positive solutions are provided by first order upwind differencing for advection (Uittenbogaard, van Kester, and Stelling, 1992).

5.3.3.1 The Ozmidov Length Scale

The *k*-*ε* model is the only turbulence closure model currently available for the Delft3D *Z*-level model, however, the *k*-*ε* turbulence model is incapable of reproducing the turbulence resulting from interfacial instabilities associated with strongly stratified flow. These instabilities are referred to as Kelvin-Helmholtz billows and Holmboe waves.

Therefore, in strongly stratified flows, the turbulent eddy viscosity at the interface reduces to zero and the vertical mixing reduces to molecular diffusion. In order to account for this shortcoming in the *k*-*ε* turbulence model, the minimal eddy diffusivity, D_V, may be based on the Ozmidov length scale, L_{OZ} (Deltares, 2014):

$$D_V = max\left(D_{3D}, 0.2L_{OZ}^2\sqrt{-\frac{g}{\rho}\frac{\partial\rho}{\partial z}}\right) \tag{5-16}$$

The Ozmidov scale represents the largest eddy size that can be supported by a given turbulent dissipation rate within a region of specified stratification:

$$L_{OZ} = (\varepsilon/N^3)^{\frac{1}{2}} \tag{5-17}$$

ε represents the rate of dissipation of turbulent kinetic energy. N is the Brunt–Väisälä buoyancy frequency or tendency of a fluid parcel to oscillate:

$$N = \left(\frac{-g}{\rho_0}\frac{\partial \rho}{\partial z}\right)^{\frac{1}{2}} \tag{5-18}$$

The condition for stable stratification exists when $N^2 > 0$ and unstable stratification exists when $N^2 < 0$. The Ozmidov length scale parameter may be used as a calibration adjustment to control the position of the leading edge of the saltwater wedge in numerical simulations.

5.4 Wetting and drying

The water level is defined at the center of the computational cell in Delft3D, however due to the handling of the bottom depth (stair stepping) the bottom depth is not necessarily uniquely defined. The user may select how the depth of a cell is determined with information from the surrounding four bottom depth points. The choices available are maximum, mean, and minimum. The maximum depth (default method) was used for simulations conducted for this study.

For a given bottom depth, $d^{\zeta}_{m,n}$, and water level, $\zeta_{m,n}$, the total depth, $H^{\zeta}_{m,n}$, in a water level point is determined to be negative by (Deltares, 2014):

$$H^{\zeta}_{m,n} = d^{\zeta}_{m,n} + \zeta_{m,n} \leq 0 \tag{5-19}$$

then the horizontal cell is removed from the computation and the ADI half time step is repeated.

The water depth in a velocity point is determined using the upwind water level, for example for the average velocity $U_{m,n}$:

$$H_{m,n}^{U} = \begin{cases} \bar{d}^{\eta} + \zeta_{m,n}, & U_{m,n} > 0 \\ \bar{d}^{\eta} + \zeta_{m+1,n}, & U_{m,n} < 0 \\ \bar{d}^{\eta} + \max\left(\zeta_{m,n}, \zeta_{m+1,n}\right), & U_{m,n} = 0 \end{cases} \tag{5-20}$$

Upwinding the water level at the velocity points enhances the computed discharge, but taking the maximum of the two surrounding water levels at a dry cell face prevents the velocity point from being kept artificially dry. Further details on the wetting and drying criteria for the *Z*-level model may be found in the Delft3D Hydro-Morphodynamics user manual (Deltares, 2014).

5.5 Application of Wind Stress to the Free Water Surface

Delft3D uses the quadratic expression to determine the wind stress at the free surface, which is then applied to the momentum equations (reference Equation 4-13),

$$|\vec{\tau_s}| = \rho_{air} C_d U_{10}^2 \tag{5-21}$$

where:

ρ_{air} is the density of air

U_{10} is the wind speed 10 meters above the free surface

C_d is the wind drag coefficient, dependent on U_{10}.

Several methods are available to determine the wind drag coefficient including an empirical relationship that was utilized for this study (Deltares, 2014):

$$C_d(U_{10}) = \begin{cases} C_d^A, U_{10} \le U_{10}^A \\ C_d^A + (C_d^B + C_d^A)\dfrac{U_{10} - U_{10}^A}{U_{10}^B - U_{10}^A}, U_{10}^A \le U_{10} \le U_{10}^B \\ C_d^B + (C_d^C - C_d^B)\dfrac{U_{10} - U_{10}^B}{U_{10}^C - U_{10}^B}, U_{10}^B \le U_{10} \le U_{10}^C \\ C_d^C, \quad U_{10}^C \le U_{10} \end{cases} \tag{5-22}$$

where:

C_d^i is the user-defined wind drag coefficients at respectively the wind speed $U_{10}^i (i = A, B, C)$.

U_{10}^i are the defined wind speeds $(i = A, B, C)$

Numerous relationships for the wind drag coefficient and wind speed are possible. Figure 5-1 shows the default relationship in Delft3D where A=0.00063 at 0.0 m/s and B=C=0.00723 at 100 m/s. The default coefficients were used in all simulations in this study.

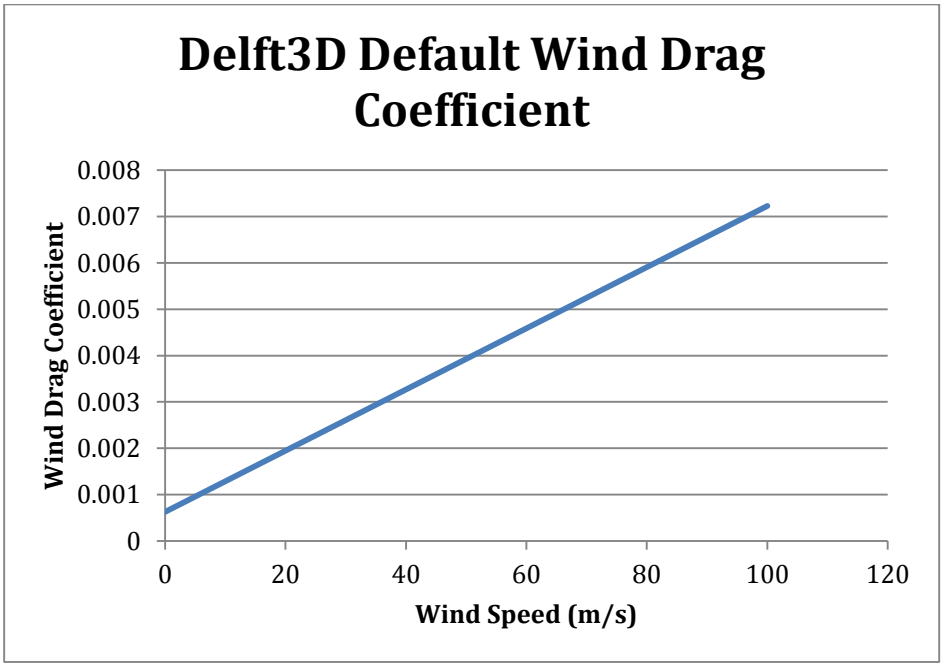

Figure 5-1 Delft3D Default Wind Drag Coefficient

5.6 Free Surface Heat Flux

Delft3D provides several methods to model the temperature exchange between the top water layer and the atmosphere. The total heat flux through the free surface may be expressed as (Deltares, 2014):

$$Q_{tot} = Q_{sn} + Q_{an} - Q_{br} - Q_{ev} - Q_{co} \quad (5\text{-}23)$$

where Q_{sn} is the net incident short wave solar radiation, Q_{an} is the net incident long wave atmospheric radiation, Q_{br} is the long wave back radiation, Q_{ev} is the latent heat or evaporative heat flux, and Q_{co} is the convective heat flux or sensible heat.

The change in temperature in the top layer T_s is:

$$\frac{\partial T_s}{\partial t} = \frac{Q_{tot}}{\rho_w c_p \Delta z_s} \tag{5-24}$$

where Q_{tot} (J/m^2-s) is the total heat flux through the free surface, c_p is the specific heat capacity of sea water or 3930 J/kg-K, ρ_w is the specific density of water (kg/m3) and Δz_s (m) is the thickness of top layer.

Several of the heat exchange models in Delft3D require knowledge of the solar radiation, however, this information was not readily available. Therefore, a method was selected that does not account for the solar radiation explicitly, namely the excess temperature model which only requires knowledge of the ambient atmospheric temperature.

5.7 *Z*-level model bottom shear stress considerations

In Delft3D, the bed shear stress is dependent on the current above the bed using a quadratic relationship (Deltares, 2014):

$$\vec{\tau}_{bed} = \frac{g\rho_0 \vec{u}_b |\vec{u}_b|}{C_{3D}^2} \tag{5-25}$$

C_{3D} represents a user selected Chézy coefficient and $\vec{u}_b$ represents the magnitude of the horizontal velocity in the first layer above the bed where:

$$\vec{u}_b = \frac{\vec{u}_*}{\kappa} \ln\left(1 + \frac{\Delta z_b}{2z_0}\right) \tag{5-26}$$

κ is the Von Kármán constant ($\kappa \approx 0.41$), the roughness height, z_0, is user defined through assignment of a roughness coefficient and Δz_b represents the distance to the computational grid point closest to the bed. The bottom stress is defined as:

$$|\vec{\tau}_b| = \rho_0 \vec{u}_* |\vec{u}_*| \tag{5-27}$$

The roughness height, z_0, is related to the 3D friction coefficient through:

$$C_{3D} = \frac{\sqrt{g}}{\kappa} \ln\left(1 + \frac{\Delta z_b}{2z_0}\right) \tag{5-28}$$

In the Delft3D *Z*-level model, the bed stress term is computed using a logarithmic boundary layer relation (Deltares, 2014):

$$u_* = \frac{u_{bottom+1}\kappa}{\ln\left(1 + \frac{\frac{\Delta z_{bottom+1}}{2} + \Delta z_{bottom}}{z_0}\right)} \tag{5-29}$$

The bed stress term is computed using the velocity at one grid point above the bed because the Z-level model is subject to an uneven distribution of bottom layer thicknesses which would tend to introduce large errors in the water level gradient caused by a local maxima of the turbulent energy level computed by the turbulence closure model that tends to affect the vertical viscosity term and the vertical velocity. The contribution of the vertical velocity component is neglected in determination of the velocity vector for shear stress considerations.

The vertical layer scheme of the Delft3D *Z*-level model can lead to thin cells at the bottom and free-surface. These thin cells lead to inaccuracies and discontinuities in the bottom shear stress, velocity profiles and water levels. The bottom layer may be re-mapped to reduce the inaccuracies and discontinuities in the bottom layer shear stress, an especially important consideration for sediment transport simulations. Mass conservation of transported constituents is achieved through modification of constituent concentrations. The re-mapping concept is shown schematically in Figure 5-2.

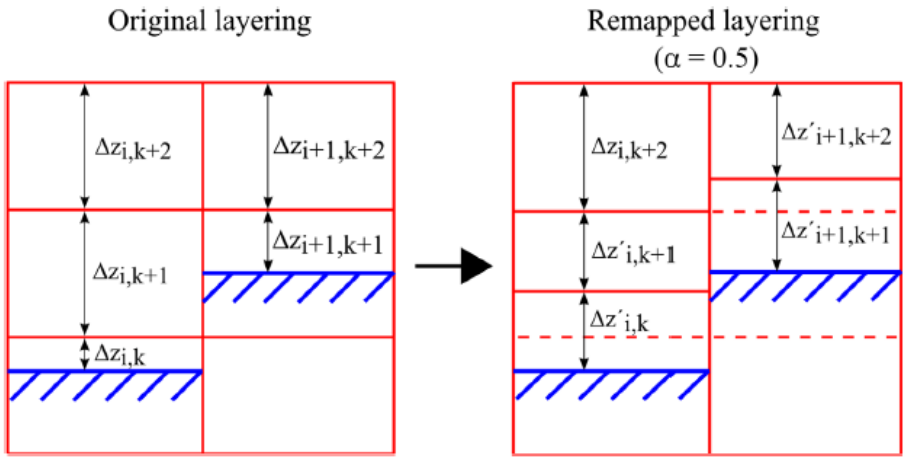

Figure 5-2 Remapping of two near-bed layers to an equidistant layering. Figure from Platzek et al. (2014).

The re-mapping causes horizontally neighboring cells to be vertically shifted with respect to each other. This may have some effect on the horizontal transport through advection and diffusion, with resultant spurious mixing. This introduced mixing is commonly less than mixing due to the inaccuracies and discontinuities of the original layering with thin cells. Figure 5-3 displays test results of this bottom layer remapping technique on the bottom shear stress profile over a bottom sill (Platzek et. al., 2014).

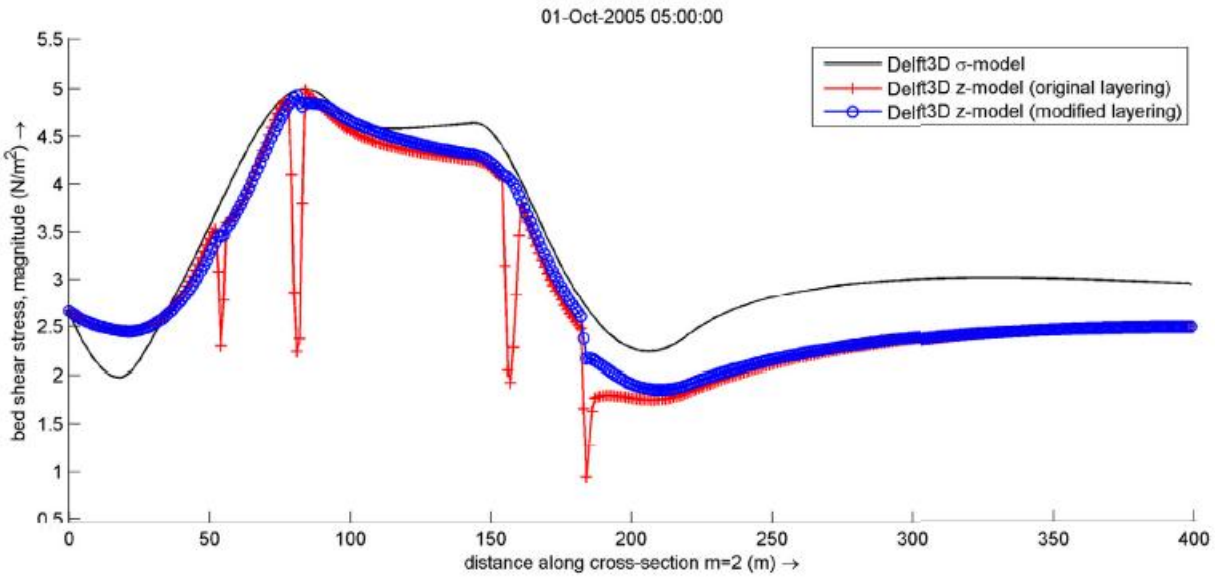

Figure 5-3 Bottom shear stress for the flow over a bottom sill using the Delft3D σ-layer model, Z-level model with original layering and Z-level model with modified layering. Figure from Platzek, et al., (2014).

5.8 *Z*-level model sediment transport considerations

The *Z*-level model sediment capabilities were introduced recently in 2013 and are considered by Deltares to still be research level capabilities. This study was limited to evaluation of the cohesive sediment transport capabilities of the model as the purpose was to examine saltwater effects on fine sediment transport. The effect of sediment on fluid density may be considered by the *Z*-level model. This feature was utilized in this study, reference equation 3-16 for the procedure.

5.8.1 Cohesive sediment transport

By default, the Delft3D *Z*-level model uses the Partheniades-Krone formulations to determine fine sediment fluxes between the water column and the bed. Refer to section 4.9 for details of the Partheniades-Krone formulations.

5.8.2 Indirect simulation of flocculation

When clay particles in fresh water enter a saline environment such as the salinity wedge interface in the Mississippi River, the cohesive sediment tends to flocculate to form sediment "flocs", with the degree of flocculation depending on the salinity of the water. These "flocs" are much larger than the individual sediment particles and settle at a faster rate. The Delft3D-FLOW module accounts for this phenomenon by altering the settling velocity of cohesive sediment in accordance with the salinity level. The user supplies two settling velocities and a maximum salinity. The first velocity, $w_{s,f}^{(l)}$, is the settling velocity of the sediment fraction in fresh water (salinity = 0). The second velocity, $w_{s,max}^{(l)}$, is the settling velocity of the fraction in water having a salinity value equal to S_{max}. The non-hindered settling velocity, $w_{s,0}^{(l)}$, of the sediment "flocs" is calculated as follows (Deltares, 2014):

$$w_{s,0}^{(l)} = \frac{w_{s,max}^{(l)}}{2}\left(1 - \cos\left(\frac{\pi S}{S_{max}}\right)\right) + \frac{w_{s,f}^{(l)}}{2}\left(1 + \cos\left(\frac{\pi S}{S_{max}}\right)\right), \quad \text{when } S \leq S_{max} \qquad (5\text{-}30)$$

$$w_{s,0}^{(l)} = w_{s,max}^{(l)}, \quad \text{when } S > S_{max} \qquad (5\text{-}31)$$

where:

$w_{s,0}^{(l)}$	the (non-hindered) settling velocity of sediment fraction (l)
$w_{s,max}^{(l)}$	settling velocity of sediment fraction (l) at maximum salinity concentration, S_{max}
$w_{s,f}^{(l)}$	fresh water settling velocity of sediment fraction (l)
S	salinity
S_{max}	maximal salinity at which $w_{s,max}^{(l)}$ is specified

The shape of this function can be seen in Figure 5-4, which is a hypothetical plot of the computed non-hindered settling velocity of a typical sediment size class. For this example application, S_{max} was set to 2.5 ppt, $w_{s,f}^{(l)}$ is 2.4E-06 m/s, and $w_{s,max}^{(l)}$ is 1.7E-04 m/s.

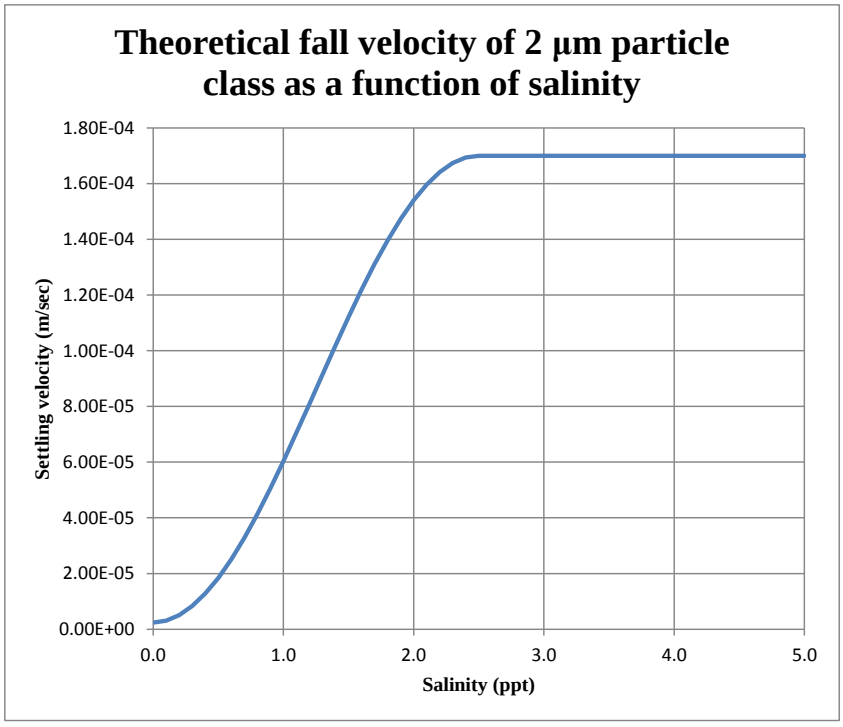

Figure 5-4 Delft3D example application of settling velocity function.

Adjustment to the three variables, S_{max}, $w_{s,max}^{(l)}$, and $w_{s,f}^{(l)}$ will be made in order to tailor the fall velocity characteristics in the Delft3d model to replicate the concentration characteristics as observed in the lower Mississippi River.

5.9 Structures

In order to simulate sub-grid structures that influence flow patterns such as breakwaters and dikes, Delft3D permits the edge of a cell to block flow through the placement of thin dams along these cell edges. Thin dams are infinitely thin objects defined at velocity points which prevent flow exchange between adjacent computational cells. Thin dams were used in this study to simulate the jetties and timber pile dikes shown in Chapter 1.

6 COMPUTATIONAL GRID DESIGN CONSIDERATIONS

Delft3D provides the option to use a curvilinear grid structure to define the study domain and this option was utilized to develop a grid encompassing the modern Mississippi River delta, reference Figure 6-1 for grid footprint. Southwest Pass is the main distributary and flow path in the modern Mississippi River delta. Therefore, a grid was constructed with gridlines that follow the Mississippi River main channel to Head of Passes and smoothly transition into Southwest Pass and out into the Gulf of Mexico. The curvilinear aspect of the grid permitted accommodation of the sharp turn at Head of Passes as the main flow path transitions into the Southwest Pass as shown in Figure 6-2. A continuous grid structure through the main channel and into Southwest Pass eliminates errors brought on by channel edge grid stair stepping for the majority of the flow in the River system. Unfortunately, the other distributaries will feature some channel edge grid stair stepping, this is unavoidable as no grid configuration will permit smooth channel edges for all of the major distributaries.

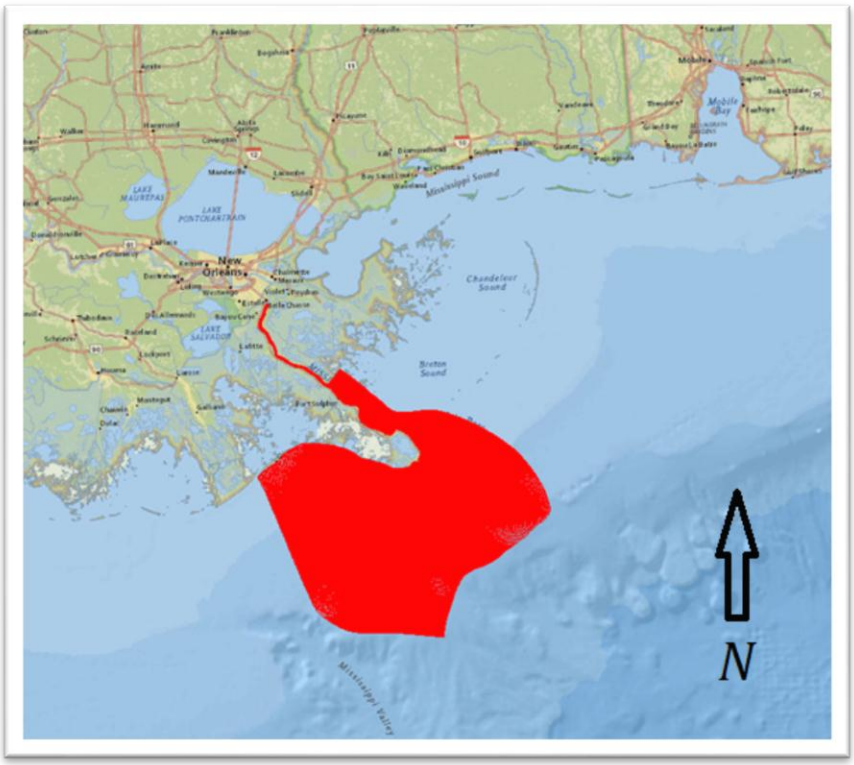

Figure 6-1 Location of computational grid

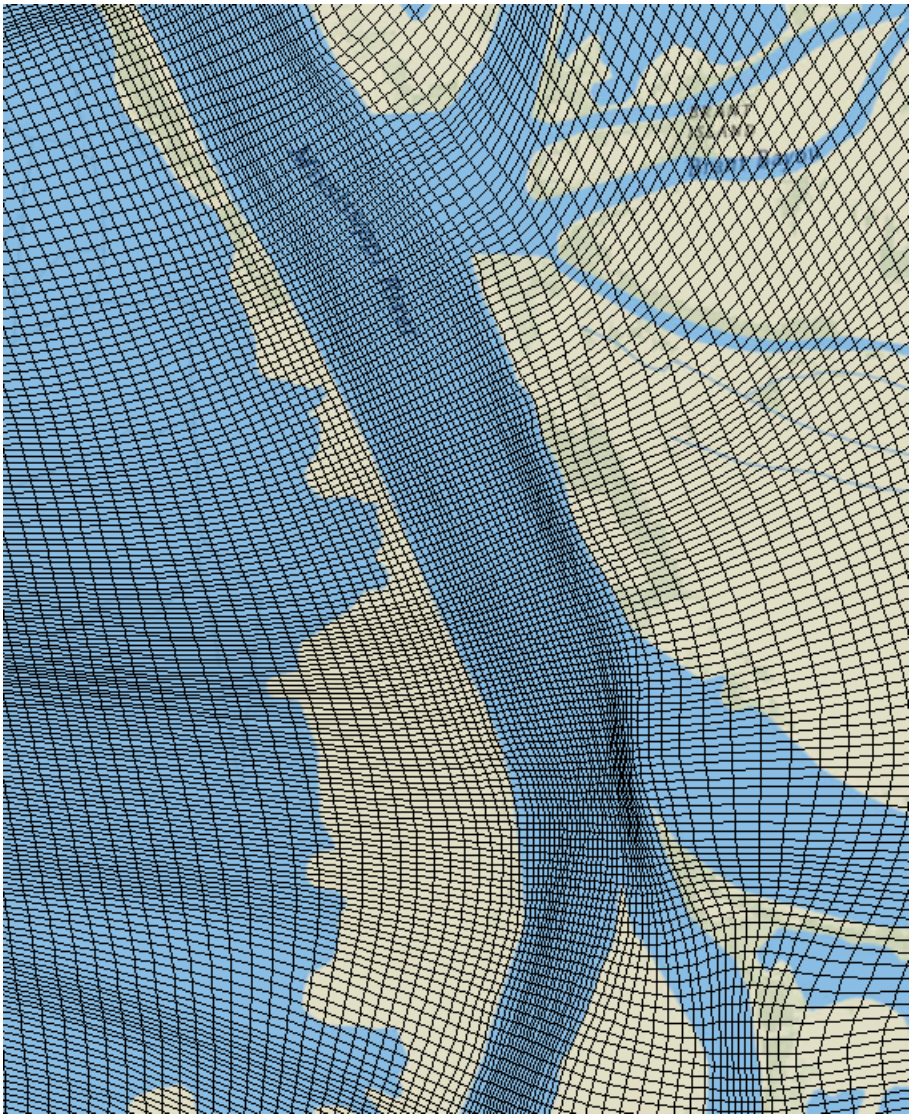

Figure 6-2 Grid continuity through the lower river channel and Southwest Pass

The Delft3D-RGFGRID software was used for all grid development. Shape files were developed from imagery outlining bank lines and levee alignments as a guideline for the curvilinear aspects of the grid development. The maximum grid extents are 2612 x 320 (M x N) cells resulting in a grid with 835,840 cells. Of the 835,840 maximum cell number, there are 478,804 active computational cells. The 1 X 1 grid configuration is shown in Figure 6-3 and the curvilinear grid is shown in Figure 6-4. Corresponding grid reference points are shown in the curvilinear and 1 X 1 grid.

Figure 6-3 1X1 grid cell map

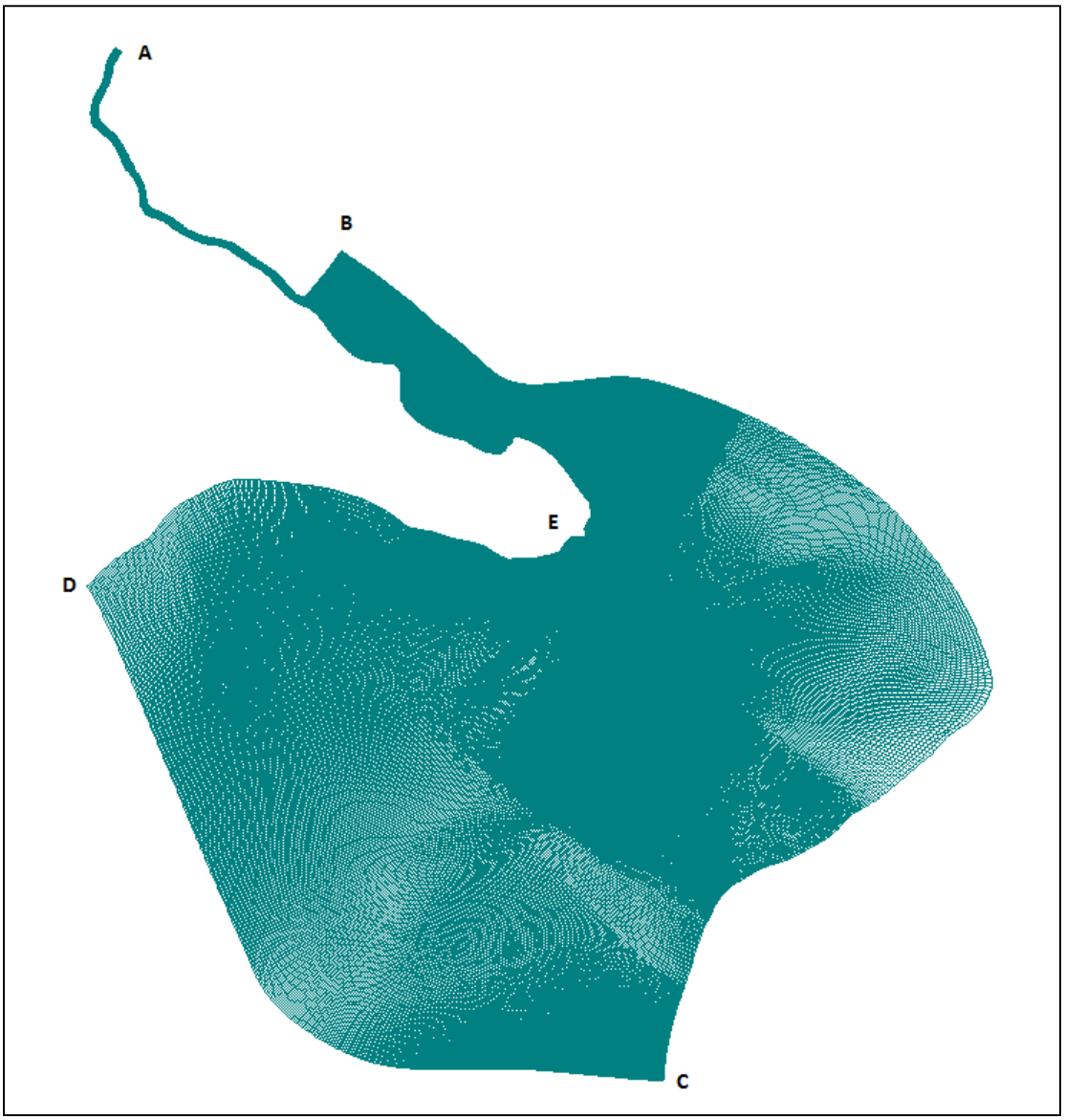

Figure 6-4 Curvilinear grid configuration

The upstream limit of the Mississippi river channel in the grid is located near Belle Chasse, LA at the site of the USGS discharge range no. 07374525 (RK 120 AHP). The curvilinear grid was designed to follow the 200 meter depth contour in the Gulf of Mexico and include all major distributaries of the Mississippi River in the delta. The extreme western limit of the grid in the Gulf portion is located on the west bank of Caminada Pass. From this western extreme the grid extends southeast to the 200 meter depth contour in the Gulf of Mexico and then roughly follows this contour to the most eastern point in the grid southeast of Pass a Loutre. From this eastern extreme, the grid edge extends back to the northwest to the lower limit of the east bank protection levee and was designed to include the receiving basin for river water leaving the main channel at the Ft. St. Phillip crevasse. This design also allows simulation of exchange of water and constituents with the Barataria basin through the use of a water level and concentration boundary along the barrier islands of the basin.

Thin dams were situated throughout the grid to define the flow obstructions that jetty and timber pile dikes create. Figure 6-5 displays thin dam placement in the grid to simulate the effect of jetties and dikes at the entrance to Southwest Pass.

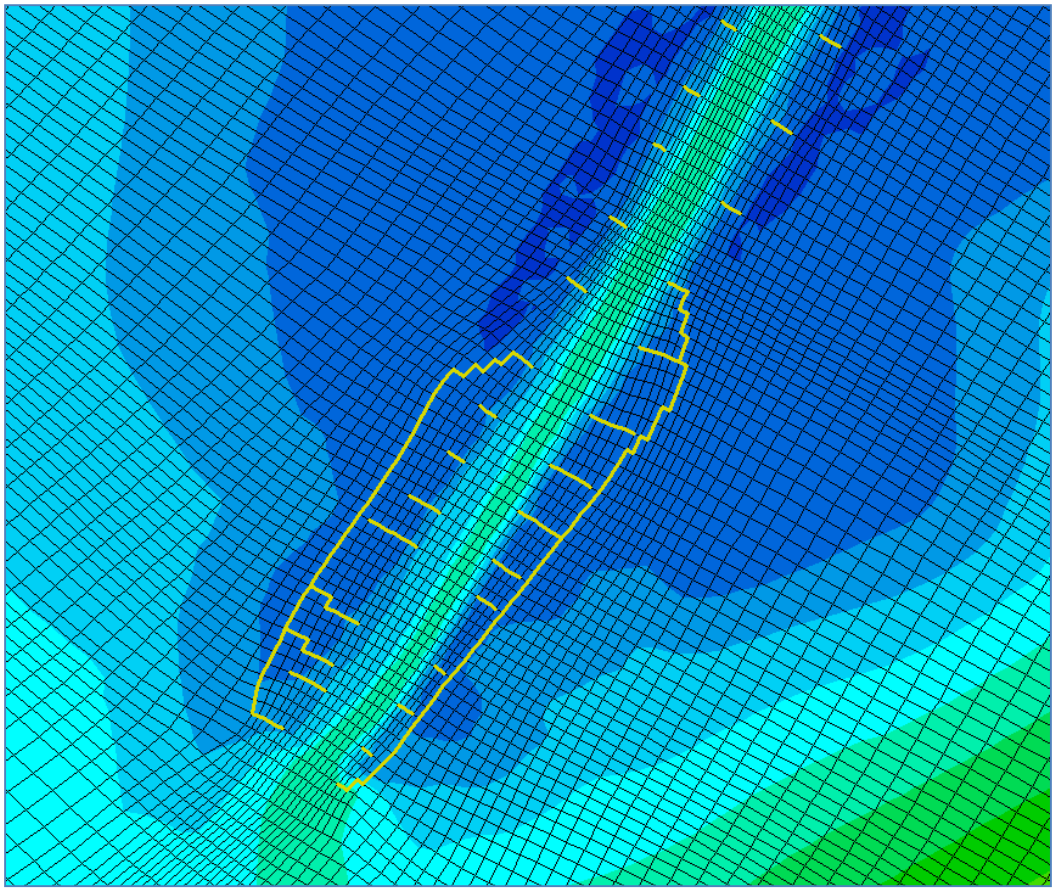

Figure 6-5 Thin dam placement at the entrance to Southwest Pass

Given the parallel computing environment, a grid was constructed to optimize the constraints imposed by the Delft3D message passing interface (MPI) configuration. The MPI subdivision algorithm in Delft3D subdivides the grid along the largest grid dimension. The larger grid dimension for this grid design is parallel to the alignment of the main river channel and Southwest Pass. With this in mind, an effort was made to construct the grid with the minimal resolution necessary in the river cross channel direction to resolve flow exchange between the main flow channels and the receiving waters through distributary channels and crevasses. A total of 224 compute cores were used for the majority of the simulations executed. This was found to be about the maximum number of cores permitted given the constraints of the MPI subdivision algorithm. Compute times continued to decrease up to this maximum limit of cores as the number of cores was increased. Reference Figure 6-6 for 224 compute cores distribution load.

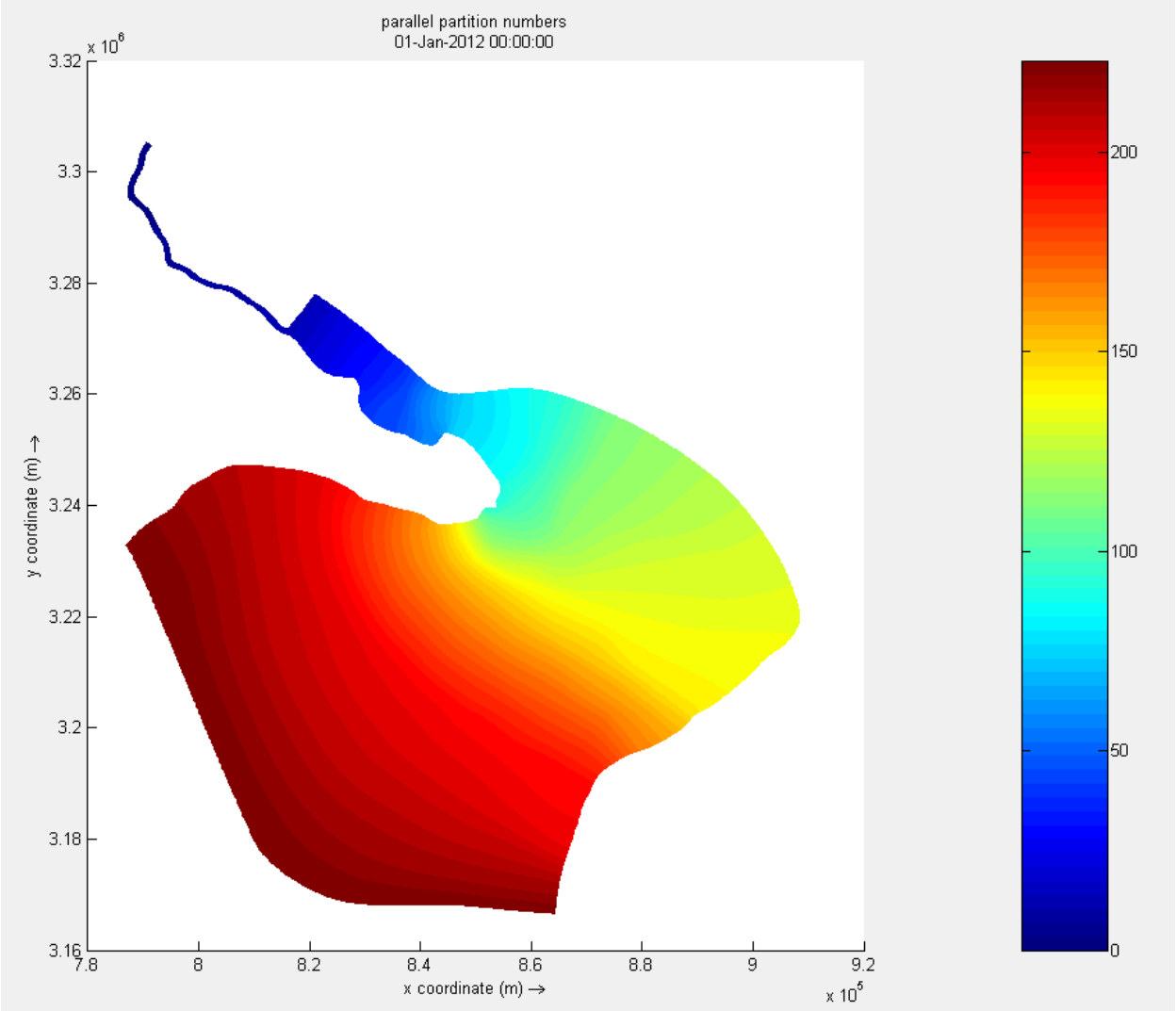

Figure 6-6 Compute core partition schematic

7 COMPUTATIONAL GRID BOUNDARY CONDITIONS

7.1 Overview

Data collected in the drought year of 2012 was available to provide prototype performance targets for the model and inform calibration adjustments to model parameters. Vertical salinity and temperature profile data were collected by the U. S. Army Corps of Engineers (USACE) New Orleans District to track the location of the salinity wedge during the drought. Once per month ADCP discharge information was collected in the delta by the USACE and was used to adjust the flow distribution through the passes in the model. Stage data at various locations collected by the USACE and USGS was available to verify water level reproduction of the model. Water quality point samples including fine sediment concentration and salinity were collected for the LCA Mississippi Hydrodynamic and Delta Study in September 2012 and were used to verify salinity reproduction and calibration of suspended sediment aspects. Suspended sediment data were collected on 23 April 2012 for the LCA White Ditch diversion investigation and is utilized in this study. Boundary data representing conditions for the calendar year 2012 were constructed from various sources as detailed in the following sections.

7.2 Bed Level

The bed level for each simulation (or series of runs) was largely based on the ADCIRC SL16 mesh bathymetry (Bunya et al., 2010), reference Figure 7-1 and Figure 7-2 for final bathymetry plots. Additional detail was added in the vicinity of Ft. St. Phillip based on imagery and calibration of the model flow to ADCP flow measurements along with limited survey data collected in 2003 in the Ft. St. Phillip area. The West Bay diversion outflow channel was also modified from the ADCIRC bathymetry with bathymetry data taken from the ADH model (Brown et al., 2009).

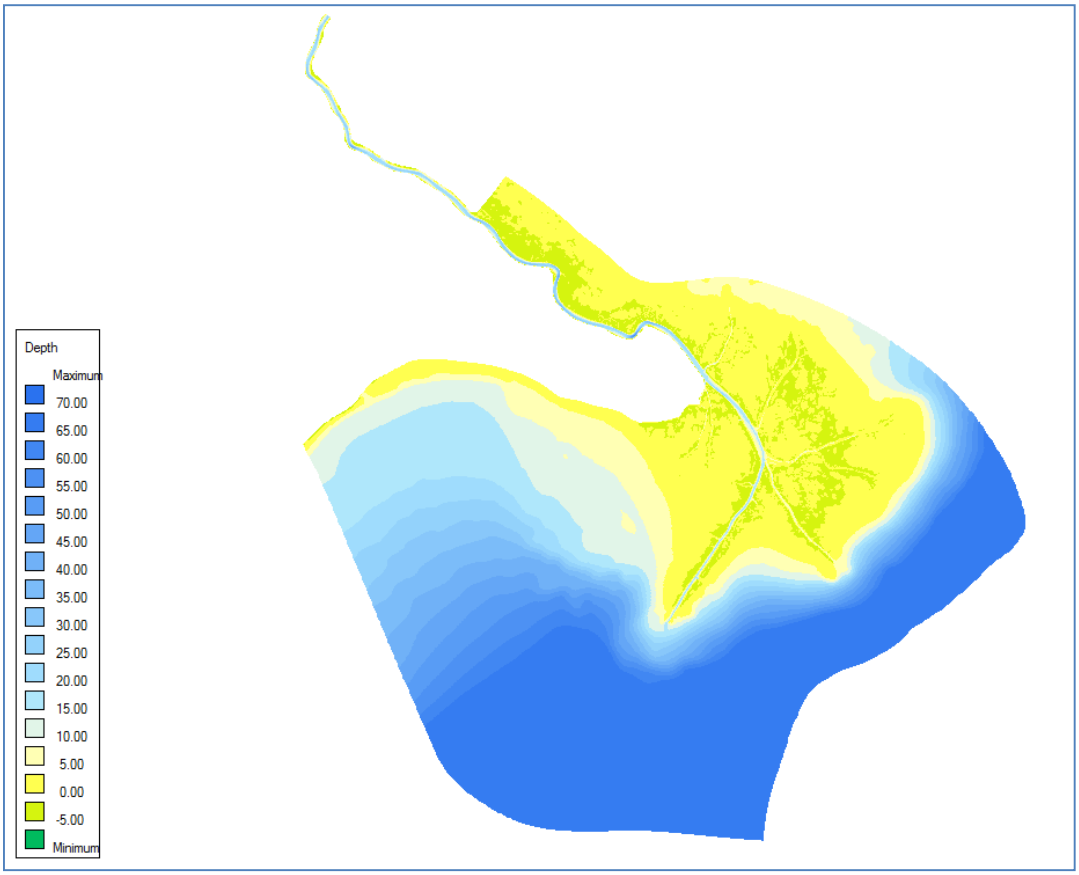

Figure 7-1 Grid bathymetry

Figure 7-2 Detail of grid bathymetry in the birdfoot delta

During the course of this investigation, it was determined that the bathymetry of the four lateral outlets along Southwest Pass, namely Outlet W-1, Outlet W-2, Joseph Bayou, and Burrwood Bayou was inadequately defined in the ADCIRC bathymetry source. Multi-beam acoustic data were collected along these four outlet channels to refine the bathymetry in the model and improve flow exchange fidelity with the surrounding bays in order to improve the realism of salt wedge dynamics in Southwest Pass. Doppler flow measurements have shown that under certain tide conditions, the four outlets together are capable of conveying up to 48% of the total flow entering Southwest Pass from the Mississippi River (Ayres, 2015). Reference Figure 7-3 for locations of these four outlets and extent of acoustic data collected.

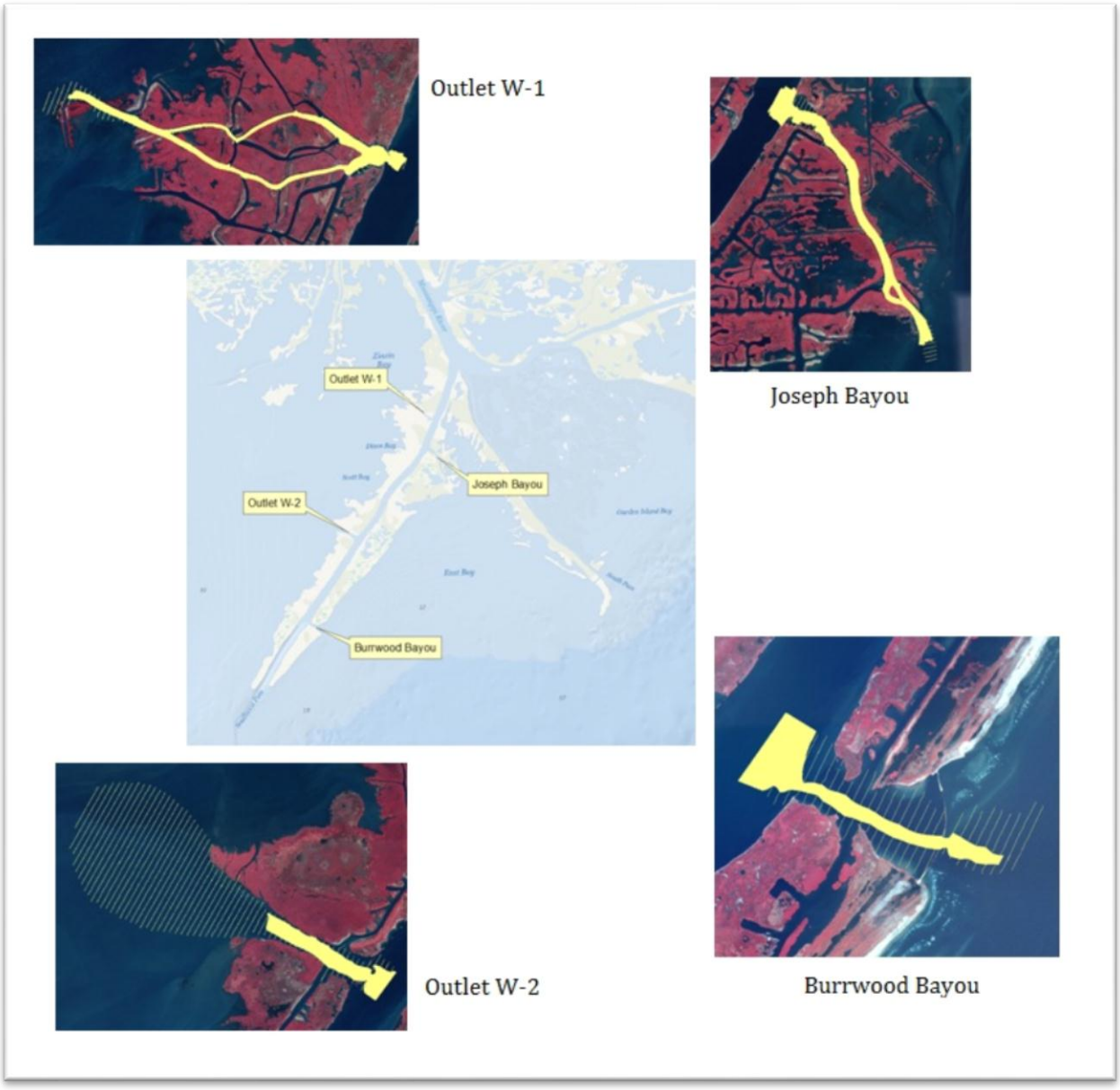

Figure 7-3 Southwest Pass lateral outlets multi-beam extent

The USACE constructed a subaqueous barrier sill at RK 102 during July/August 2012 to halt salinity intrusion from progressing further upstream, therefore simulations performed during the timeframe the barrier sill was in place required a modification to the depth levels to represent the barrier sill. Actual multi-beam survey data was used to represent the sill geometry in the model. The average depth at the crown of the sill is around 15 meters.

7.3 Water to Water Boundaries

There are seven discrete open water boundaries imposed as water to water grid boundaries including one river inflow boundary at Belle Chasse, LA, and six tide water level boundaries. During model development and testing, the boundaries were referred to as the Belle Chasse flow, and the East, West, South, Northeast, Southeast and Barataria Estuary tide. Water level alone is not sufficient information for the numerical scheme to resolve Gulf currents; therefore, the current in the Gulf of Mexico portion of the grid which is heavily influenced by external forcing, was not reproduced in the model.

The tide water level boundaries are defined by two endpoints and linear interpolation is used to define boundary water levels along the boundary at every grid node using the two endpoints. In addition to water level, constituent concentrations are defined at these endpoints with linear interpolation defining the concentrations at each grid node along the boundary. Figure 7-4 shows the location of the open water boundaries and tide endpoints.

Figure 7-4 Location of model grid open water boundaries

The information to define these open water boundaries was collected for most of the 2012 calendar year to overlap the data collection periods. Details on the methods used to define these open water boundaries are discussed in the following sections. Sufficient information was collected to allow model investigations of salinity, temperature, and fine sediment processes in the lower Mississippi River and Southwest Pass.

7.3.1 Mississippi River at Belle Chasse Open Water Boundary

The Mississippi River open water grid boundary was located at the site of the USGS gage no. 07374525. The USGS provides gage height, average velocity, and Mississippi River discharge as well as periodic water quality analyses at this location. The instrumentation

tower is located on the left descending bank at approximately RK 120 AHP. See Figure 7-5 for location of gage.

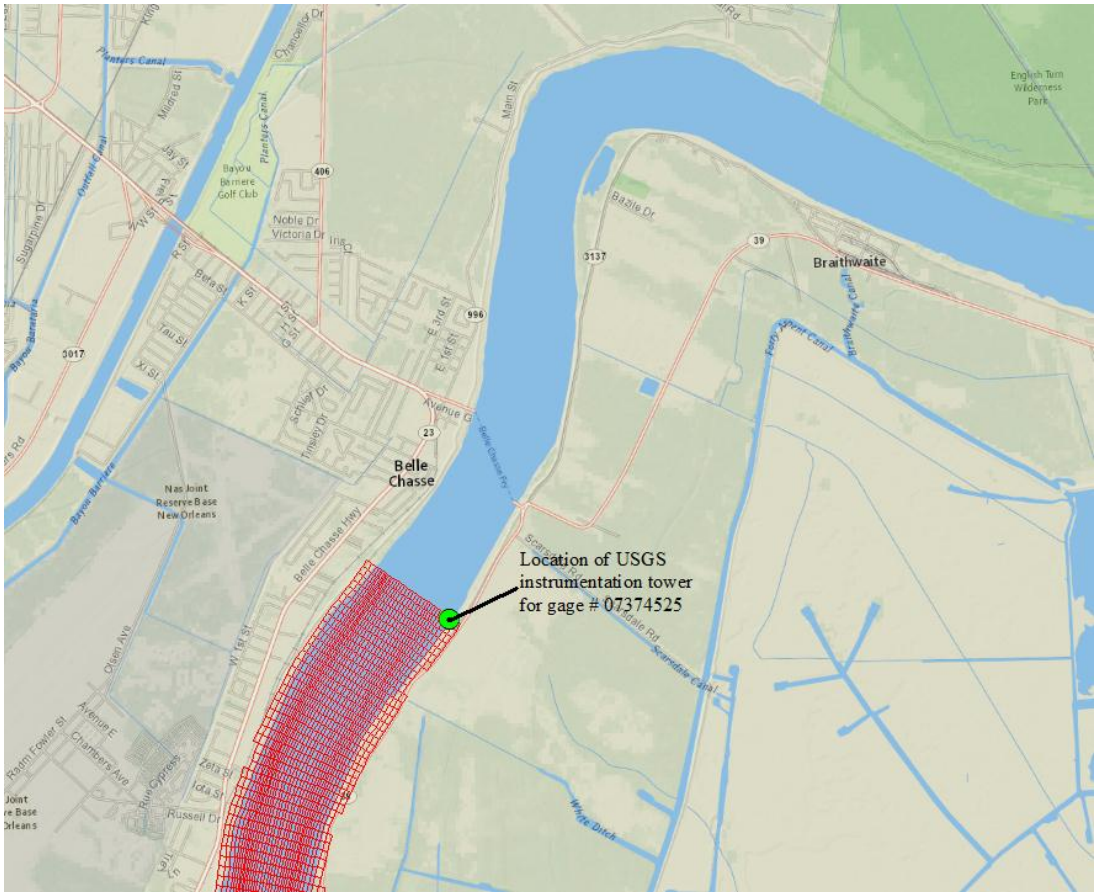

Figure 7-5 Location of Belle Chasse Open Water Boundary

7.3.1.1 Mississippi River at Belle Chasse Open Water Boundary - Total Discharge

Available Mississippi River discharge information during 2012 includes the USACE discharge range at Tarbert Landing, the USGS range at Baton Rouge, and the USGS range at Belle Chasse, reference Figure 7-6 for locations. The USGS instantaneous discharge values were provided in 15-minute intervals. The flows at Tarbert Landing are measured twice a week by the USACE and the rating curve is checked and adjusted regularly based on these measured flows. A daily discharge is provided by the USACE based on this monitored dynamic stage/discharge relationship.

Figure 7-6 Mississippi River Discharge Ranges

Initially, the Belle Chasse data were used as an inflow boundary condition at the upstream boundary of the grid. However, the data proved to be inadequate as a boundary condition for the model due to the high variability in the data due to tidal influence and the data proved to be too high at low flows especially when the gage site was under the influence of the salinity wedge. These elevated flows as compared to measured flows at Tarbert Landing are very apparent in August of 2012 when the toe of the wedge was located upstream of the gage site as seen in Figure 7-7. The presence of the wedge would cause elevated stages due to the underlying layer of saline water and result in erroneous discharge measurements from a stage/discharge rating relationship.

The daily flows at Tarbert Landing were ultimately selected as the boundary condition in part due to the twice weekly regularity of the flow measurements at the site. The data at Baton Rouge was not selected as it showed some tidal influence and did not visually show any improved fit to the Belle Chasse data over that of the Tarbert Landing data, reference Figure 7-7 for hydrograph data at each discharge range.

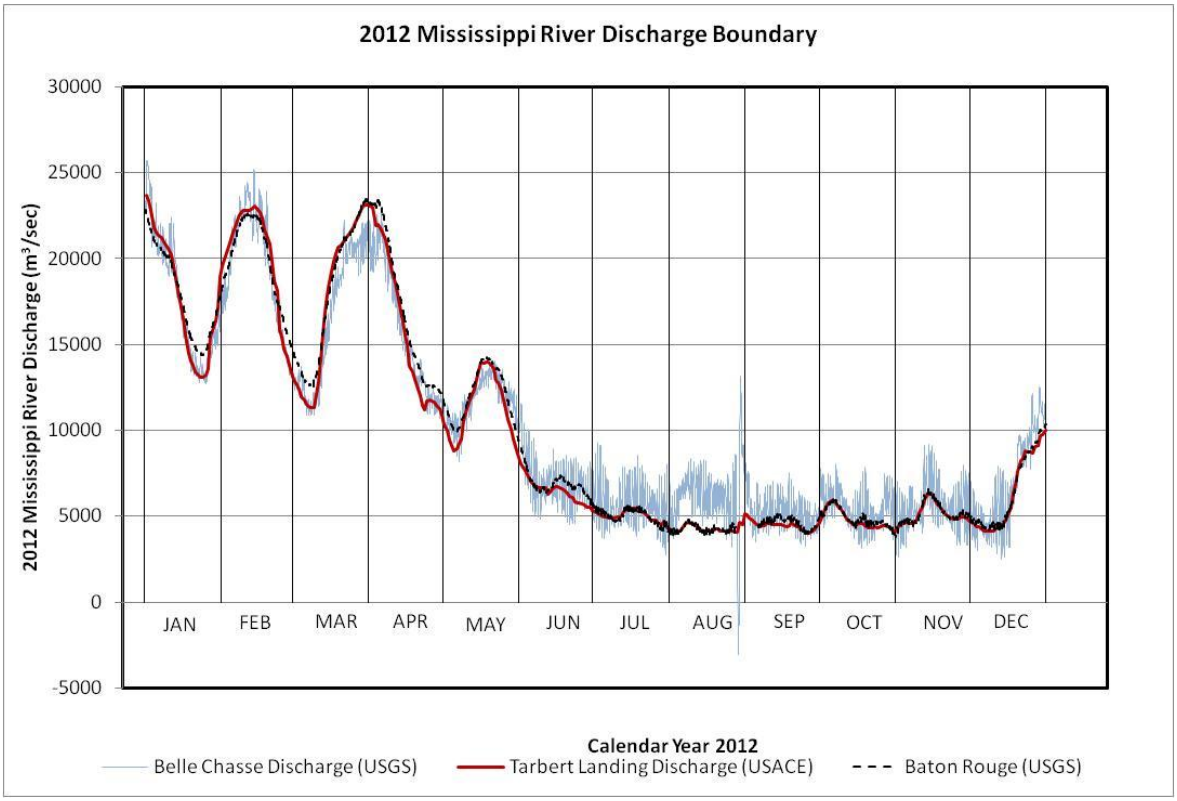

Figure 7-7 2012 Mississippi River Discharge Boundary Condition

7.3.1.2 Mississippi River at Belle Chasse Open Water Boundary – Salinity Concentration

The Mississippi River freshwater background salinity was set to a constant 0.17 ppt for all simulations based on data measured at Audubon Park, New Orleans, LA by the Louisiana Universities Marine Consortium (LUMCON). The salinity was assumed to be uniform throughout the water column at the inflow boundary.

7.3.1.3 Mississippi River at Belle Chasse Open Water Boundary - Temperature

USGS 2012 Baton Rouge daily water surface temperature data was used to construct a continuous water temperature time series at Belle Chasse by fitting the continuous series at Baton Rouge to the irregular time series at Belle Chasse. Figure 7-8 shows the daily time series at Baton Rouge and the fitted data to the irregular data at Belle Chasse. As with the salinity constituent, temperature was assumed to be uniform throughout the water column at the inflow boundary.

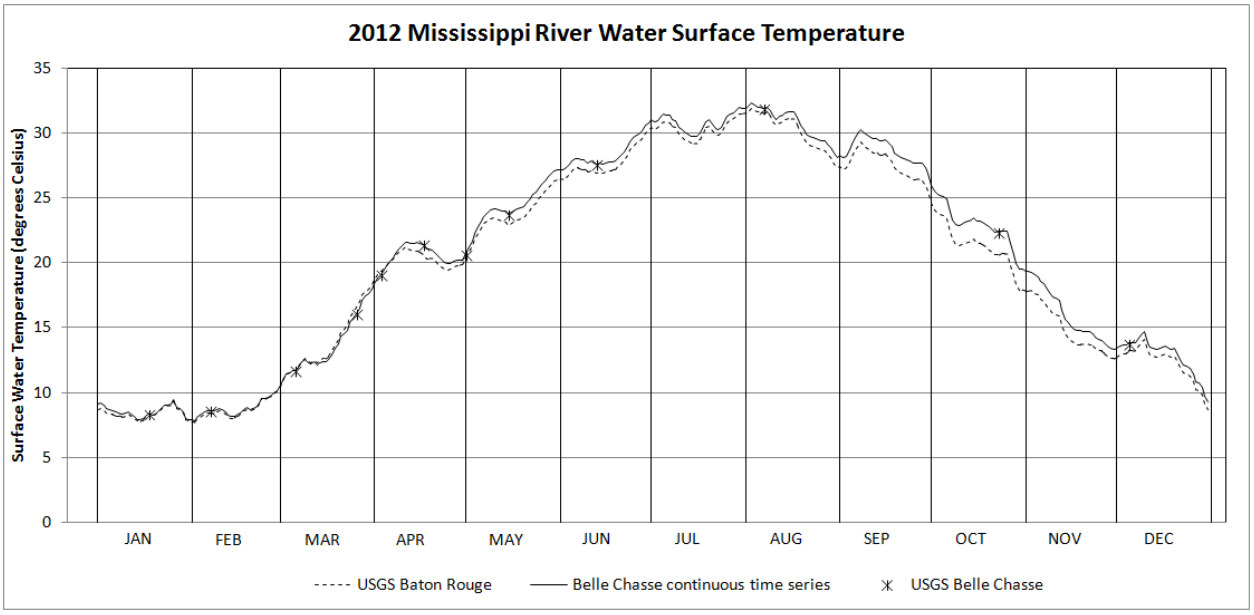

Figure 7-8 Mississippi river surface temperature

7.3.1.4 Mississippi River at Belle Chasse Open Water Boundary – Fine Sediment Concentration

In addition to measurement of water quality parameters, including turbidity, periodic suspended sediment sampling is conducted by the USGS at Belle Chasse using isokinetic depth integrated sampling methods under the National Stream Quality Accounting Network (NASQAN). These published suspended sediment data were analyzed to determine the wash load or fines concentration, i.e., that portion of the suspended load consisting of particles finer than 0.0625 mm in diameter. The remaining portion is considered to be the sand load or that portion of the suspended load consisting of particles

greater than 0.0625 mm in diameter. Table 7-1 shows the resultant wash load concentration and suspended sand load for sampling events from November 2007 through August 2013.

Table 7-1 Suspended sediment concentration and turbidity data at Belle Chasse, LA

Date	Instantaneous river discharge (m^3/s)	Turbidity (NTRU)	Total suspended sediment concentration (kg/m^3)	Fine sediment percentage of sample (portion < 0.0625 mm diameter)	Suspended fine sediment concentration (kg/m^3)	Suspended sand concentration (kg/m^3)
11/13/2007	7957	44	0.0580	100	0.0580	0.0000
12/17/2007	7306	17	0.0390	96	0.0374	0.0016
1/14/2008	10874	68	0.0990	99	0.0980	0.0010
2/19/2008	19171	200	0.4420	89	0.3934	0.0486
3/12/2008	21266	110	0.2510	69	0.1732	0.0778
3/26/2008	25202	110	0.2520	73	0.1840	0.0680
4/9/2008	31998	100	0.3660	75	0.2745	0.0915
4/23/2008	33131	82	0.2450	64	0.1568	0.0882
5/7/2008	31149	59	0.1720	62	0.1066	0.0654
5/19/2008	26306	61	0.0990	84	0.0832	0.0158
8/20/2008	11553	130	0.1910	100	0.1910	0.0000
10/22/2008	7306	23	0.0340	100	0.0340	0.0000
11/10/2008	5918	23	0.0380	99	0.0376	0.0004
1/21/2009	17698	110	0.2130	81	0.1725	0.0405
2/18/2009	13309	67	0.1060	97	0.1028	0.0032
3/4/2009	14781	110	0.1730	93	0.1609	0.0121
4/8/2009	19935	93	0.2110	76	0.1604	0.0506
4/20/2009	22993	76	0.2100	73	0.1533	0.0567
5/6/2009	21577	66	0.1390	84	0.1168	0.0222
5/18/2009	28317	88	0.2270	69	0.1566	0.0704
6/3/2009	31715	66	0.1590	66	0.1049	0.0541
6/16/2009	23871	5	0.1210	71	0.0859	0.0351
8/10/2009	12828	70	0.1180	99	0.1168	0.0012
10/6/2009	13252	58	0.0990	98	0.0970	0.0020
12/9/2009	17273	60	0.1280	85	0.1088	0.0192
1/11/2010	24862	100	0.2200	64	0.1408	0.0792
2/1/2010	21832	81	0.2180	73	0.1591	0.0589
3/8/2010	20048	46	0.1150	63	0.0725	0.0426
3/23/2010	18321	36	0.1000	70	0.0700	0.0300
4/5/2010	24664	70	0.1980	73	0.1445	0.0535

4/19/2010	21662	46	0.1060	75	0.0795	0.0265
5/3/2010	12799	71	0.1150	98	0.1127	0.0023
5/17/2010	21549	80	0.1770	77	0.1363	0.0407
6/14/2010	17415	56	0.1140	91	0.1037	0.0103
8/9/2010	14328	140	0.2300	99	0.2277	0.0023
10/25/2010	9316	35	0.0600	99	0.0594	0.0006
12/6/2010	10336	28	0.0720	99	0.0713	0.0007
1/12/2011	9033	35	0.0610	99	0.0604	0.0006
2/7/2011	8070	2.9	0.0450	99	0.0446	0.0005
3/9/2011	19142	250	0.9830	97	0.9535	0.0295
3/23/2011	26165	95	0.2470	70	0.1729	0.0741
4/4/2011	28147	44	0.1750	63	0.1103	0.0648
4/18/2011	20530	53	0.1330	78	0.1037	0.0293
5/10/2011	33697	60	0.1940	66	0.1280	0.0660
5/17/2011	33131	75	0.2060	58	0.1195	0.0865
5/24/2011	32848	66	0.1840	63	0.1159	0.0681
5/31/2011	31715	46	0.1250	64	0.0800	0.0450
6/8/2011	30865	37	0.1140	64	0.0730	0.0410
6/14/2011	27864	42	0.1160	72	0.0835	0.0325
6/21/2011	25089	34	0.1210	60	0.0726	0.0484
6/28/2011	20303	55	0.1360	84	0.1142	0.0218
7/12/2011	19454	67	0.1320	89	0.1175	0.0145
7/26/2011	15376	65	0.1460	98	0.1431	0.0029
8/23/2011	10534	38	0.0880	100	0.0880	0.0000
10/26/2011	6881	11	0.0270	100	0.0270	0.0000
12/7/2011	17103	100	0.2390	93	0.2223	0.0167
1/18/2012	16027	46	0.1040	84	0.0874	0.0166
2/7/2012	21662	110	0.2540	77	0.1956	0.0584
3/6/2012	12431	37	0.0780	97	0.0757	0.0023
3/26/2012	21181	69	0.1450	79	0.1146	0.0305
4/3/2012	23248	58	0.1500	74	0.1110	0.0390
4/17/2012	14951	42	0.0840	97	0.0815	0.0025
5/1/2012	11383	30	0.0650	98	0.0637	0.0013
5/15/2012	12629	57	0.1100	99	0.1089	0.0011
6/13/2012	6088	9.8	0.0210	99	0.0208	0.0002
10/23/2012	4899	6.8	0.0100	100	0.0100	0.0000
12/5/2012	5550	6.2	0.0090	100	0.0090	0.0000
1/16/2013	14640	150	0.3200	99	0.3168	0.0032
2/19/2013	20105	120	0.2130	83	0.1768	0.0362
3/6/2013	13790	100	0.1460	97	0.1416	0.0044
3/19/2013	14668	57	0.1130	92	0.1040	0.0090
4/9/2013	16933	74	0.1320	88	0.1162	0.0158
4/23/2013	17443	68	0.1360	93	0.1265	0.0095

5/7/2013	24806	130	0.2770	77	0.2133	0.0637
5/21/2013	26533	37	0.1370	64	0.0877	0.0493
6/4/2013	23786	38	0.1100	69	0.0759	0.0341
6/18/2013	24013	120	0.1860	84	0.1562	0.0298
7/16/2013	16933	87	0.1540	96	0.1478	0.0062
8/20/2013	11440	48	0.0770	100	0.0770	0.0000

The turbidity and fine sediment concentration data were plotted as shown in Figure 7-9 and a polynomial best fit relationship was determined using Microsoft Excel.

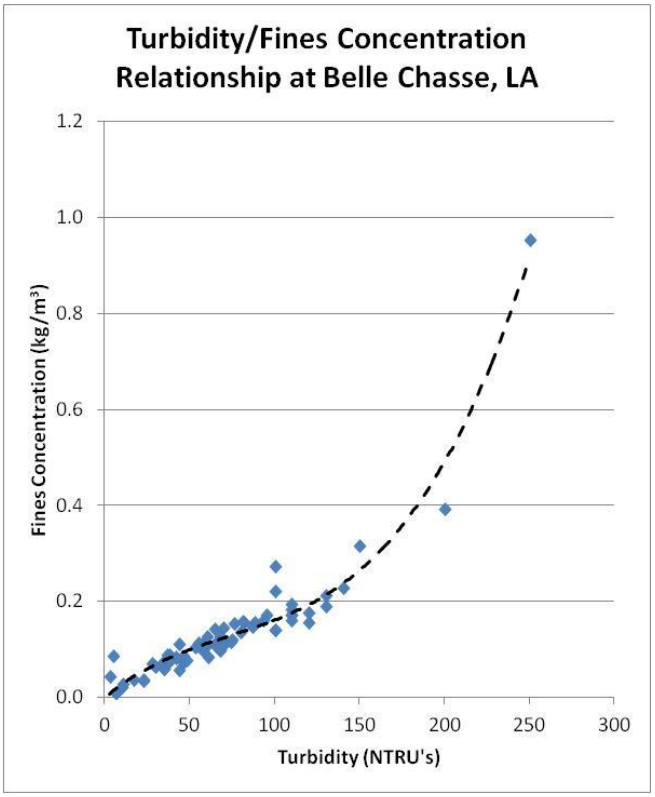

Figure 7-9 Belle Chasse turbidity/fines relationship

The relationship between turbidity and fine sediment concentration using this data was determined to be:

$$Concentration\left\{\frac{kg}{m^3}\right\} = (1.0651\ \mathrm{X}\ 10^{-7})(Turbidity^3\{NTRU's\}) - (2.3542\mathrm{X}\ 10^{-5})(Turbidity^2\{NTRU's\}) + (2.9007\mathrm{X}\ 10^{-3})(Turbidity\{NTRU's\}) - (8.1515\mathrm{X}\ 10^{-4}), with\ R^2 = 0.95 \quad (7\text{-}1)$$

Beginning on 29 February 2012, the USGS began continuous recording of turbidity data at Belle Chasse. These hourly turbidity data were used to create a continuous fine sediment concentration time series at Belle Chasse using the Turbidity/Concentration relationship. This concentration time series was then fitted to the observed concentration data collected during 2012 as shown in Figure 7-10.

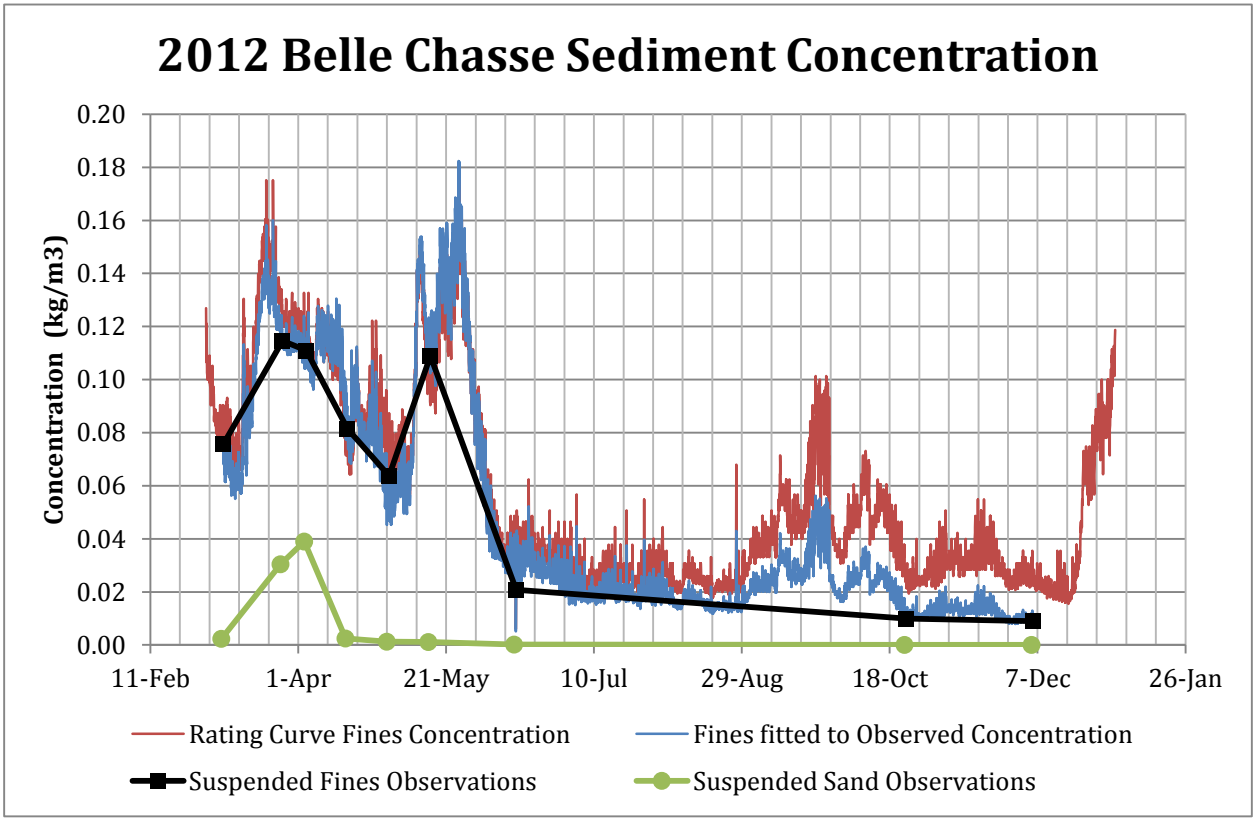

Figure 7-10 2012 Delft3D Fine Sediment Concentration time series for the Belle Chasse open water boundary

As the gradation of fine sediment was not analyzed by the USGS at Belle Chasse during 2012, the closest data source is used to provide insight into the possible gradation of fine sediments at Belle Chasse. Tarbert Landing is the closest data source for fine sediment gradation data during 2012. Table 7-2 displays the percentage of total fines for the Wentworth fine sediment classes, namely all Clay, Very Fine Silt (VFM), Fine Silt (FM), Medium Silt (MM), and Coarse Silt (CM) and the corresponding Mississippi River discharge for the period from 2 October 2008 through 4 October 2012. The bottom withdrawal method was used to evaluate the fine sediment gradation of samples collected at Tarbert Landing. The four year average percentages for the wash load were Clays - 34.6%, Very Fine Silt – 12.6%, Fine Silt – 8.2%, Medium Silt – 18.8% and Coarse Silt – 25.7%.

Table 7-2 Tarbert Landing fine sediment fractions

Sample date	Local Mississippi River Discharge ($m^3 s^{-1}$)	Clay Suspended fine sediment fraction (percent)	VFM Suspended fine sediment fraction (percent)	FM Suspended fine sediment fraction (percent)	MM Suspended fine sediment fraction (percent)	CM Suspended fine sediment fraction (percent)
10/2/2008	14388	42.4	16.0	4.5	16.8	20.2
11/6/2008	6908	26.3	10.6	16.0	21.3	25.7
12/4/2008	6158	28.2	10.2	11.7	26.1	23.8
12/16/2008	9026	41.2	3.2	8.4	22.2	24.9
1/8/2009	20308	27.1	14.4	7.7	18.3	32.5
1/29/2009	10537	31.8	14.6	10.4	21.7	21.6
2/12/2009	12476	27.8	13.8	11.7	21.7	25.0
2/26/2009	17062	36.1	15.4	7.0	14.5	27.1
3/12/2009	13405	35.1	13.6	8.9	17.5	24.9
3/26/2009	18617	50.8	15.8	6.0	12.9	14.5
4/1/2009	19645	46.7	7.1	8.3	17.2	20.7
4/23/2009	22813	29.5	12.0	10.6	14.3	33.6
5/7/2009	22374	26.5	13.2	6.6	19.3	34.5
5/23/2009	33600	30.3	15.8	6.0	15.3	32.5
6/19/2009	20124	42.5	12.0	8.1	16.3	21.0
7/10/2009	13312	40.8	18.4	8.7	17.0	15.0
8/6/2009	12178	30.9	18.0	6.3	26.7	18.0

9/3/2009	8764	44.1	19.5	9.4	16.1	10.9
10/1/2009	12056	43.3	13.3	6.9	14.5	22.1
11/5/2009	24923	24.3	5.2	6.5	12.9	51.2
12/3/2009	18899	42.8	4.9	11.6	14.1	26.6
12/18/2009	20139	30.4	10.6	5.5	18.1	35.5
1/6/2010	26355	35.3	14.3	4.8	19.1	26.6
1/28/2010	19112	33.9	9.9	5.6	20.6	30.0
2/11/2010	28971	36.5	18.8	7.1	10.6	27.0
2/25/2010	24205	36.0	12.7	4.1	15.8	31.5
3/10/2010	17891	33.3	18.1	7.1	18.8	22.6
4/8/2010	24973	41.0	15.3	8.3	15.1	20.3
4/22/2010	19162	34.6	11.7	9.2	20.5	24.1
5/5/2010	16898	28.0	12.3	6.0	21.7	31.9
5/20/2010	25047	34.1	19.7	6.1	15.0	25.0
6/17/2010	16032	37.1	13.9	9.9	25.5	13.5
7/1/2010	17745	46.9	17.2	7.3	14.6	13.9
8/5/2010	15335	38.5	16.6	13.7	17.5	13.8
9/1/2010	12250	40.9	17.4	5.3	18.5	17.8
10/7/2010	9665	42.4	22.3	10.7	16.0	8.6
11/10/2010	6540	41.1	14.9	9.6	22.4	12.0
12/9/2010	11048	29.3	13.8	8.4	23.5	25.0
12/27/2010	8483	37.1	12.6	13.1	21.2	16.0
1/13/2011	10520	24.9	5.6	7.4	16.0	46.1
1/26/2011	7810	18.3	8.6	15.0	16.0	42.1
2/14/2011	10210	26.8	11.8	7.8	26.0	27.6
2/28/2011	11052	35.2	7.1	10.0	20.7	26.9
3/10/2011	22260	26.3	7.1	8.9	17.7	40.0
3/24/2011	26610	30.7	12.2	9.4	15.1	32.6
4/14/2011	21226	26.1	9.0	6.8	23.2	34.9
4/28/2011	23937	36.6	15.9	2.9	16.9	27.6
5/15/2011	42359	47.4	11.3	6.3	13.1	21.9
5/30/2011	40260	31.6	9.1	11.8	12.6	34.9
6/23/2011	21460	32.6	17.1	5.2	17.6	27.5
7/14/2011	18501	41.5	11.1	8.9	19.5	19.0
8/4/2011	12363	33.5	10.9	7.4	27.4	20.9
9/8/2011	9513	30.0	9.9	5.9	23.4	30.8
10/6/2011	8199	39.5	11.6	10.9	17.8	20.3
11/9/2011	7373	28.4	12.4	12.7	24.9	21.7

12/1/2011	15167	31.3	15.6	6.4	17.2	29.6
12/14/2011	23046	33.1	7.8	7.2	16.3	35.6
1/5/2012	22071	35.1	11.2	5.3	11.7	36.8
1/23/2012	13491	33.1	9.6	9.0	18.1	30.3
2/6/2012	22240	37.9	8.3	8.4	13.4	32.0
2/22/2012	16809	35.4	11.2	6.1	19.4	28.0
3/5/2012	11667	32.9	17.1	5.7	16.8	27.4
3/19/2012	20816	34.0	9.9	9.4	17.8	28.8
4/12/2012	16570	32.1	10.0	10.5	17.8	29.6
4/26/2012	12010	27.4	8.3	9.9	22.2	32.3
5/10/2012	11638	37.1	20.2	8.0	14.1	20.7
5/24/2012	12277	43.4	16.4	6.6	21.8	11.8
6/7/2012	6251	33.6	12.6	9.3	20.8	23.7
7/5/2012	4833	39.1	10.4	8.8	27.2	14.5
8/2/2012	4010	37.2	2.0	11.7	24.7	24.3
9/6/2012	4506	24.7	9.6	8.7	31.4	25.7
10/4/2012	6131	30.8	19.9	0.9	25.8	22.6
	Percent Averages	34.6	12.6	8.2	18.8	25.7

Table 7-3 Wentworth classes and representation of wash load at Tarbert Landing for October 2008 - October 2012

Wentworth Sediment Class	Grain Size mm	Geometric Mean mm	Average Wash Load Fraction percent
Clay	< 1/256		34.6
Very fine silt (VFM)	1/256 - 1/128	0.0054	12.6
Fine silt (FM)	1/128 - 1/64	0.0108	8.2
Medium silt (MM)	1/64 - 1/32	0.0221	18.8
Coarse silt (CM)	1/32 - 1/16	0.0442	25.7

The river wash load is chiefly dependent on upstream watershed and river conditions; therefore a correlation between local river conditions and wash load does not necessarily exist. A continuous time series of Silt and Clay concentration was constructed using the measured Silt and Clay fractions at Tarbert Landing as a guideline. For modeling purposes, the wash load is split among the Clay and Silt sizes in order to evaluate the

effects of flocculation due to salinity on the Clay constituent. The four silt classes are combined and evaluated as an additional constituent. Figure 7-11 displays the temporal suspended concentrations of the two constituents at the Belle Chasse inflow boundary.

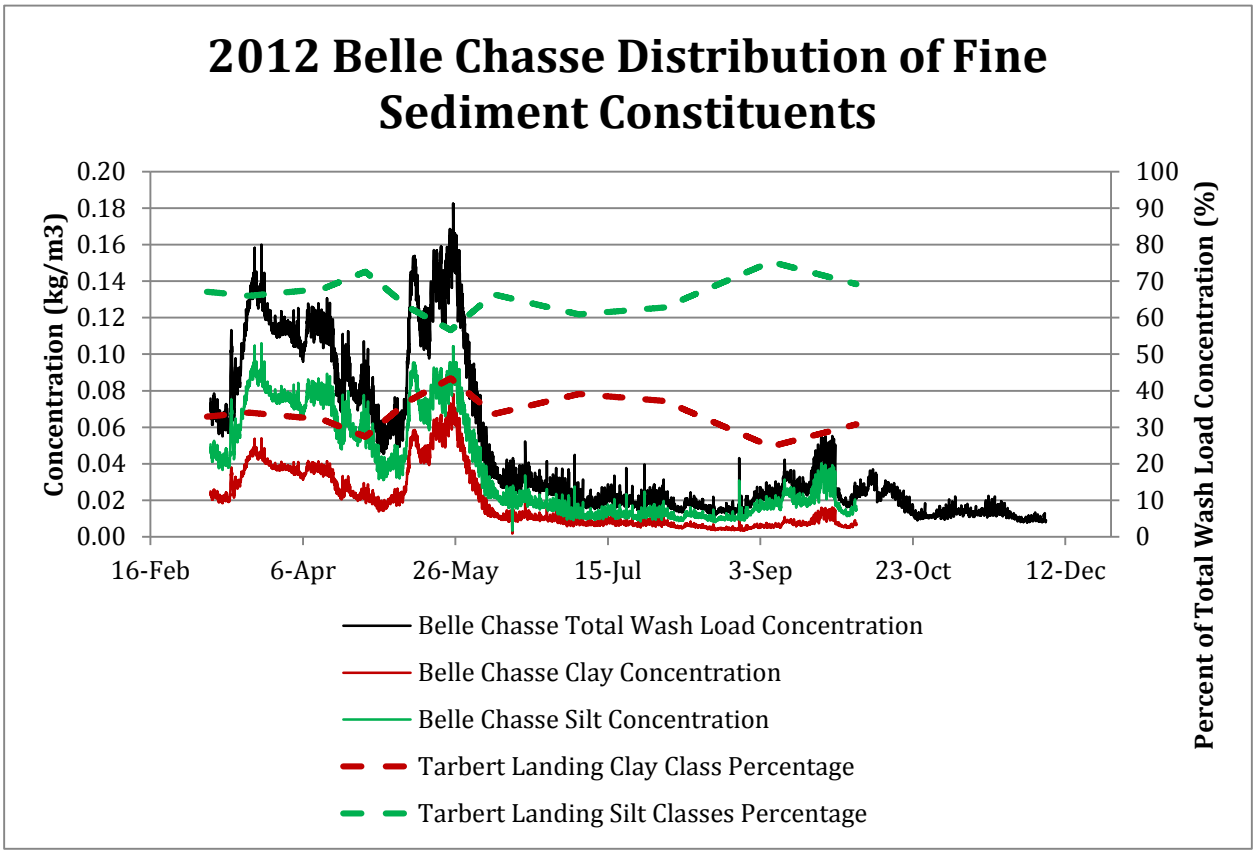

Figure 7-11 Wash Load boundary distribution

7.3.2 Tide Boundaries

Water level alone is insufficient data to resolve current patterns in the model domain that are subject to influence from external forcings such as the loop currents in the Gulf of Mexico. The offshore currents south of Louisiana are influenced by the shedding of loop currents from a persistent current that flows northward from the Caribbean Sea, into the Gulf of Mexico and out again through the Straits of Florida as can be seen in the U. S. Navy Coastal Ocean Model (NCOM) results shown in Figure 7-12. In Delft3D, current data may be imposed at the open boundaries to resolve these currents in the model domain resulting from exterior influences. This is an important consideration when the aim is to reproduce temperature and salinity fluxes across the model boundaries. Numerous tide

boundary configurations were tested throughout the model development process including using current boundaries as a means to reproduce these externally influenced currents in the model. However, it was found that in doing so, the model spin-up time was significantly increased compared to the spin-up time with water level boundaries. Also, the water level reproduction in the river channel became unacceptable when using current tide boundaries. As the focus of this investigation is on salt wedge dynamics and sediment processes in the river channel, water level boundaries were used to define the tidal forcing due to the resultant superior reproduction of water levels in the river channel over that which would result through the use of current boundaries.

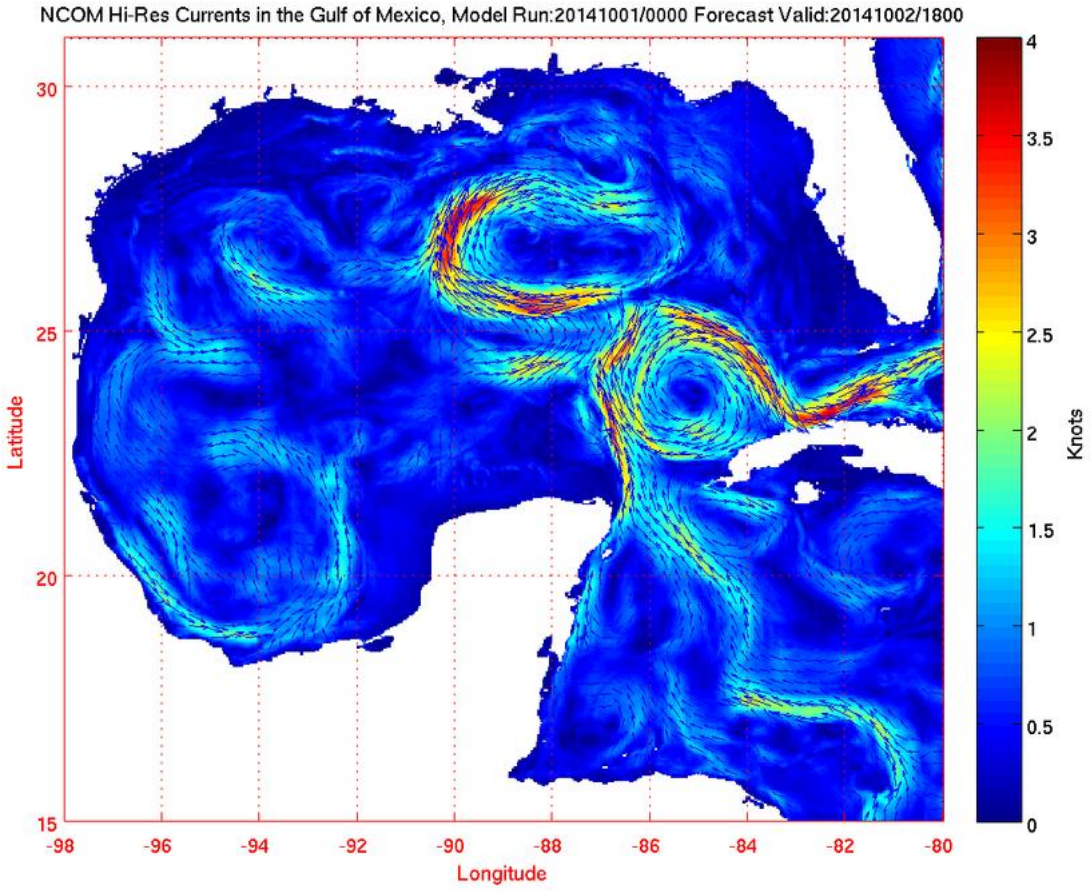

Figure 7-12 Typical current patterns in the Gulf of Mexico (source: http://www.opc.ncep.noaa.gov/)

Salinity, temperature, and sediment concentration profiles must also be defined at the Gulf open water boundaries in order to inform a 3D model. As observation data does not typically exist in the deep Gulf waters, results from a larger domain 3D model may be used to define these boundary profiles. Data from the American Seas (AMSEAS) model has been made available starting with results from 5 April 2010. The AMSEAS model is an operational ocean prediction system for the Gulf of Mexico and Caribbean. AMSEAS has a resolution of 1/36 degree (~3km) in the horizontal and 40 levels in the vertical (see Figure 7-13 for AMSEAS model domain). Three hour interval solution data are available that contains temperature, salinity, eastward and northward currents, elevation, and the atmospheric forcing fields from a 15 km application of the U. S. Navy's Coupled Ocean/Atmosphere Mesoscale Prediction System model. Open water boundary conditions for the AMSEAS model are applied from the Naval Oceanographic Office's operational 1/8 degree global NCOM model.

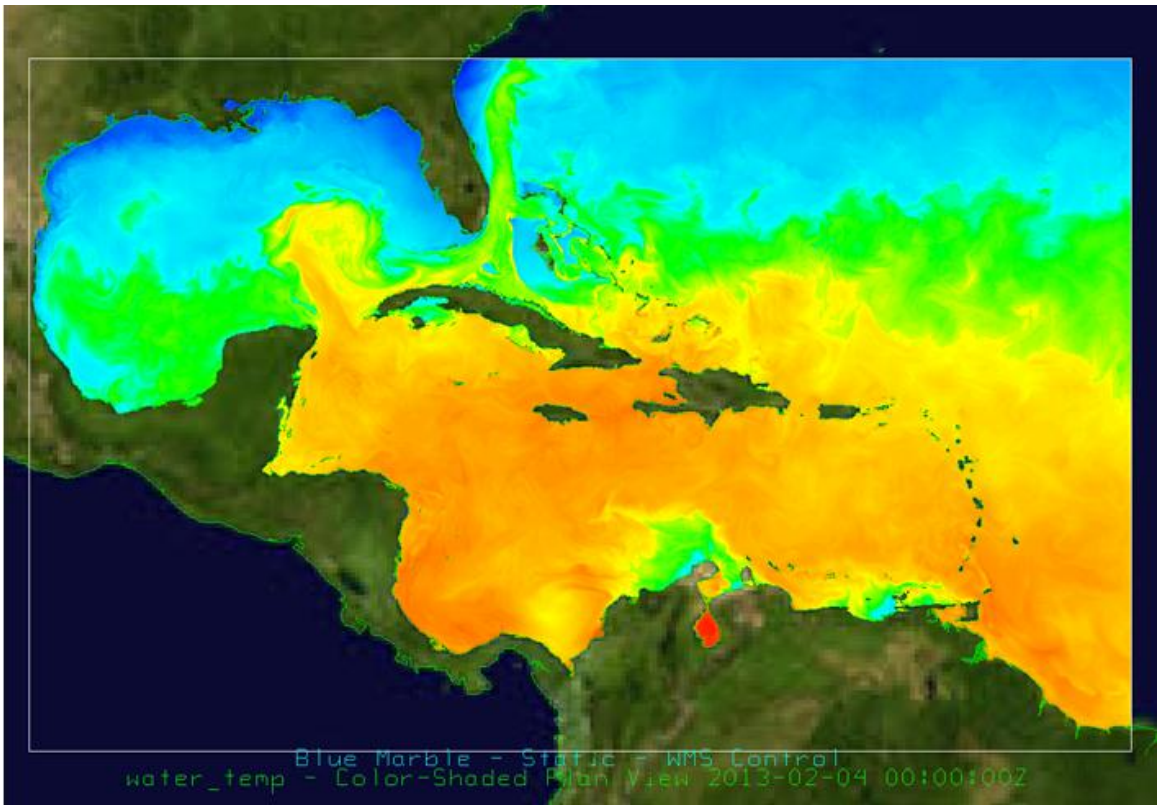

Figure 7-13 Typical AMSEAS model surface temperature results showing the model domain extent (source: http://ecowatch.ncddc.noaa.gov/amseas/)

7.3.2.1 Tide Boundaries – Water Level

Boundary water levels were defined from three gage sources; the Pilots Station East, Southwest Pass, LA (NOAA id # 8760922), the Grand Isle, LA gage (NOAA id # 8761724), and the Northeast Bay Gardene near Point-a-la-Hache gage (USGS id # 07374527). These gages were found to have the most complete records for 2012. The locations of these gages are shown in Figure 7-14.

Figure 7-14 Locations of boundary tide level data sources

As explained previously, the tide boundaries are defined by providing a water level time series at the two endpoints; linear interpolation defines the water level at the intermediary nodes along the tide boundary. The three gage sources for tide levels were used to build a continuous water level along the grid boundaries in the Gulf from Grand Isle to Bay Gardene. Figure 7-15 displays how the gage data were distributed along the Gulf

boundaries. The phase of the water level data was not temporally shifted to transfer the data from the gage site to the boundary end points.

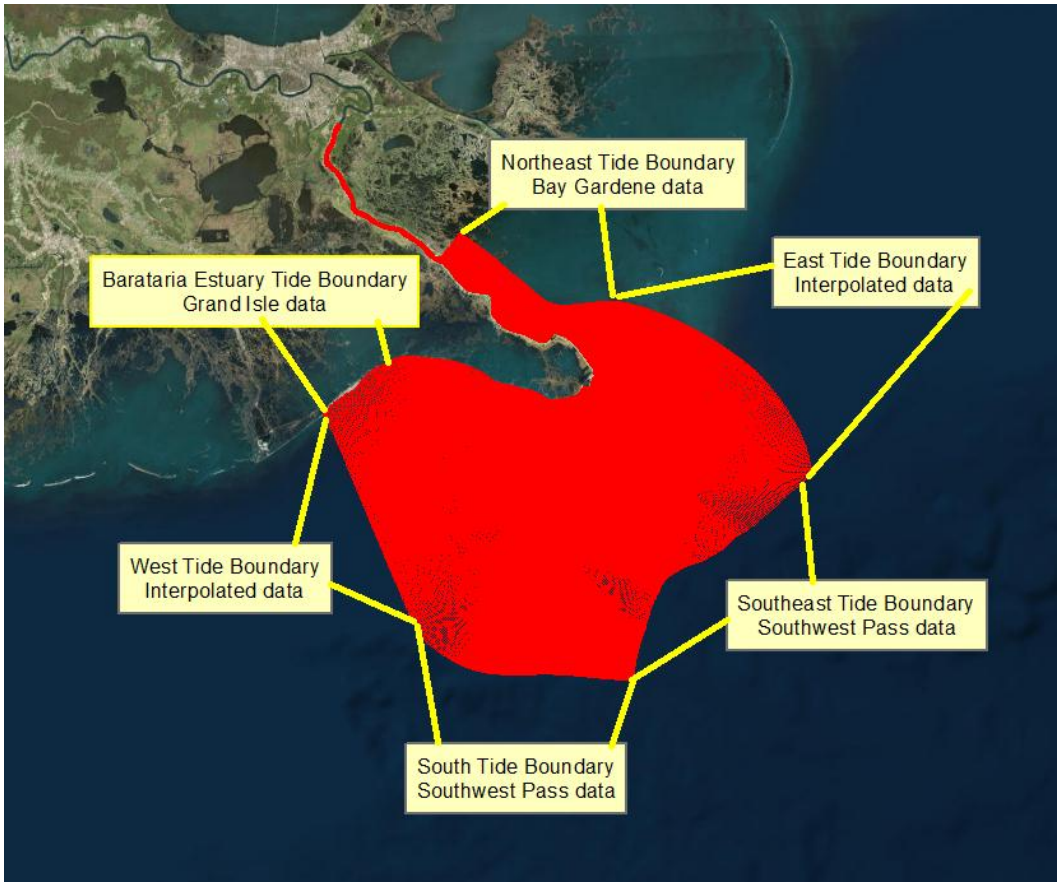

Figure 7-15 Gage water level data distribution along the Gulf boundary

The vertical reference to NAVD88 was not available for these gages; therefore, a visual comparison was made to the NAVD88 referenced USACE Southwest Pass Jetty gage (01670) and the data at the three sites were vertically adjusted to match the levels observed in the USACE Southwest Pass Jetty gage. These adjustments were necessary to prevent unrealistic current set up due to erroneous tide gradients. The NOAA Jetty data were adjusted by adding 0.4 meters to the data. The Grand Isle MSL data was raised 0.14 meters to approximate NAVD88 levels. The Bay Gardene local datum was raised 0.25 meters to approximate NAVD88 levels. The tide level data for the Pilots Station East station are shown in Figure 7-16.

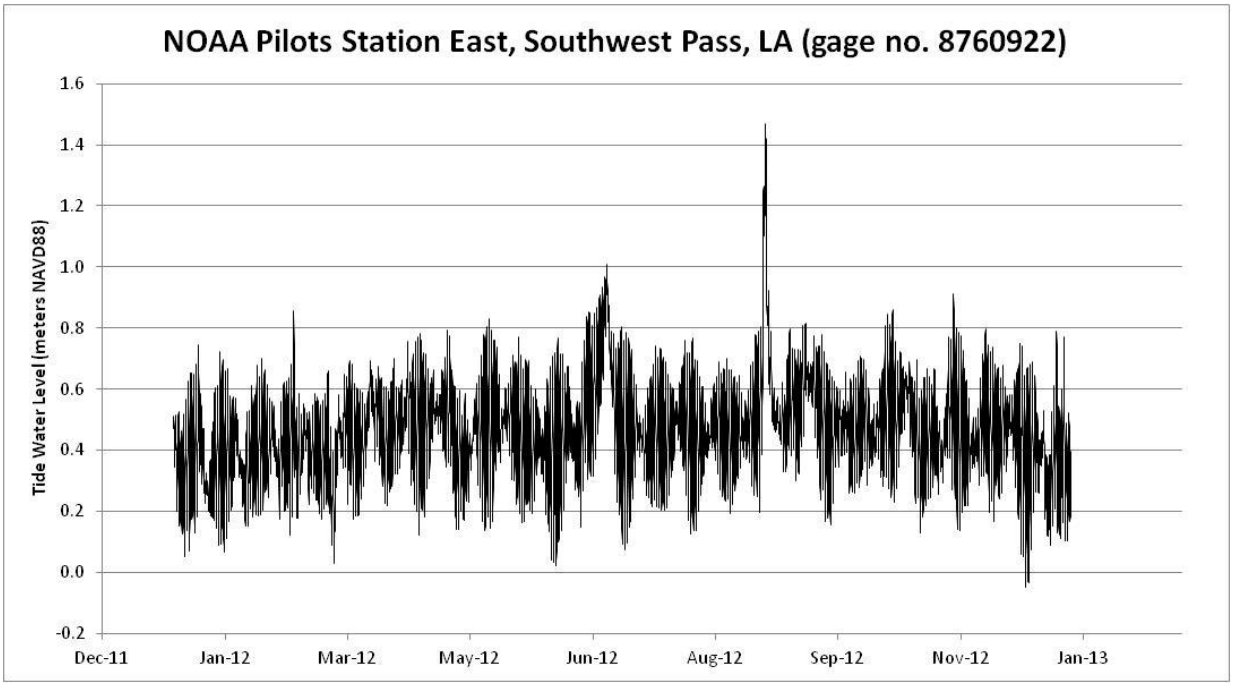

Figure 7-16 Water levels at Southwest Pass adjusted to NAVD88

7.3.2.2 Tide Boundaries – Salinity

The salinity profile at each tide boundary endpoint must be specified for the simulation duration. Salinity data from the USGS Bay Gardene and USGS Grand Isle sites along with AMSEAS model data were used to define the salinity concentration at the tide boundaries. The salinity was assumed to be uniform throughout the water column for the shallower endpoints that used observed data at Grand Isle and Bay Gardene. The model used linear interpolation to define salinity values for intermediary layers between the surface and bottom for those deeper tide endpoints that used the AMSEAS model data. Figure 7-17 displays the source of salinity data for the tide boundaries. Figure 7-18, Figure 7-19, Figure 7-20, Figure 7-21, and Figure 7-22 show the data used to define the salinity concentration boundaries.

Figure 7-17 Salinity and temperature boundary data sources

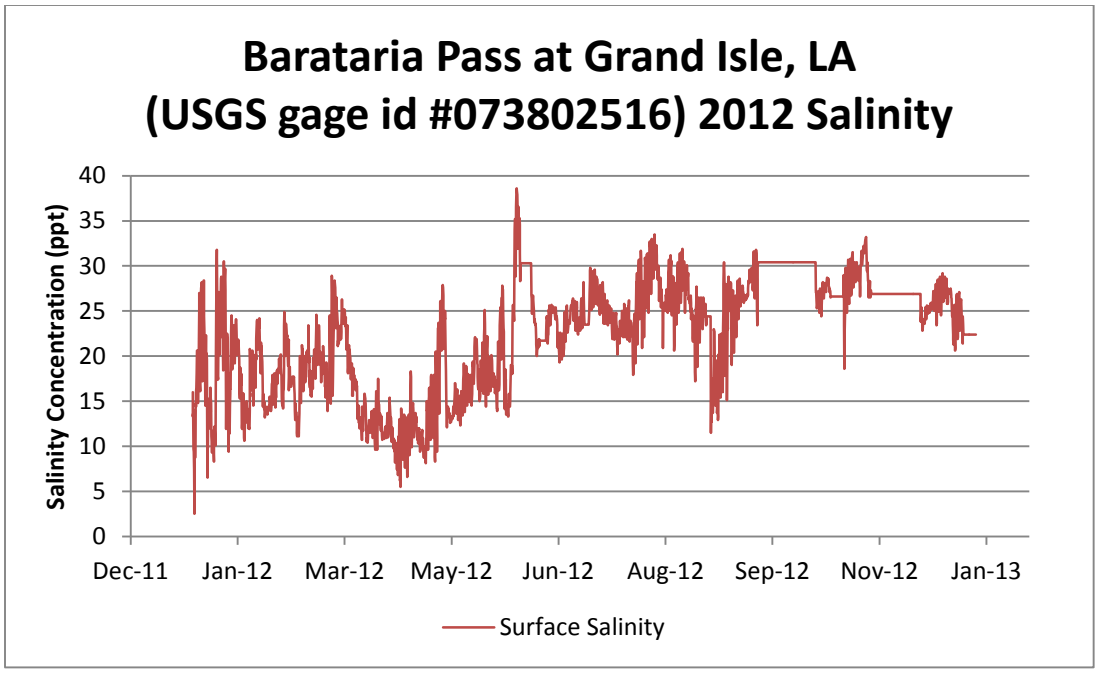

Figure 7-18 Salinity at USGS Grand Isle site

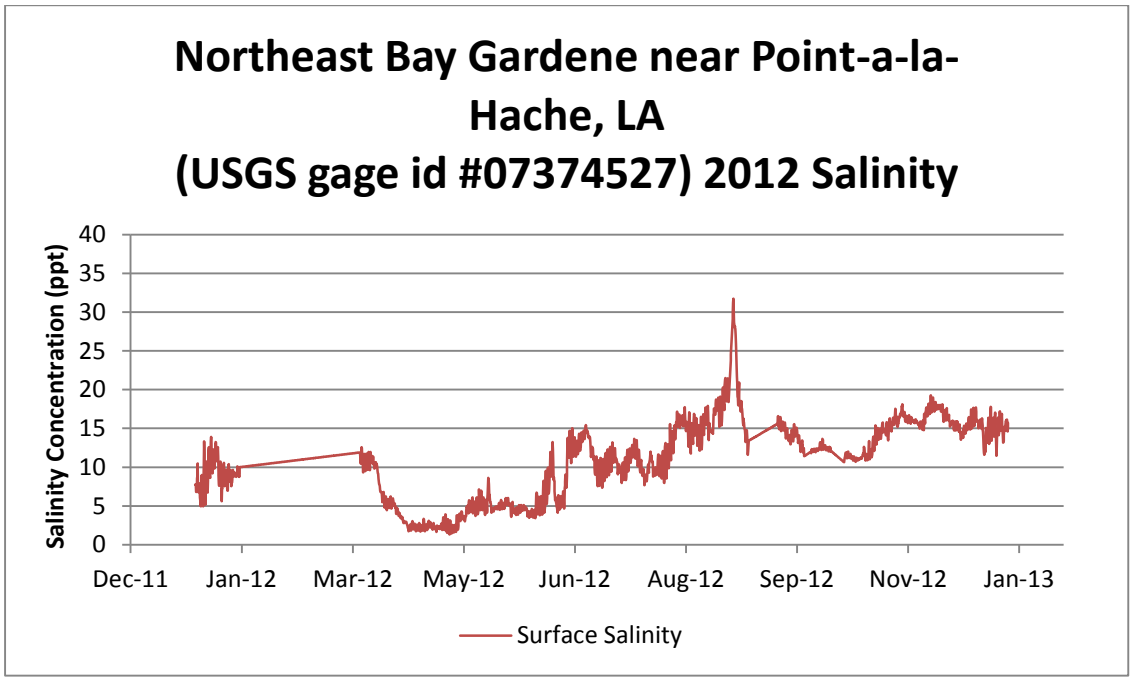

Figure 7-19 Salinity at USGS Bay Gardene site

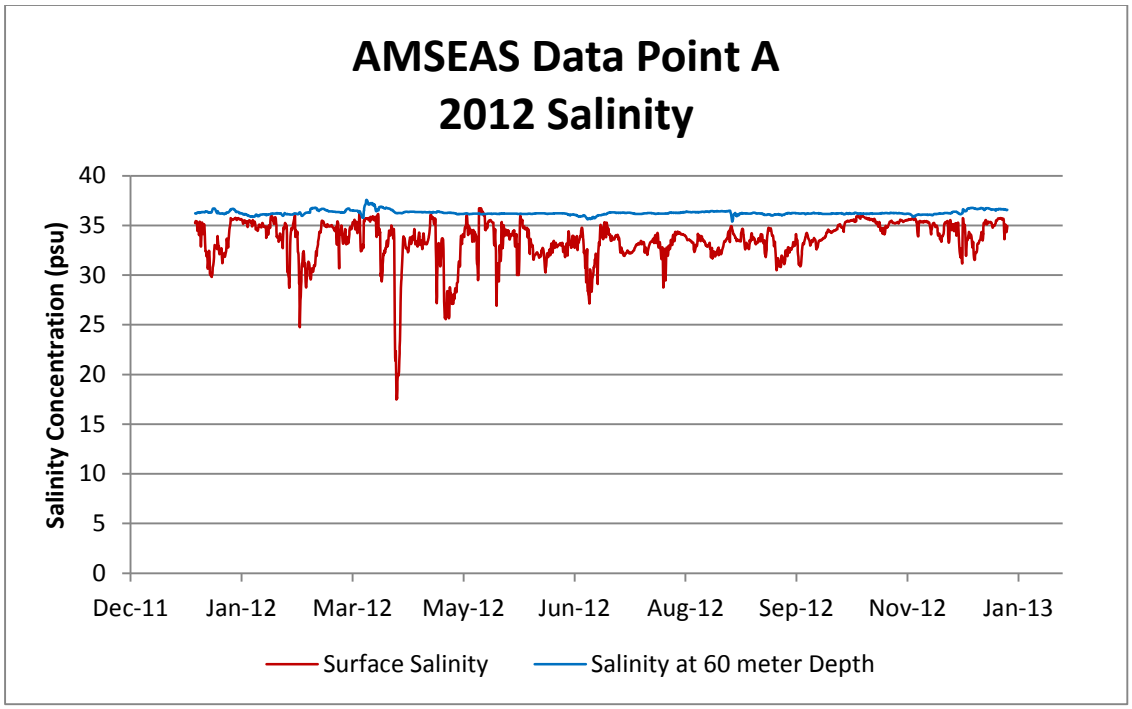

Figure 7-20 Salinity at AMSEAS Data Point A

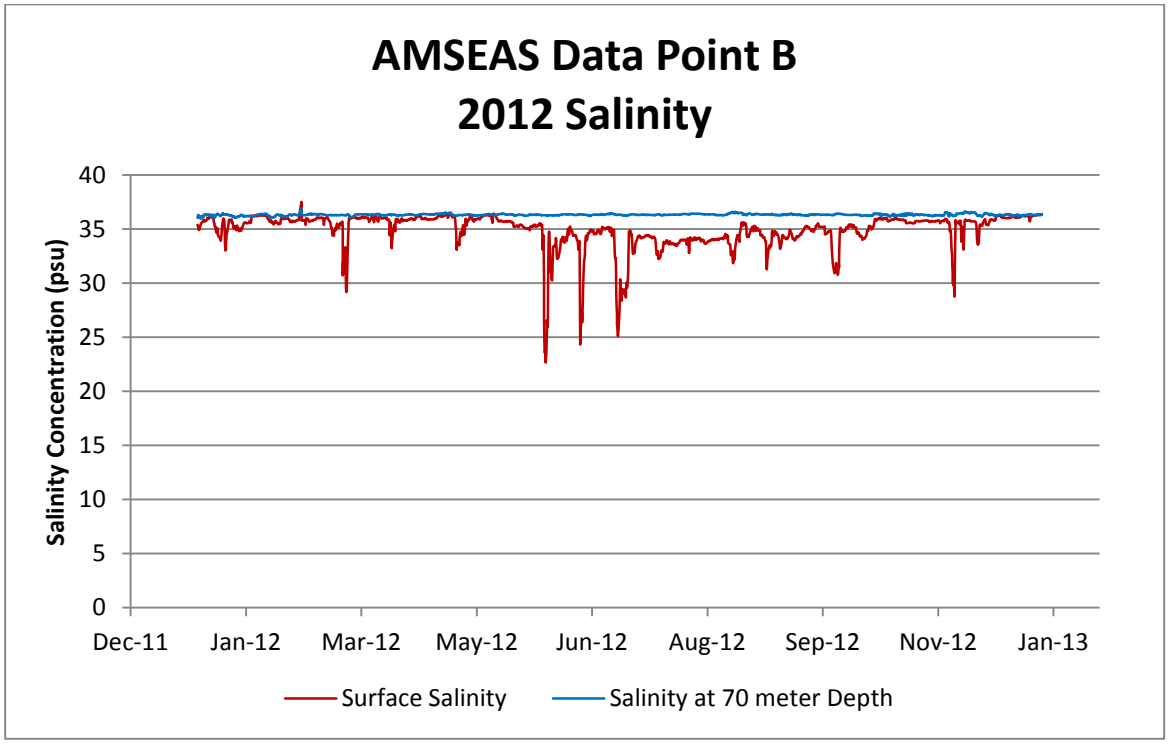

Figure 7-21 Salinity at AMSEAS Data Point B

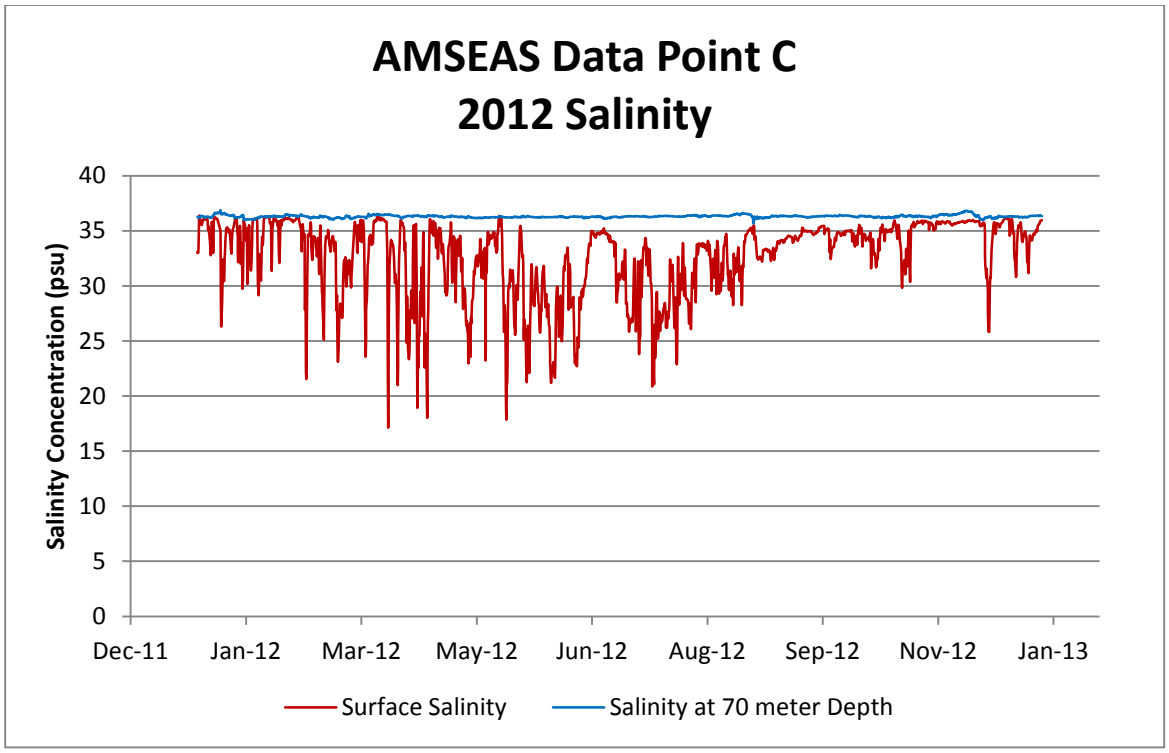

Figure 7-22 Salinity at AMSEAS Data Point C

7.3.2.3 Tide Boundaries – Temperature

The temperature profile at each tide boundary endpoint must be specified for the simulation duration. Temperature data from the USGS Bay Gardene and NOAA Grand Isle sites along with AMSEAS model data were used to define the temperature at the tide boundaries. The assumption was made that the temperature would be uniform in the shallower tide endpoints that used observed data from Grand Isle and Bay Gardene. Only the surface and bottom temperatures were used in the deeper tide endpoints that used the AMSEAS model data. The model used linear interpolation for the intermediary layers at the boundary. Figure 7-17 shows the source of temperature data for the tide boundaries. Figure 7-23, Figure 7-24, Figure 7-25, Figure 7-26, and Figure 7-27 show the data used to define the temperature boundaries.

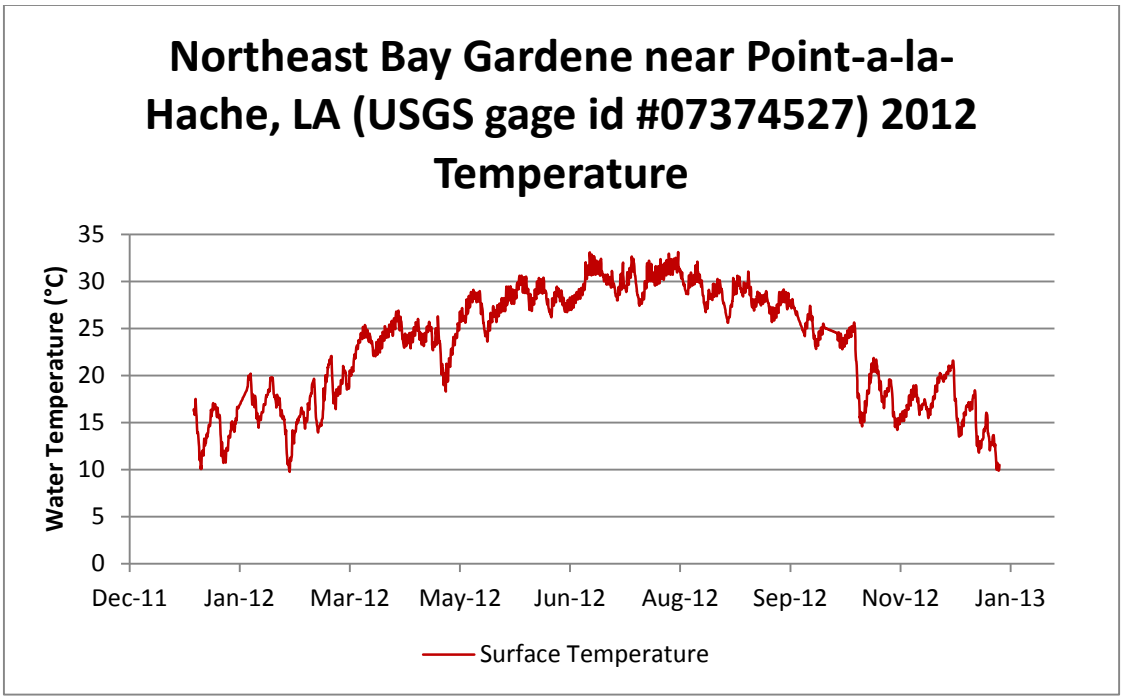

Figure 7-23 Temperature at USGS Bay Gardene site

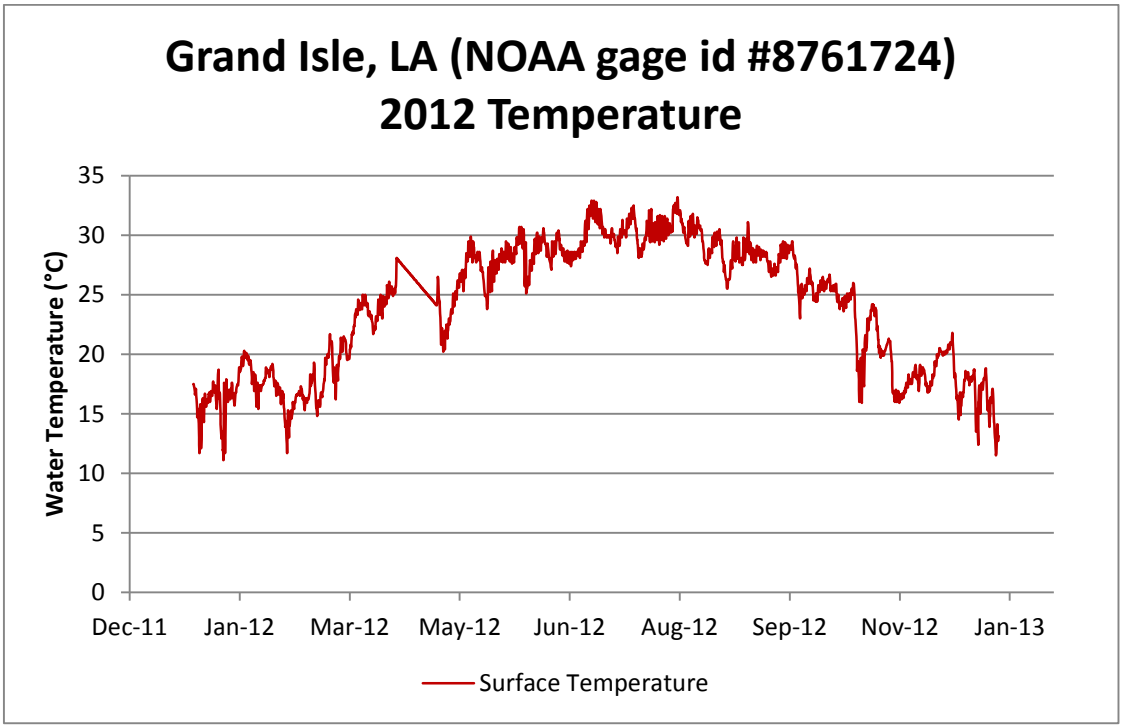

Figure 7-24 Temperature at NOAA Grand Isle site

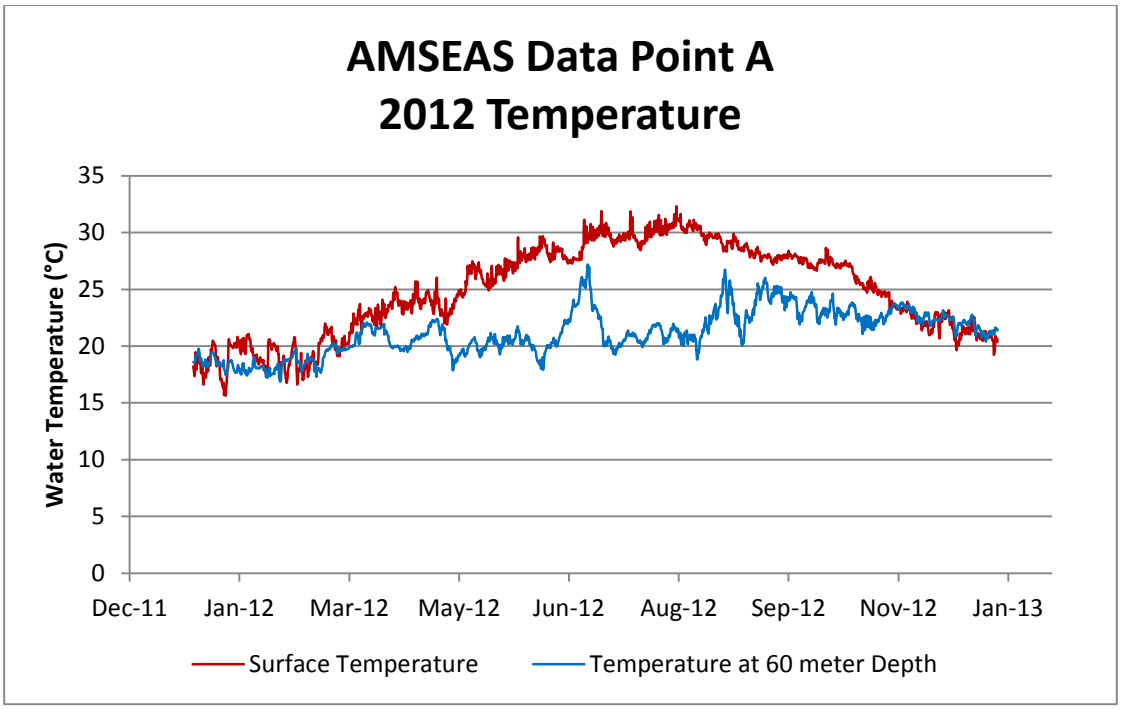

Figure 7-25 Temperature at AMSEAS Data Point A

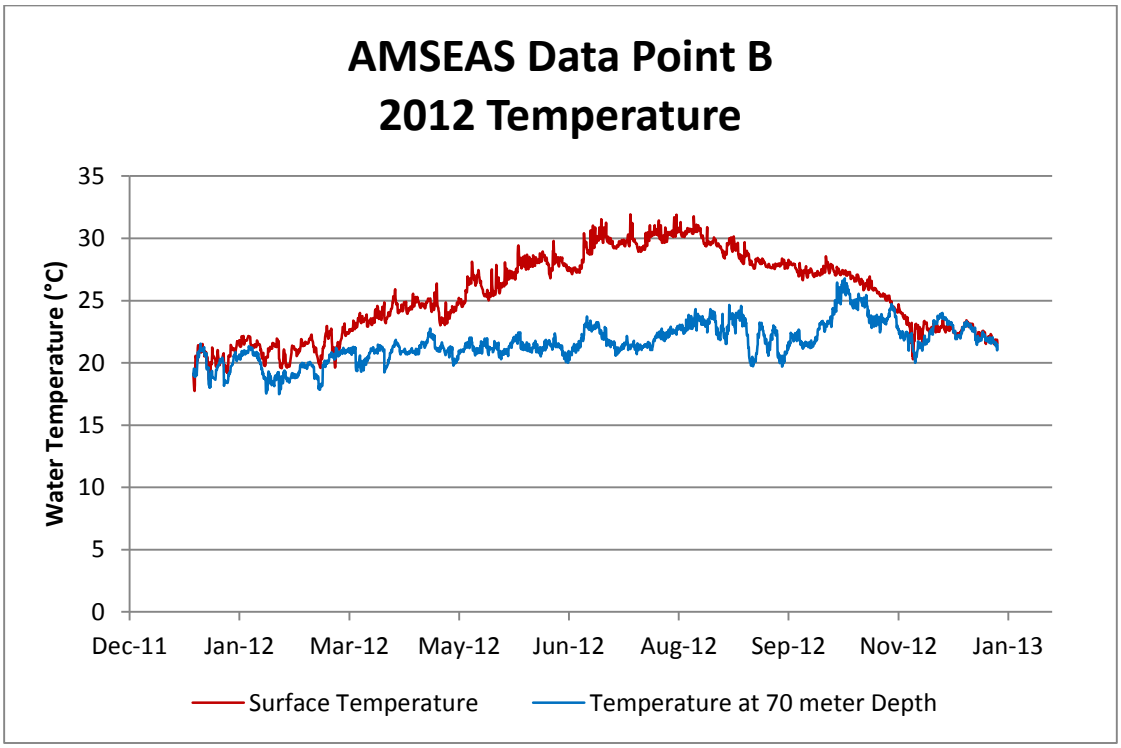

Figure 7-26 Temperature at AMSEAS Data Point B

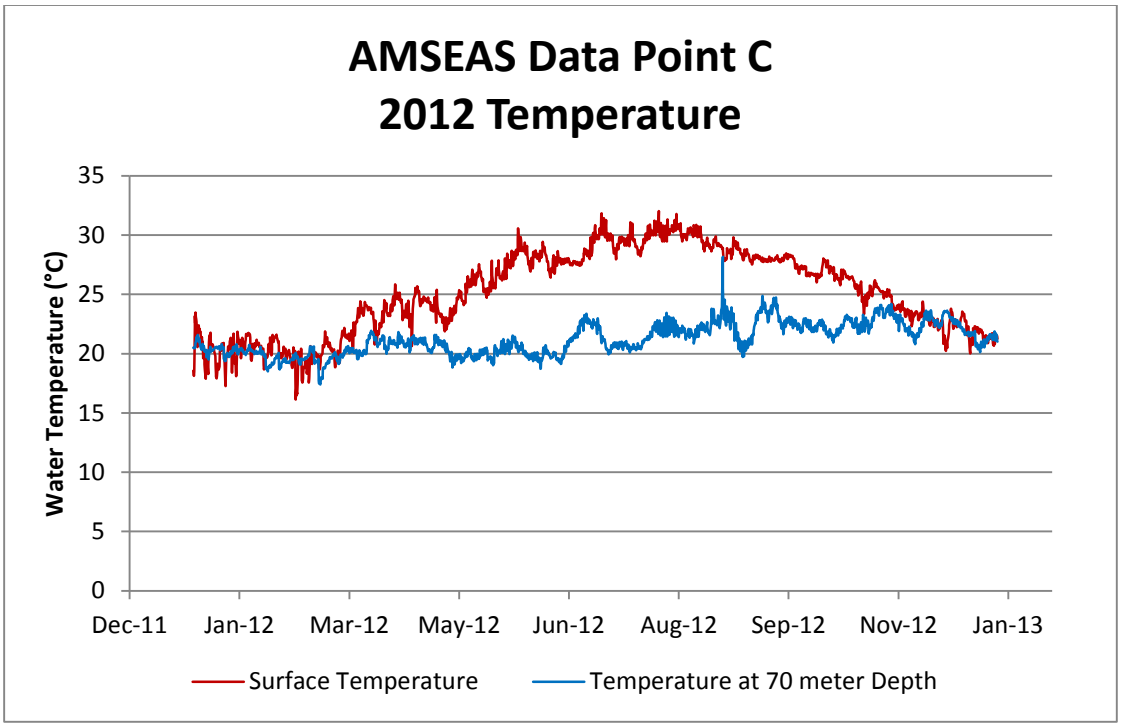

Figure 7-27 Temperature at AMSEAS Data Point C

7.3.2.4 Tide Boundaries – Fine Sediment Concentration

A sediment concentration constant value of 0.001 kg/m^3 was applied to all of the tide boundaries. This value is intended to represent the background concentration of sediment in the Gulf of Mexico.

7.4 Free Water Surface

A uniform prevailing wind was applied at the free surface for all simulations using wind speed and direction data provided by the National Data Buoy Center of the National Oceanic and Atmospheric Administration. The 2012 6-minute interval data from the Pilottown, LA station (id # 8760721) were used. The Delft3D default linear wind drag coefficient with 0.00063 at 0.0 m/s and 0.00723 at 100 m/s was applied for all wind speeds. An example of typical data from the station are displayed in Figure 7-28.

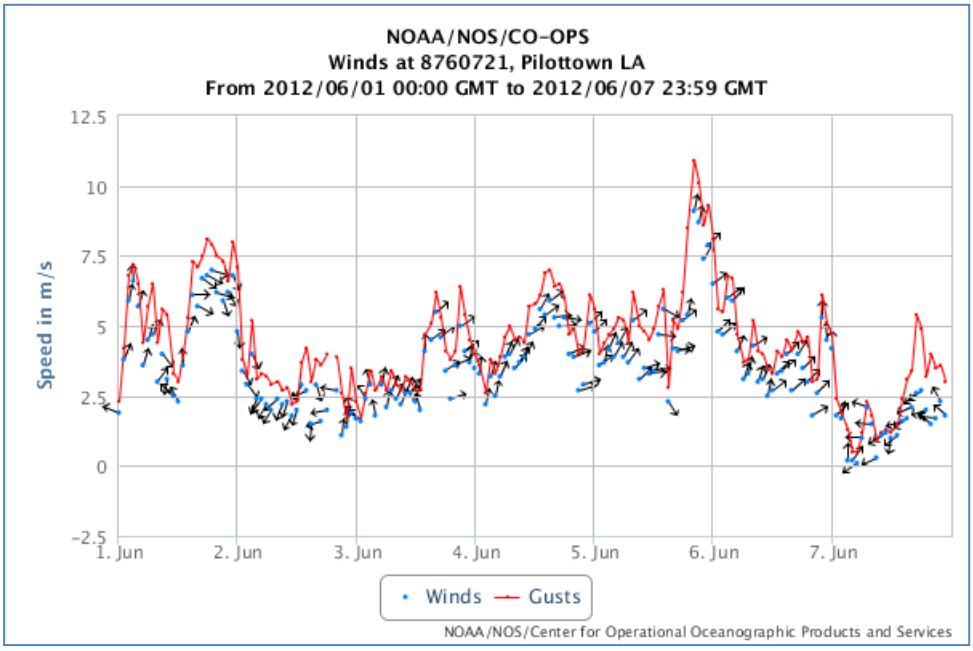

Figure 7-28 Example of wind speed data at Pilottown, LA

The excess temperature heat flux model was applied to each simulation with data from the same NOAA data source that supplied the wind data at Pilottown. See Figure 7-29 for the corresponding temperature data to the wind data shown in Figure 7-28 and reference Figure 7-30 for the calendar year 2012 entire air temperature data set.

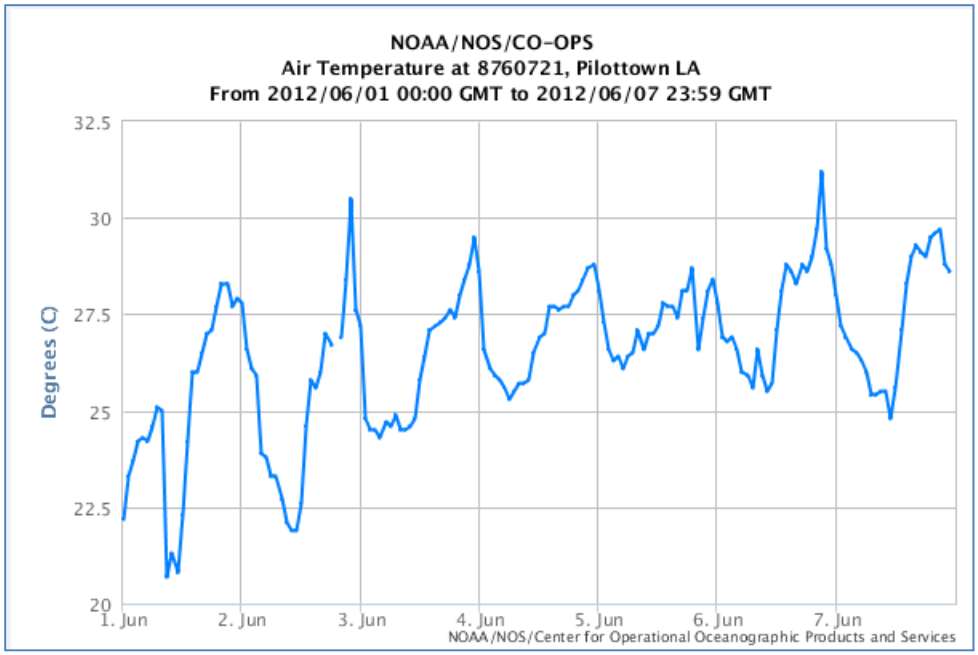

Figure 7-29 Detail of hourly air temperature fluctuations at Pilottown, LA

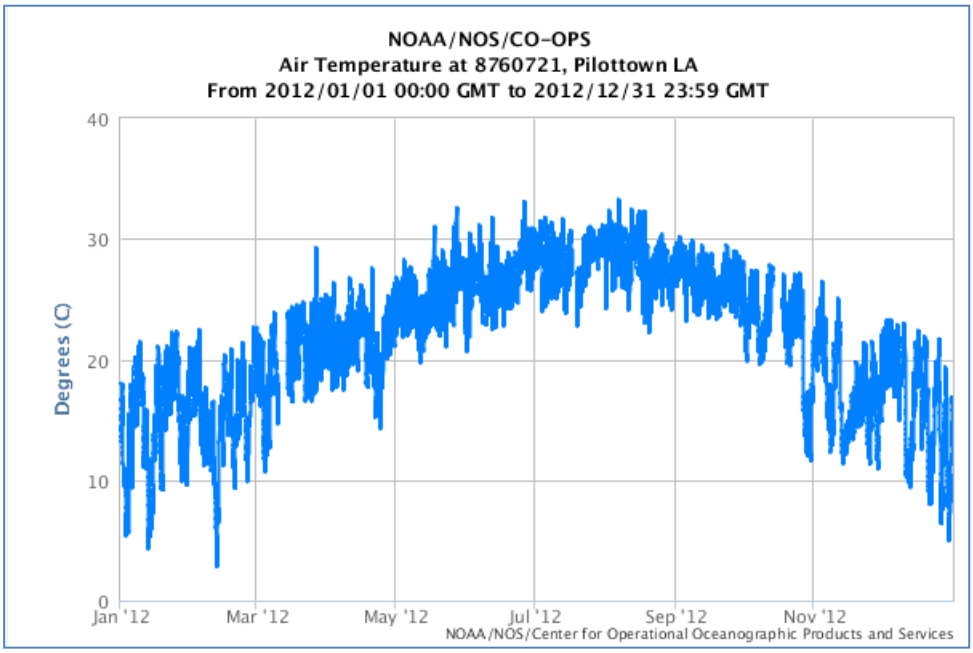

Figure 7-30 2012 air temperature at Pilottown, LA

8 MODEL CALIBRATION AND RESULTS

8.1 Overview

The grid and boundary conditions presented in the previous chapters were used to simulate various periods of the year 2012 in order to compare model results to observed data and refine various model parameters to improve model performance. All simulations were performed on a Cray XE6 using 224 compute cores as described in Chapter 6.

Suspended sediment data collected on 23 April 2012 was used to calibrate total fine sediment concentrations in the upper part of the model domain in the main river channel from RK 84 to RK 111. The Mississippi River discharge at Tarbert Landing was around 11,200 m^3/s on this date, this is considered a below average flow for this time of year but would be of sufficient magnitude to keep silt in suspension above Venice in order to test this aspect of the model.

Suspended sediment and salinity data collected in the 20 - 24 September 2012 period in the lower delta was used to calibrate fine sediment characteristics under the influence of salinity induced flocculation. The river flow at Tarbert Landing averaged about 4,370 m^3/s during this period; this is considered a very low discharge in the river. The river would not be expected to carry the heavier silts to the lower delta area under these low flow conditions. Figure 8-1 displays these data set collection dates in context with 2012, minimum, maximum, and average river discharge conditions.

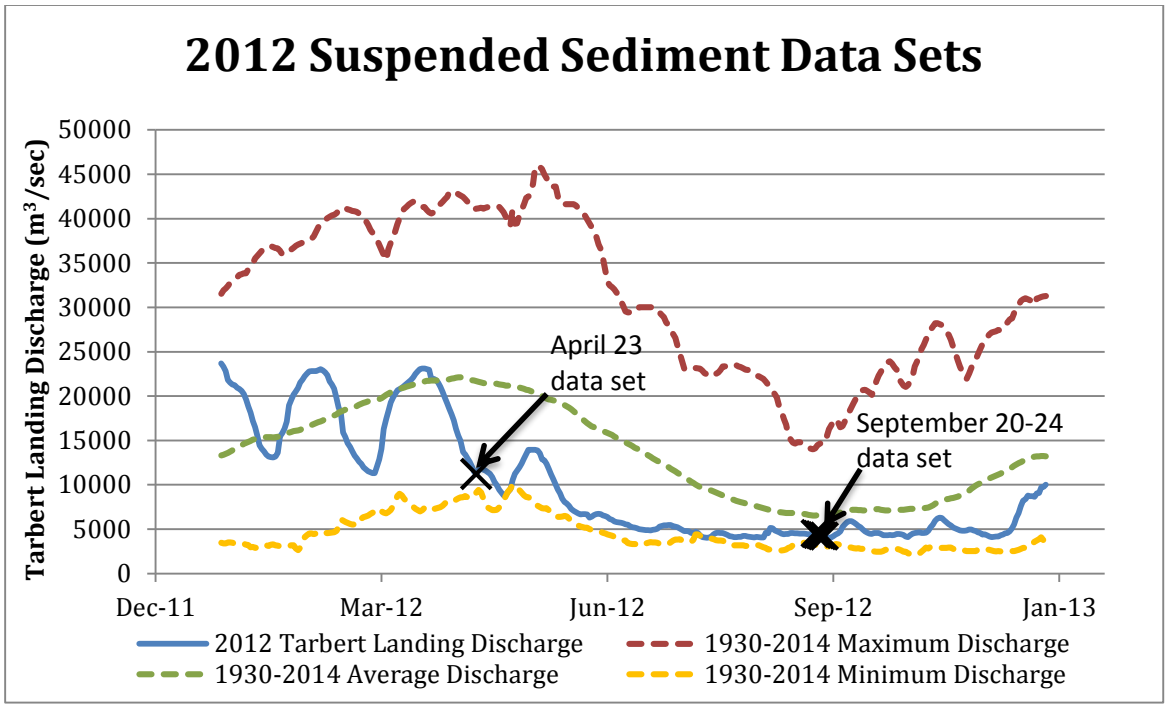

Figure 8-1 Suspended sediment data sets collected in 2012

Available observed water level and discharge are compared to model results during these simulation periods. As this was a drought year, the USACE monitored salinity wedge progression throughout the low water period. Therefore, in-situ salinity and temperature measurements are available for comparison to model results.

8.2 Vertical Layer Design

The results presented in this chapter were computed using a 14-layer design. Many vertical layer designs were tested, but this level of resolution was found to be a good compromise between the desired level of resolution needed to define the pycnocline observed in the prototype and the resultant computational burden. The top layer (Z-level model layer number 14) incorporates the entire water level range of the free surface in order to eliminate the computational demands of turning cells on and off as the water surface fluctuates. An additional feature of this layer design is increased vertical resolution (2 meters) at the elevations the pycnocline typically develops in order to improve density gradient resolution during periods of stratified flow. Table 8-1 summarizes this 14-layer design.

Table 8-1 Z-level model layer design summary

Z-level layer number	Thickness (meters)	Bottom (NAVD88 meters)	Top (NAVD88 meters)
1	20	-70	-50
2	12	-50	-38
3	8	-38	-30
4	5	-30	-25
5	4	-25	-21
6	3	-21	-18
7	2	-18	-16
8	2	-16	-14
9	2	-14	-12
10	2	-12	-10
11	2	-10	-8
12	3	-8	-5
13	3	-5	-2
14	6	-2	+4

8.3 Bottom Roughness

Adjustment to the bottom roughness was the primary means of adjusting model stage and discharge to match observed stages and flow measurements. The Chézy bottom roughness was defined in blocks and was spatially varied. For the most part, the grid lines followed channel alignments, which allowed a grid block to define the spatial footprint of the channel. Areas between channels were also defined as a block which allowed the friction coefficient to be adjusted during the calibration process. A strip of higher friction values was defined at the open water grid perimeters in an attempt to dampen spurious velocity disturbances entering the domain as well as node to node oscillations observed at the deep open water boundaries.

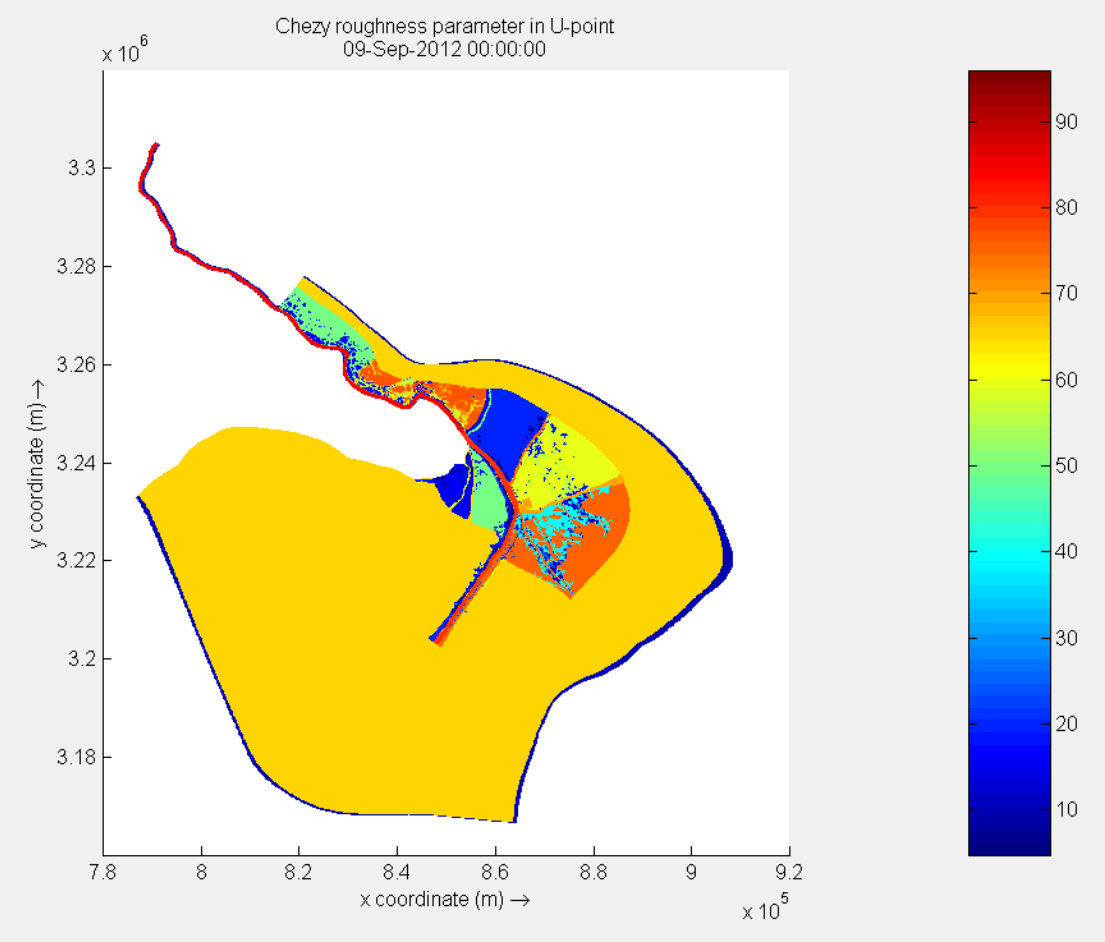

Figure 8-2 Chézy bottom roughness coefficients

8.4 Turbulence Adjustments

The default background horizontal eddy viscosity value of 1.0 m^2/s was used to produce the model results presented in this chapter. The horizontal eddy diffusivity was set to 2.0 m^2/s from the default value of 10.0 m^2/s; the default value is more applicable to coarse grids with cell sizes of hundreds of meters. The background vertical eddy viscosity was set to 0.0001 m^2/s and the background vertical diffusivity was set to 0.0 m^2/s to minimize any artificially induced vertical mixing.

Through trial and error, the Ozmidov length scale was set to 0.07 m. This value was achieved through comparison of the most upstream advance of the salinity wedge to observed values in 2012.

8.5 Fine Sediment Parameters

Through the model calibration process, the fine sediment parameters were adjusted from the default values in order to improve model results as compared to measured values of suspended sediment concentrations. Comparison of model results to the April 2012 and September 2012 suspended sediment data sets was the primary means for informing the calibration process. Table 8-2 contains the values used for this study.

Table 8-2 Selected fine sediment parameters

Parameter	Variable Name	Units	Delft3D default value	Clay value used	Silt value used
Reference density for hindered settling	Cref	kg/m^3	1.6000000E+03	1.6000000E+03	1.6000000E+03
Specific density	RhoSol	kg/m^3	2.6500000E+03	2.6500000E+03	2.6500000E+03
Salinity for saline settling velocity	SalMax	ppt	-	2.0000000E+01	0.0000000E+00
Settling velocity fresh water	WS0	m/s	2.5000000E-01	9.0000000E-06	5.0000000E-04
Settling velocity saline water	WSM	m/s	-	5.0000000E-05	5.0000000E-04
Critical bed shear stress for sedimentation	TcrSed	N/m^2	1.0000000E+03	1.0000000E-04	1.0000000E-01
Critical bed shear stress for erosion	TcrEro	N/m^2	5.0000000E-01	1.0000000E-02	2.0000000E-01
Erosion parameter	EroPar	$kg/m^2/s$	1.0000000E-04	1.0000000E-05	1.0000000E-05
Dry bed density	CDryB	kg/m^3	5.0000000E+02	5.0000000E+02	5.0000000E+02
Initial sediment layer thickness at bed	IniSedThick	m	5.0000000E-02	0.0000000E+00	0.0000000E+00
FacDSS*SedDia=Initial suspended sediment diam.	FacDSS	-	1.0000000E+00	1.0000000E+00	1.0000000E+00

8.6 2012 Model Results

8.6.1 2012 water level results

Water level data is collected at several locations throughout the model domain. Those gages lying along the main flow path in the Mississippi River and Southwest Pass were evaluated to analyze model performance relative to water level. Figure 8-3 displays the locations of the gage records used in this study and Table 8-3 summarizes the vertical datum information for the gages. The following figures display model results with recorded water level information.

Figure 8-3 Location of Water Level gages along the lower Mississippi River and Southwest Pass

Table 8-3 Water Level gage vertical datum summary

Water Level Gage Name	Instrument Type	Responsible Entity	Gage ID #	Location in relation to Head of Passes (River KM)	Published Datum	Date Adjusted to NAVD88 (2004.65) DD/MM/YYYY	Shift applied to get NAVD88 (2004.65) (meters)
Mississippi River at Belle Chasse	Pressure tranducer	USGS	07374525	RK 120.4 AHP	Gage	N/A	-2.0970
Mississippi River at Alliance	Encoder	USACE	01390	RK 100.6 AHP	NAVD88 (2004.65)	18/07/2008	0.0000
Mississippi River at West Pointe a la Hache	Pressure tranducer	USACE	01400	RK 78.4 AHP	NAVD88 (2004.65)	24/09/2006	0.0000
Mississippi River at Empire	Pressure tranducer	USACE	01440	RK 47.5 AHP	NAVD88 (2004.65)	07/07/2007	0.0000
Mississippi River at Venice	Encoder	USACE	01480	RK 17.3 AHP	NGVD29		-0.1768
Mississippi River at West Bay	Pressure tranducer	USACE	01515	RK 10.9 AHP	NAVD88 (2004.65)	30/01/2009	0.0000
Mississippi River at Head of Passes	Pressure tranducer	USACE	01545	RK 2.0 BHP (in South Pass)	NAVD88 (2004.65)	15/01/2008	+0.0427
Southwest Pass RK 12.1 BHP	Encoder	USACE	01575	RK 11.9 BHP	NAVD88 (2004.65)	19/08/2010	0.0000
Southwest Pass East Jetty	Radar	USACE	01670	RK 28.6 BHP	NAVD88 (2004.65)	15/01/2008	0.0000

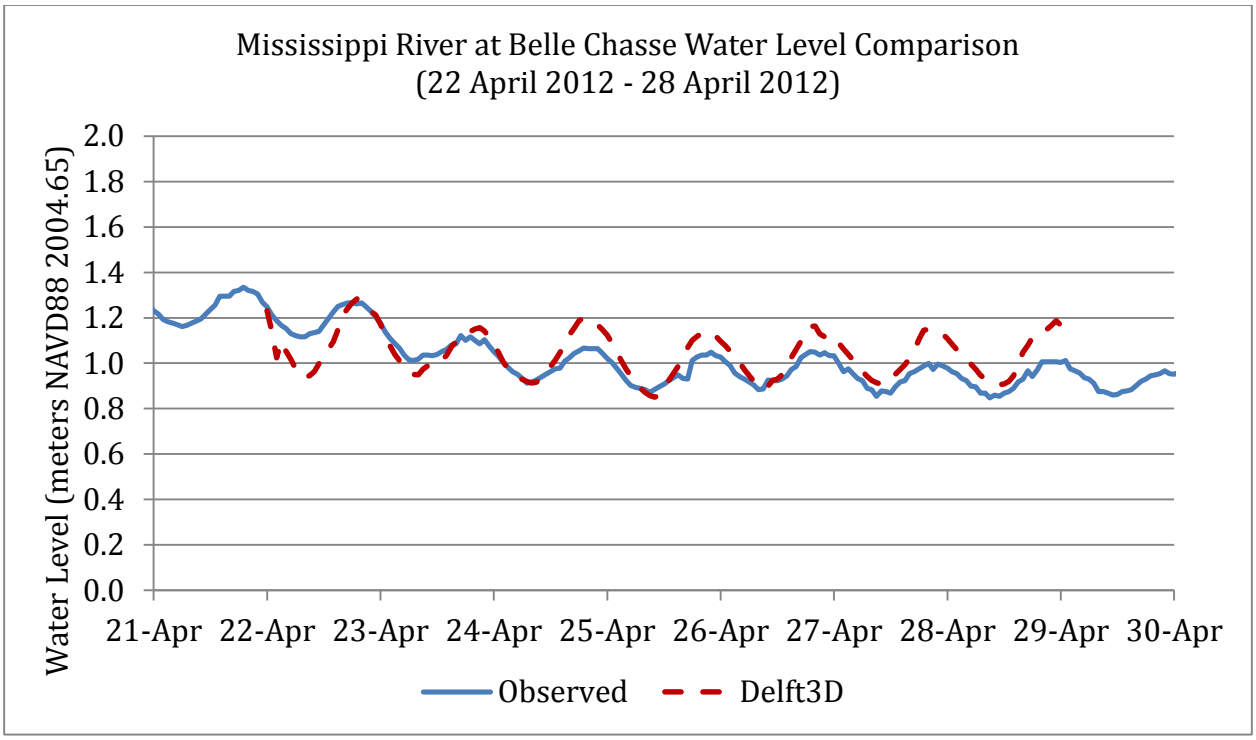

Figure 8-4 April 2012 Mississippi River at Belle Chasse water level comparison

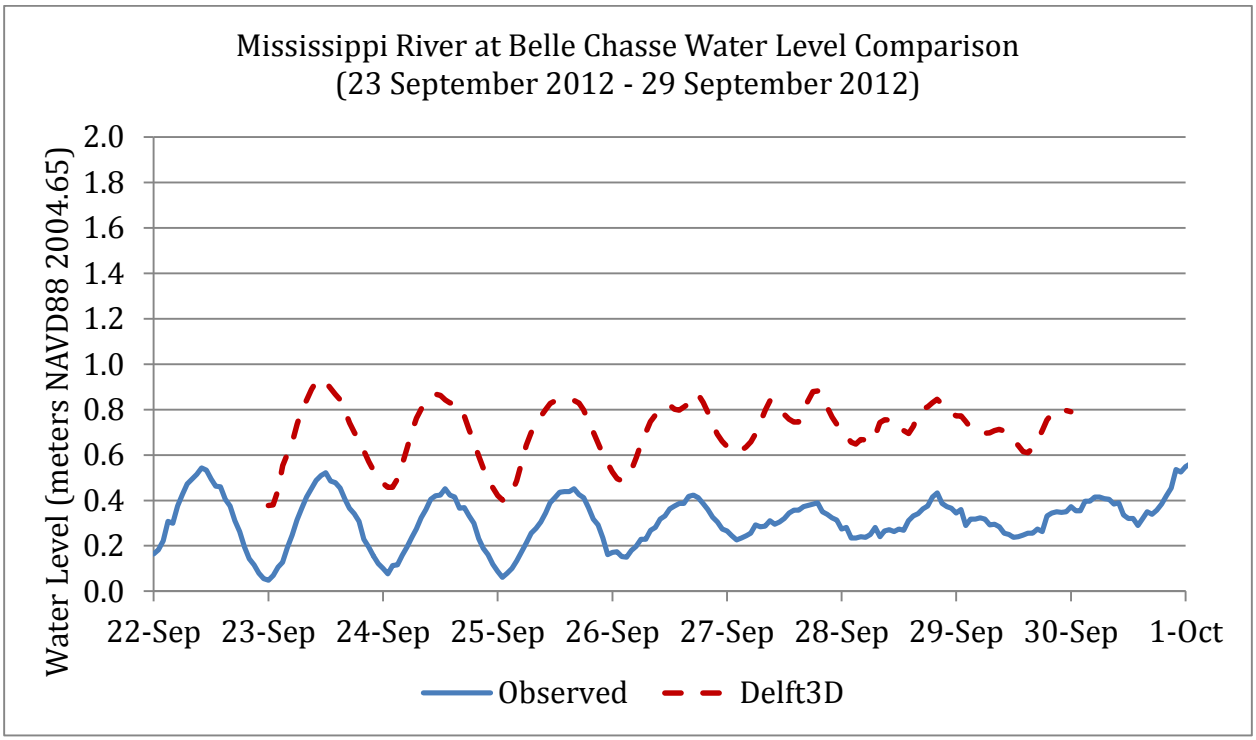

Figure 8-5 September 2012 Mississippi River at Belle Chasse water level comparison

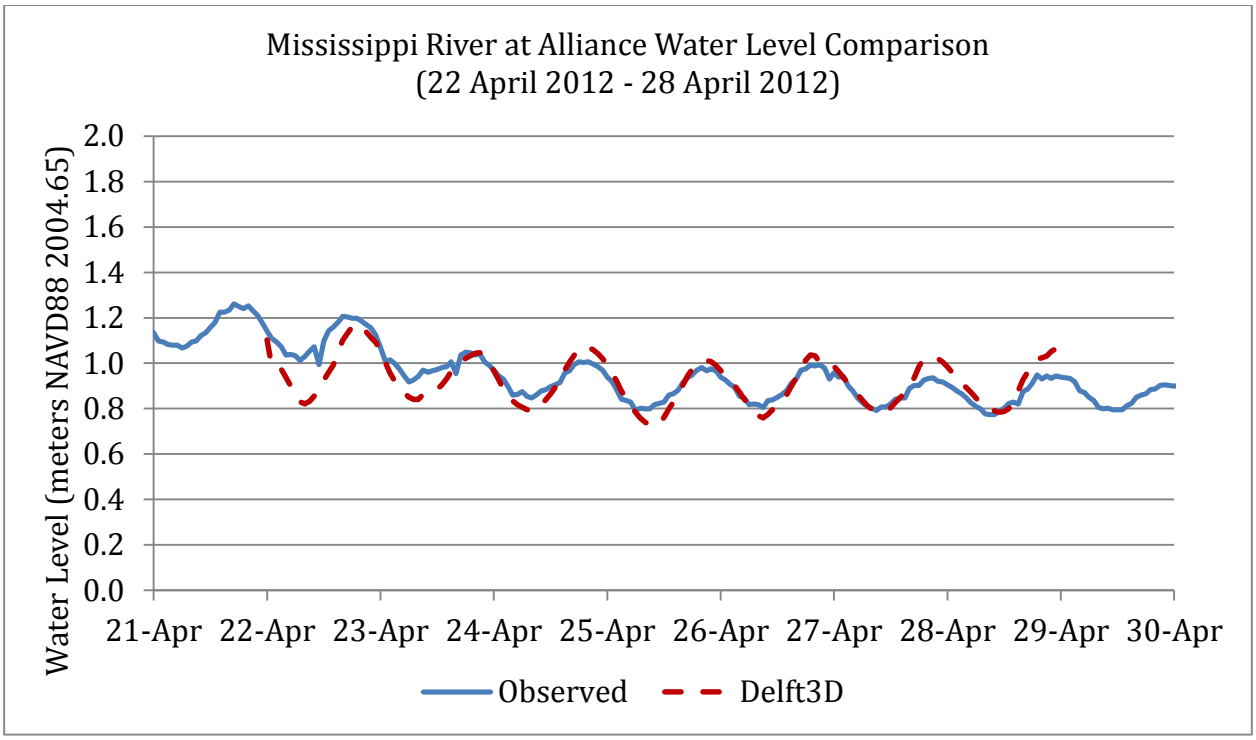

Figure 8-6 April 2012 Mississippi River at Alliance water level comparison

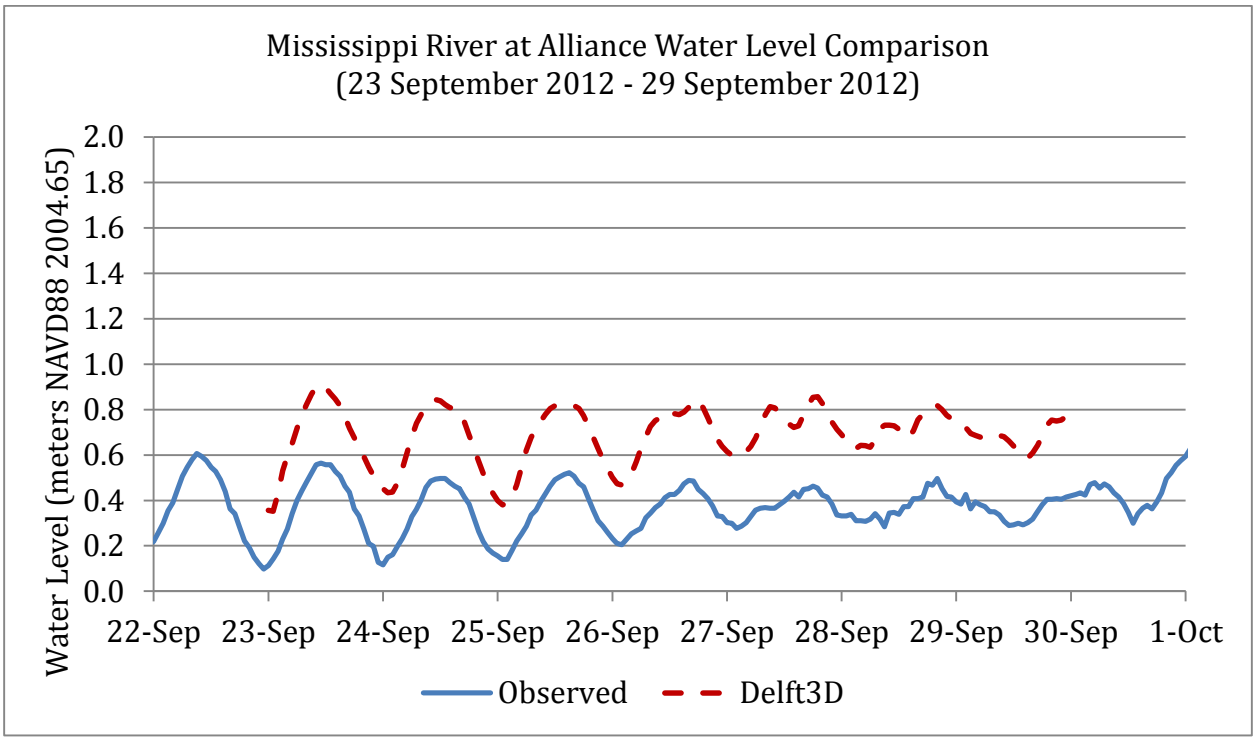

Figure 8-7 September 2012 Mississippi River at Alliance water level comparison

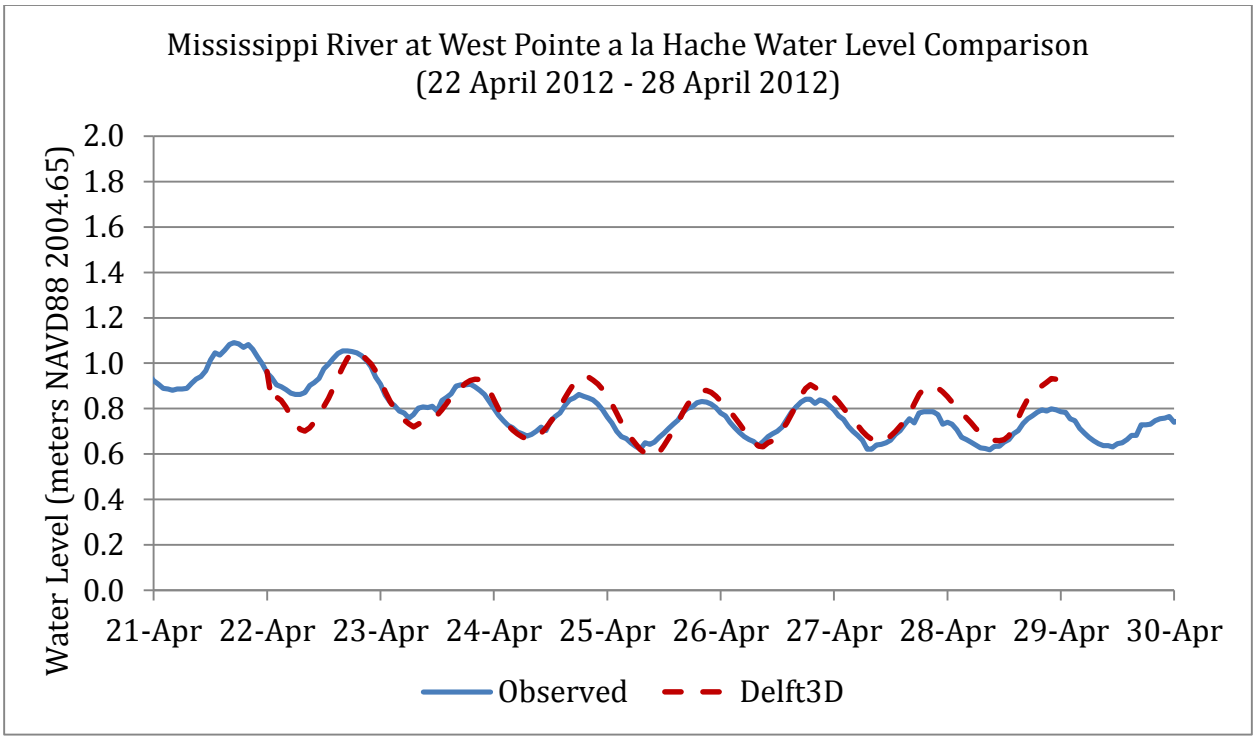

Figure 8-8 April 2012 Mississippi River at West Pointe a la Hache water level comparison

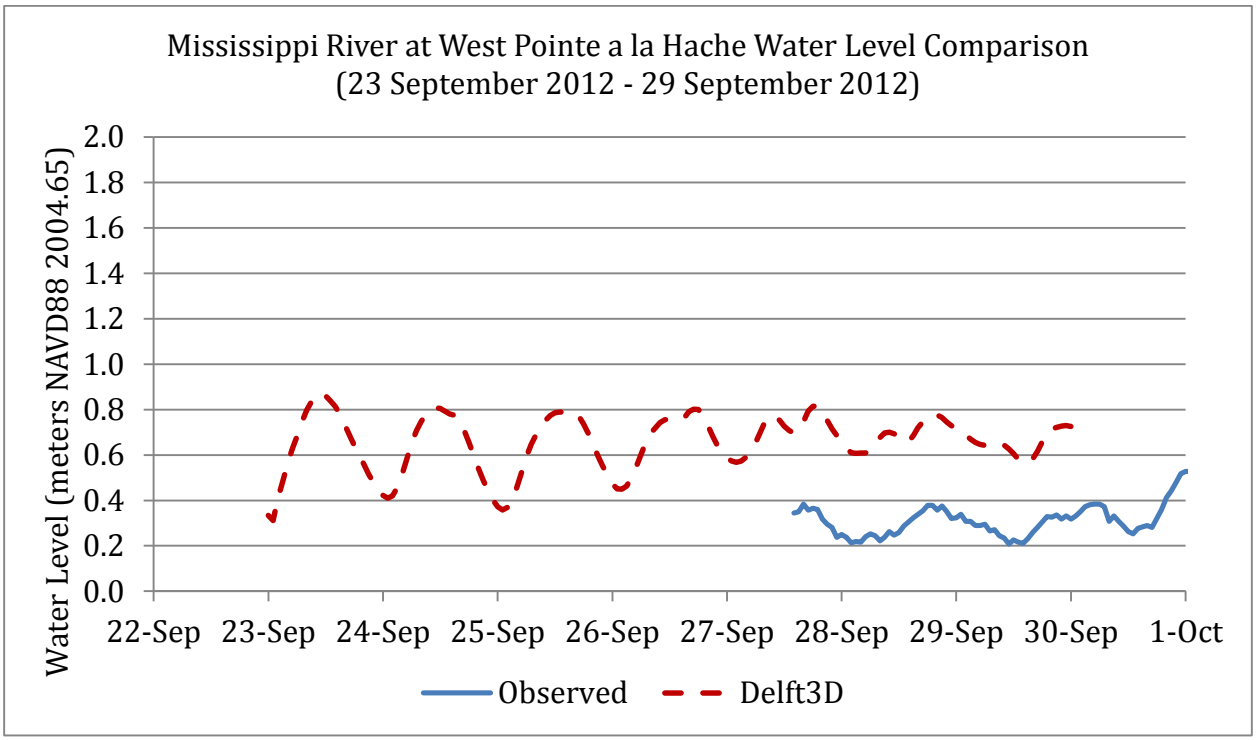

Figure 8-9 September 2012 Mississippi River at West Pointe a la Hache water level comparison

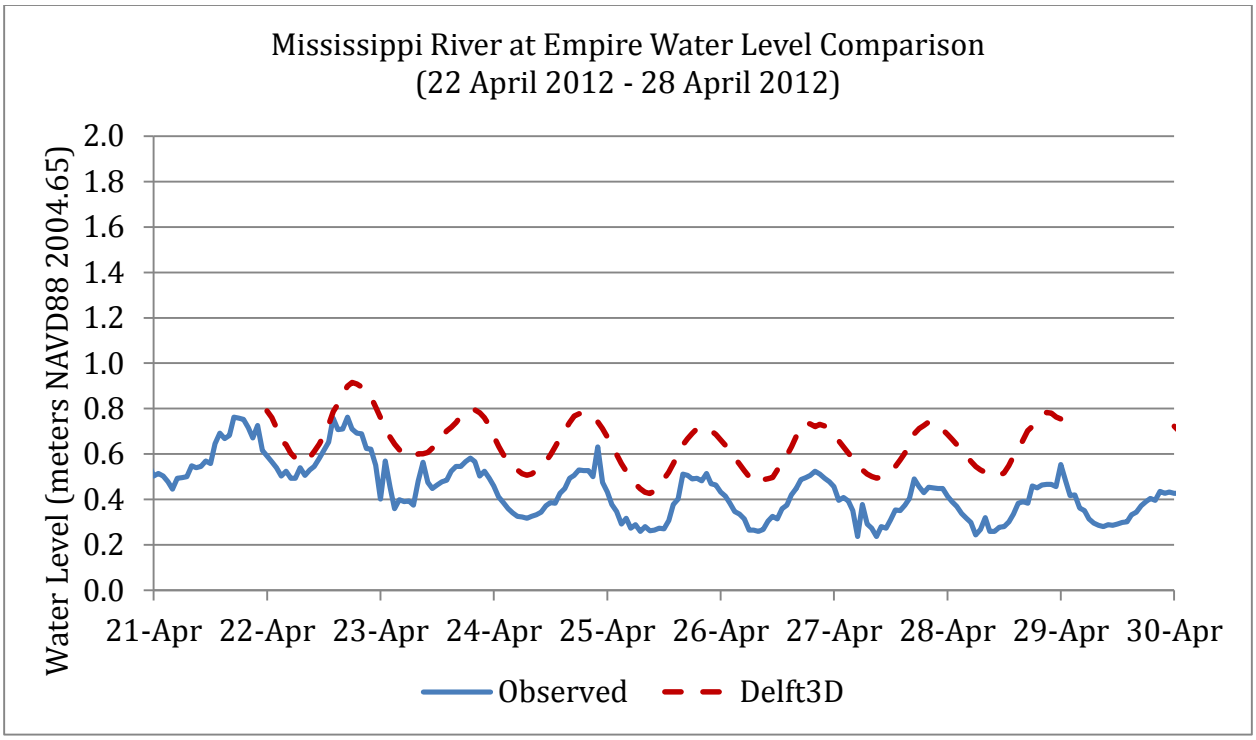

Figure 8-10 April 2012 Mississippi River at Empire water level comparison

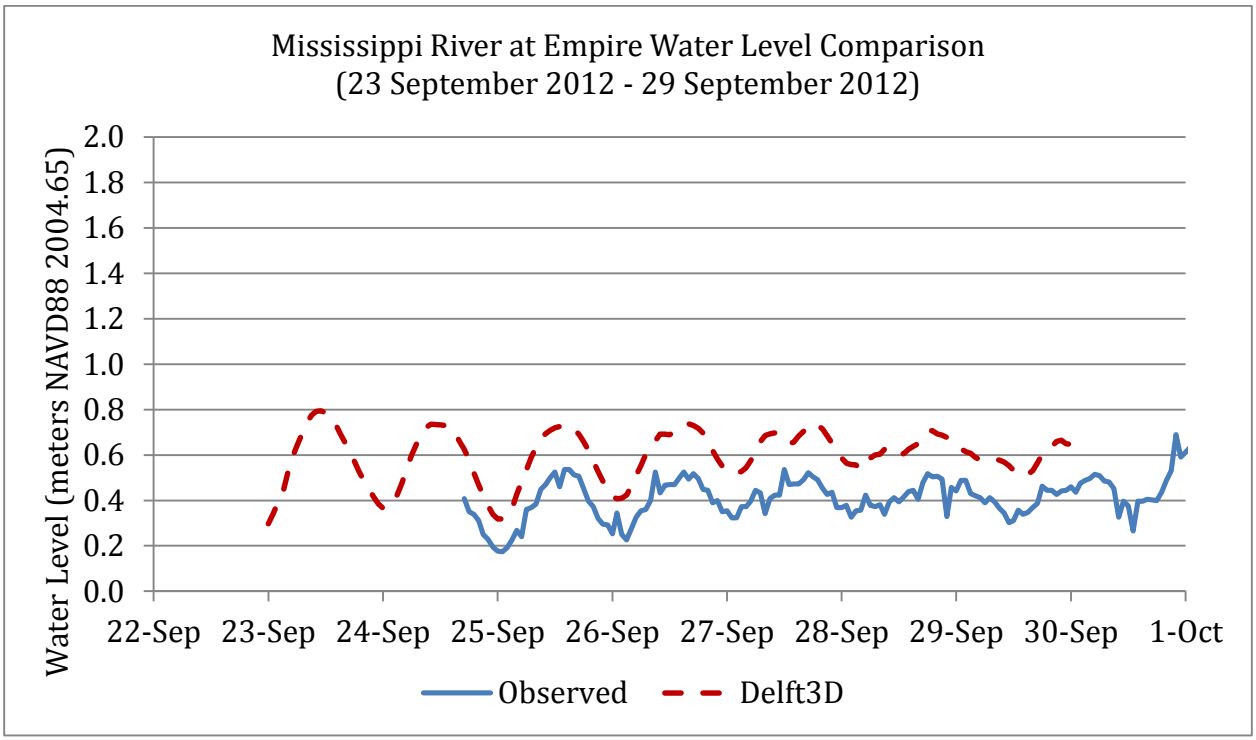

Figure 8-11 September 2012 Mississippi River at Empire water level comparison

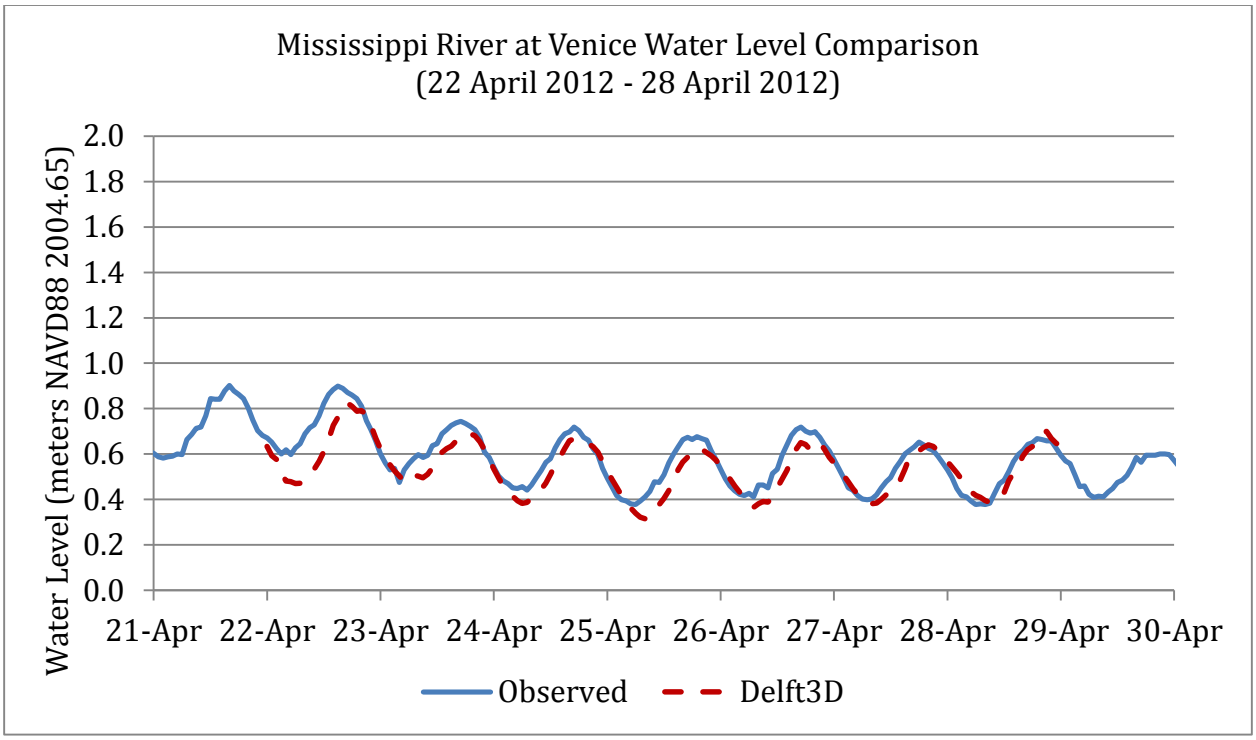

Figure 8-12 April 2012 Mississippi River at Venice water level comparison

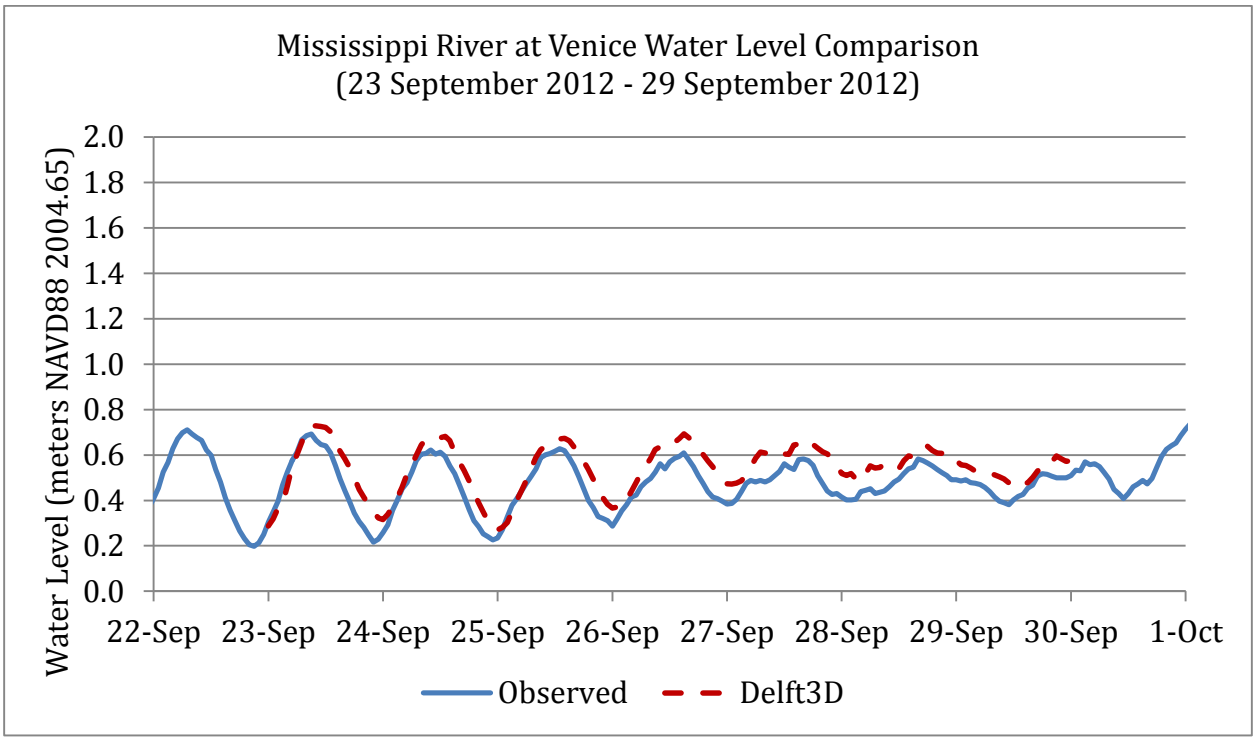

Figure 8-13 September 2012 Mississippi River at Venice water level comparison

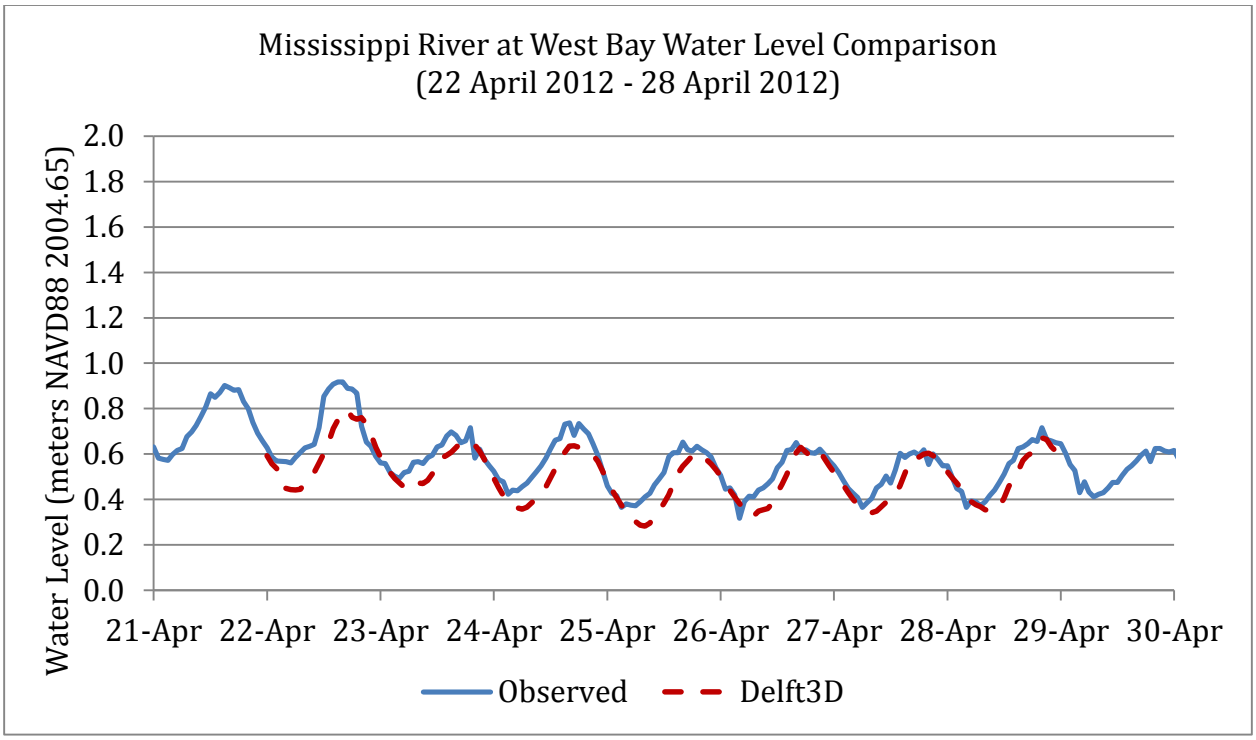

Figure 8-14 April 2012 Mississippi River at West Bay water level comparison

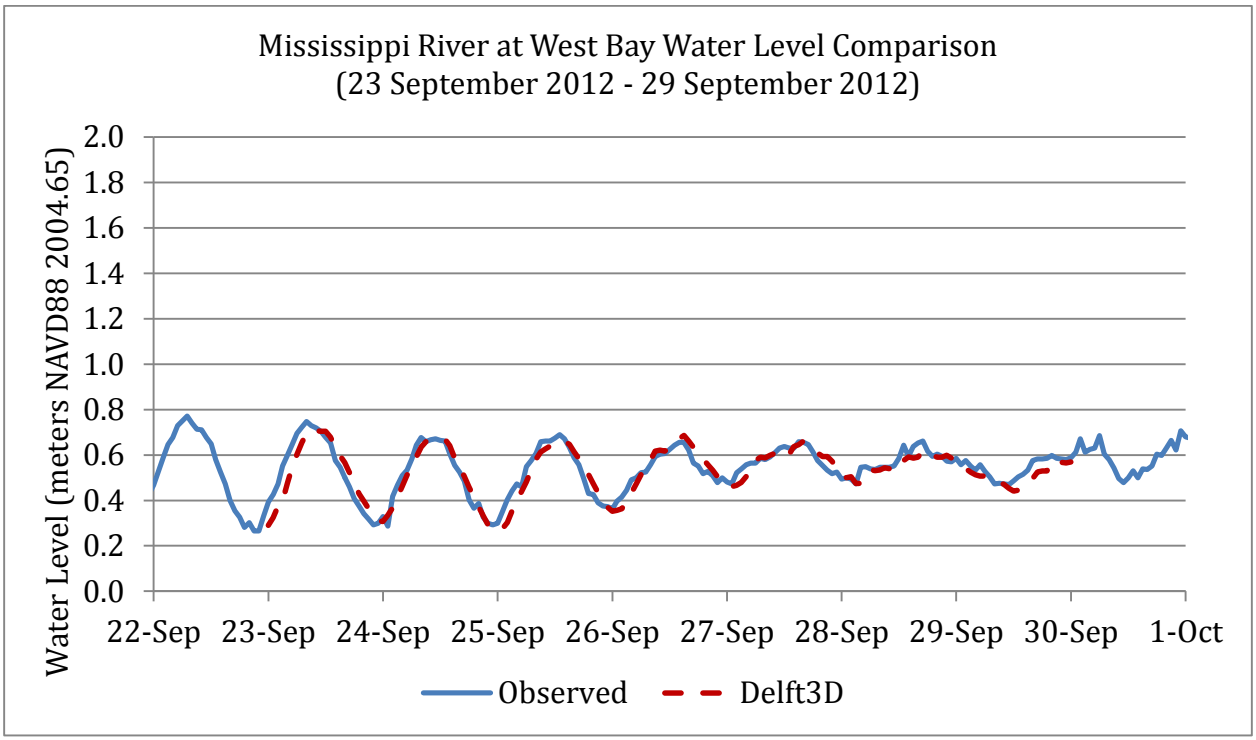

Figure 8-15 September 2012 Mississippi River at West Bay water level comparison

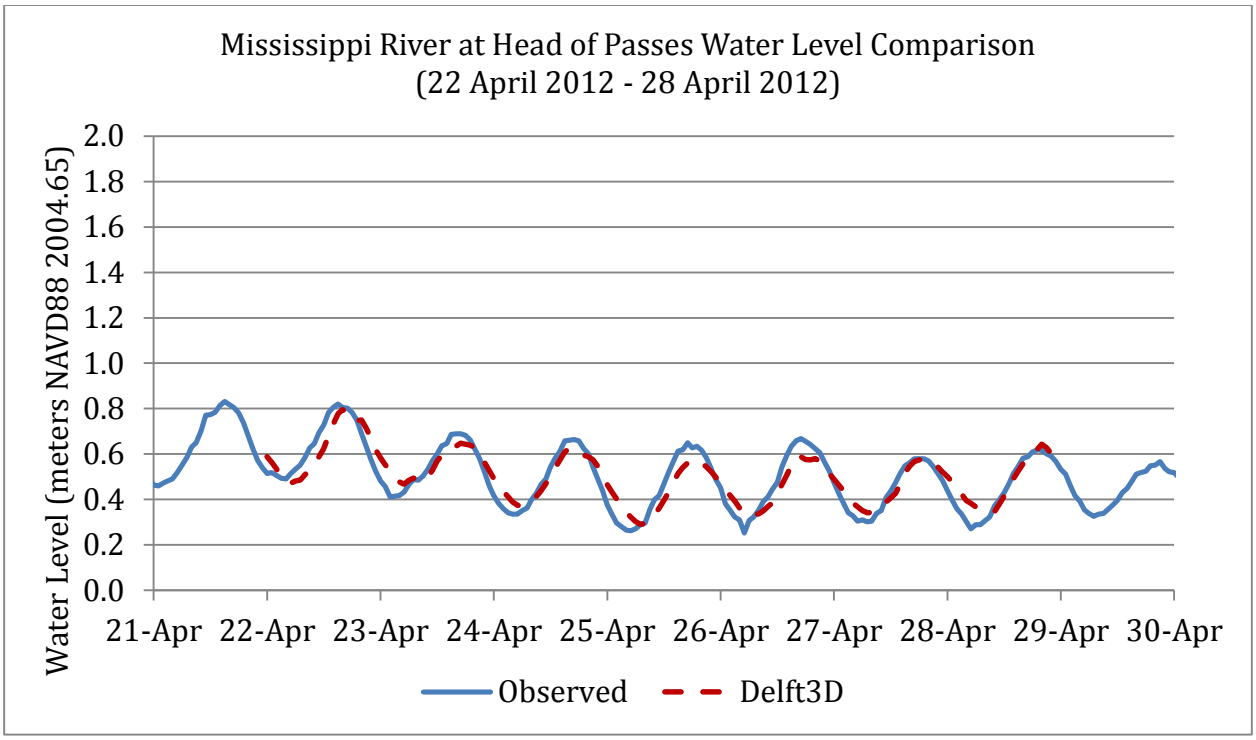

Figure 8-16 April 2012 Mississippi Rivver at Head of Passes water level comparison

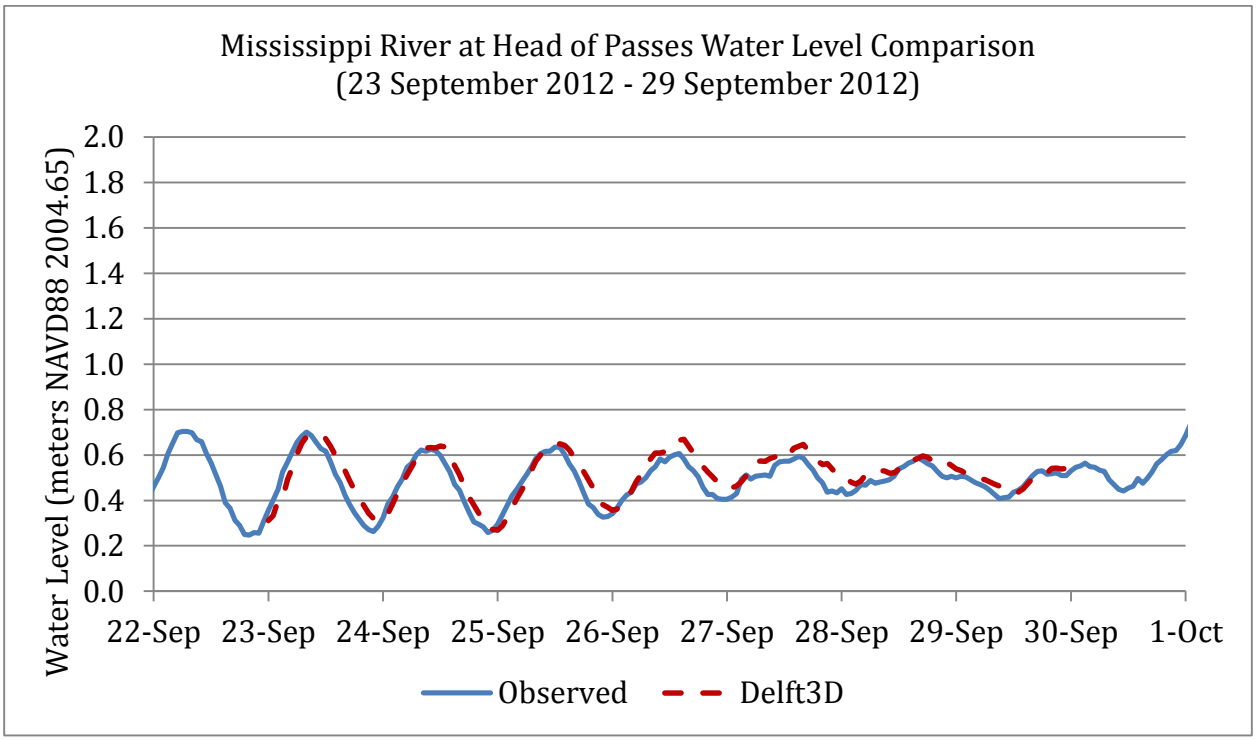

Figure 8-17 September 2012 Mississippi River at Head of Passes water level comparison

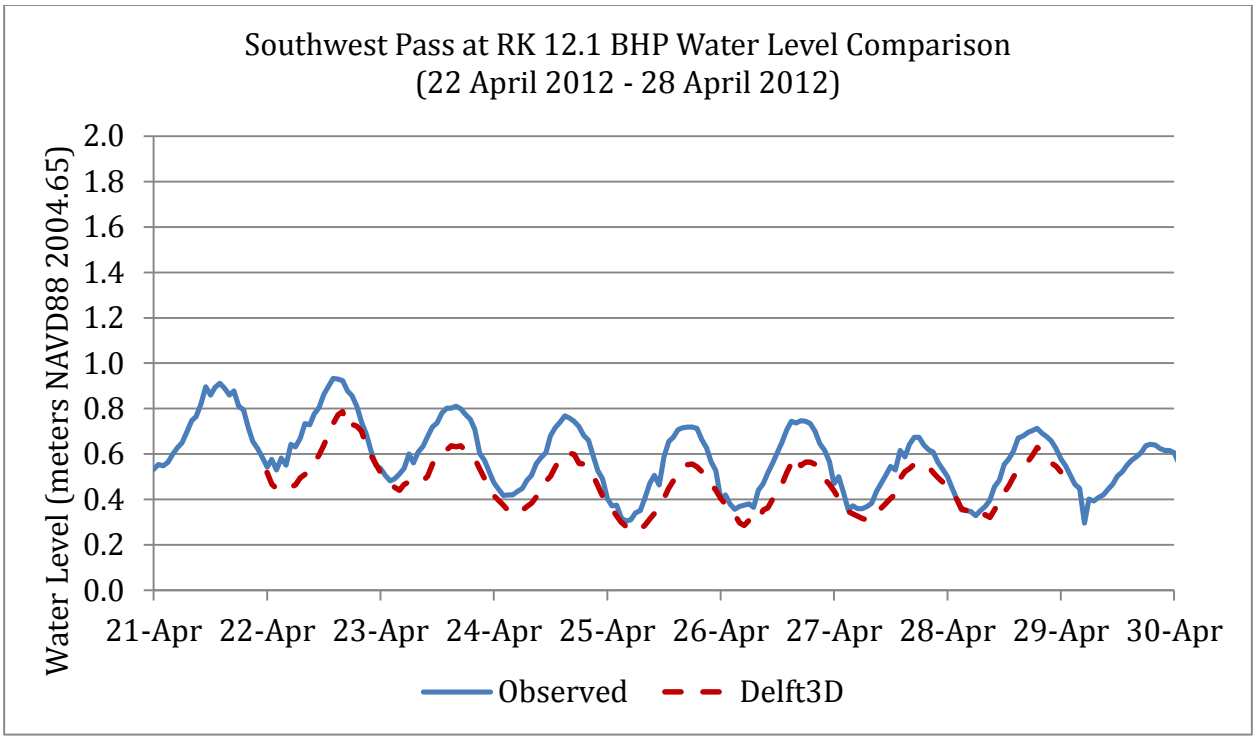

Figure 8-18 April 2012 Southwest Pass at RK 12.1 BHP water level comparison

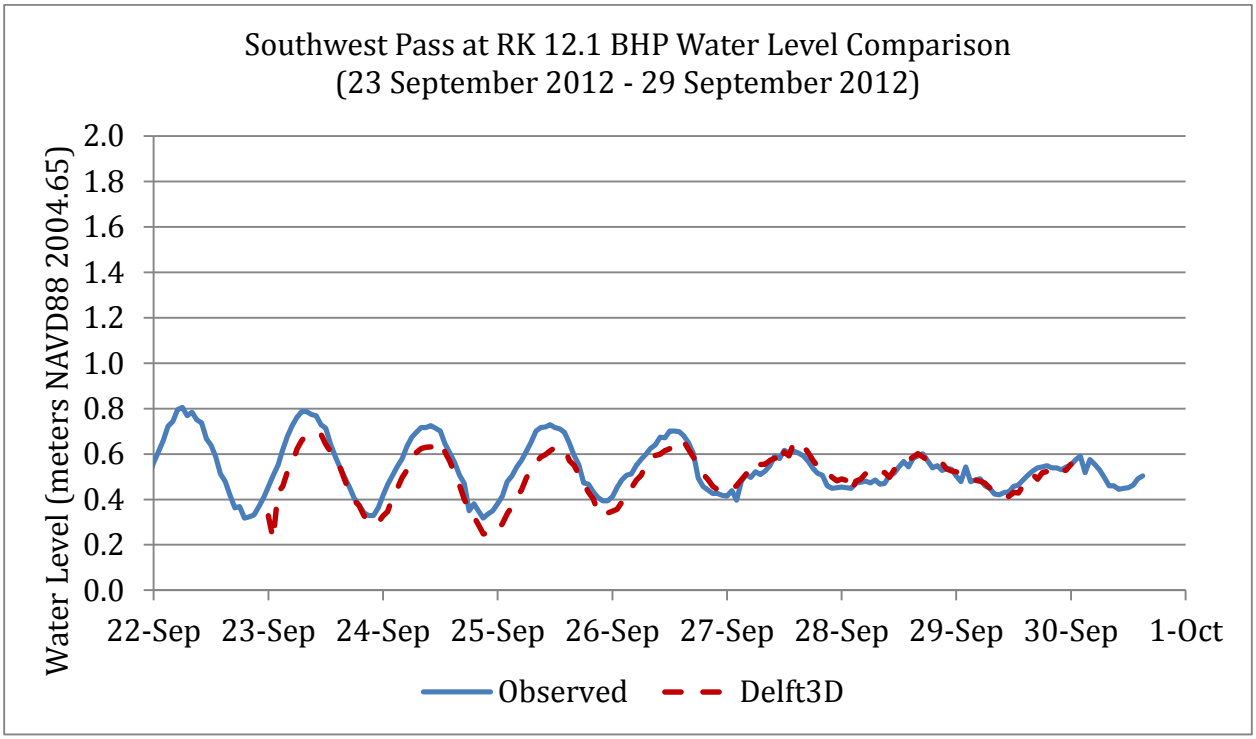

Figure 8-19 September 2012 Southwest Pass at RK 12.1 BHP water level comparison

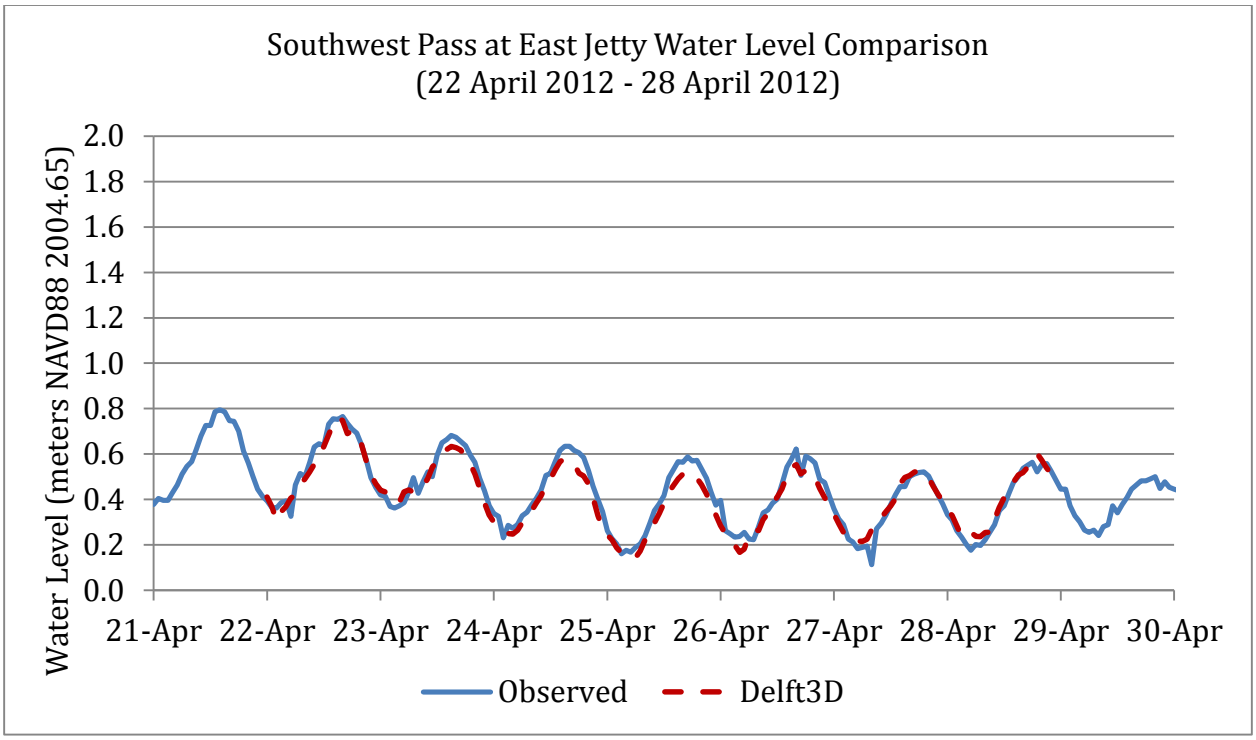

Figure 8-20 April 2012 Southwest Pass at East Jetty water level comparison

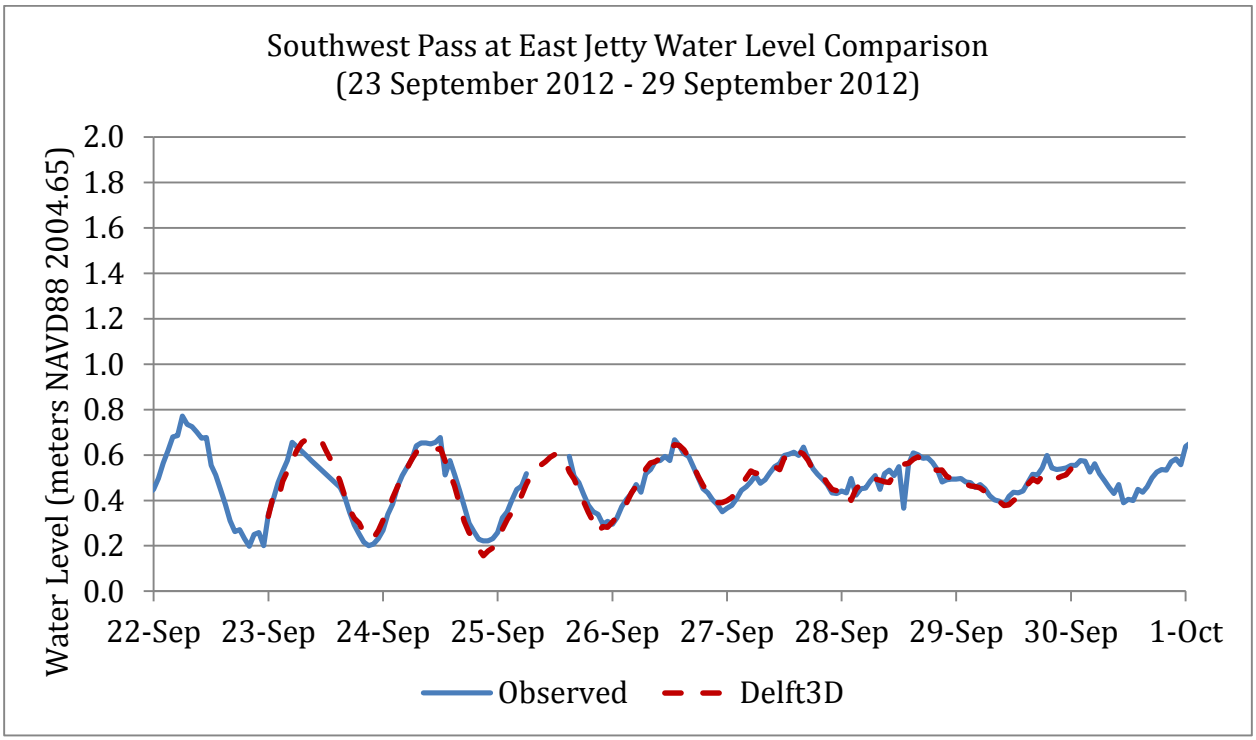

Figure 8-21 September 2012 Southwest Pass at East Jetty water level comparison

8.6.2 April 2012 suspended sediment results

Suspended sediment samples were collected on 23 April 2012 at the eight locations shown in Figure 8-22 by the USGS for the LCA White Ditch study. At each location, five vertical concentration sites were selected across the river channel. Model results compared to these samples are shown in the following figures. At some locations, two vertical sites were situated in very close proximity and were represented by the same computational cell in the model. In these cases, the two vertical sites are displayed on the same plot. In particular, at the RK 96.6 location, vertical site 5 was represented by a dry cell in the model, therefore, no comparison to the model is available.

Figure 8-22 White Ditch suspended sediment sample sites

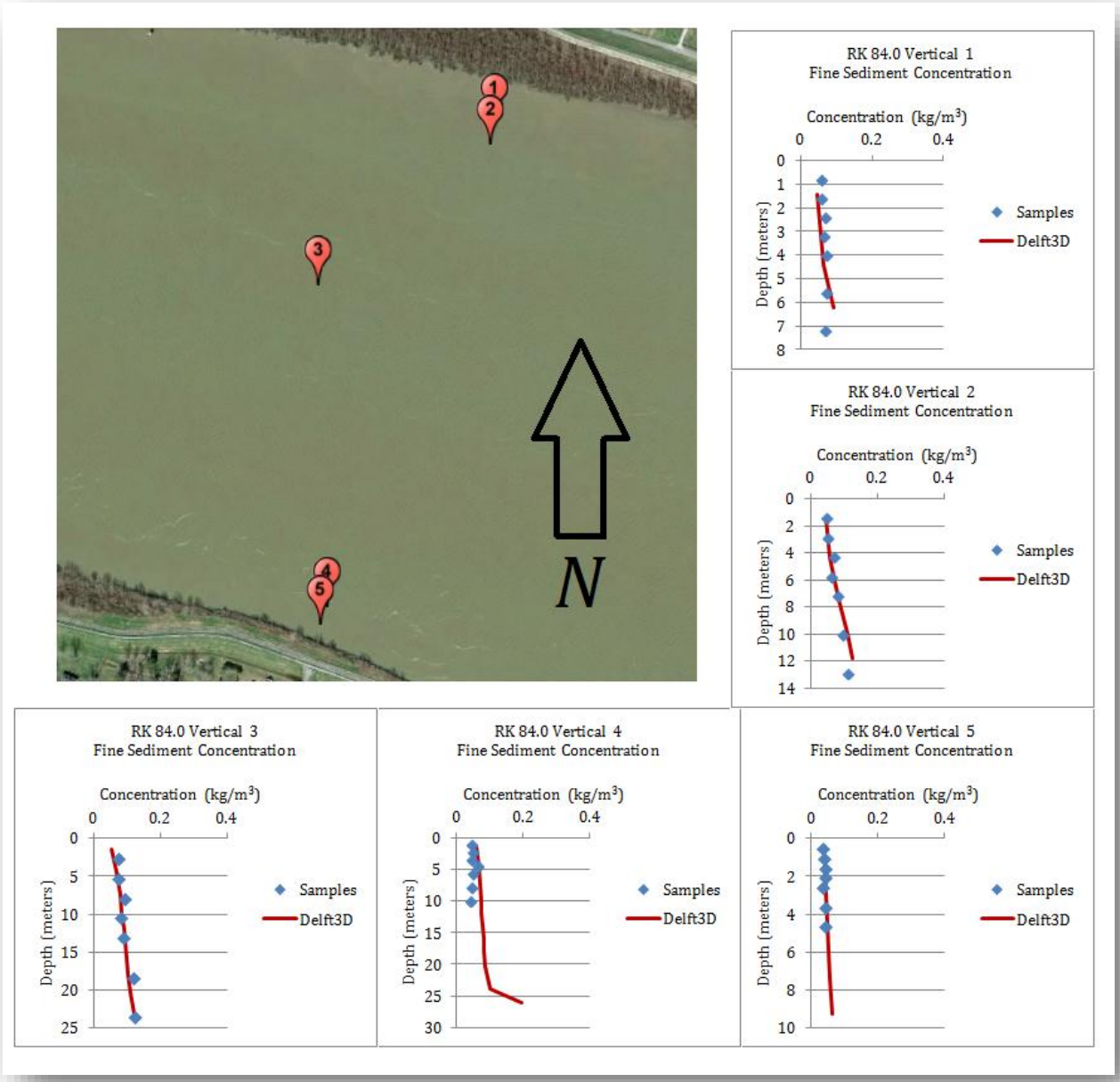

Figure 8-23 23 April 2012 RK 84.0 fine sediment concentration comparison

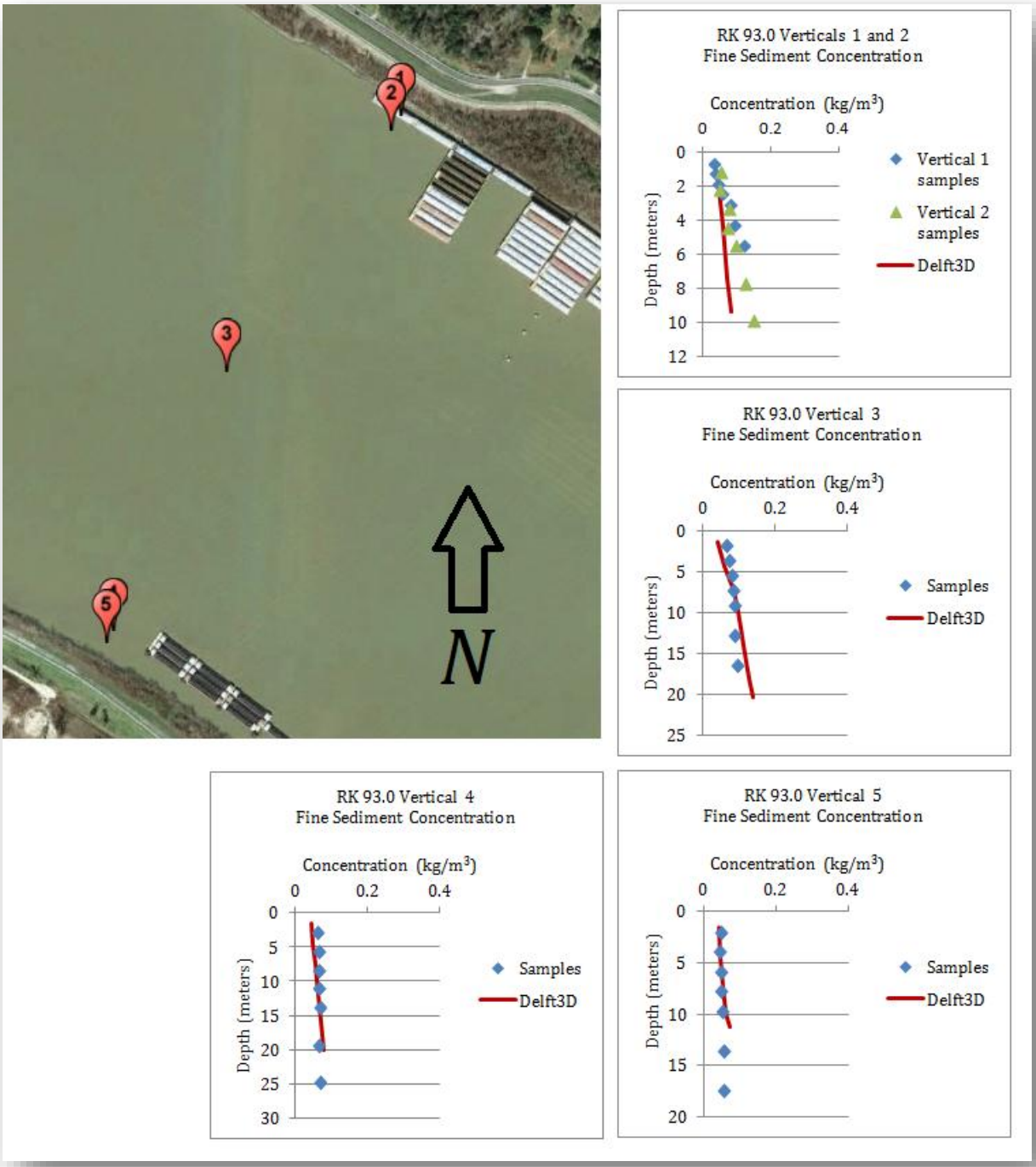

Figure 8-24 23 April 2012 RK 93.0 fine sediment concentration comparison

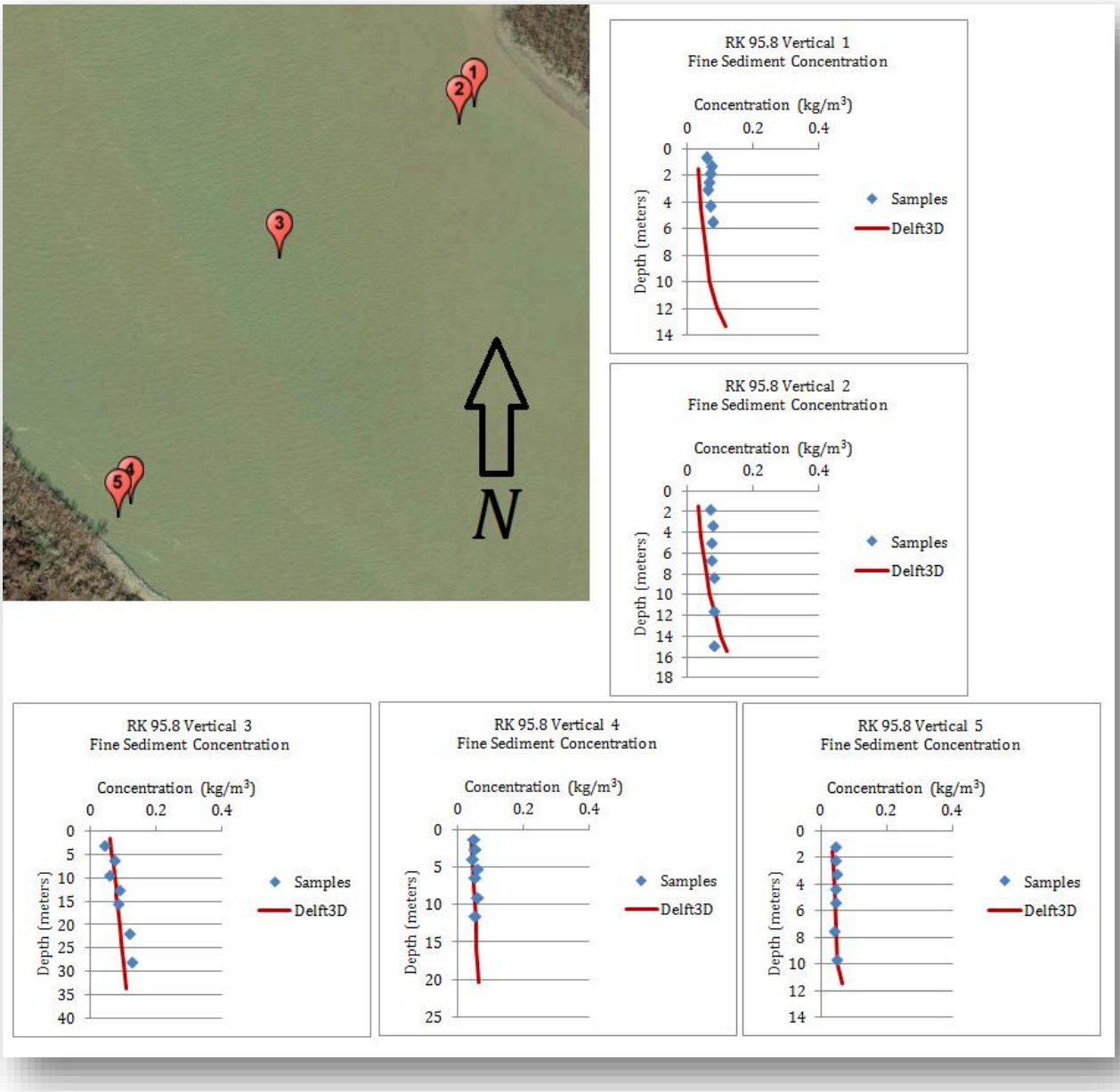

Figure 8-25 23 April 2012 RK 95.8 fine sediment concentration comparison

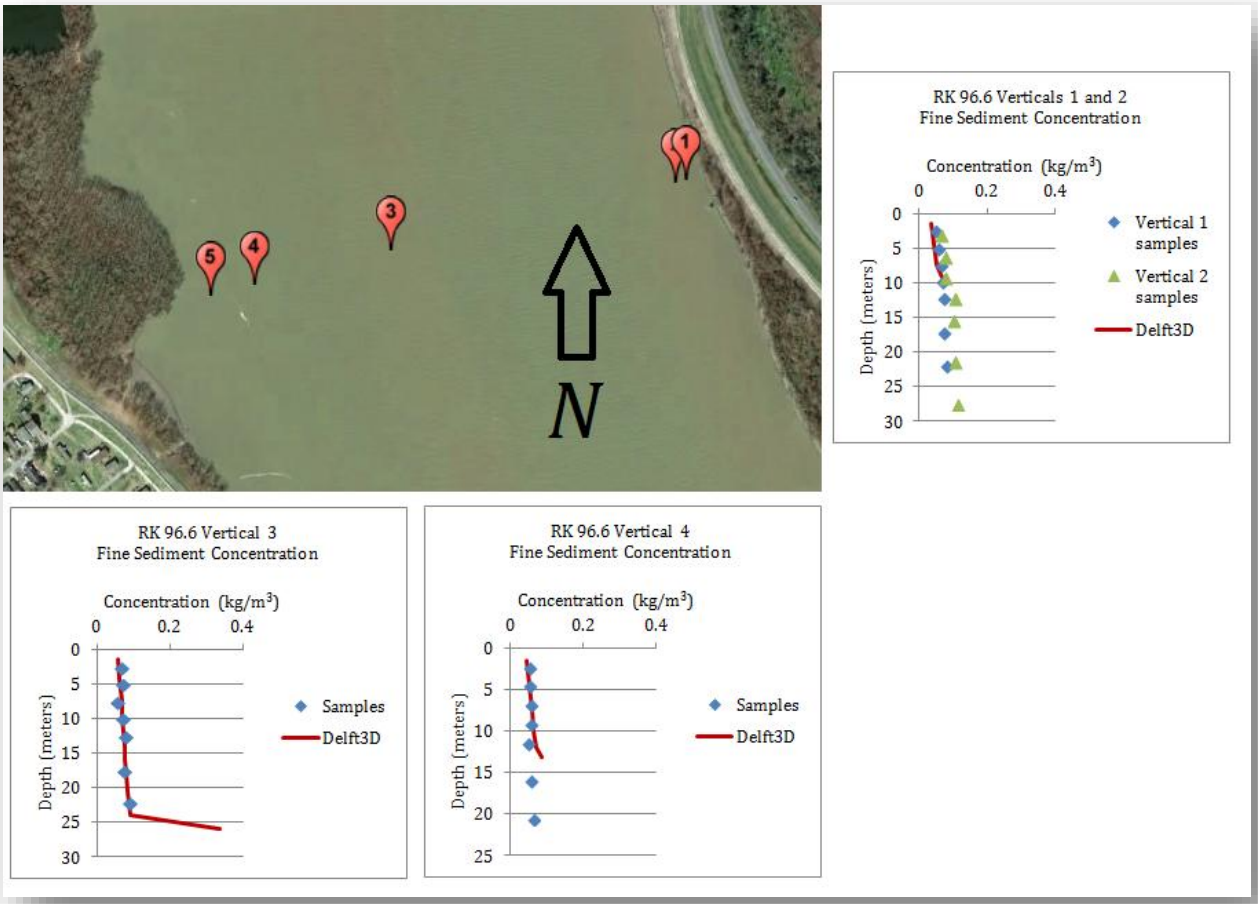

Figure 8-26 23 April 2012 RK 96.6 fine sediment concentration comparison

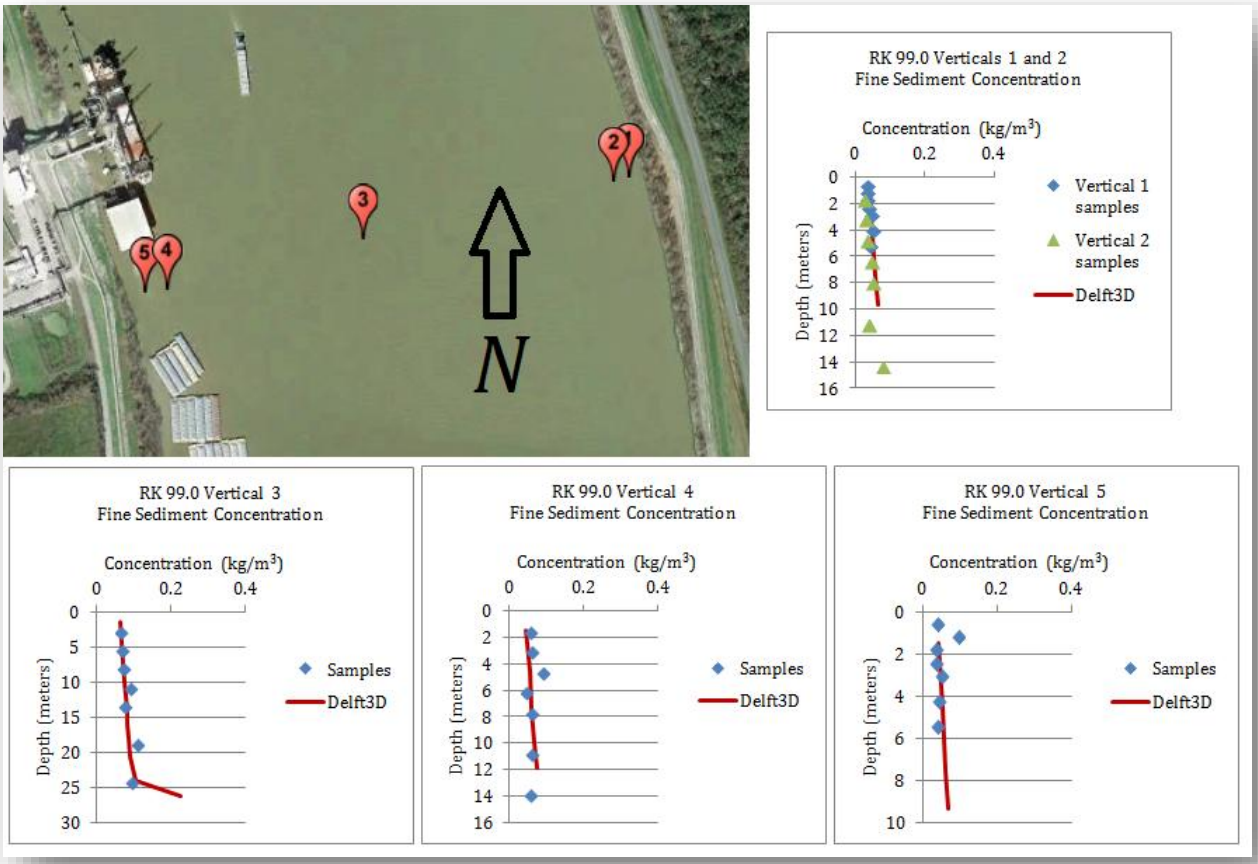

Figure 8-27 23 April 2012 RK 99.0 fine sediment concentration comparison

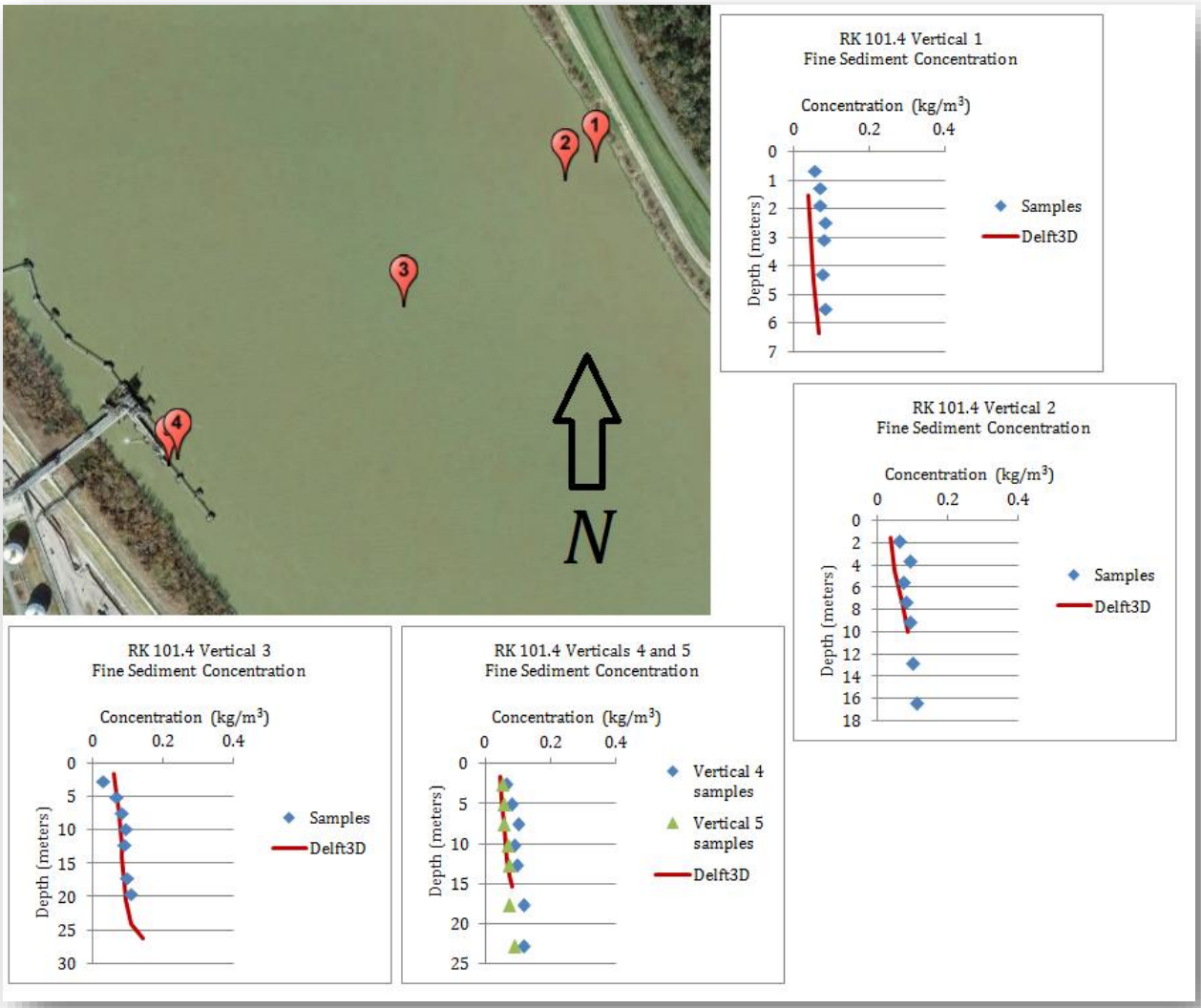

Figure 8-28 23 April 2012 RK 101.4 fine sediment concentration comparison

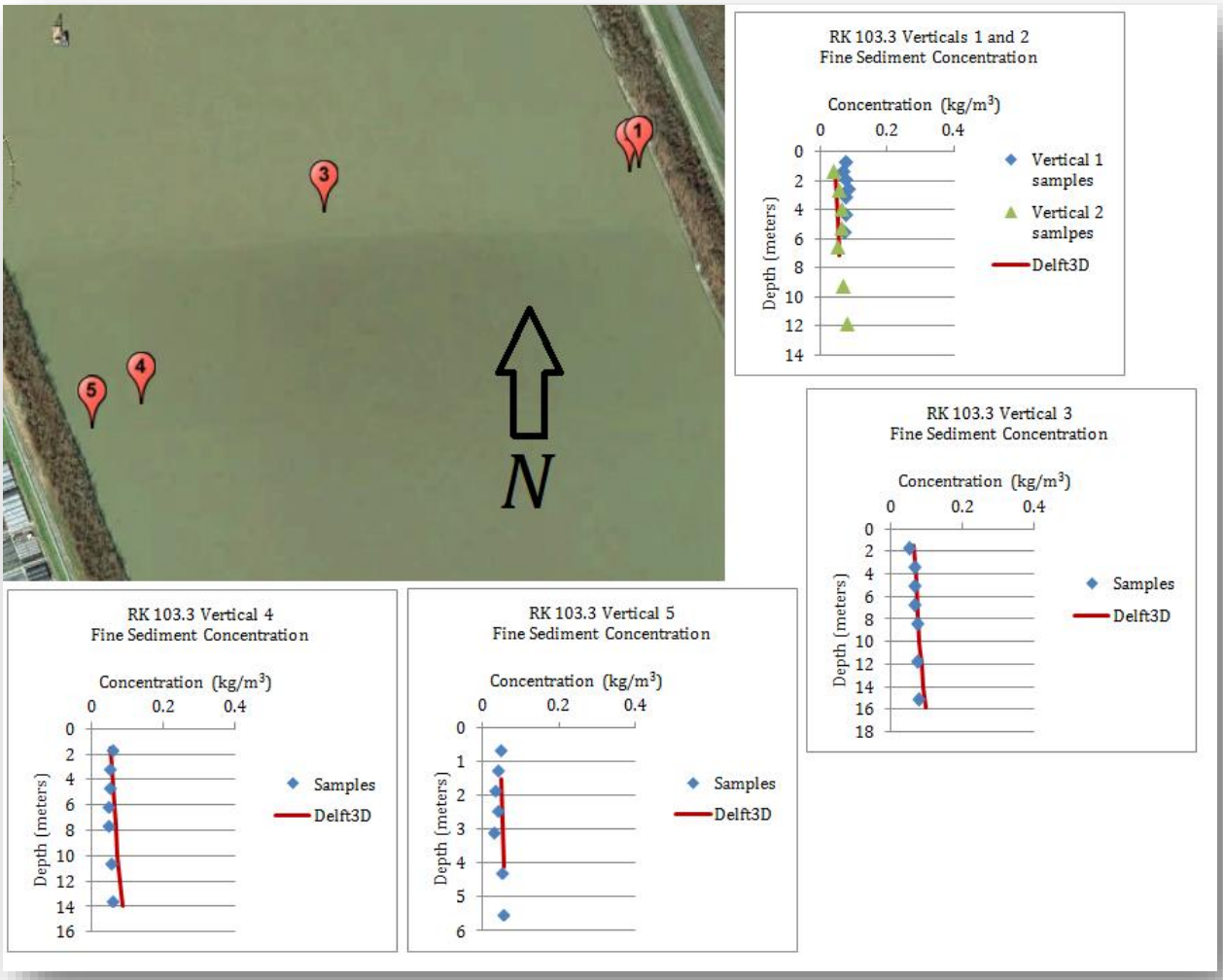

Figure 8-29 23 April 2012 RK 103.3 fine sediment concentration comparison

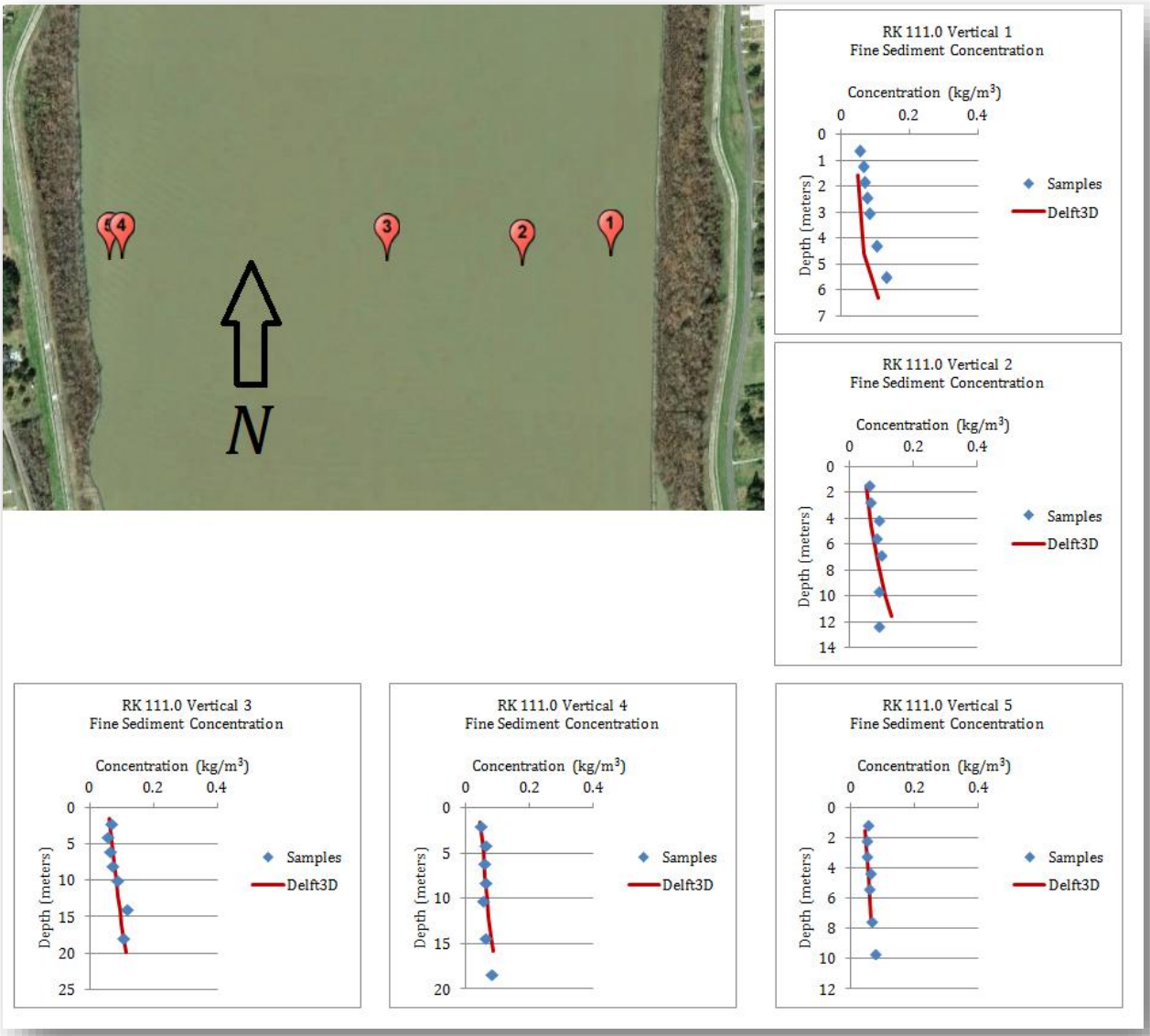

Figure 8-30 23 April 2012 RK 111.0 fine sediment concentration comparison

8.6.3 September 2012 suspended sediment and salinity results

Van Dorn bottle samples were collected and processed in the 20-24 September 2012 time frame at various locations along the lower Mississippi River channel as shown in Figure 8-31. The purpose of the field surveys was to capture low freshwater discharge events in the river when the salt wedge enters the main stem of the river above Head of Passes and to define the limits of the wedge and its sediment and salinity properties (Allison, 2014). The salinity and fine sediment concentration of the samples were compared to model results as shown in Figure 8-32 through Figure 8-38. The model data shown in the plots represents the top of the hour results closest to the reported sample collection time noted on the plots.

Figure 8-31 September 2012 Suspended Sediment and Salinity Van Dorn Bottle sample sites

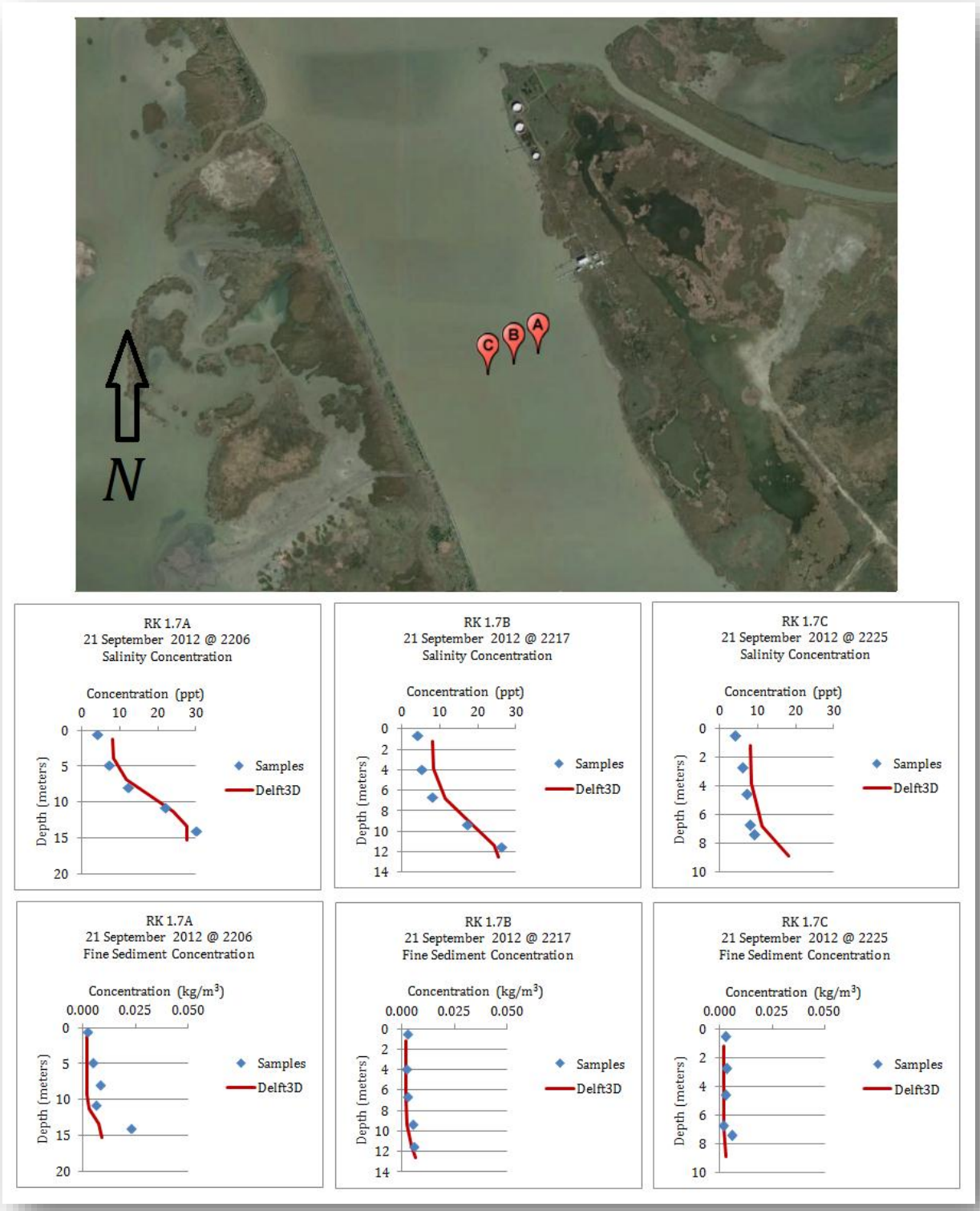

Figure 8-32 Model results compared to Van Dorn Bottle samples at RK 1.7

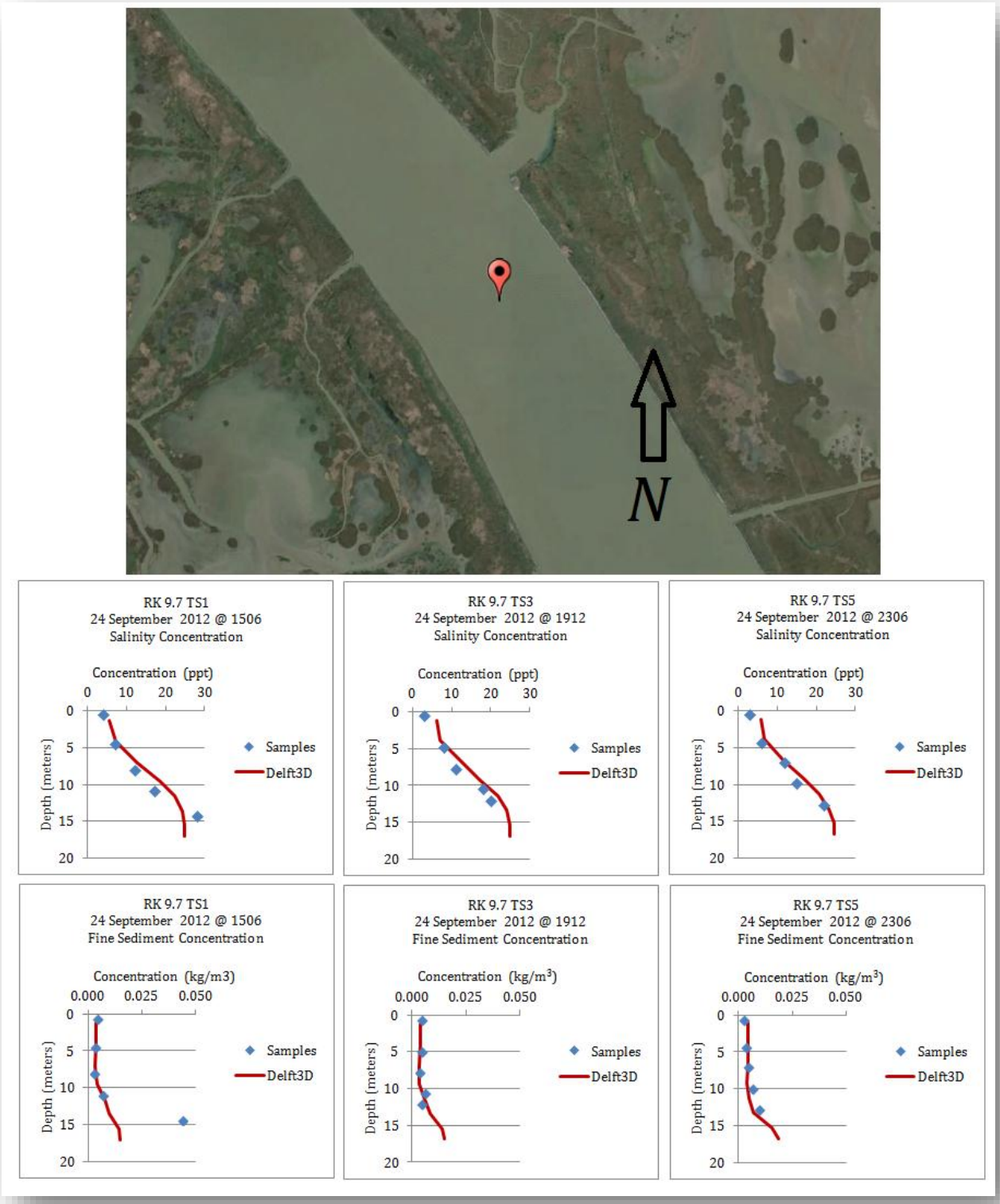

Figure 8-33 Model results compared to Van Dorn Bottle samples at RK 9.7

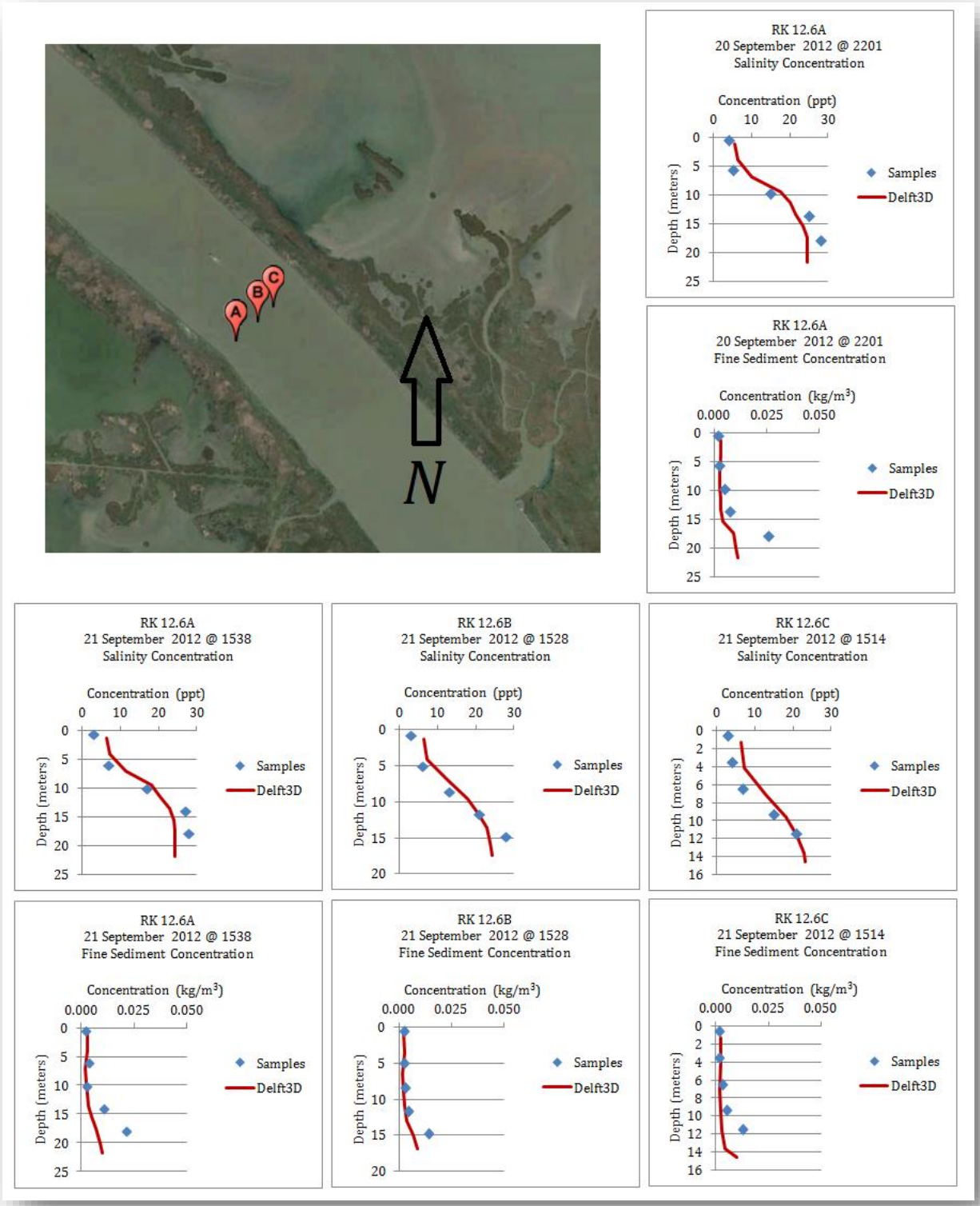

Figure 8-34 Model results compared to Van Dorn Bottle samples at RK 12.6

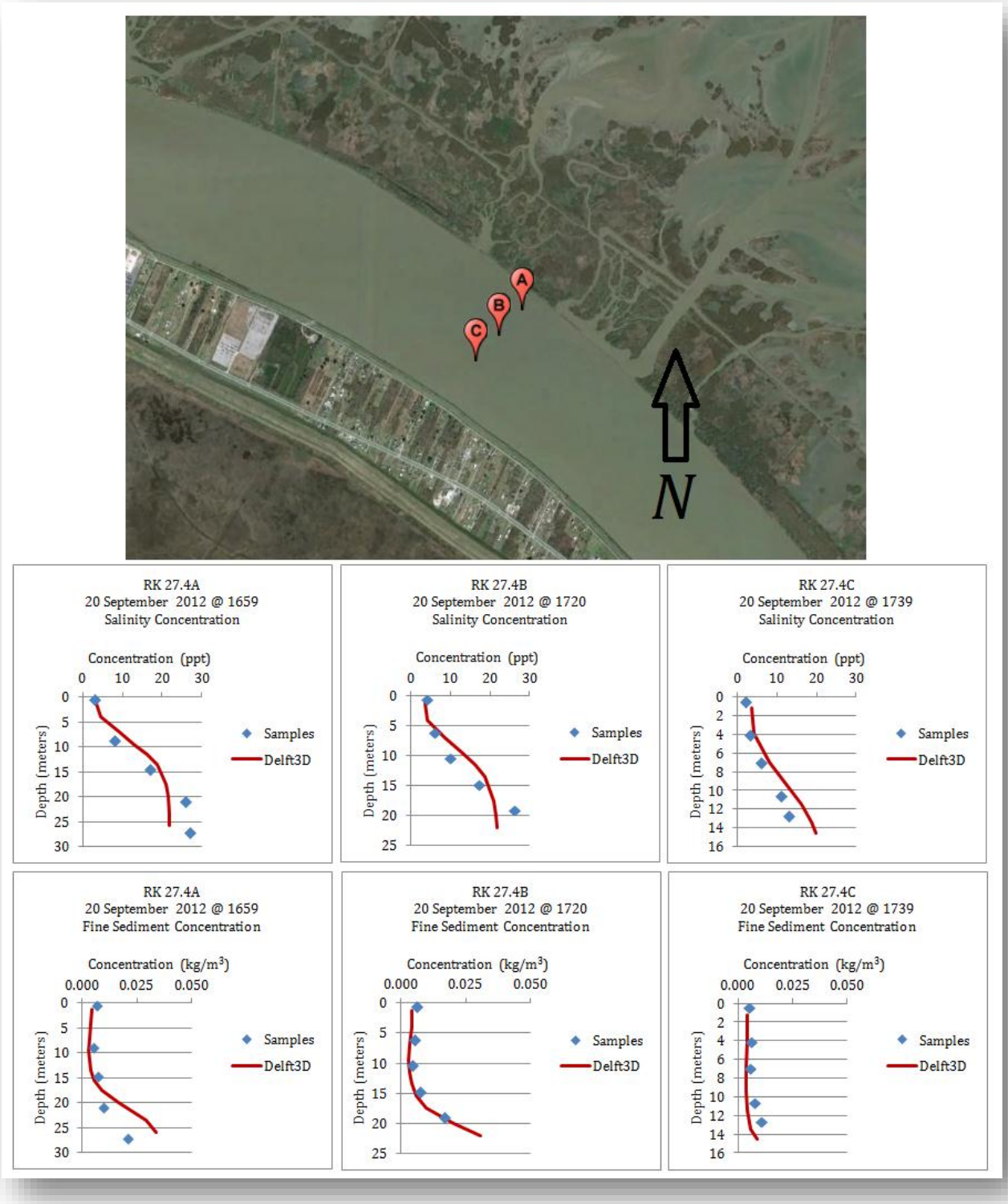

Figure 8-35 Model results compared to Van Dorn Bottle samples at RK 27.4

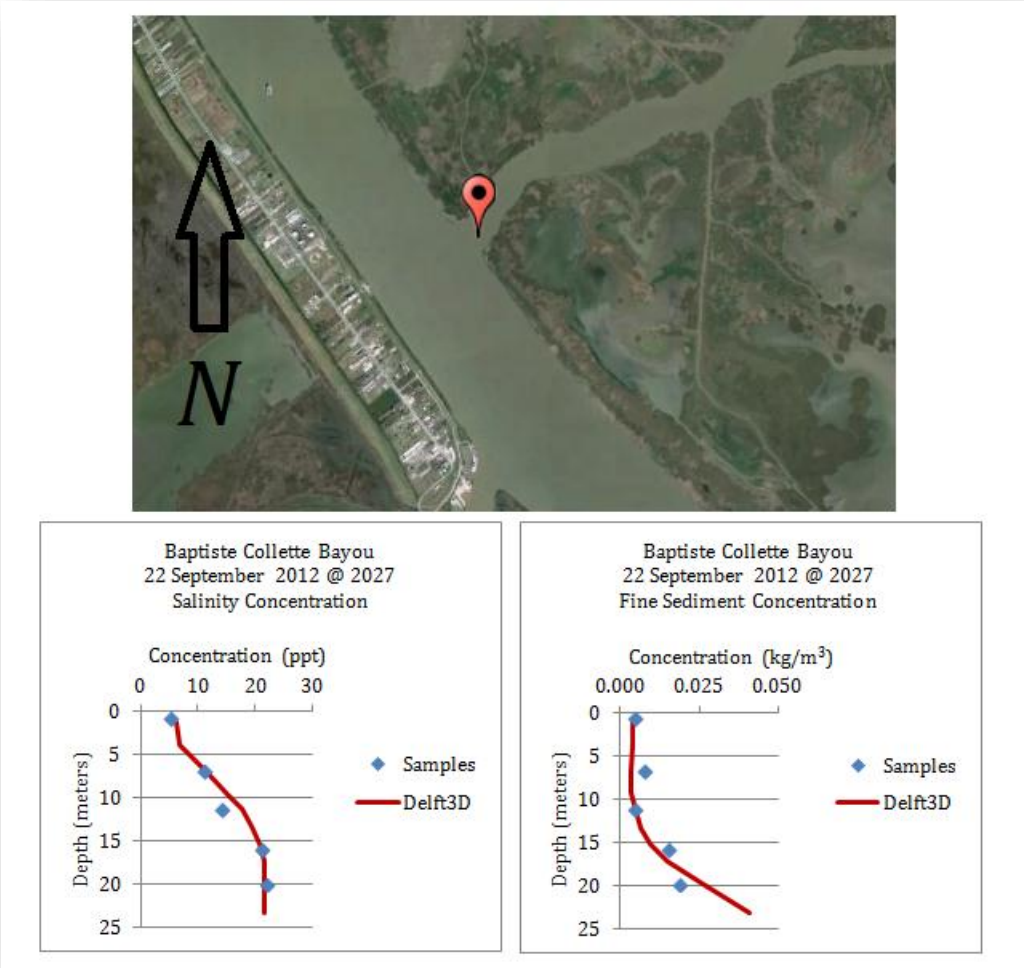

Figure 8-36 Model results compared to Van Dorn Bottle samples at Baptiste Collette Bayou

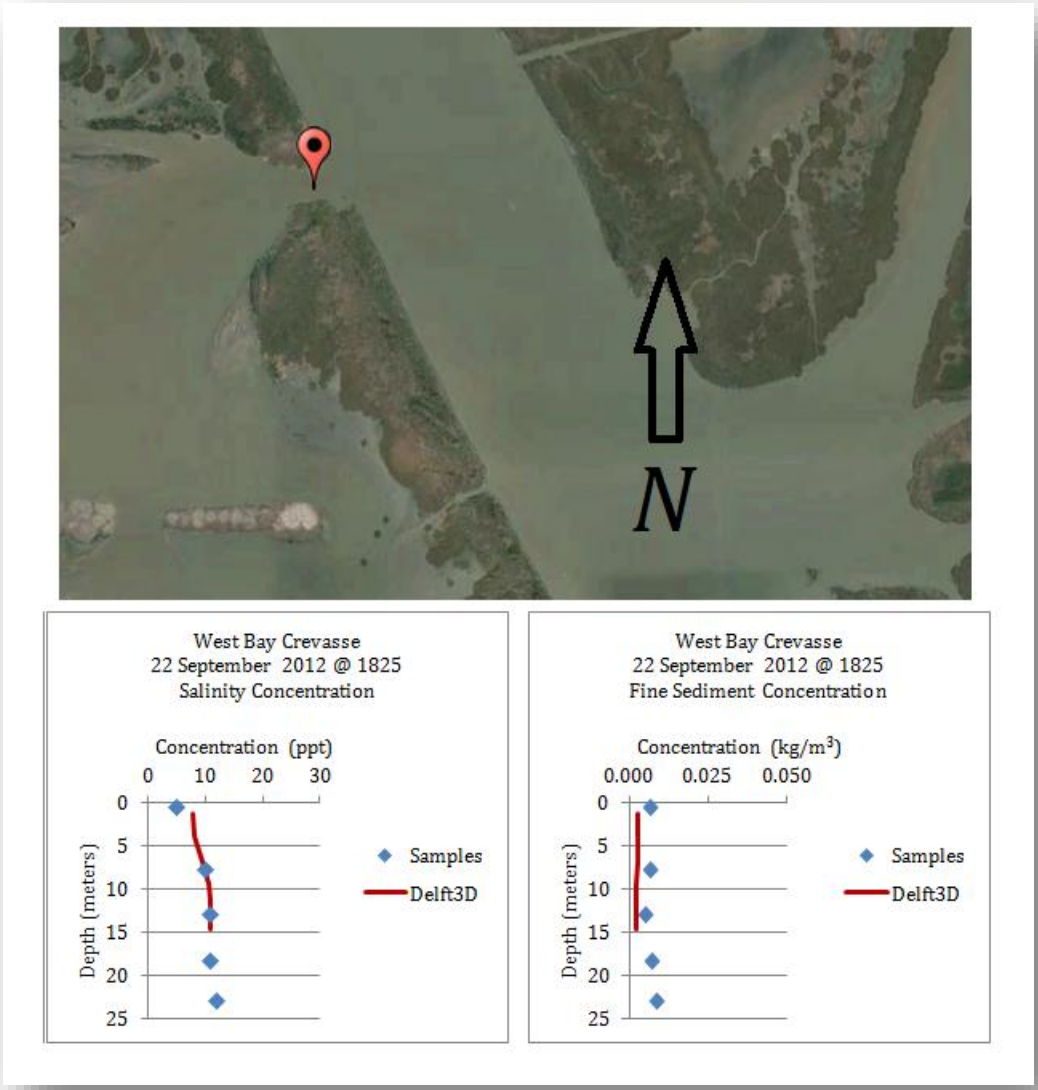

Figure 8-37 Model results compared to Van Dorn Bottle samples at West Bay Crevasse

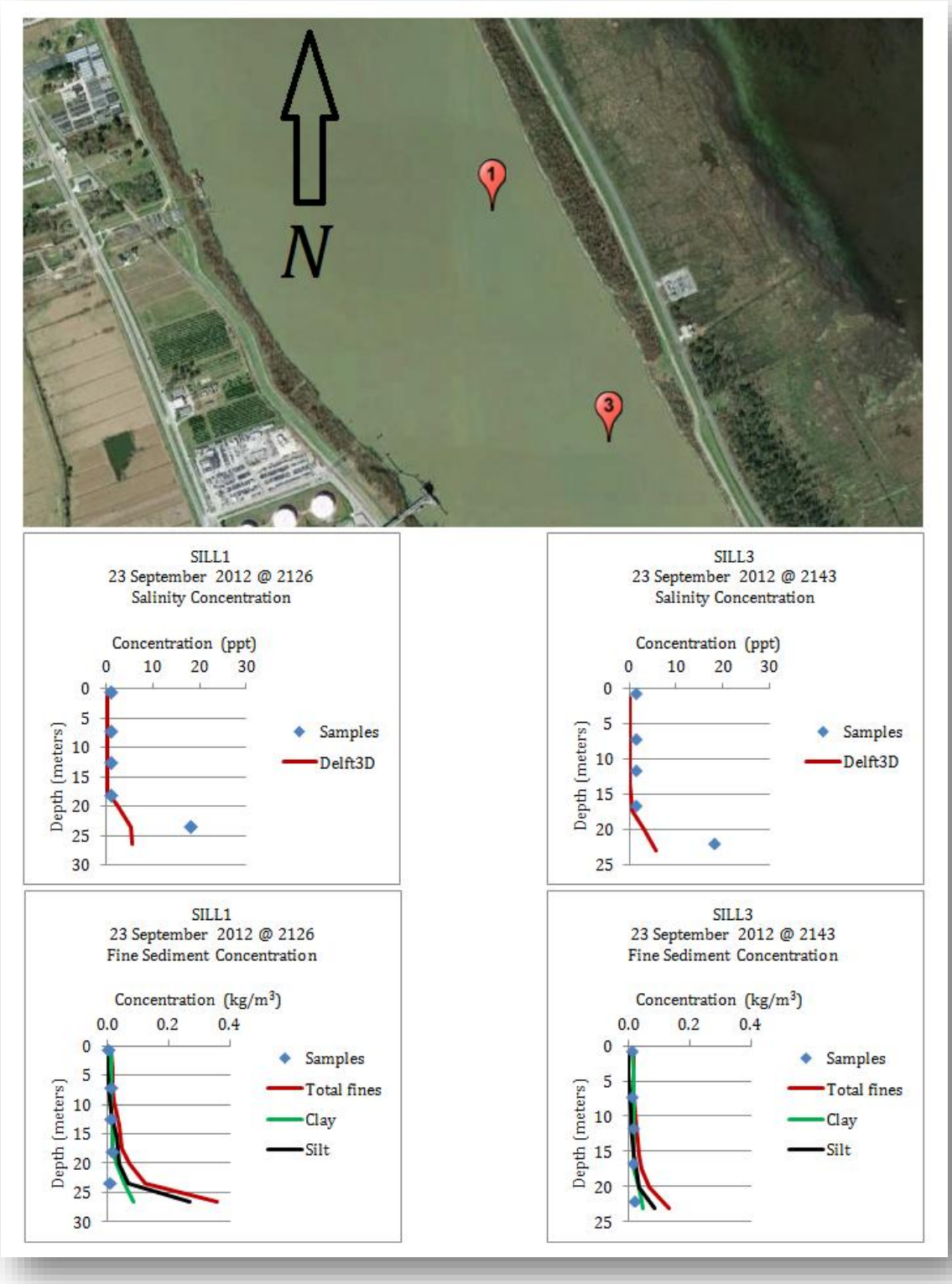

Figure 8-38 Model results compared to Van Dorn Bottle samples at the barrier sill

8.6.4 June 2012 Salinity and Temperature results

The USACE conducted in-river measurements of temperature, conductivity and depth along the thalweg of the channel to track the progress of the salinity wedge with a YSI Castaway CTD profiler. The following figures show the comparison of model results to the measured temperature and instrument derived salinity. The model data shown in the plots represents the top of the hour results closest to the instrument cast time.

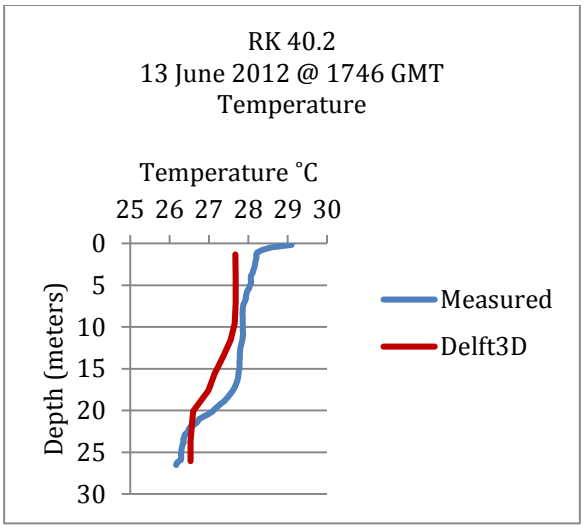

Figure 8-39 CTD cast and Delft3D temperature results

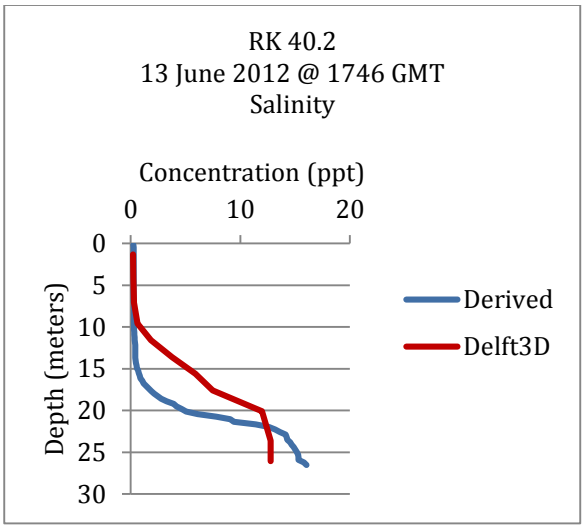

Figure 8-40 CTD cast and Delft3D salinity results

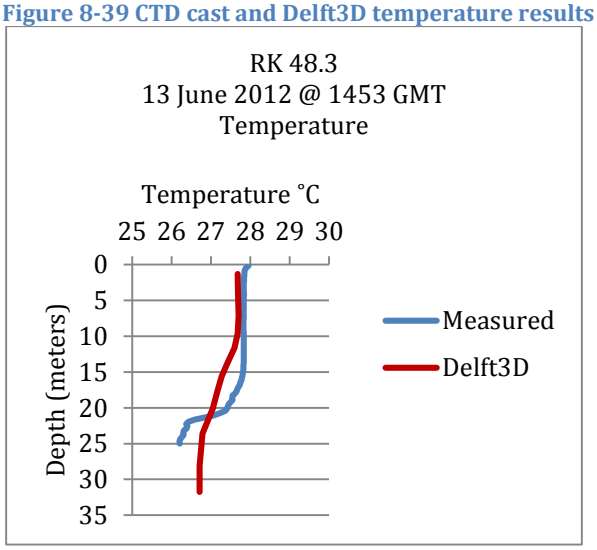

Figure 8-41 CTD cast and Delft3D temperature results

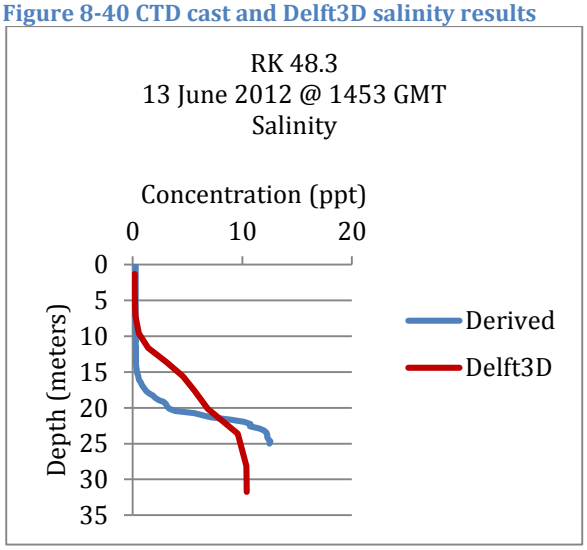

Figure 8-42 CTD cast and Delft3D salinity results

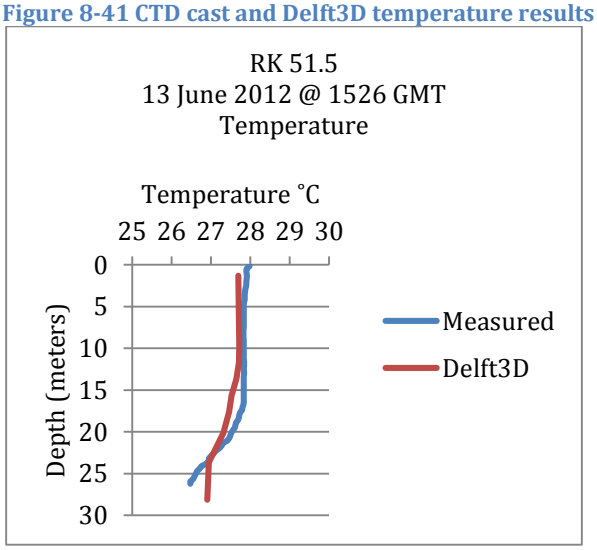

Figure 8-43 CTD cast and Delft3D temperature results

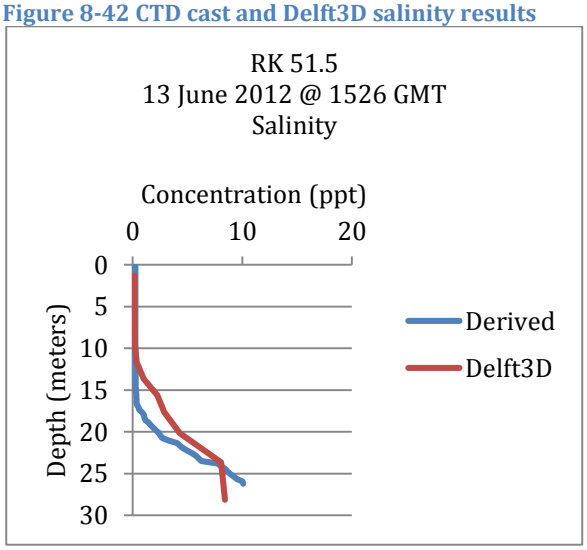

Figure 8-44 CTD cast and Delft3D salinity results

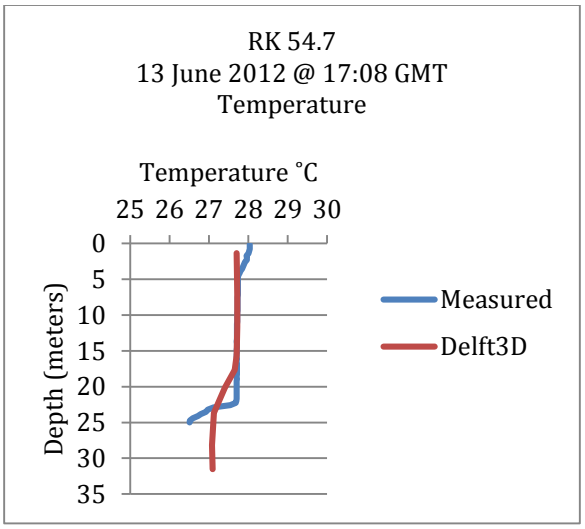

Figure 8-45 CTD cast and Delft3D temperature results

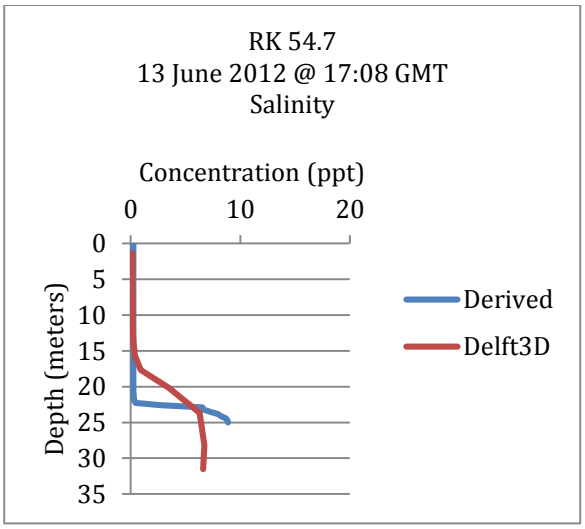

Figure 8-46 CTD cast and Delft3D salinity results

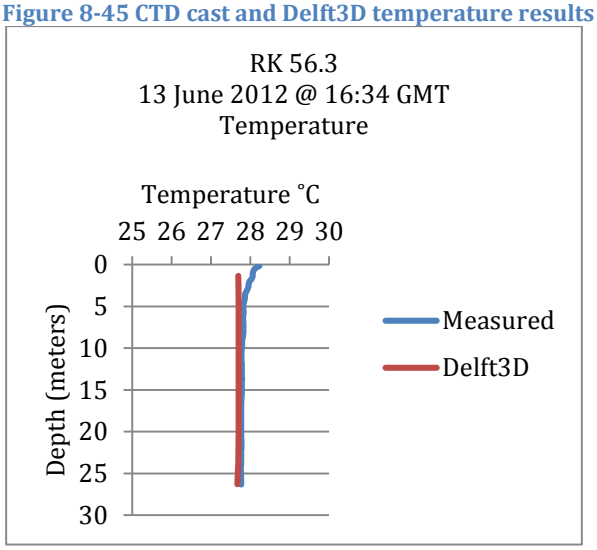

Figure 8-47 CTD cast and Delft3D temperature results

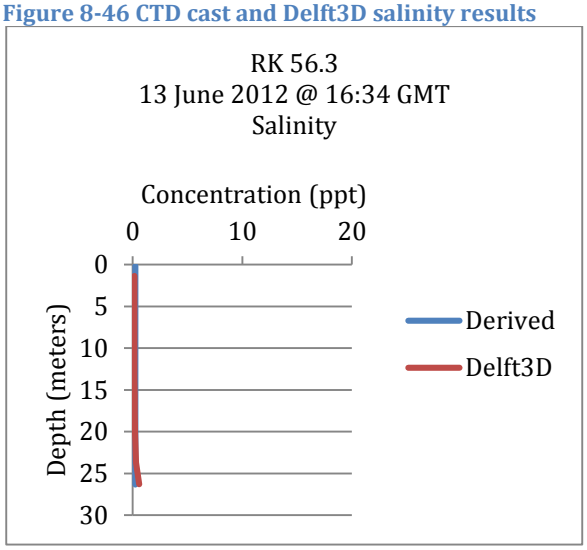

Figure 8-48 CTD cast and Delft3D salinity results

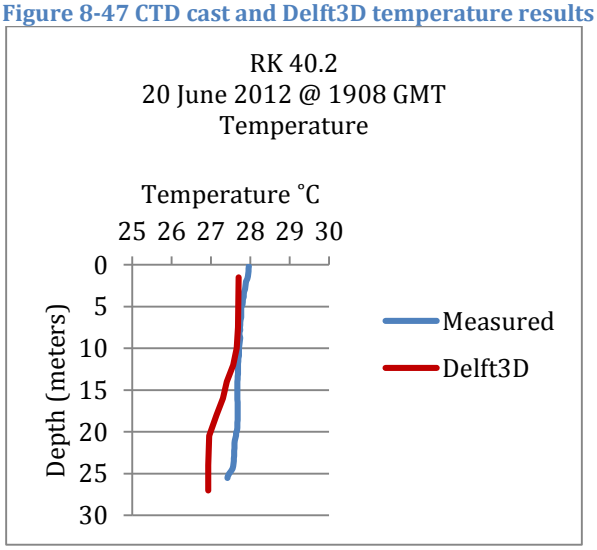

Figure 8-49 CTD cast and Delft3D temperature results

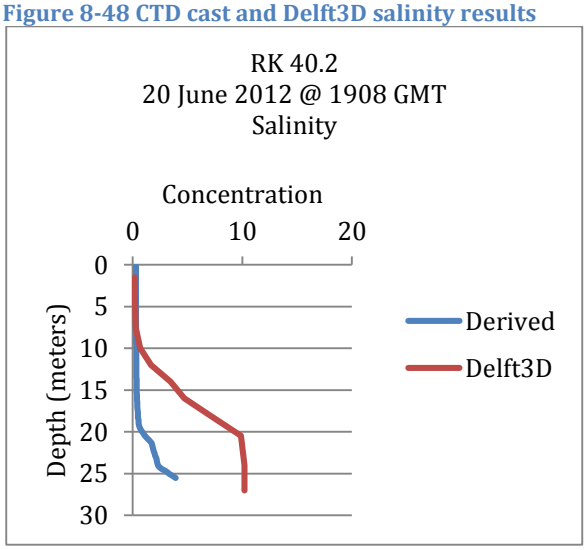

Figure 8-50 CTD cast and Delft3D salinity results

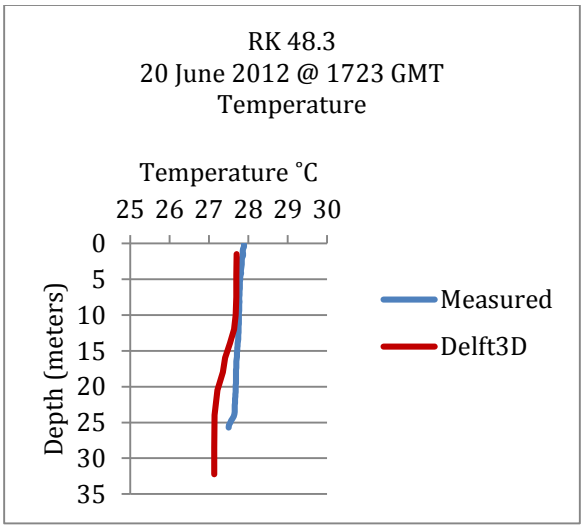

Figure 8-51 CTD cast and Delft3D temperature results

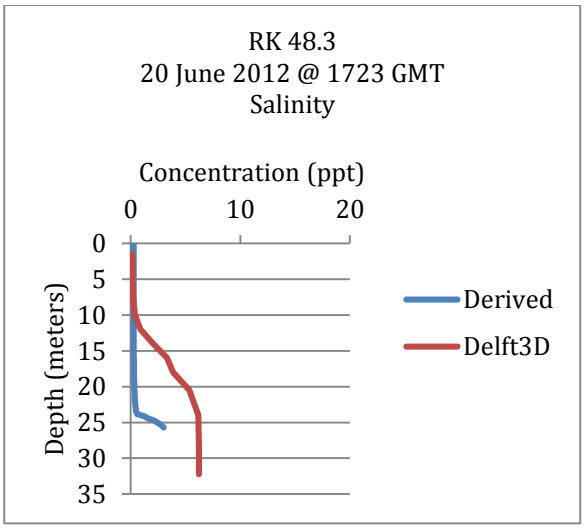

Figure 8-52 CTD cast and Delft3D salinity results

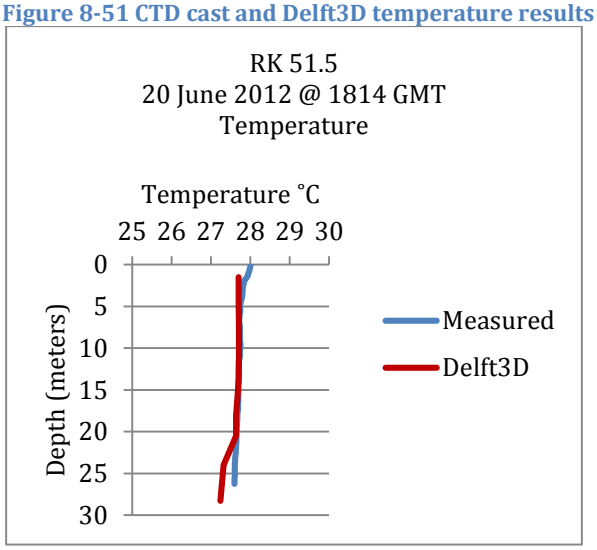

Figure 8-53 CTD cast and Delft3D temperature results

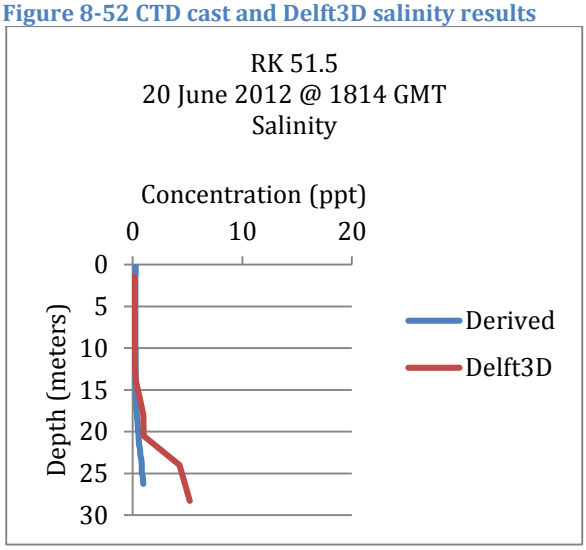

Figure 8-54 CTD cast and Delft3D salinity results

9 DISCUSSION

9.1 Water Level

The one week average observed and model water level data from April and September 2012 are plotted on Figure 9-1 and Figure 9-2. Examination of Figure 9-1 reveals that the Southwest Pass at RK 12.1 and the Mississippi River at Empire gages do not follow the expected trend of increasing stage in the upriver direction. This is most likely due to gage datum error. The observed data in Figure 9-2 reveals an adverse slope in the water level in the upstream direction during the low flow conditions in September. Also, a divergence between observed and model water level data in the upper part of the model domain is apparent in Figure 9-2. The September model results are approximately 0.3 to 0.4 meters higher at the location of the three upstream river gages at Belle Chasse, Alliance, and West Pointe a la Hache.

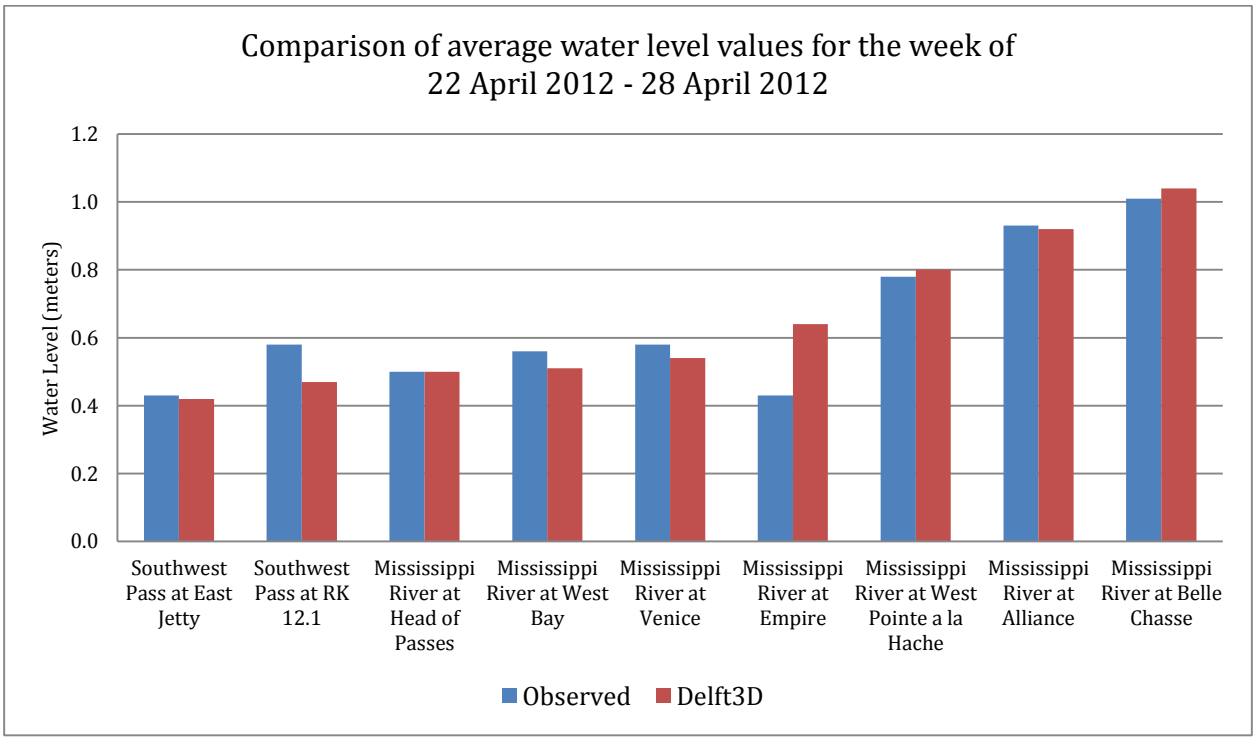

Figure 9-1 Comparison of average water level values in April 2012

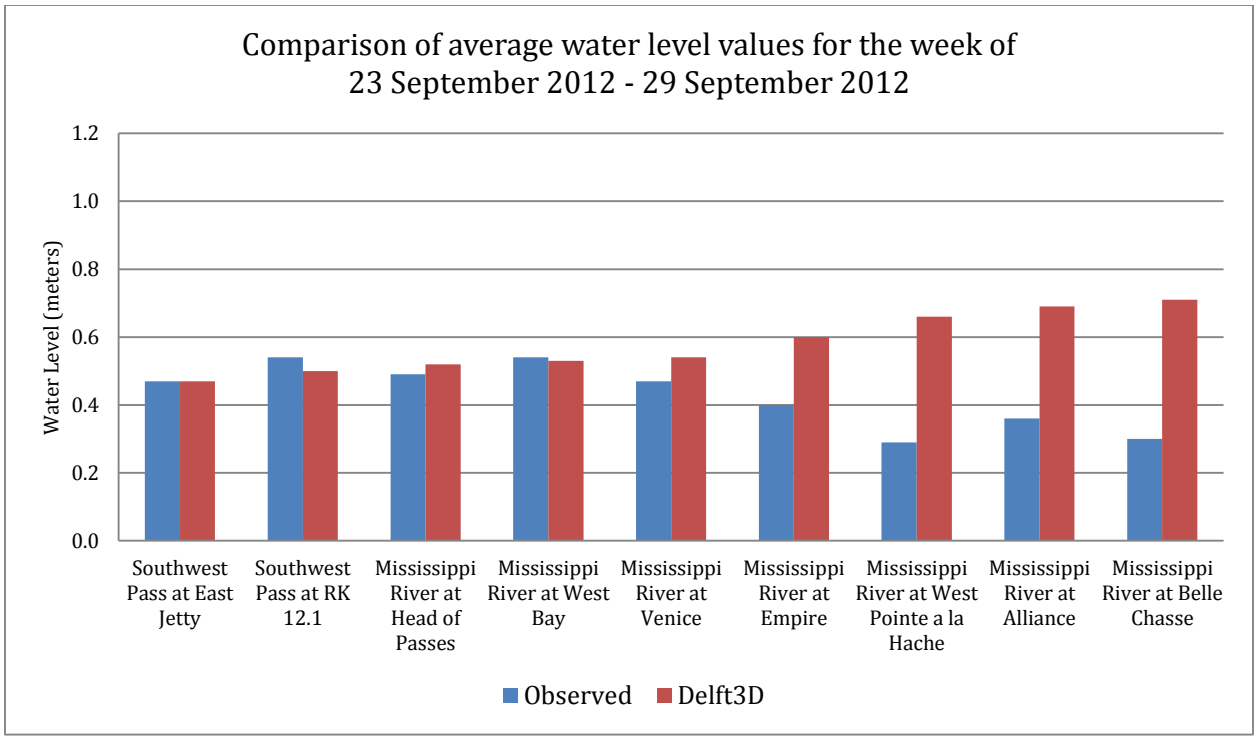

Figure 9-2 Comparison of average water level values in September 2012

Gage data from five river sites are plotted on Figure 9-3 and Figure 9-4. As can be seen in Figure 9-3, the stage progressively increases in the upstream direction except for the Empire data which is believed to be due to gage datum error. This slope in the profile is to be expected under these moderate flow conditions in April. However, as shown in Figure 9-4, it can be seen that the Belle Chasse stage data is consistently lower than the stage data from the downstream Venice and Alliance gages in September. Both the Venice and Alliance gages were reported as float type (encoder) gages in 2012 and the Belle Chasse gage was a pressure transducer type (reference Table 8-3).

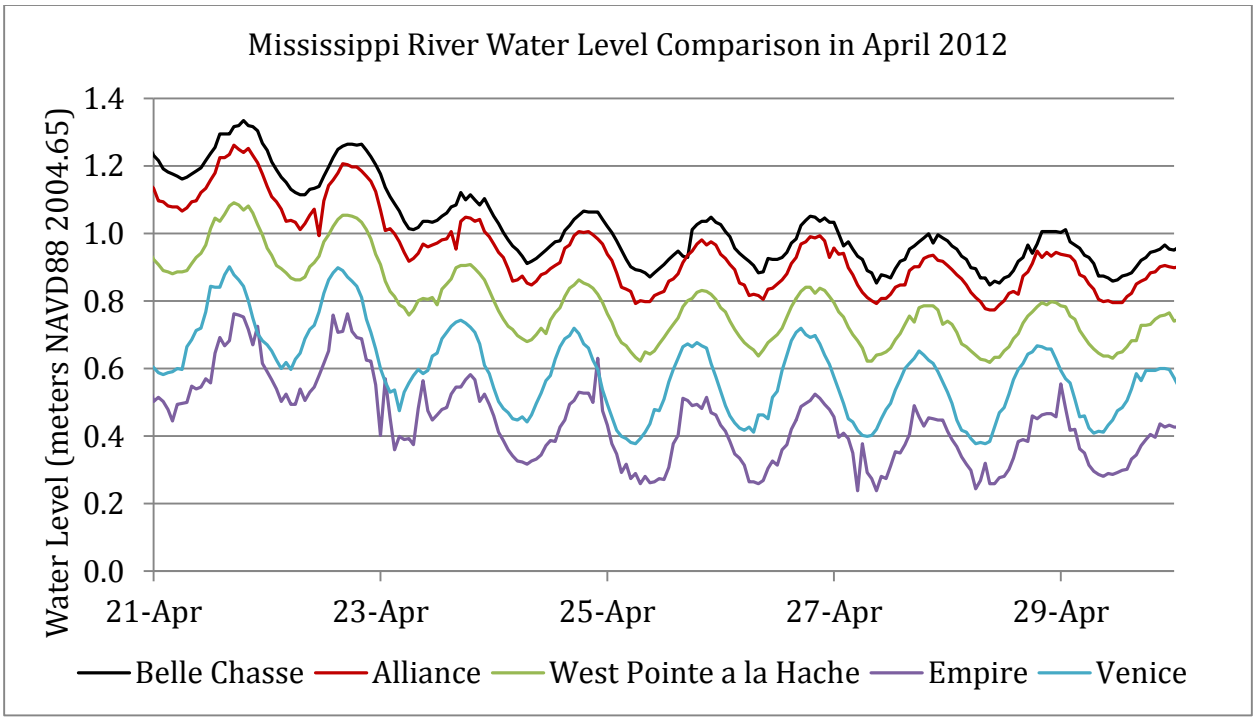

Figure 9-3 Comparison of April gage data at Belle Chasse, Alliance and West Pointe a la Hache

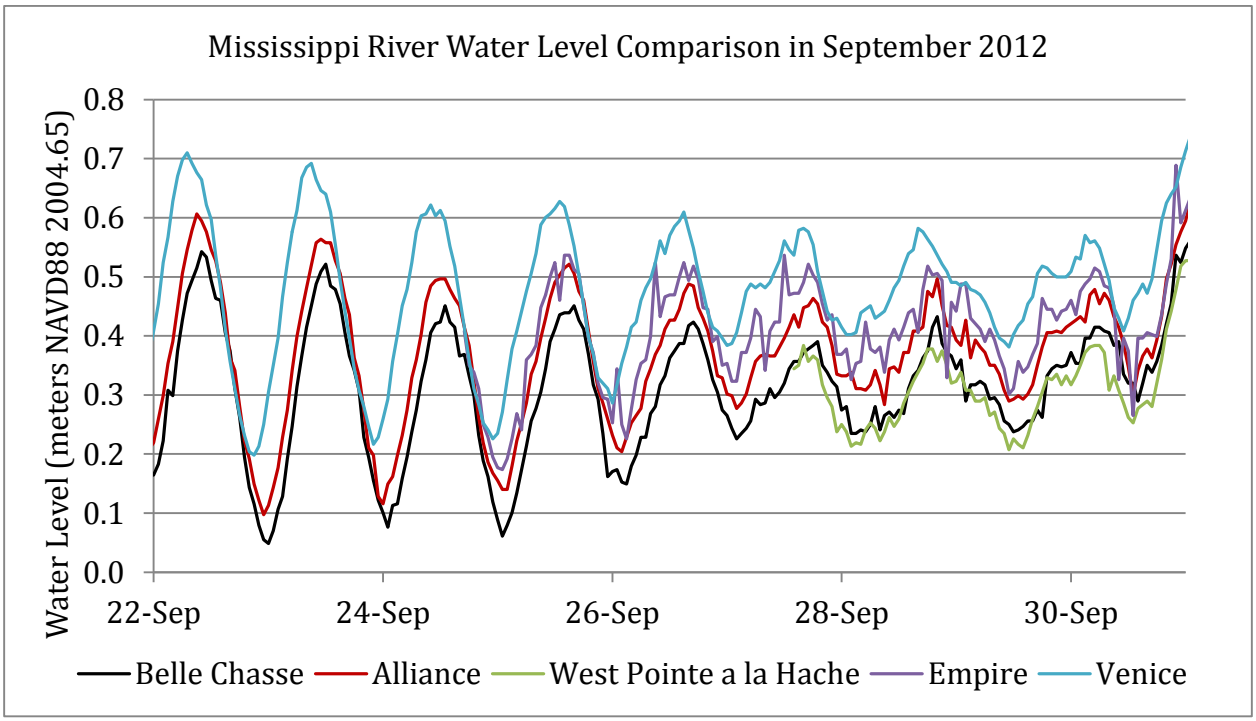

Figure 9-4 Comparison of September gage data at Belle Chasse, Alliance and West Pointe a la Hache

The adverse slope observed in the September gage data is likely caused by the buoyancy of the freshwater layer over the saline wedge if the gage records are accurate. Other possible causes for an adverse slope in the river water level during low flow conditions may stem from lateral density gradients due to higher salt concentration at the thalweg and exaggeration of this effect at river bends due to centrifugal forces. A momentum analysis should be performed to determine the effects on water level of a reverse friction force in the longitudinal direction caused by the upriver movement of the density current. However, these possible causes of the adverse slope do not explain why the model reports higher stages at the upstream gages for the September simulation.

A sensitivity test was conducted to determine if the discrepancy between the model results and the gage records was caused by bottom friction changes from April to September. The bottom friction Chézy coefficient was changed from 75 $m^{1/2}/s$ to 90 $m^{1/2}/s$ from Belle Chasse to RK 71 and the resulting computed water levels were compared in September to the previous model results with the Chézy coefficient equal to 75 $m^{1/2}/s$. The resulting change in water level was insignificant indicating that the model is insensitive to bottom friction values at these extreme low flow conditions, therefore other causes for the water level discrepancy must be investigated.

The use of an inflow record from the Tarbert Landing discharge range without tidal influence may not be providing a realistic picture of the true inflow hydrograph at Belle Chasse. In reality, the river channel between Belle Chasse and Tarbert Landing provides storage for tidal wave propagation and resultant dissipation of momentum. Extending the inflow boundary further upstream would provide additional channel storage and dissipation of momentum in the flow prior to reaching the observation gages showing the discrepancy and perhaps improve model results. Additionally, the physical connectivity of the lateral outlets at the Ft. St. Phillip bend should be checked to ensure adequate flow capacity is provided in the model to allow realistic exchange of water between the river and the gulf during low flow conditions.

During periods of extremely low flow such as that experienced in September 2012, the tide levels will dictate current patterns in the lower delta. The tide gage records should be carefully evaluated, especially, the Southwest Pass Jetty gage record which is used to set the datum of the Grand Isle and Bay Gardene tide boundary records. Any river influence on the water level at the Jetty gage may cause the Grand Isle and Bay Gardene records to be artificially elevated. This would have a direct effect on the flow exchange at Ft. St. Phillip, Baptiste Collette Bayou and Grand Pass, since the Jetty water level is used to set the downstream boundary water level of the flow leaving the river through these lateral outlets. If the downstream stage is artificially high, then insufficient flow would be allowed to leave the river. The divergence in water level record between observed and model data begins at the Venice gage in September, so improper flow exchange at these three outlets may play a part in the discrepancy.

9.2 Fine Sediment Distribution at Belle Chasse

The model results indicated that for the September 2012 simulation, the suspended sediment in the lower part of the delta would be comprised entirely of the Clay constituent. In other words, the Silt class is deposited before it reached the observation site at RK 27.4. However, immediately downstream of the location of the barrier sill, at observation sites SILL1 and SILL3, the model predicted that Silt would be in suspension, whereas the samples indicated a very low concentration indicative of Clay being the main sediment class in suspension. Comparing the total wash load concentrations at Baton Rouge and Belle Chasse indicates that much of the heavier silt load may drop out of suspension between Baton Rouge and Belle Chasse during drought conditions as indicated in Figure 9-5.

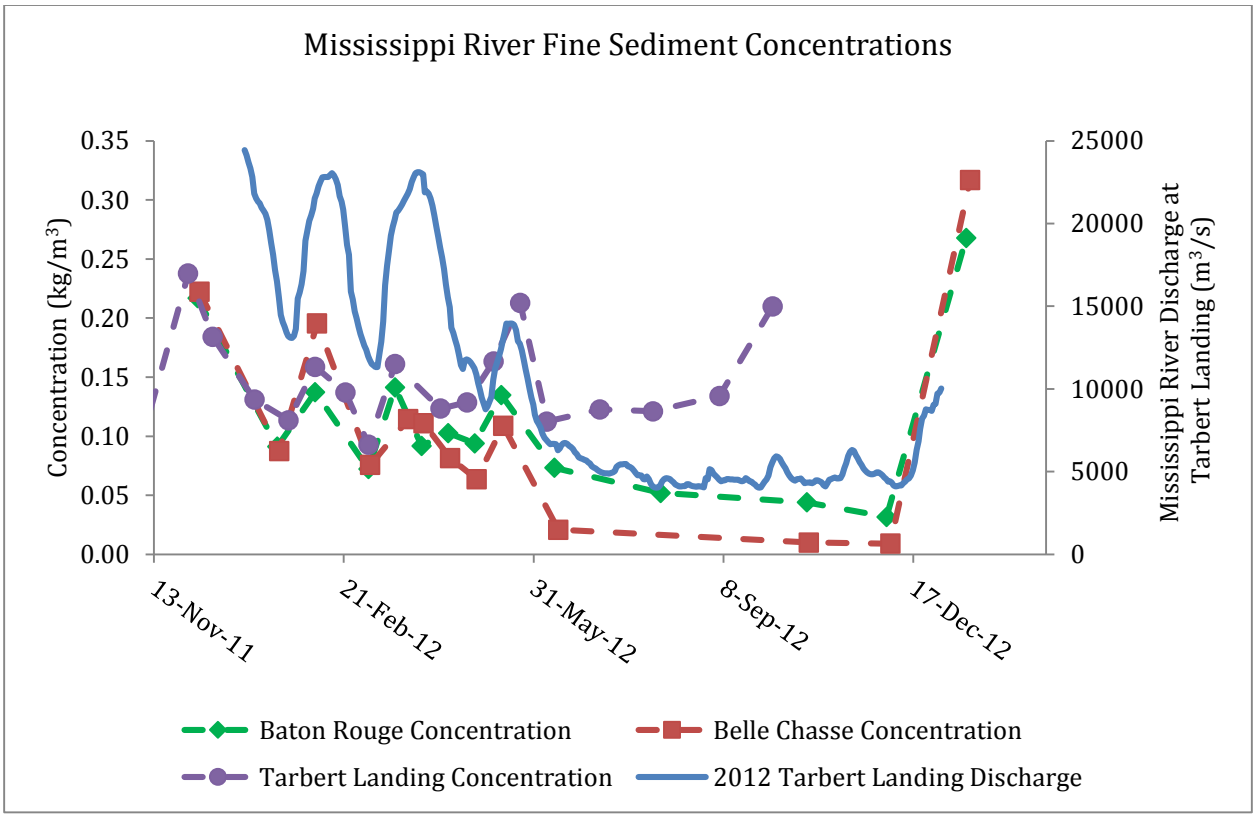

Figure 9-5 Observed fine sediment concentration in the Lower Mississippi River

As the concentration of Silt and Clay are not provided at Belle Chasse, a time series distribution based on records at Tarbert Landing was constructed for this study. If the distribution at Belle Chasse shifts toward a higher percentage of the load being comprised of Clay at extremely low River discharges, the boundary load will introduce an unrealistic higher load of Silt which could tend to bias the concentration higher at the observation sites at the Sill (SILL1 and SILL3).

A sensitivity analysis was performed on the Belle Chasse sediment load by assuming the total Belle Chasse load would be comprised of 70 % Clay and 30 % Silt with the same total load. The results of this sensitivity analysis are shown in Figure 9-6 through Figure 9-22. In essence the model proved to be somewhat insensitive to the shift in the boundary concentration shift between the Clay and Silt sediment classes. The Clay concentration increased proportionately throughout the water column without a significant concentration gradient change in the vertical profiles.

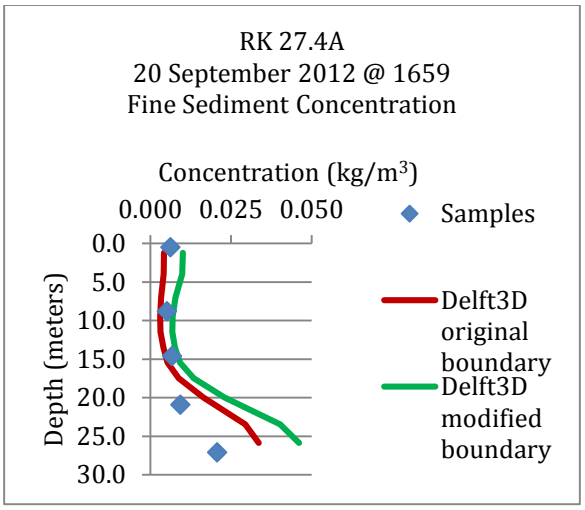

Figure 9-6 Sediment sensitivity results at RK 27.4A

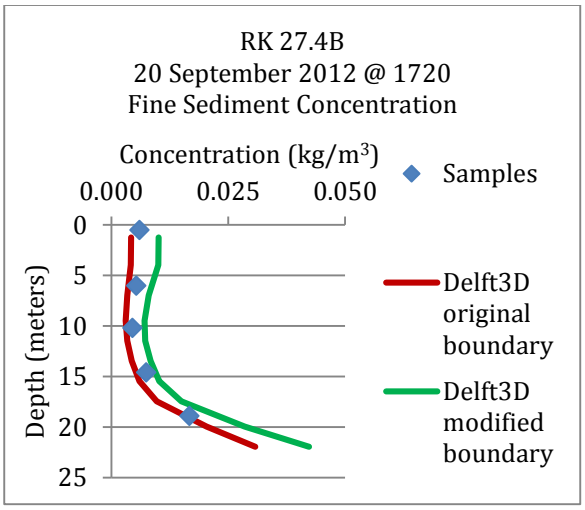

Figure 9-7 Sediment sensitivity results at RK 27.4B

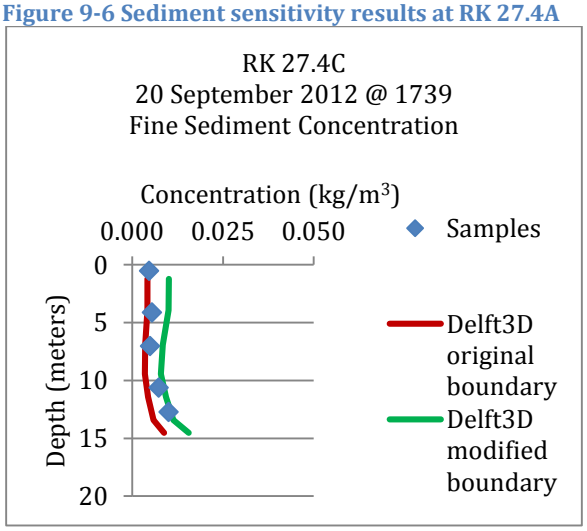

Figure 9-8 Sediment sensitivity results at RK 27.4C

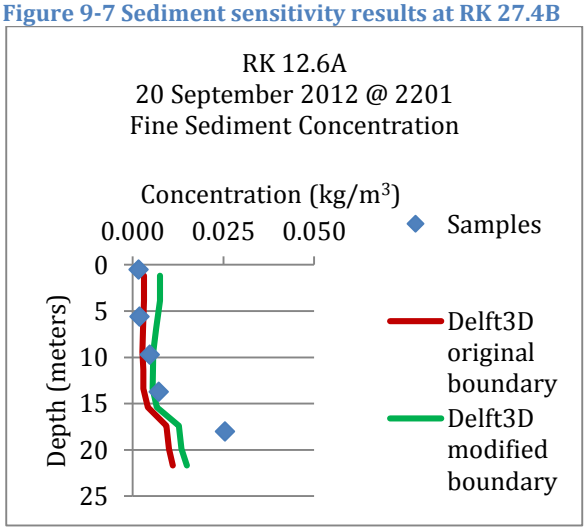

Figure 9-9 Sediment sensitivity results at RK 12.6A

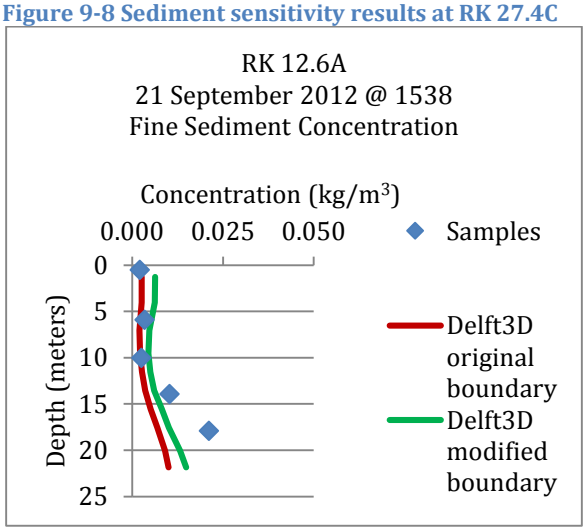

Figure 9-10 Sediment sensitivity results at RK 12.6A

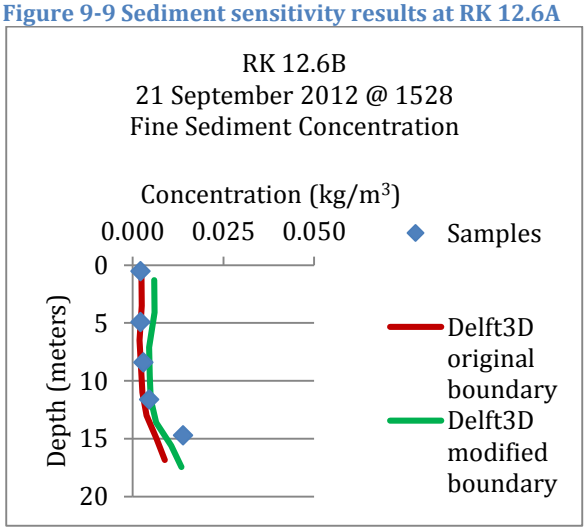

Figure 9-11 Sediment sensitivity results at RK 12.6B

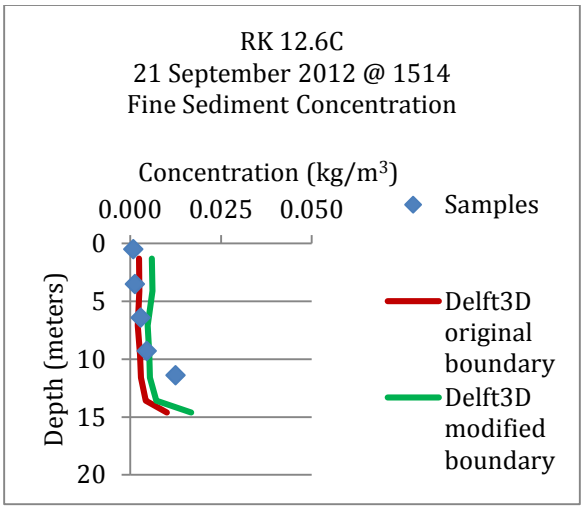

Figure 9-12 Sediment sensitivity results at RK 12.6C

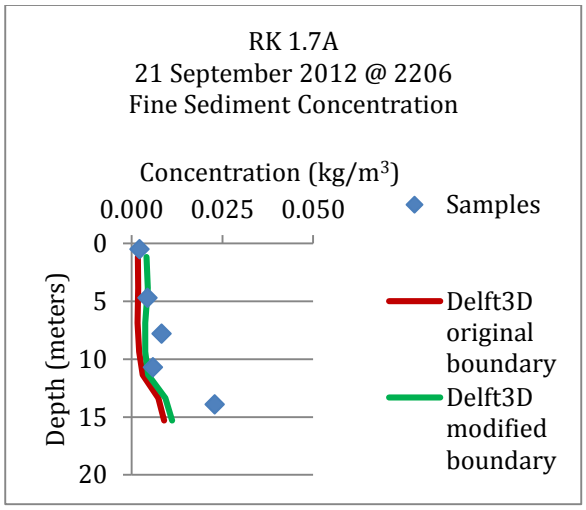

Figure 9-13 Sediment sensitivity results at RK 1.7A

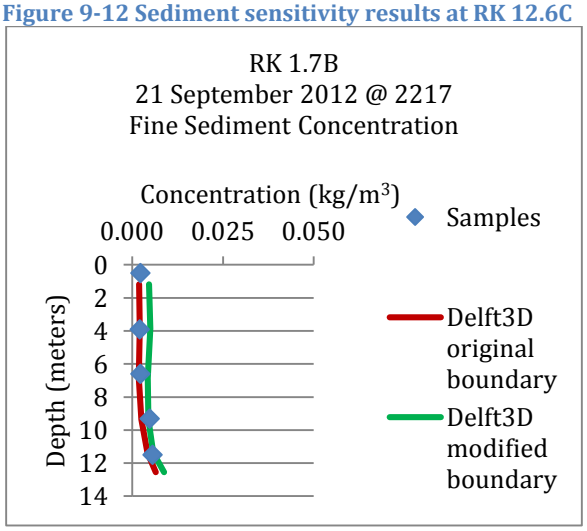

Figure 9-14 Sediment sensitivity results at RK 1.7B

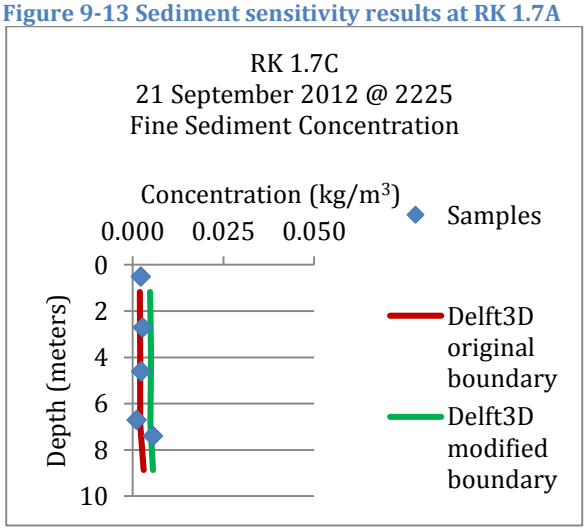

Figure 9-15 Sediment sensitivity results at RK 1.7C

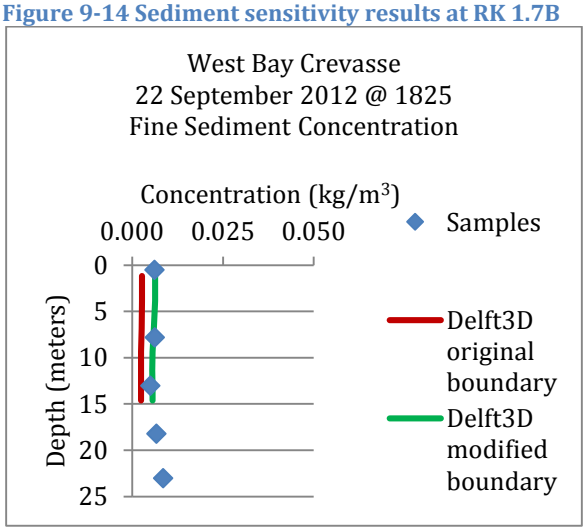

Figure 9-16 Sediment sensitivity results at West Bay

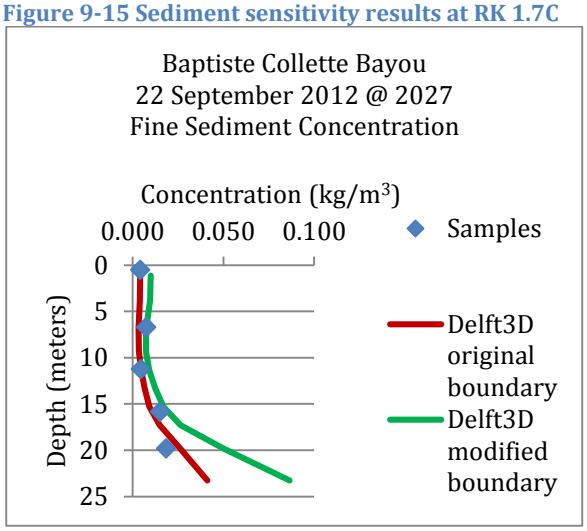

Figure 9-17 Sediment sensitivity results at Baptiste Collette Bayou

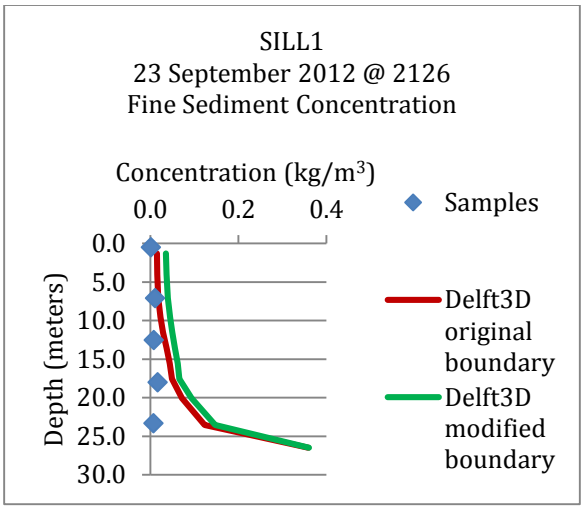

Figure 9-18 Sediment sensitivity results at SILL1

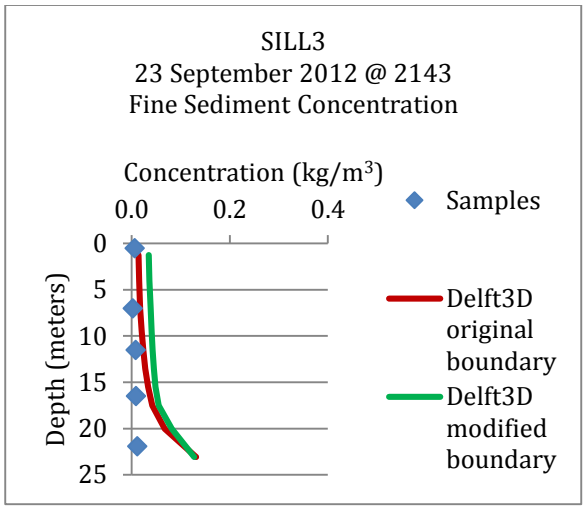

Figure 9-19 Sediment sensitivity results at RK SILL3

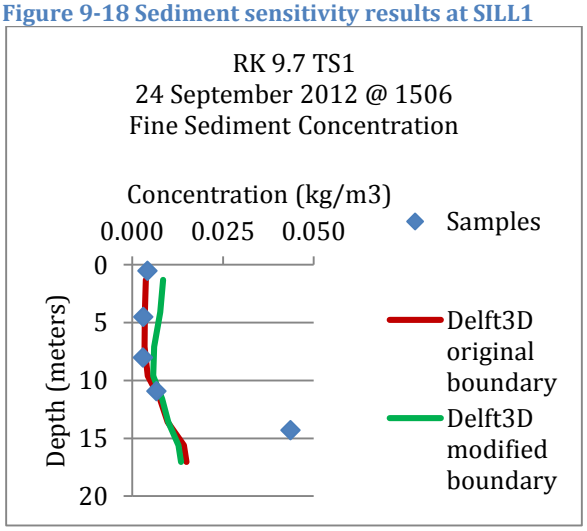

Figure 9-20 Sediment sensitivity results at RK 9.7 TS1

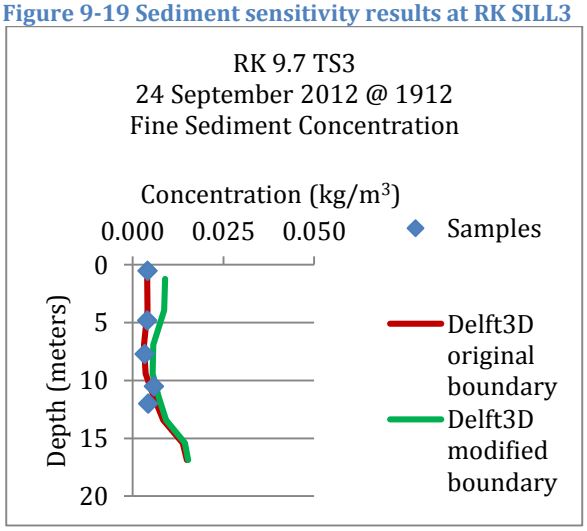

Figure 9-21 Sediment sensitivity results at RK 9.7 TS3

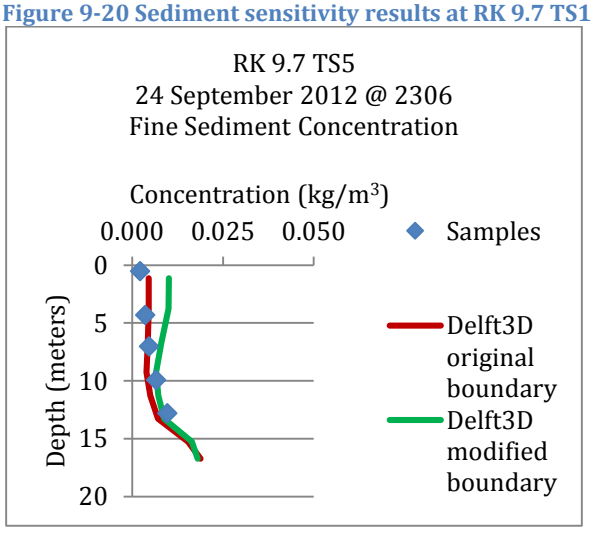

Figure 9-22 Sediment sensitivity results at RK 9.7 TS5

9.3 Vertical level resolution sensitivity

The model did not reproduce the sharp interface evidenced in the field data as indicated in the June CTD casts (Figure 8-39 through Figure 8-54). This is thought to be due to the artificial mathematical mixing that occurs to some degree in all discretization schemes. Although the *Z*-level model is capable of propagating the density current as exists in the prototype, it is still subject to some mathematical diffusion due to the stair-step nature of the boundary fitted grid cell structures. Additional vertical level designs were tested in order to evaluate the model response to increased and decreased vertical resolution around the interface. In addition to the 14-level design previously discussed, 10-level and 22-level designs were tested without sediment and compared to the June CTD cast field data. It should be noted that due to cable length limitations, the cast depth may not extend to the bottom of the channel for all observations and the most upstream extent of the density current is uncertain. The three vertical designs are summarized in Table 9-1.

Table 9-1 Vertical level design for sensitivity analysis

Z-level layer number	10 Z-levels design			14 Z-levels design			22 Z-levels design		
	Thickness (meters)	Bottom (NAVD88 meters)	Top (NAVD88 meters)	Thickness (meters)	Bottom (NAVD88 meters)	Top (NAVD88 meters)	Thickness (meters)	Bottom (NAVD88 meters)	Top (NAVD88 meters)
1	20	-70	-50	20	-70	-50	20	-70	-50
2	12	-50	-38	12	-50	-38	10	-50	-40
3	8	-38	-30	8	-38	-30	5	-40	-35
4	6	-30	-24	5	-30	-25	5	-35	-30
5	4	-24	-20	4	-25	-21	3	-30	-27
6	4	-20	-16	3	-21	-18	2	-27	-25
7	4	-16	-12	2	-18	-16	1	-25	-24
8	4	-12	-8	2	-16	-14	1	-24	-23
9	6	-8	-2	2	-14	-12	1	-23	-22
10	6	-2	+4	2	-12	-10	1	-22	-21
11				2	-10	-8	1	-21	-20
12				3	-8	-5	1	-20	-19
13				3	-5	-2	1	-19	-18
14				6	-2	+4	1	-18	-17
15							1	-17	-16
16							2	-16	-14
17							2	-14	-12
18							2	-12	-10
19							2	-10	-8
20							3	-8	-5
21							3	-5	-2
22							6	-2	+4

The 10-level design was incapable of propagating the density current to the observation sites given the same turbulence parameters as the 14-level and 22-level designs. An example comparison plot is shown in Figure 9-23 with all three vertical level designs. The 10-level design proved to be too coarse around the interface to reproduce the salinity gradient observed in the prototype.

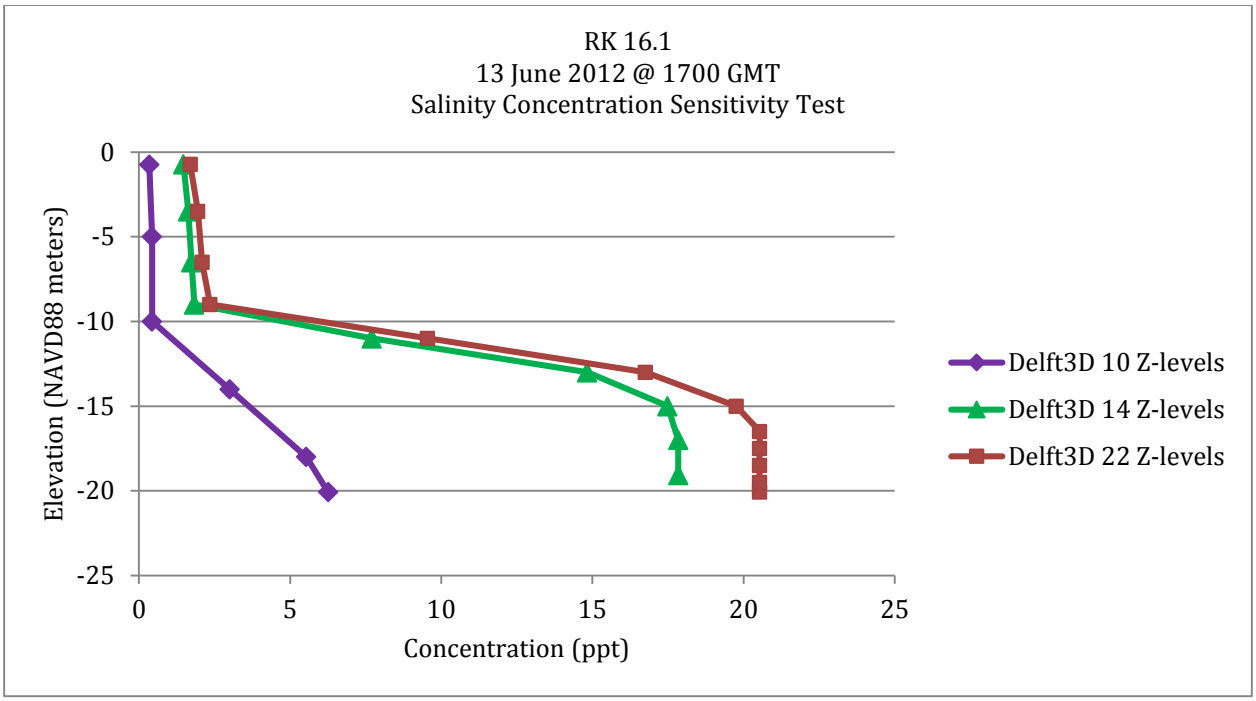

Figure 9-23 Example model results of the salinity profile with three different vertical level designs (L_{OZ} =0.07 m for all simulations)

The 22-level vertical distribution had a stronger concentration of salt in the wedge with an improved density gradient in most cases as compared to the field measurements as shown in Figure 9-24 through Figure 9-28 . However, as the upstream progression of the wedge is somewhat further for the 22-level design than that of the 14-level design, it is more subject to the effects of mathematical diffusion as the mixing length is longer and this is evident around the turning point of the profiles. All profiles exhibit higher concentrations throughout the profile compared to the observed data; this is thought to be due to the effects of mathematical diffusion and the length of the upstream mixing zone. An increase in the Ozmidov length scale for the 22-level design decreases the upstream progression of the wedge with a subsequent decrease in artificial mixing due to the shortened length of the mixing zone. An Ozmidov length scale equal to 0.09 m was required for the 22-level design to reduce the wedge progression to that observed in the 13 June 2012 data set.

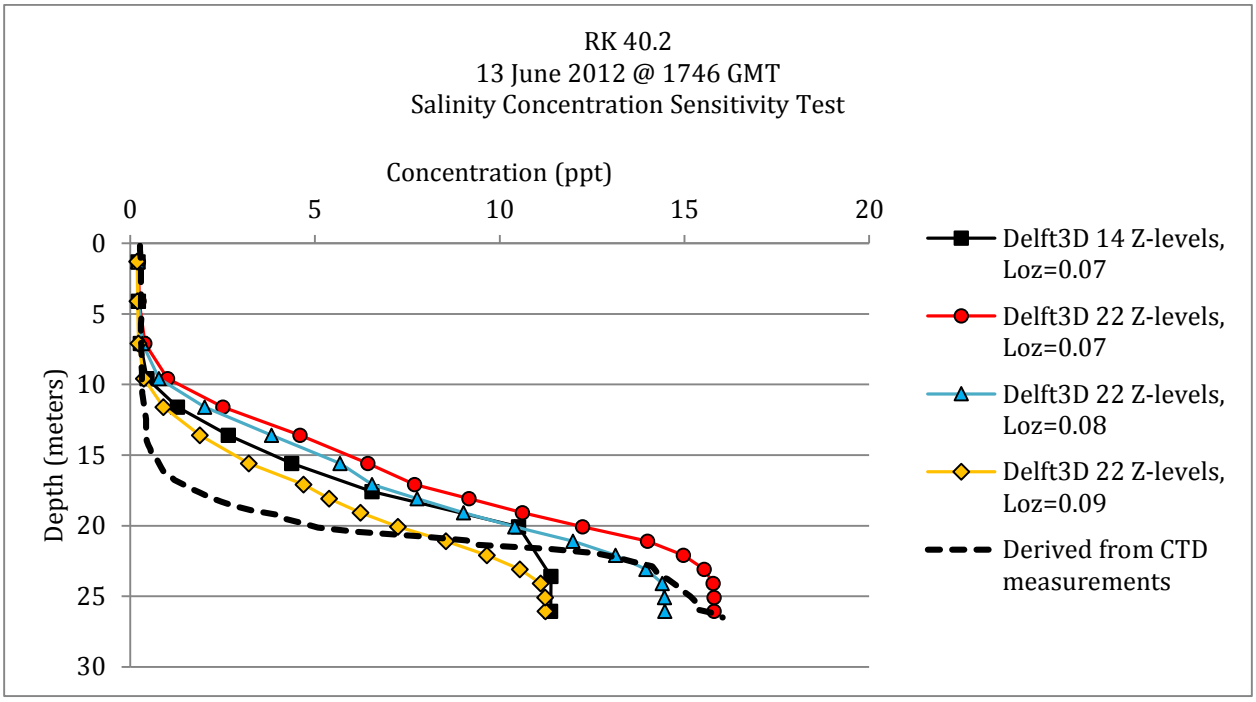

Figure 9-24 Vertical resolution sensitivity results at RK 40.2 (all model results at 1800 GMT)

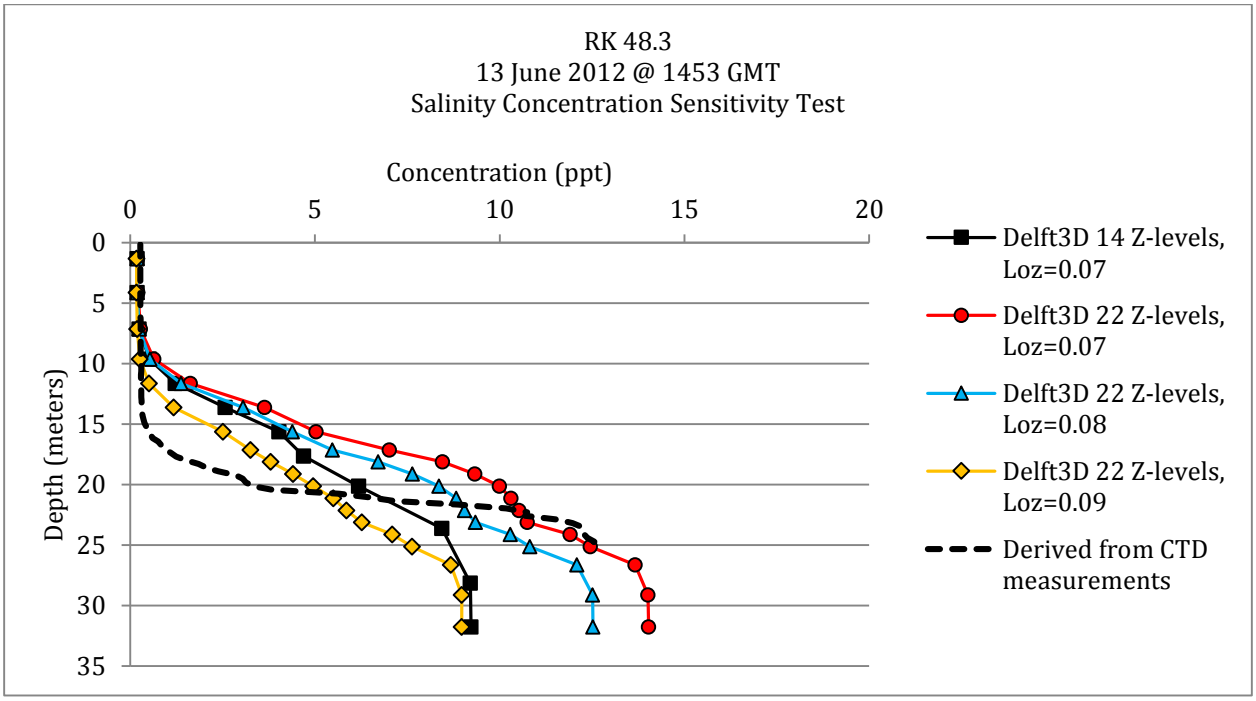

Figure 9-25 Vertical resolution sensitivity results at RK 48.3 (all model results at 1500 GMT)

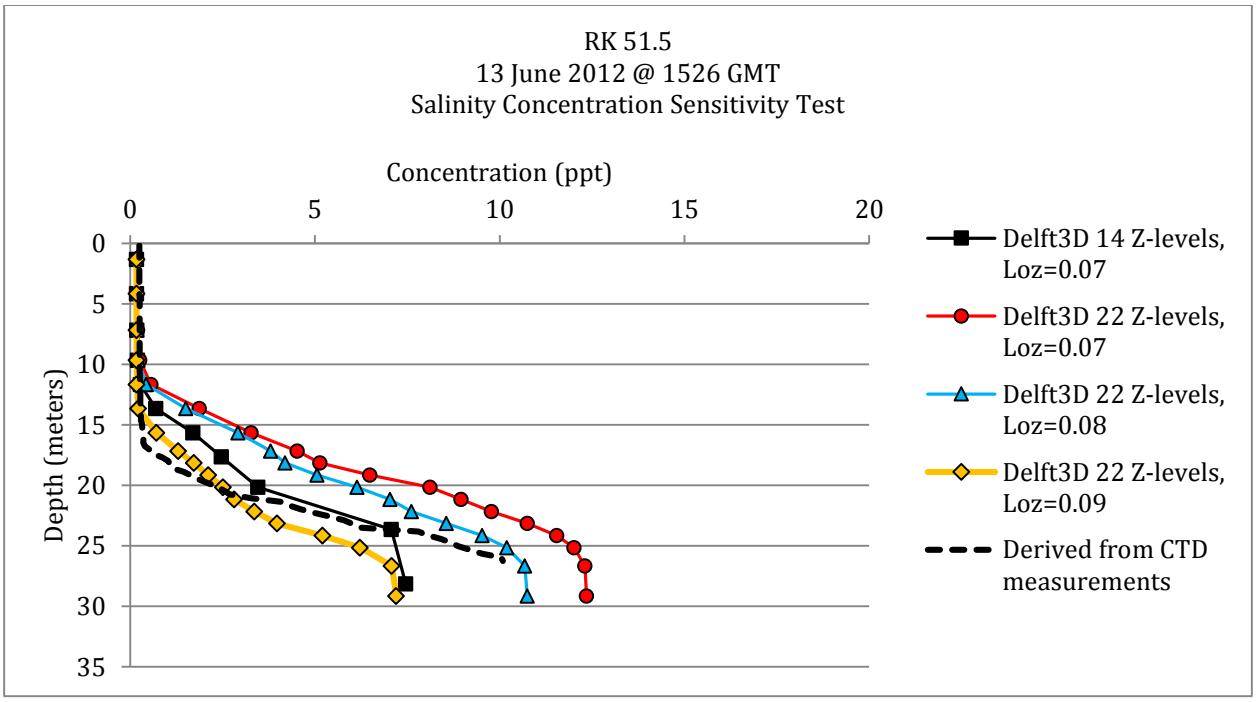

Figure 9-26 Vertical resolution sensitivity results at RK 51.5 (all model results at 1500 GMT)

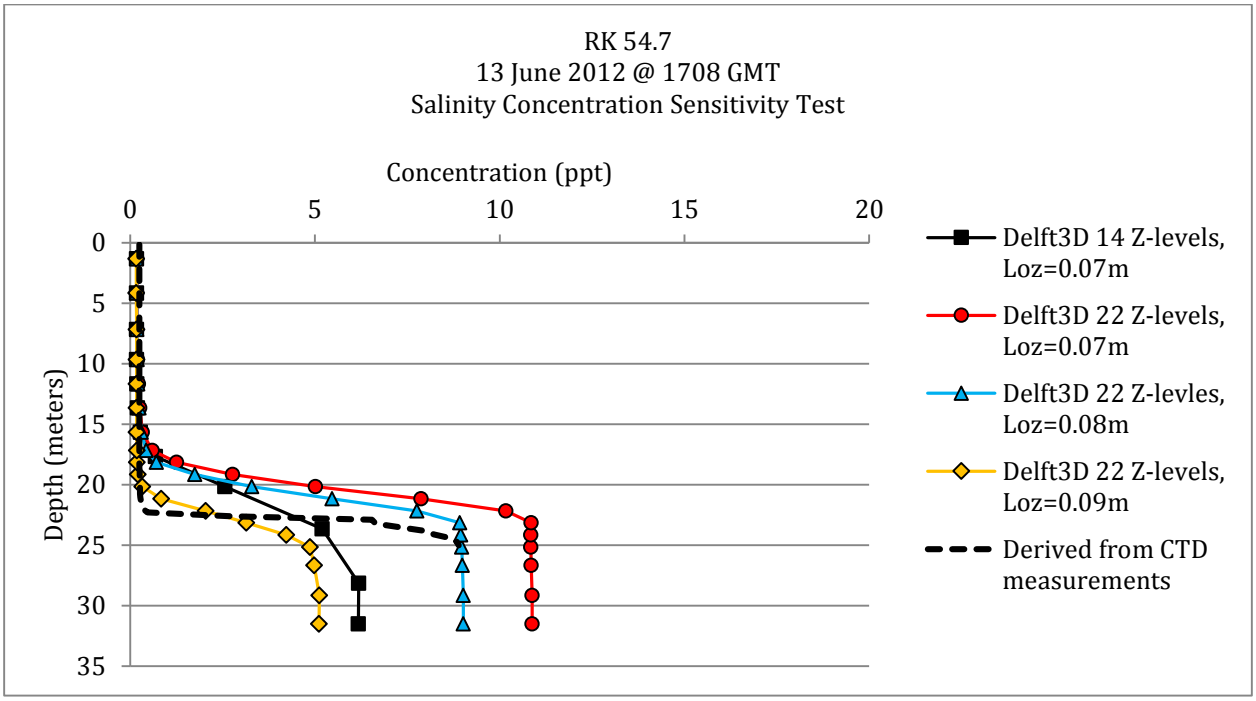

Figure 9-27 Vertical resolution sensitivity results at RK 54.7 (all model results at 1700 GMT)

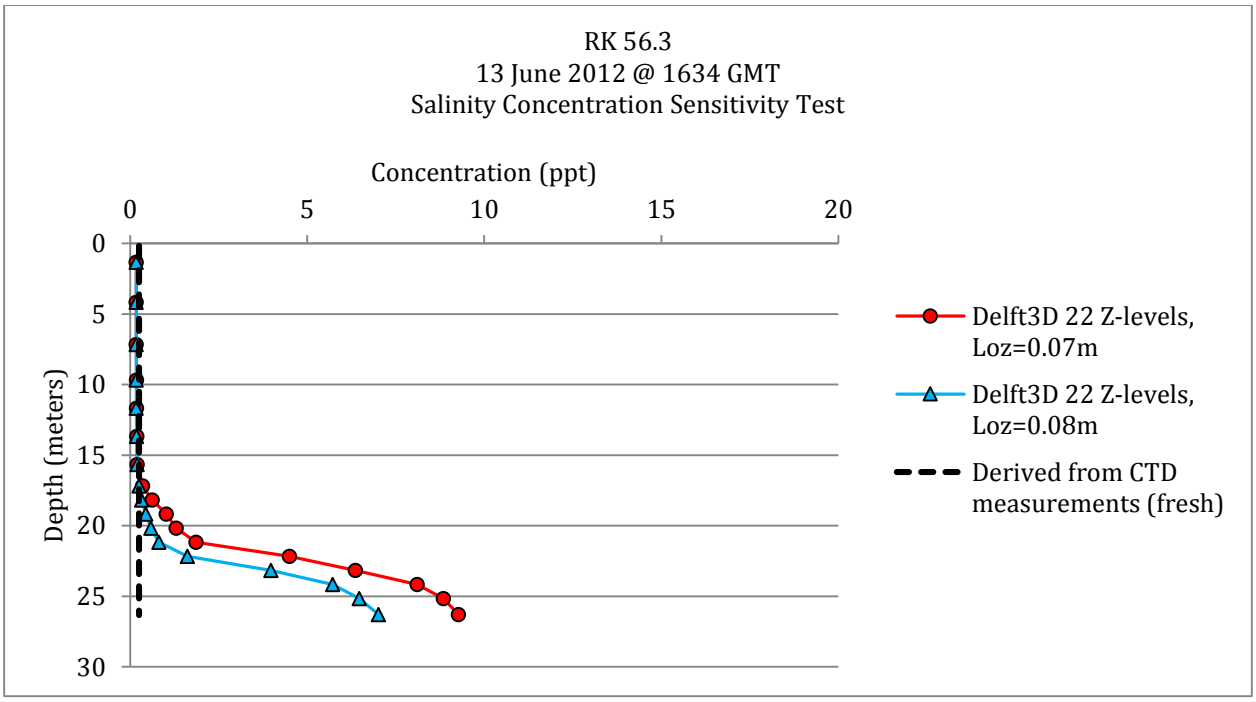

Figure 9-28 Vertical resolution sensitivity results at RK 56.3 (all model results at 1700 GMT, results for the Delft3D 14 Z-levels with Loz=0.07m and Delft3D 22 Z-levels with Loz=0.09m simulations were totally fresh and are not shown)

9.4 Sediment effects on salinity wedge dynamics

Delft3D has the ability to account for the increase in density due to suspended sediment and this feature was utilized throughout the model study (reference equation 3-16 for methodology). The 14-level vertical layer design results were evaluated with and without suspended sediment in order to examine the impact of sediment on the density profile and stratification properties.

Figure 9-29 displays the computed suspended sediment concentration at RK 40.2 at 1800 GMT on 13 June 2012. As can be seen, the concentration of clay is sharply increased in the lower part of the water column due to re-circulation of sediment in the turbidity maxima.

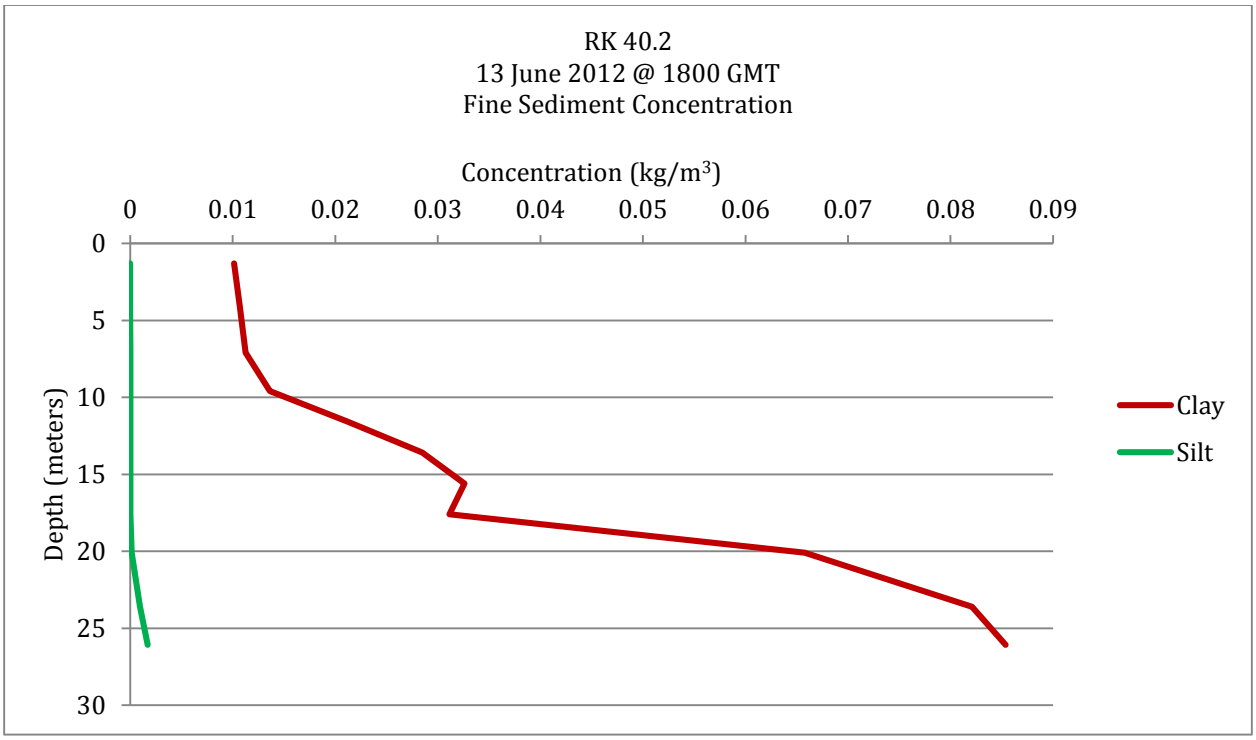

Figure 9-29 Example plot showing higher sediment concentration in the salinity wedge

The contribution of this fine sediment concentration to the total density can be seen in Figure 9-30. The impact on the salinity concentration is shown in Figure 9-31.

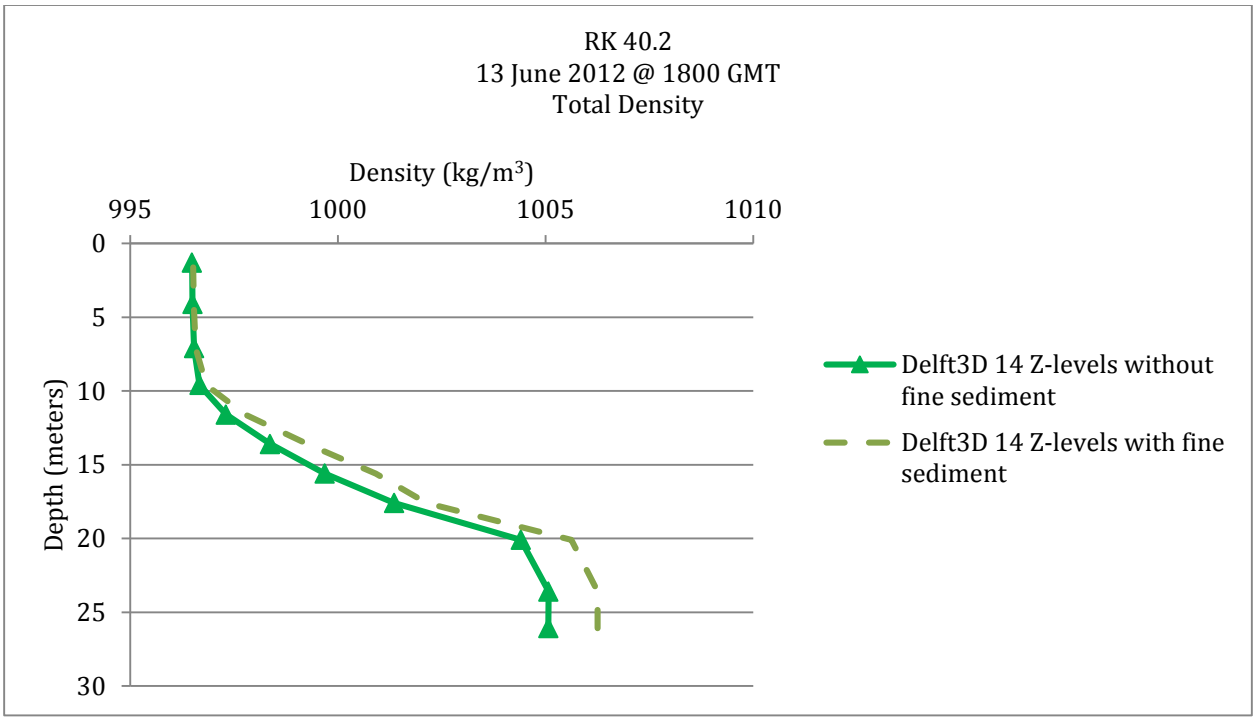

Figure 9-30 Fine sediment contribution to total density profile

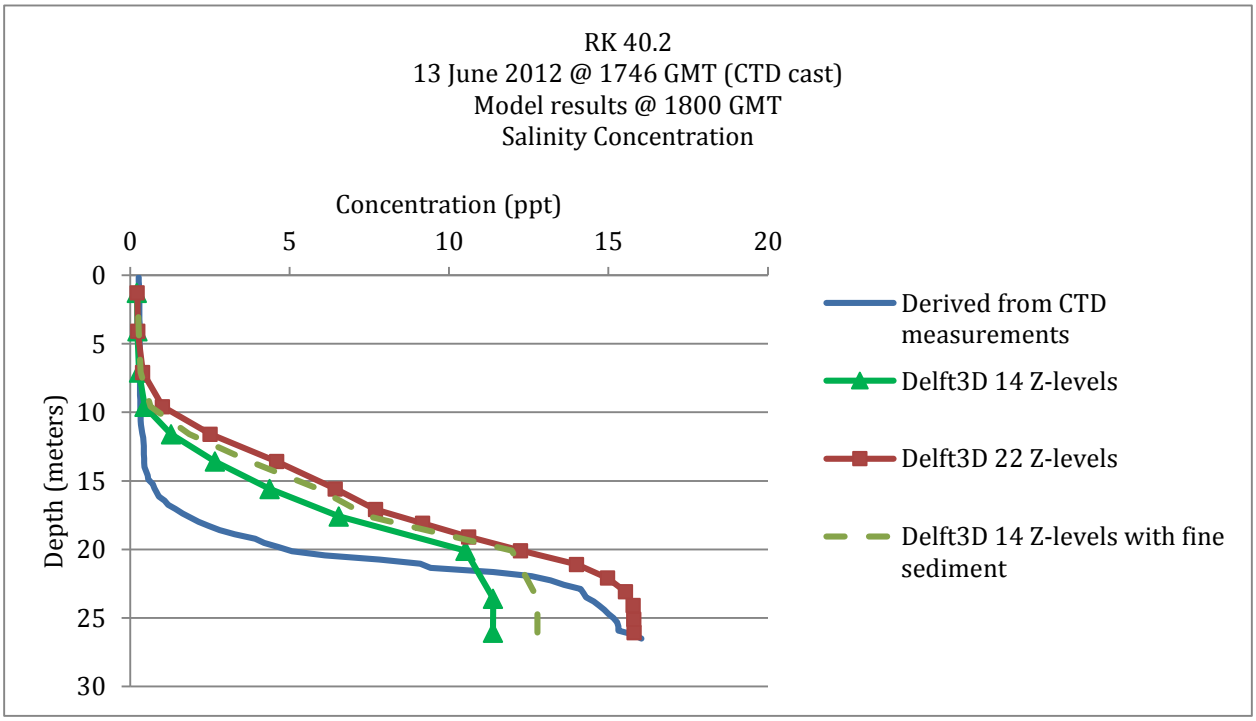

Figure 9-31 Plot showing contribution of fine sediment to salinity concentration profile

The influence of suspended sediment on the computed velocity can be seen in Figure 9-32 and Figure 9-33.

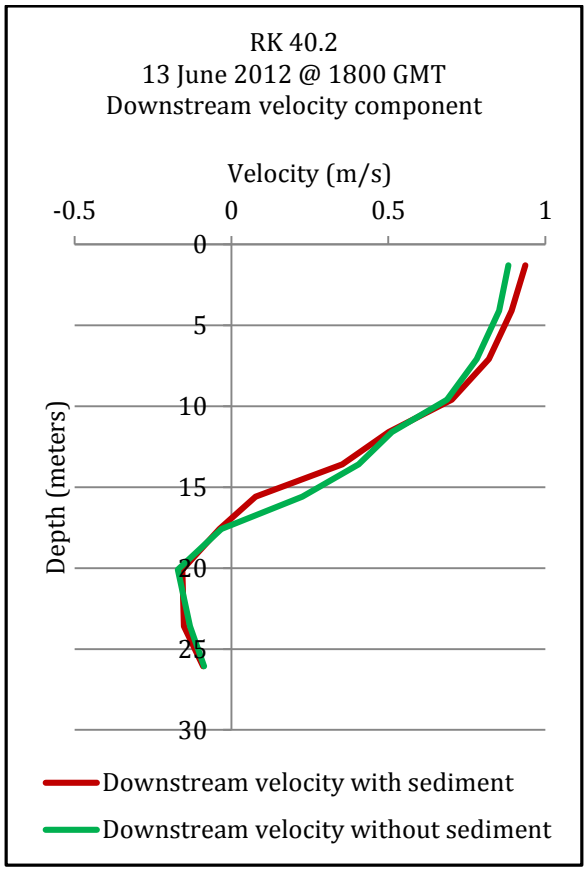

Figure 9-32 Downstream velocity sensitivity to addition of sediment

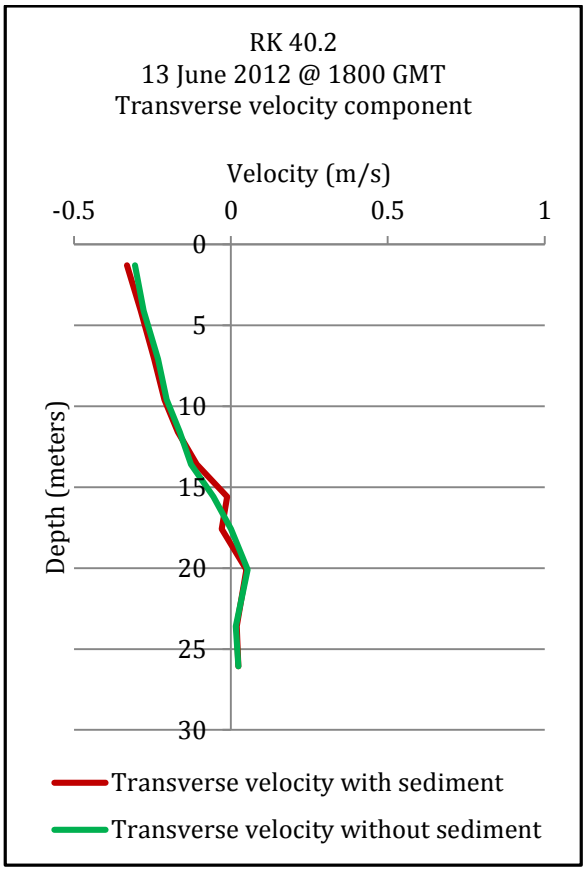

Figure 9-33 Transverse velocity sensitivity to addition of sediment

As explained in Section 2.3, the Richardson number may be used to give an indication of the stability of the flow stratification. As can be seen in Figure 9-34, the addition of sediment to the model significantly increased the stability of the stratification for this particular example. These results indicate that the contribution of sediment to the salinity wedge dynamics is an important factor to be considered in a model used to assess salinity intrusion in the Mississippi salt wedge estuary.

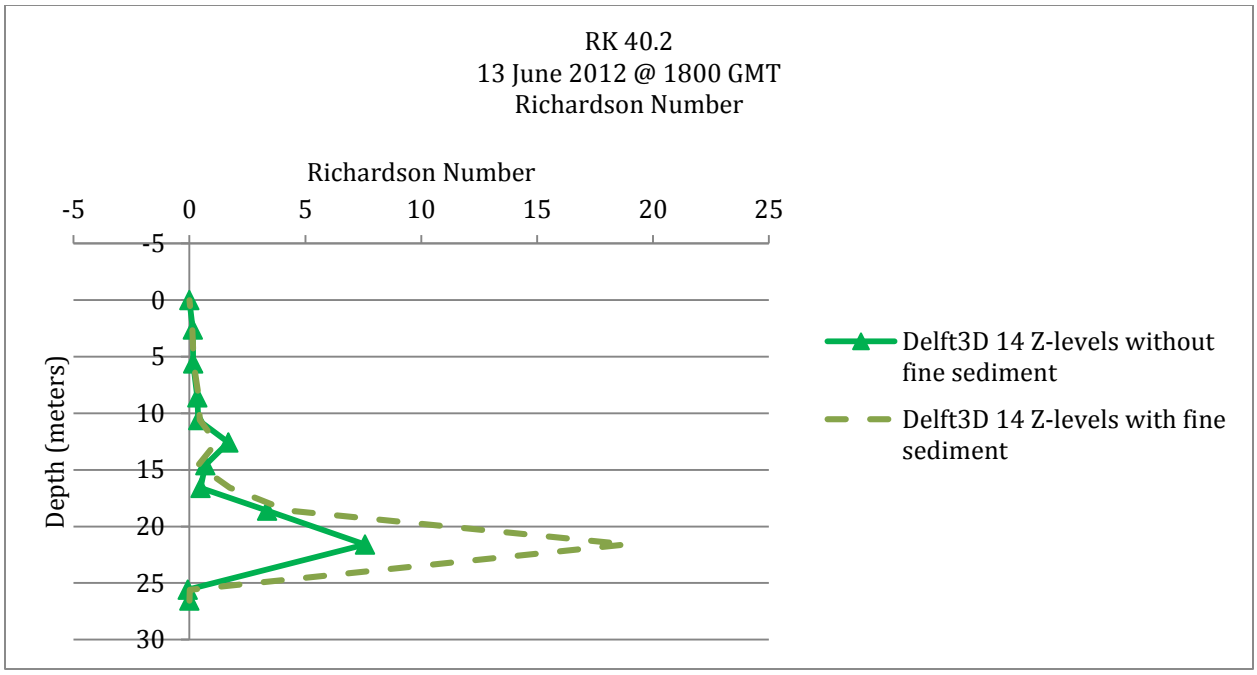

Figure 9-34 Sediment contribution to the Richardson number

9.5 Model reproduction of the turbidity maxima

The model has the capability to simulate the turbidity maxima in the Mississippi River resulting from the re-circulation of fine sediments in the leading salt mass of the salinity wedge. This is accomplished by simulating the effects of flocculation through the cosine function relating salinity concentration to particle settling velocity as explained in section 5.8.2. The results of this cosine function on the clay constituent settling velocity is shown in Figure 9-35. Figure 9-36 through Figure 9-48 show the weekly progression of the salinity wedge and corresponding turbidity maxima (using the clay concentration as an indicator) from 29 April 2012 to 22 July 2012. All of the profile plots were developed using the grid line in the middle of the Mississippi River channel and extend from Belle Chasse, LA (RK 120) to Head of Passes near Pilottown, LA (RK 0).

The salinity and sediment concentration of the arrested wedge on 30 September 2012 are shown in Figure 9-49. The barrier sill located at the tip of the wedge prevented further upstream progression of the wedge in September. The elevated sediment concentration in the Mississippi River channel due to re-circulation in the turbidity maxima

may be compared to the much lower sediment concentration in Southwest Pass shown in Figure 9-50 at the corresponding time.

These plots indicate that the deposition of sediment in the Mississippi River during drought conditions predominantly occurs in the area at the tip of the advancing salt wedge. This behavior at the tip of the salt wedge is consistent with observations made at other locations in the literature (see Postma, 1967 for example). Particularly evident in Figure 9-38 is the sediment capture and re-circulation at the tip of the wedge in the turbidity maxima with much lower concentrations at the downstream edge of the plot at Head of Passes compared to the well mixed clay entering from the upstream boundary at the left end of the plot.

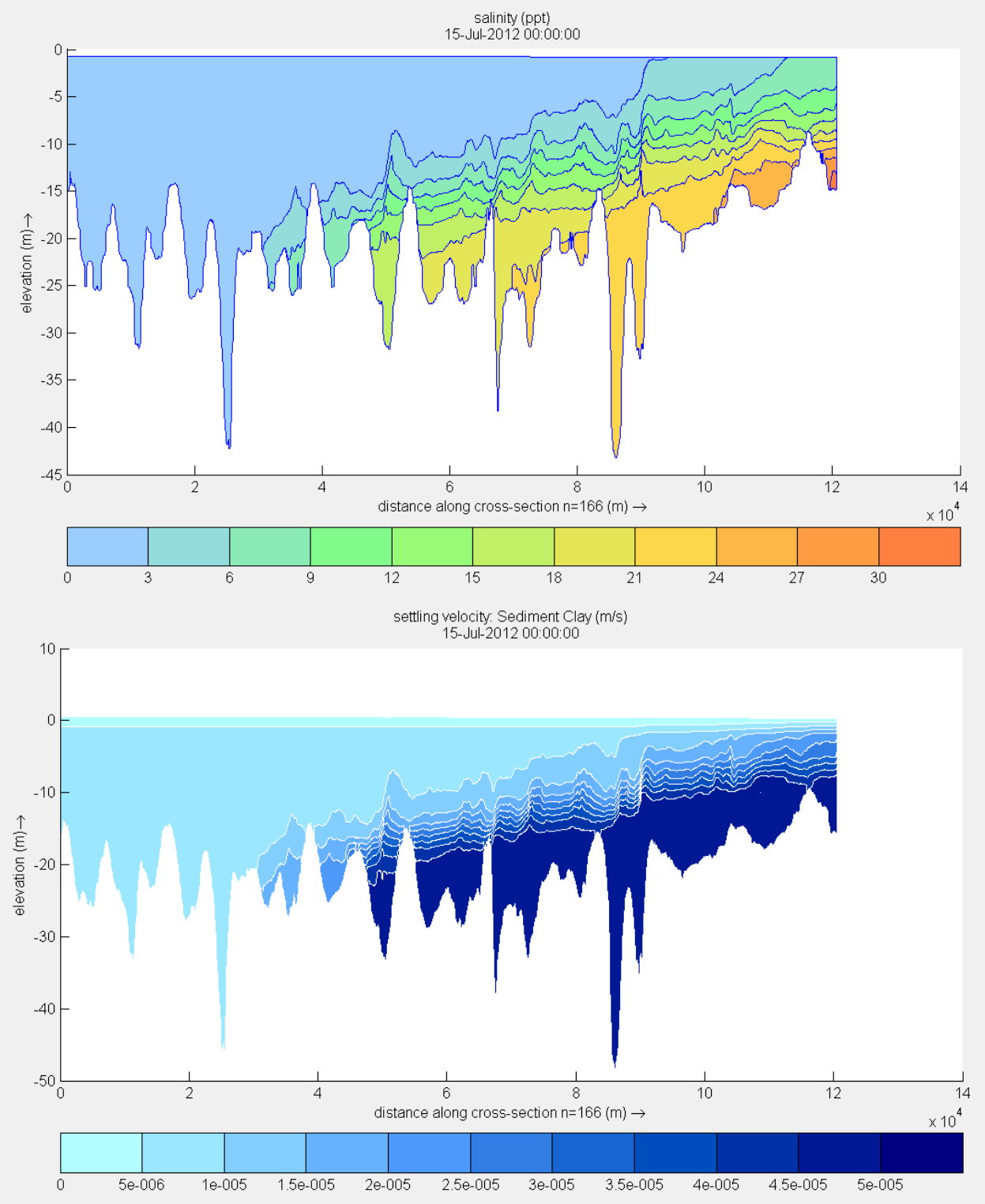

Figure 9-35 Mississippi River profile of Delft3D salinity (ppt) and settling velocity of clay (m/s) on 15 July 2012 (the left end of the plot is located at the upstream boundary at Belle Chasse and the right end of the plot is located at Head of Passes near Pilottown)

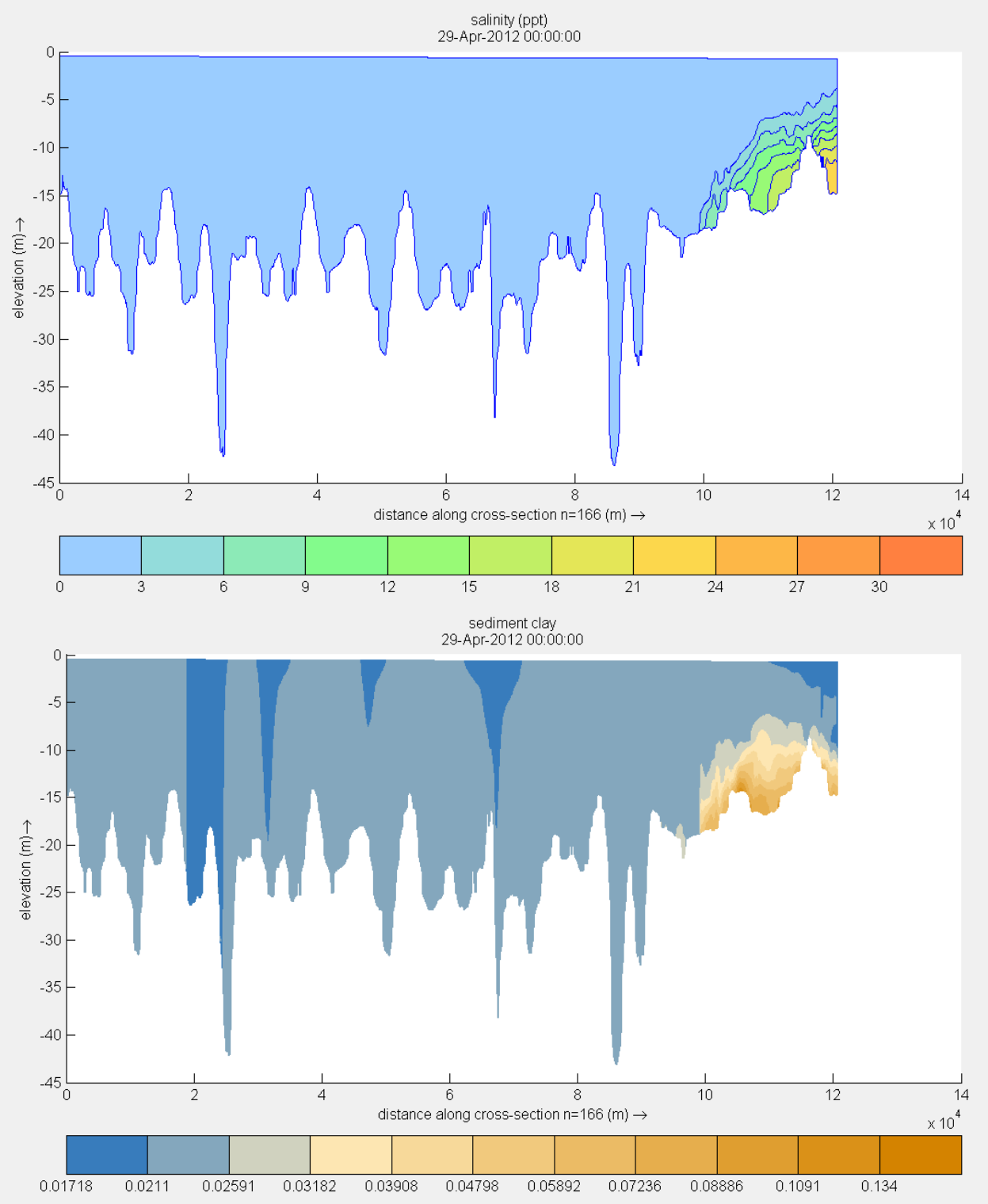

Figure 9-36 Mississippi River profile of Delft3D salinity (ppt) and clay concentration (kg/m^3) on 29 April 2012 (the left end of the plot is located at the upstream boundary at Belle Chasse and the right end of the plot is located at Head of Passes near Pilottown)

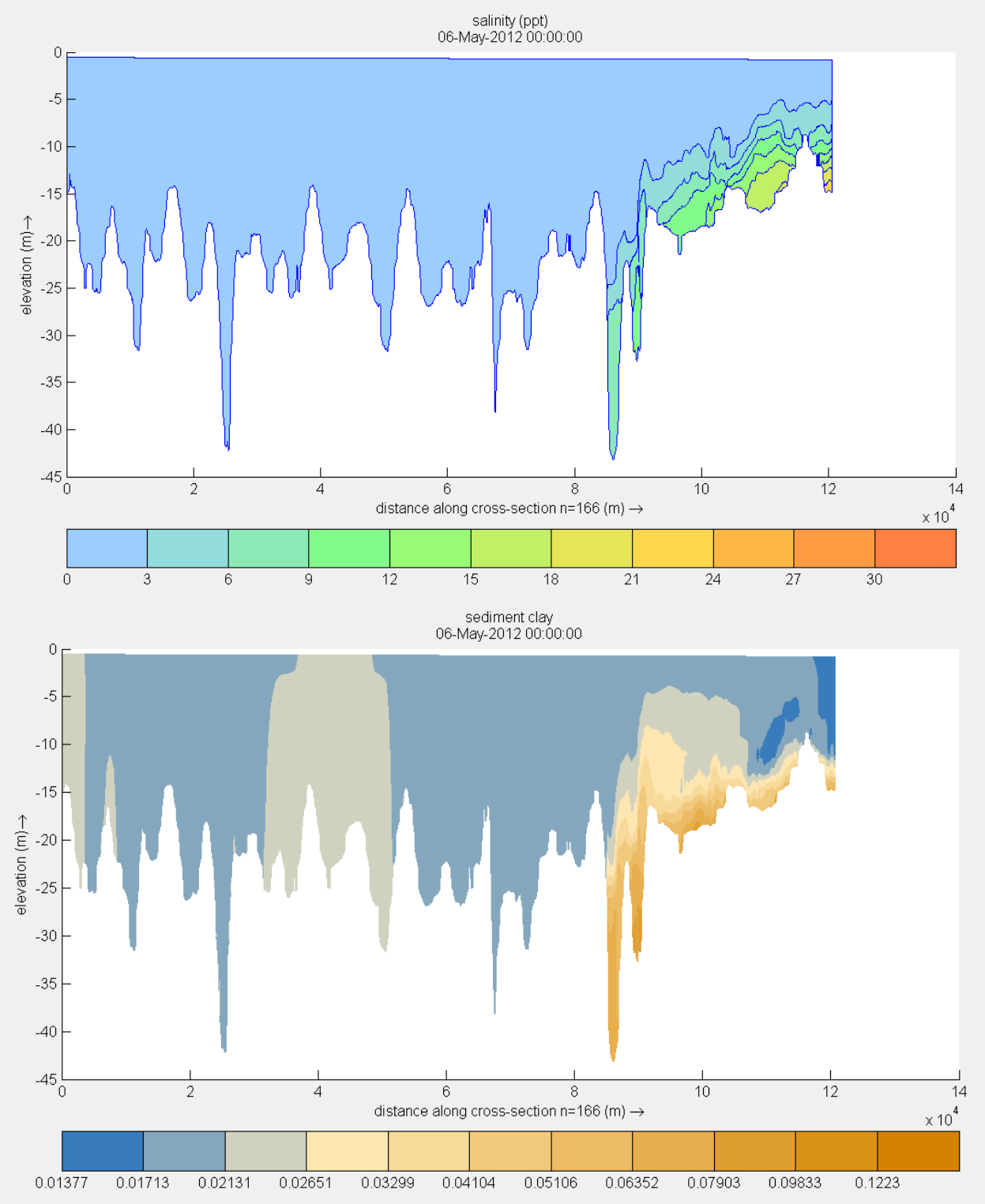

Figure 9-37 Mississippi River profile of Delft3D salinity (ppt) and clay concentration (kg/m^3) on 6 May 2012 (the left end of the plot is located at the upstream boundary at Belle Chasse and the right end of the plot is located at Head of Passes near Pilottown)

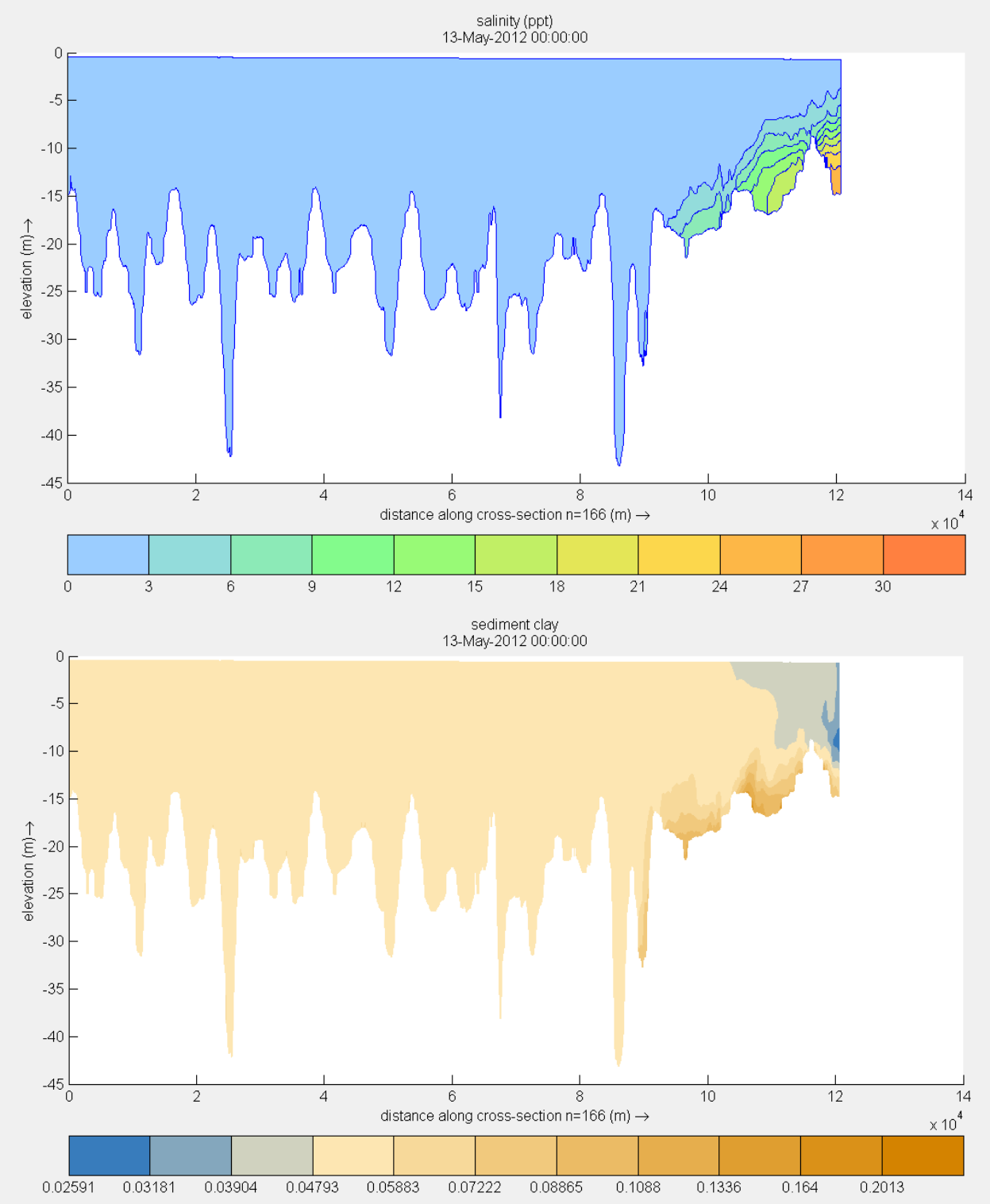

Figure 9-38 Mississippi River profile of Delft3D salinity (ppt) and clay concentration (kg/m³) on 13 May 2012 (the left end of the plot is located at the upstream boundary at Belle Chasse and the right end of the plot is located at Head of Passes near Pilottown)

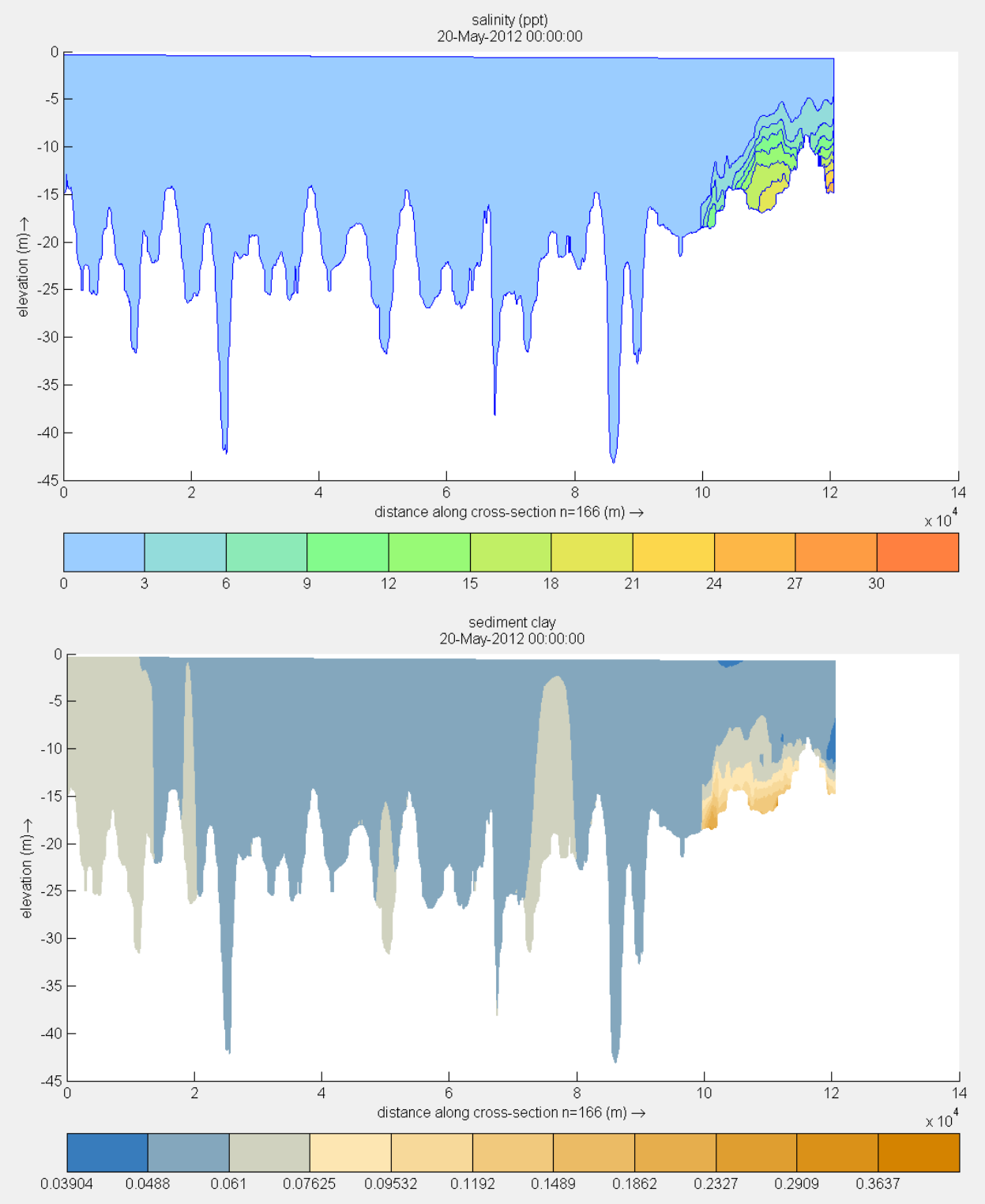

Figure 9-39 Mississippi River profile of Delft3D salinity (ppt) and clay concentration (kg/m³) on 20 May 2012 (the left end of the plot is located at the upstream boundary at Belle Chasse and the right end of the plot is located at Head of Passes near Pilottown)

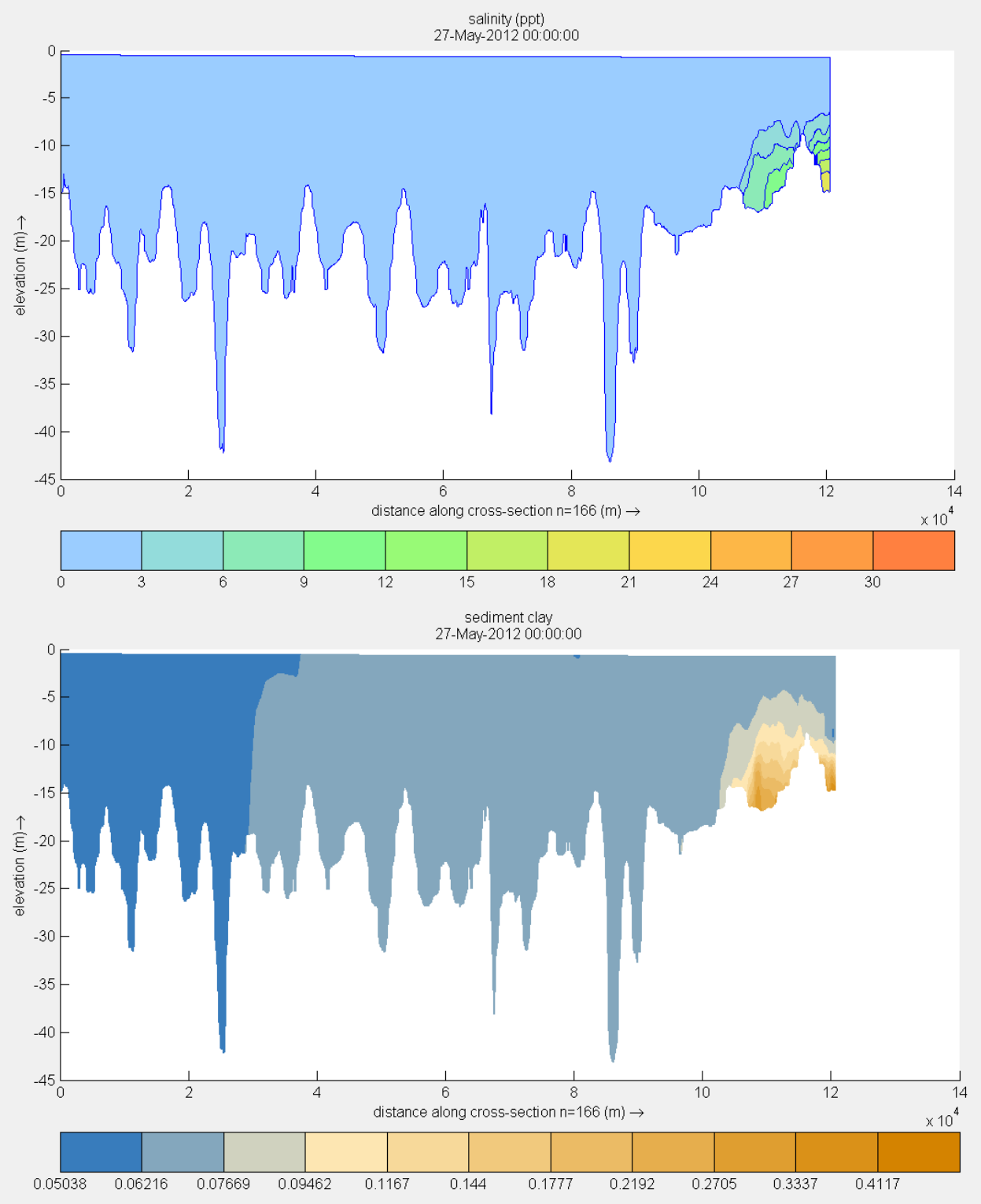

Figure 9-40 Mississippi River profile of Delft3D salinity (ppt) and clay concentration (kg/m^3) on 27 May 2012 (the left end of the plot is located at the upstream boundary at Belle Chasse and the right end of the plot is located at Head of Passes near Pilottown)

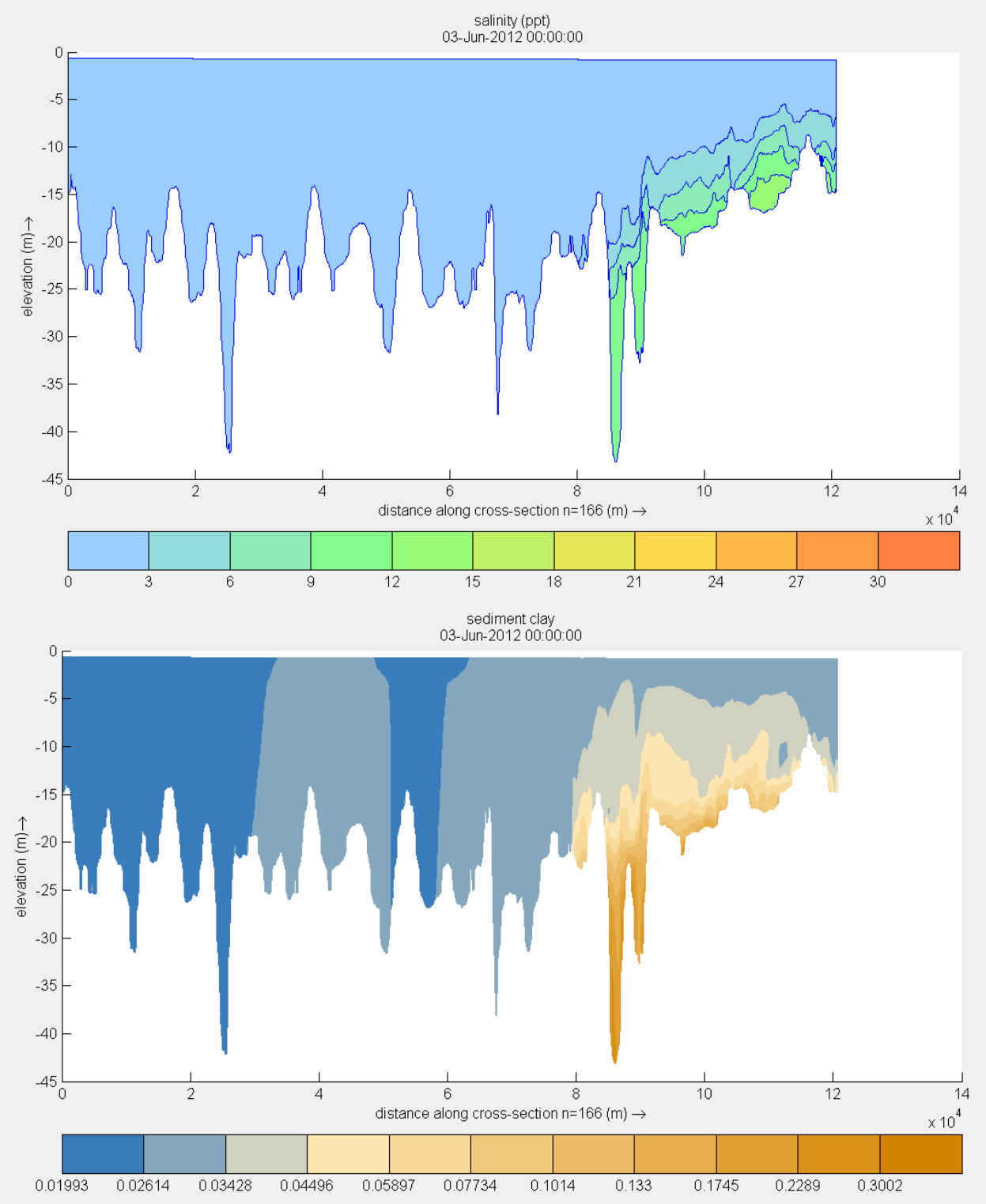

Figure 9-41 Mississippi River profile of Delft3D salinity (ppt) and clay concentration (kg/m³) on 3 June 2012 (the left end of the plot is located at the upstream boundary at Belle Chasse and the right end of the plot is located at Head of Passes near Pilottown)

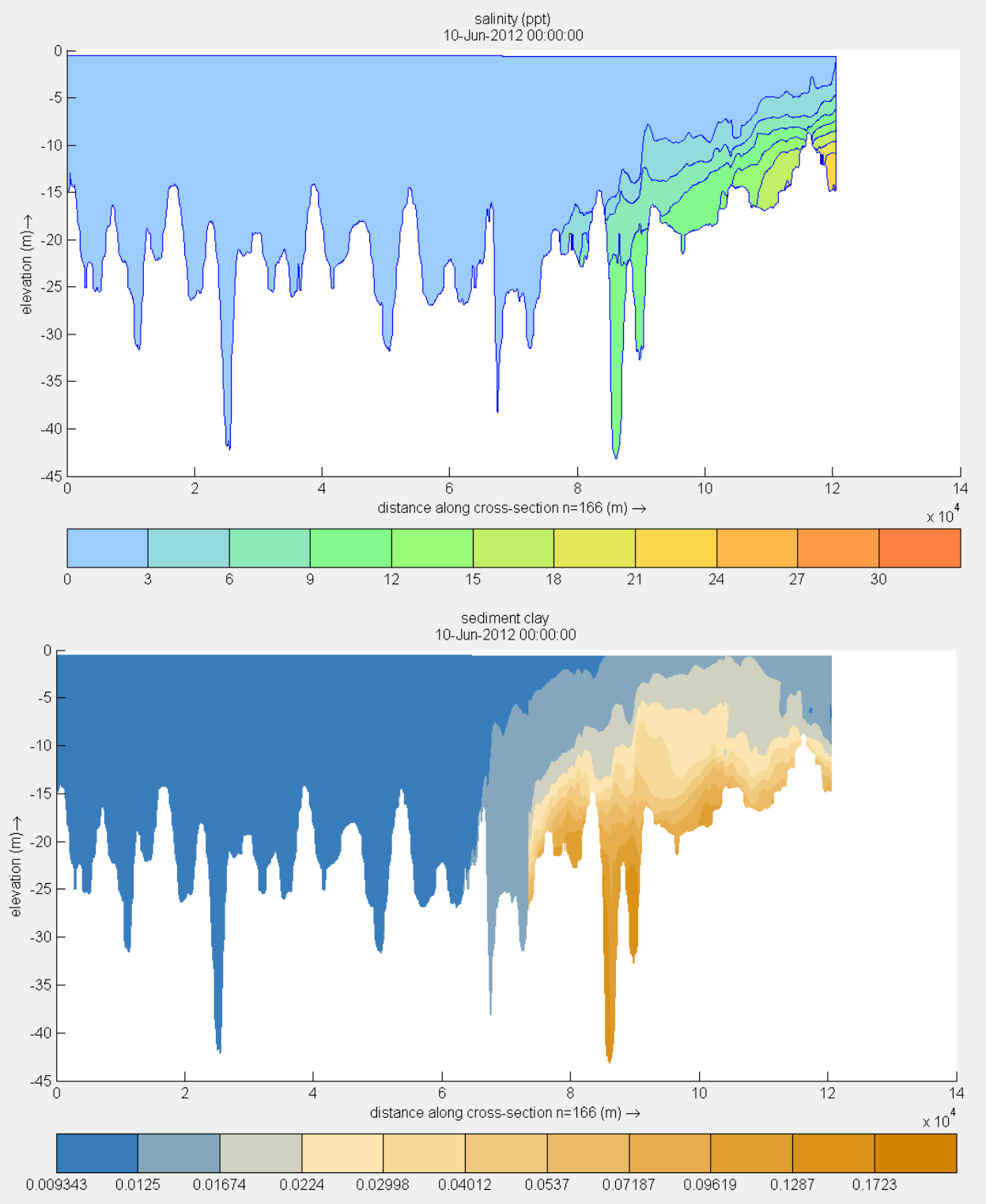

Figure 9-42 Mississippi River profile of Delft3D salinity (ppt) and clay concentration (kg/m³) on 10 June 2012 (the left end of the plot is located at the upstream boundary at Belle Chasse and the right end of the plot is located at Head of Passes near Pilottown)

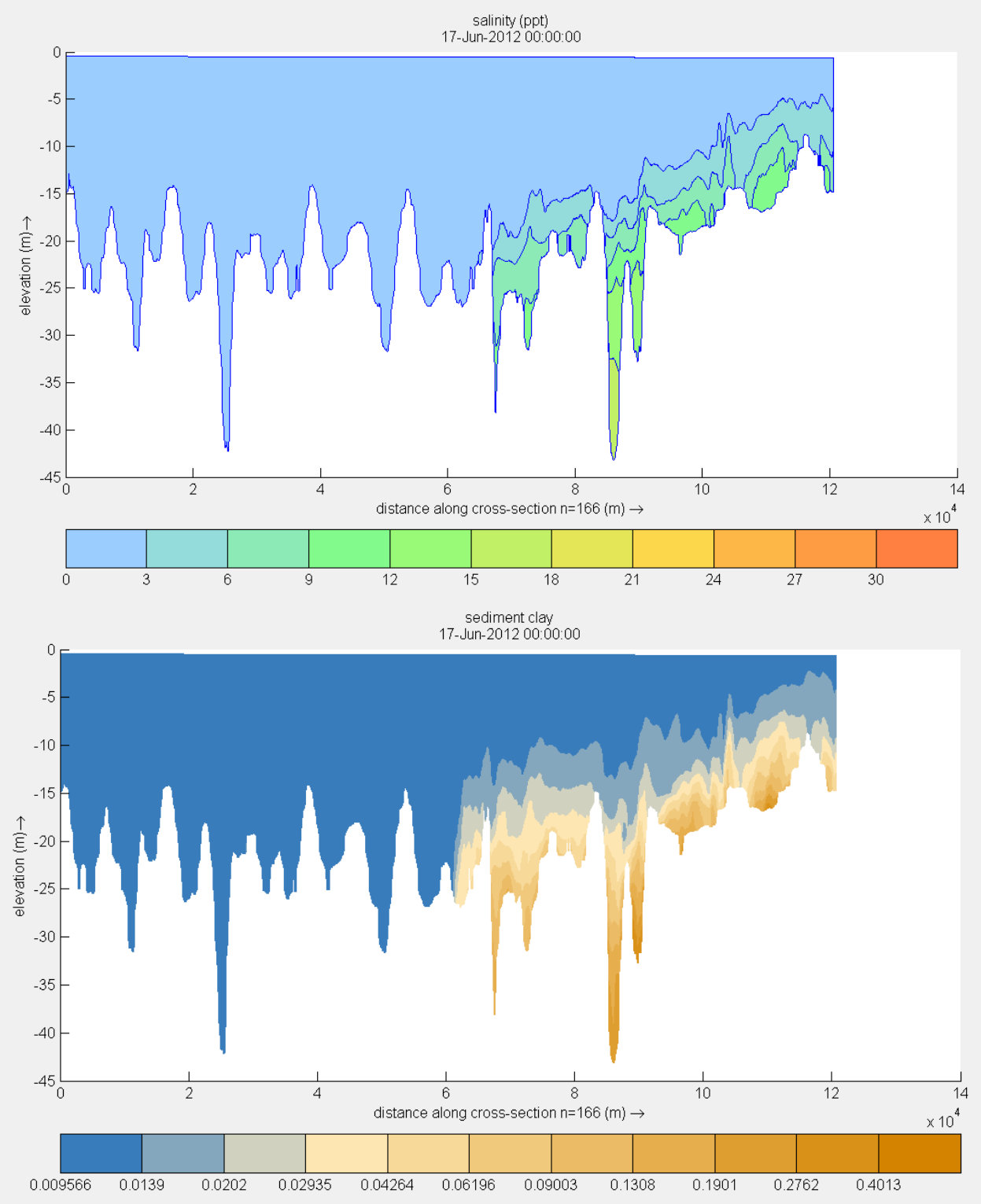

Figure 9-43 Mississippi River profile of Delft3D salinity (ppt) and clay concentration (kg/m^3) on 17 June 2012 (the left end of the plot is located at the upstream boundary at Belle Chasse and the right end of the plot is located at Head of Passes near Pilottown)

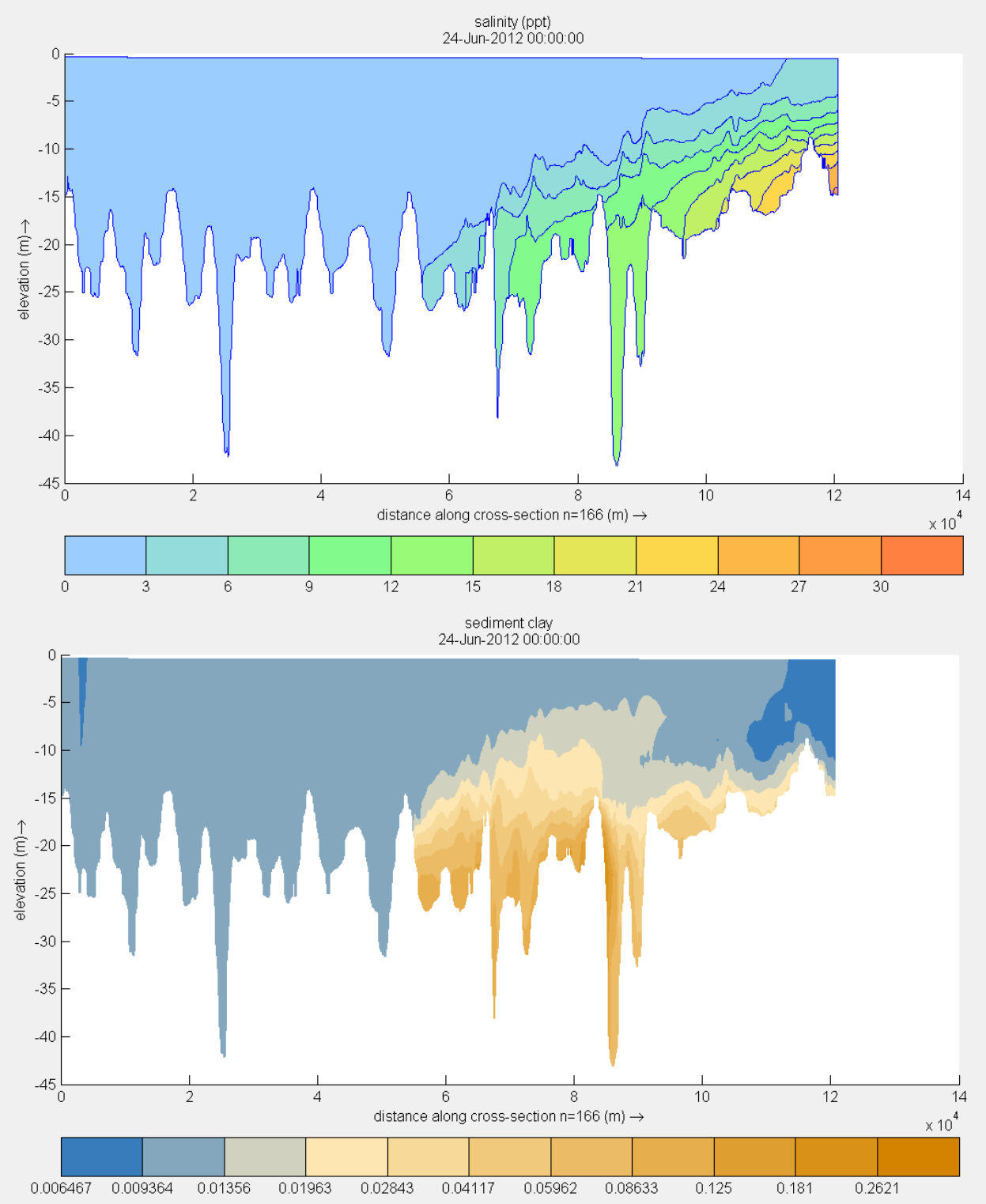

Figure 9-44 Mississippi River profile of Delft3D salinity (ppt) and clay concentration (kg/m^3) on 24 June 2012 (the left end of the plot is located at the upstream boundary at Belle Chasse and the right end of the plot is located at Head of Passes near Pilottown)

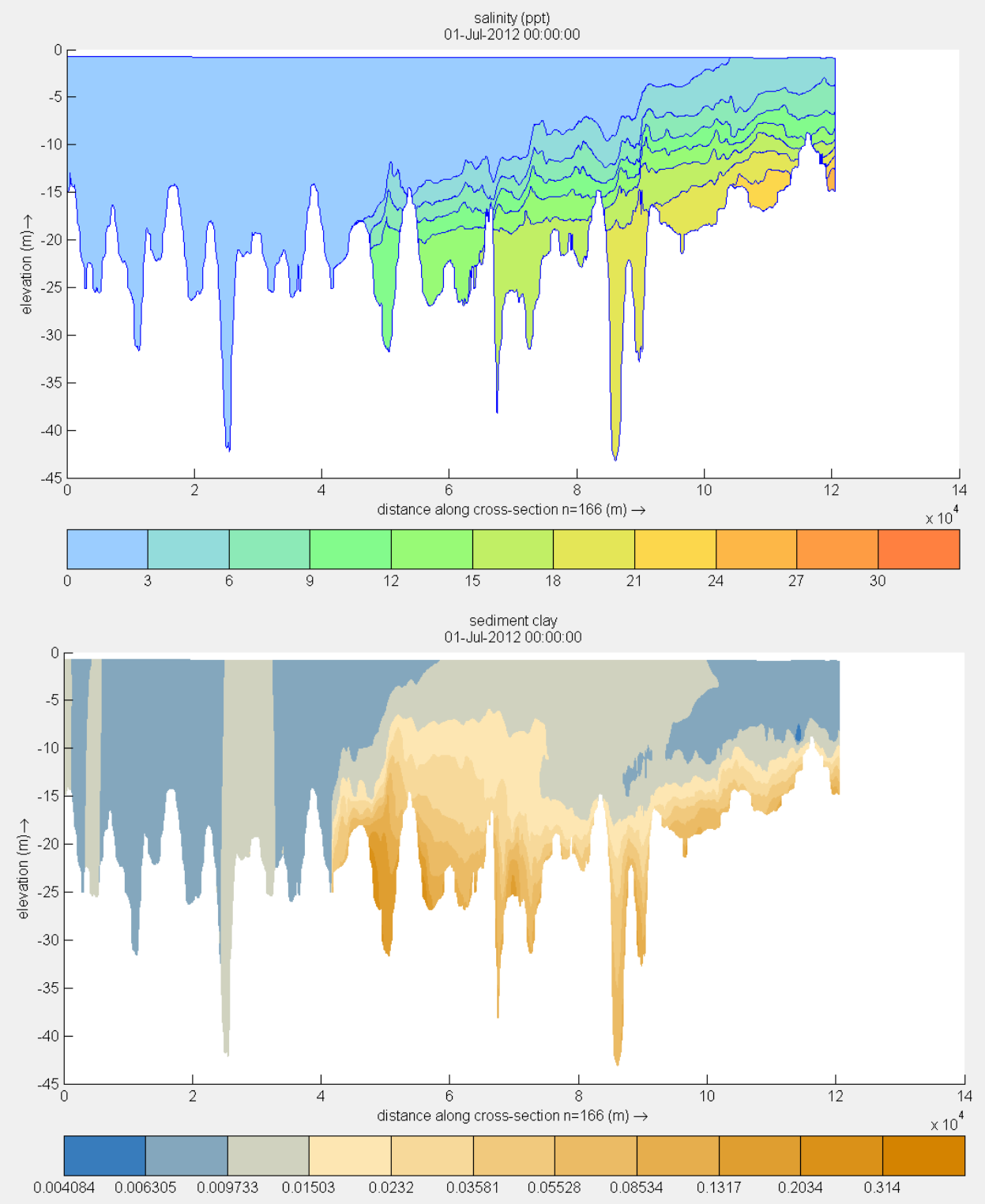

Figure 9-45 Mississippi River profile of Delft3D salinity (ppt) and clay concentration (kg/m³) on 1 July 2012 (the left end of the plot is located at the upstream boundary at Belle Chasse and the right end of the plot is located at Head of Passes near Pilottown)

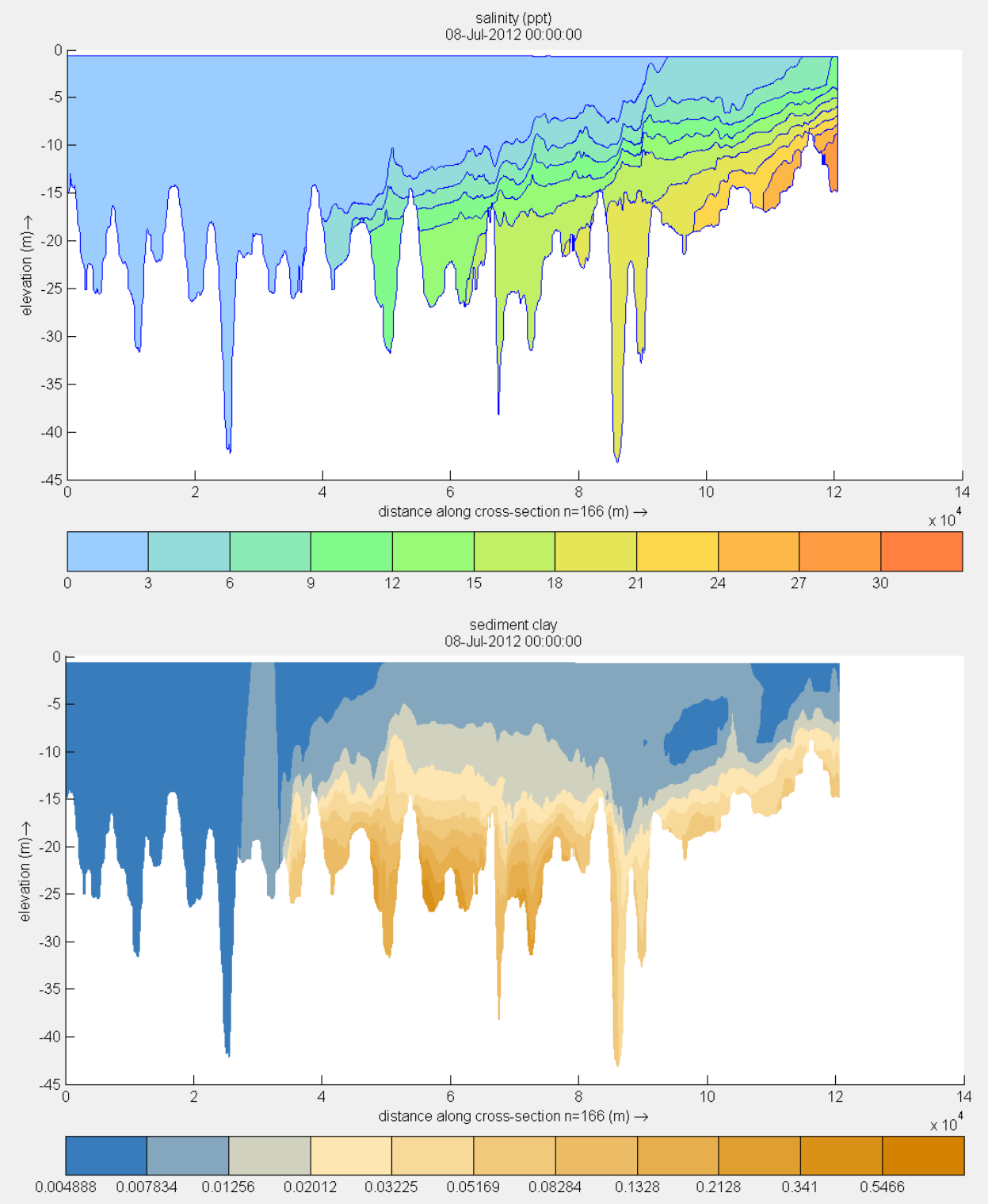

Figure 9-46 Mississippi River profile of Delft3D salinity (ppt) and clay concentration (kg/m^3) on 8 July 2012 (the left end of the plot is located at the upstream boundary at Belle Chasse and the right end of the plot is located at Head of Passes near Pilottown)

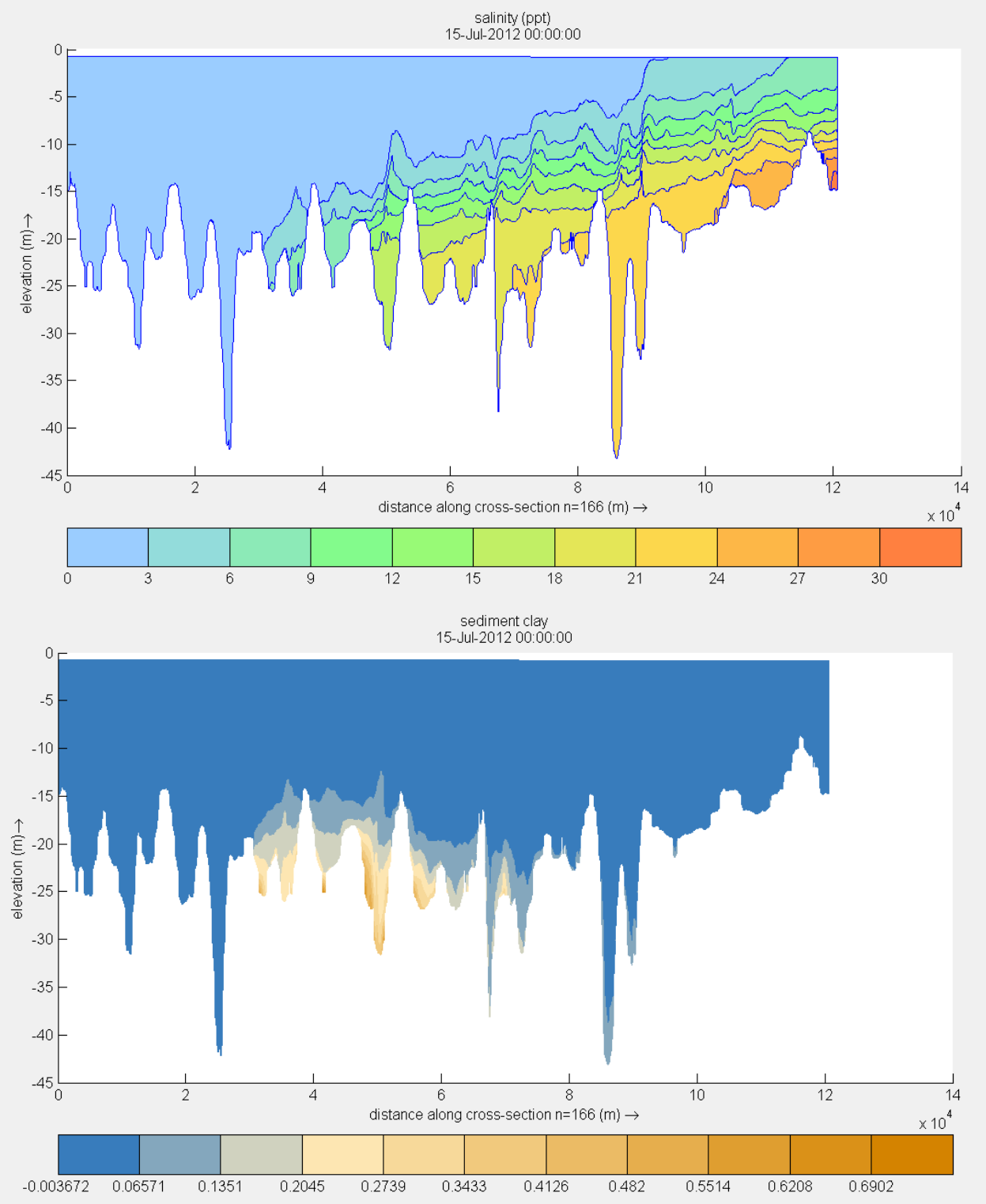

Figure 9-47 Mississippi River profile of Delft3D salinity (ppt) and clay concentration (kg/m³) on 15 July 2012 (the left end of the plot is located at the upstream boundary at Belle Chasse and the right end of the plot is located at Head of Passes near Pilottown)

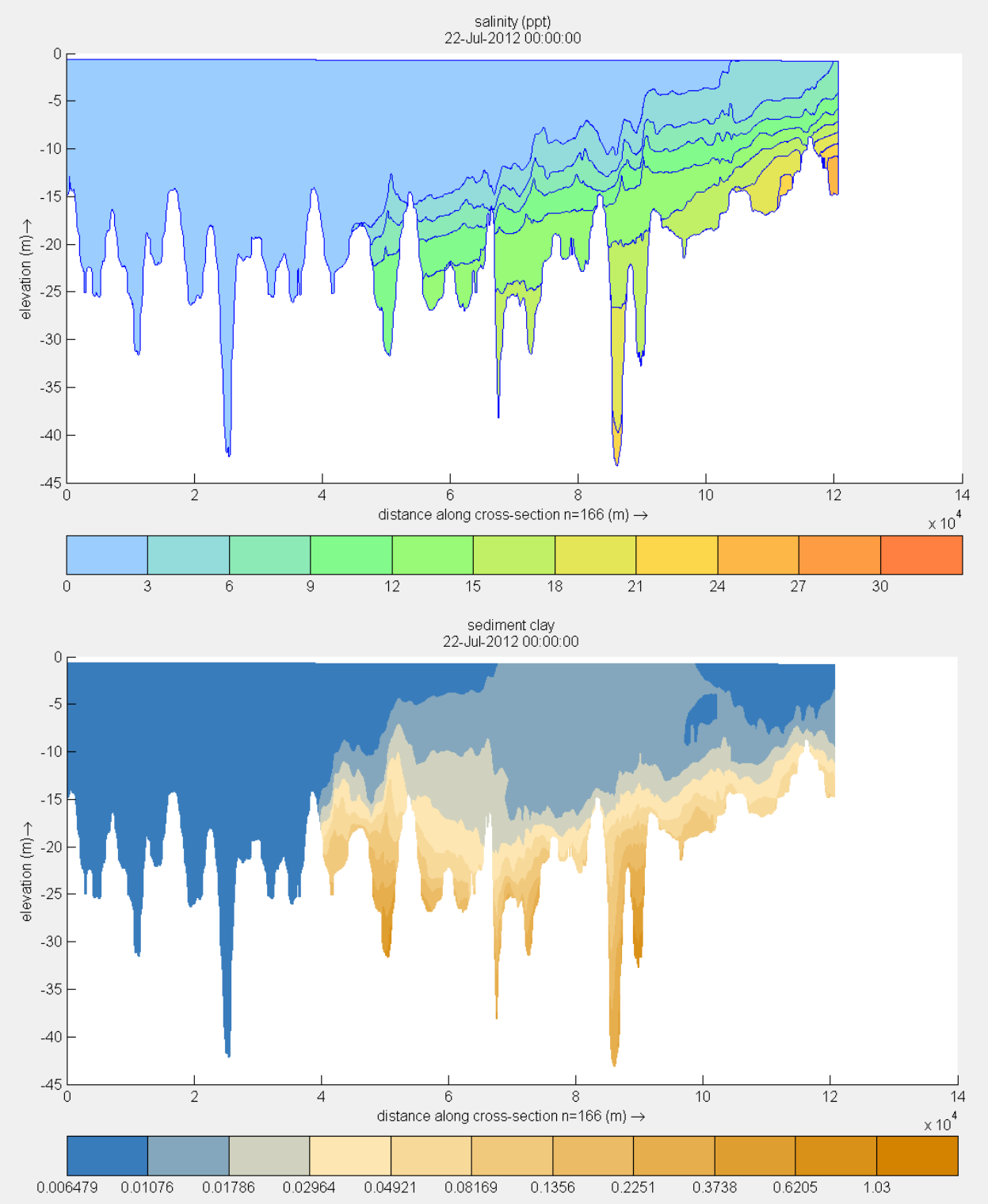

Figure 9-48 Mississippi River profile of Delft3D salinity (ppt) and logarithmic clay concentration (kg/m³) on 22 July 2012 (the left end of the plot is located at the upstream boundary at Belle Chasse and the right end of the plot is located at Head of Passes near Pilottown)

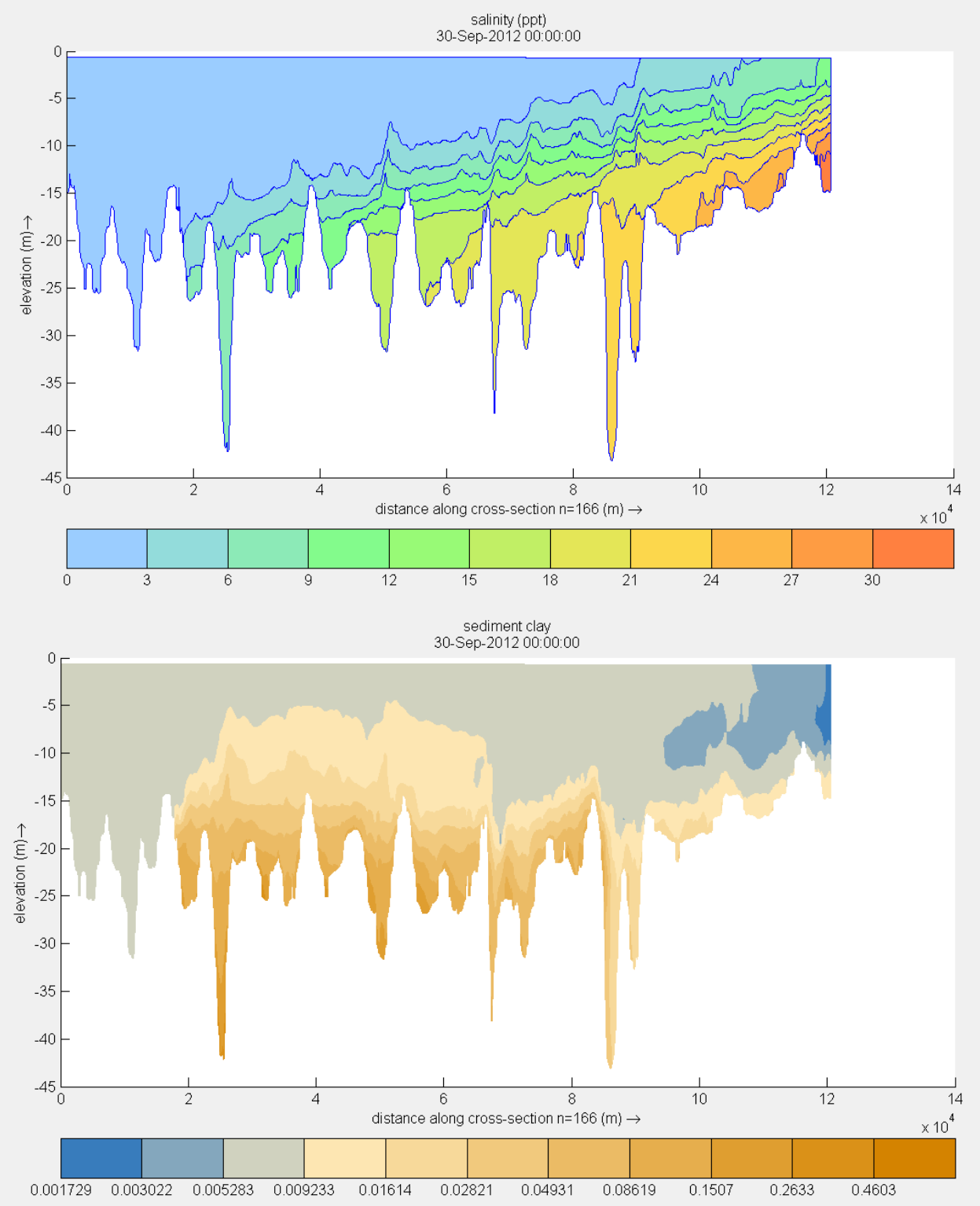

Figure 9-49 Mississippi River profile of Delft3D salinity (ppt) and logarithmic clay concentration (kg/m^3) on 30 September 2012 (the left end of the plot is located at the upstream boundary at Belle Chasse and the right end of the plot is located at Head of Passes near Pilottown)

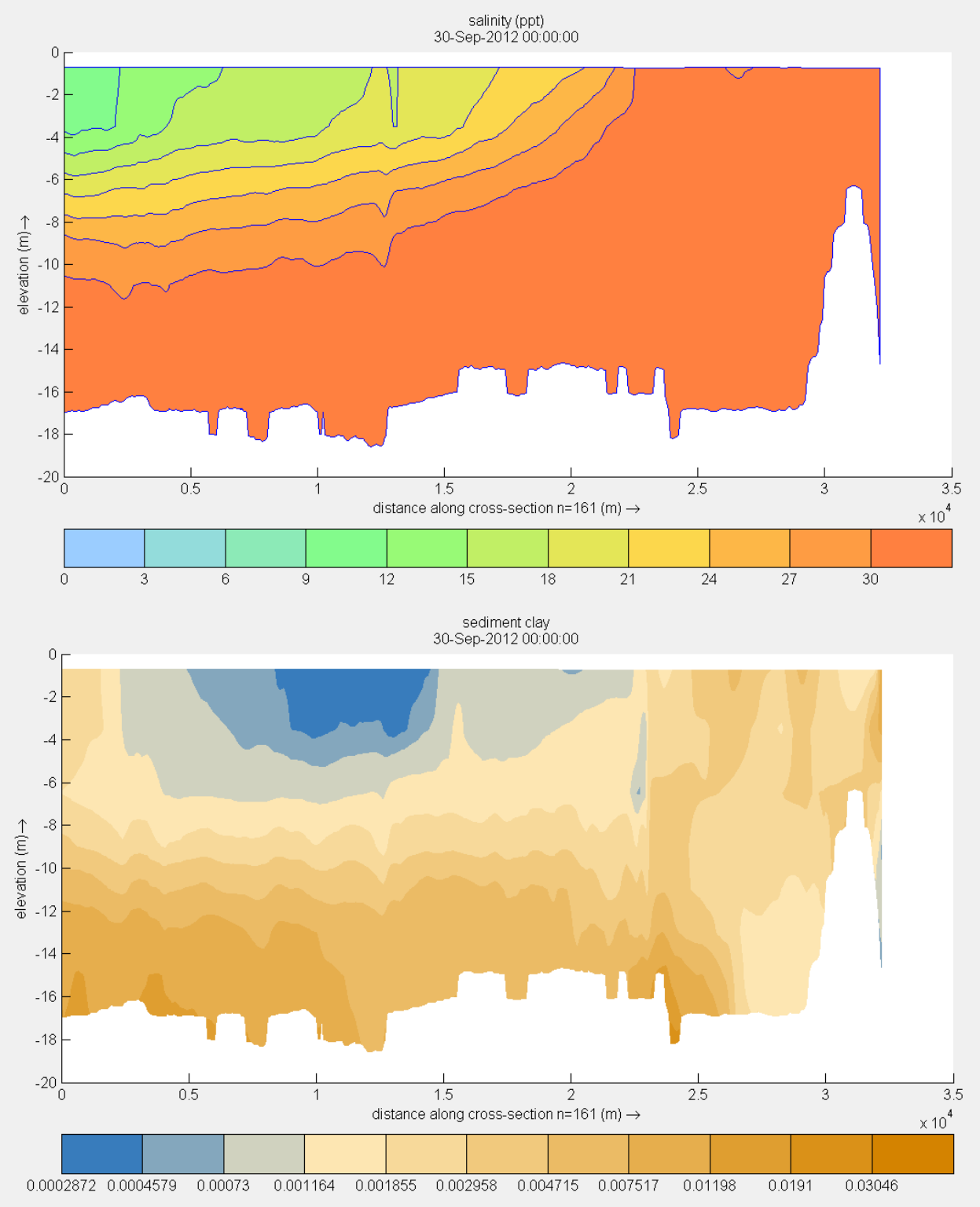

Figure 9-50 Southwest Pass profile of Delft3D salinity (ppt) and logarithmic clay concentration (kg/m^3) on 30 September 2012 (the left end of the plot is located at Head of Passes and the right end of the plot is located at the Gulf outlet)

9.6 Delft3D suspended sediment transport analysis

The sediment transport characteristics of the river and its passes for both the clay and silt constituent classes is assessed by analyzing model results for the twelve week period from 29 April 2012 through 21 July 2012. This time period features a hydrograph peak in May leading into drought conditions that lasted until December 2012. Observation cross sections are located at Belle Chasse, Ostrica Lock, Venice, the Mississippi River at West Bay water level gage, Pilottown, and at the head of seven distributaries as shown in Figure 9-51. The Mississippi River at West Bay cross section encompasses the energy losses due to the diversion or water through the Baptiste Collette Bayou and Grand Pass distributaries. The Pilottown cross section encompasses the further energy loss due to the West Bay Crevasse and Cubit's Gap. The Southwest Pass cross section location encompasses the energy loss due to the South Pass and Pass a Loutre distributaries.

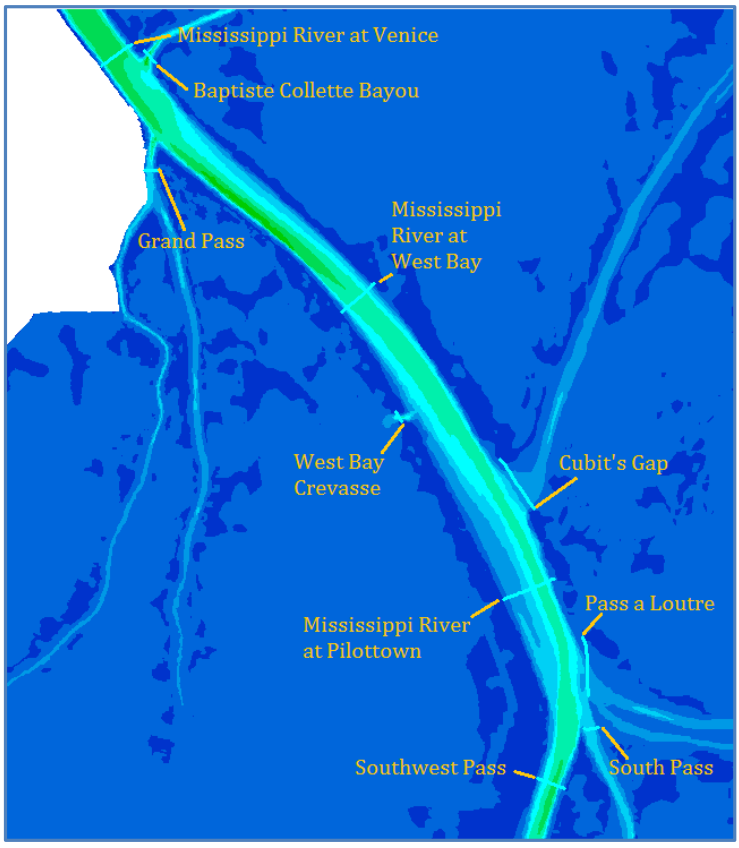

Figure 9-51 Delft3D observation cross section locations

The cumulative mass sediment load due to advective currents is plotted for the river locations and seven distributaries in the delta as shown in Figure 9-52, Figure 9-53, Figure 9-54, and Figure 9-55. According to the model results, the river does not have sufficient energy at these low flows to transport silt past Cubit's Gap and into Southwest Pass. Of the major delta distributaries, Baptiste Collette Bayou and to a lesser degree Grand Pass transport the highest load of silt to the marshes during drought conditions. The declining cumulative mass transport of clay seen in July at the Southwest Pass, Pilottown, and Mississippi River at West Bay cross sections is attributed to the transport of clay in the density current traveling upstream beneath the overlying fresh water current.

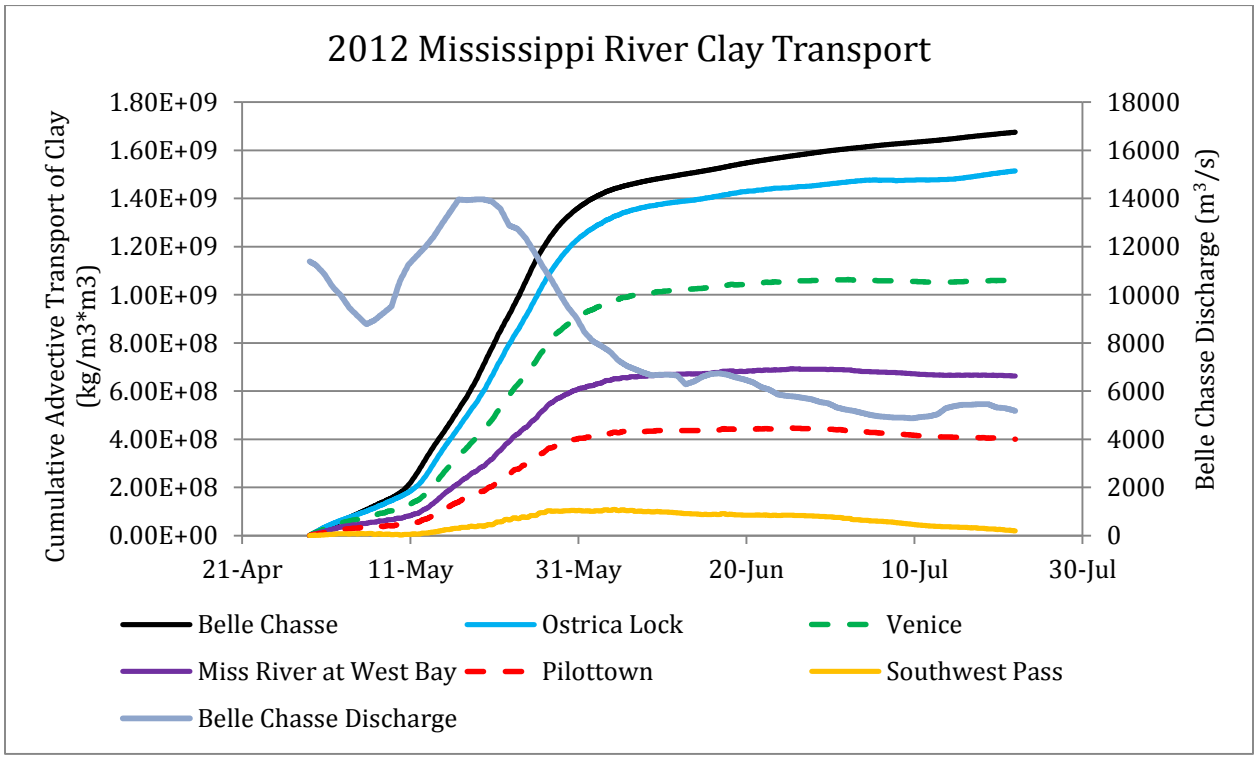

Figure 9-52 Cumulative clay transport in the Mississippi River channel from 29 April 2012 through 21 July 2012

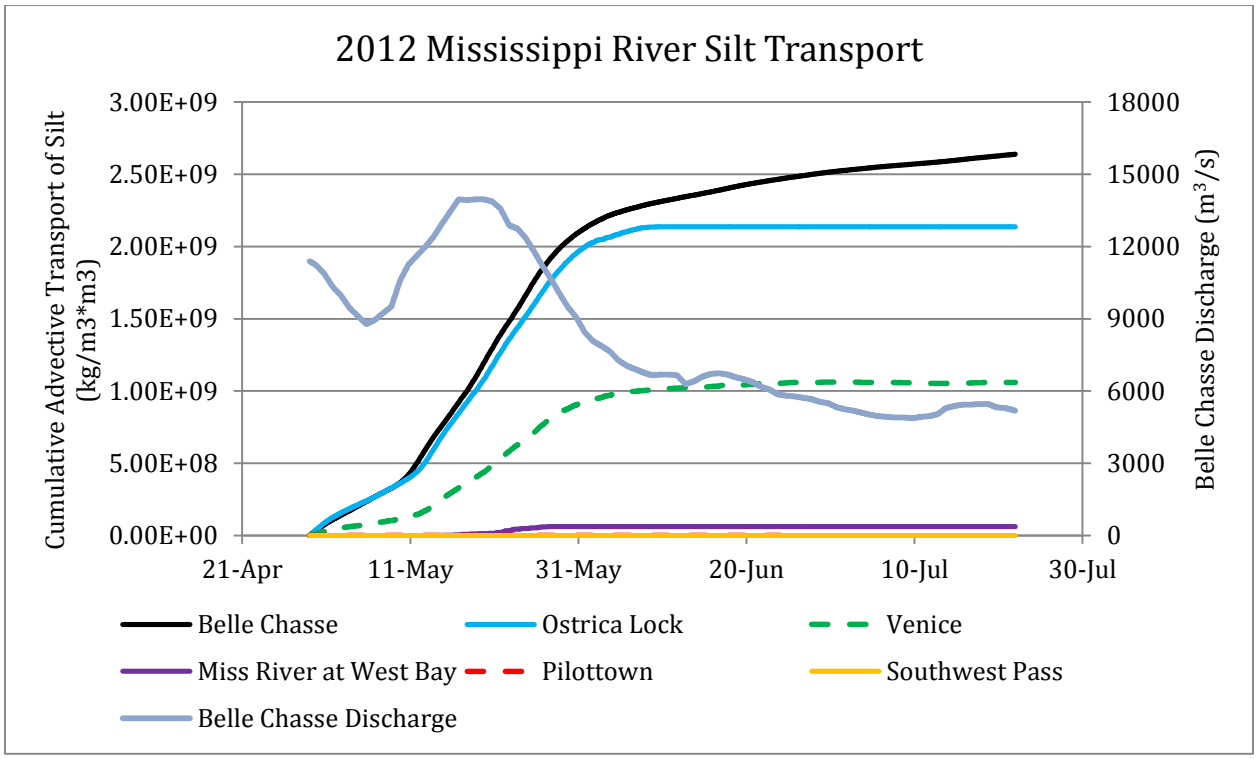

Figure 9-53 Cumulative silt transport in the Mississippi River channel from 29 April 2012 through 21 July 2012

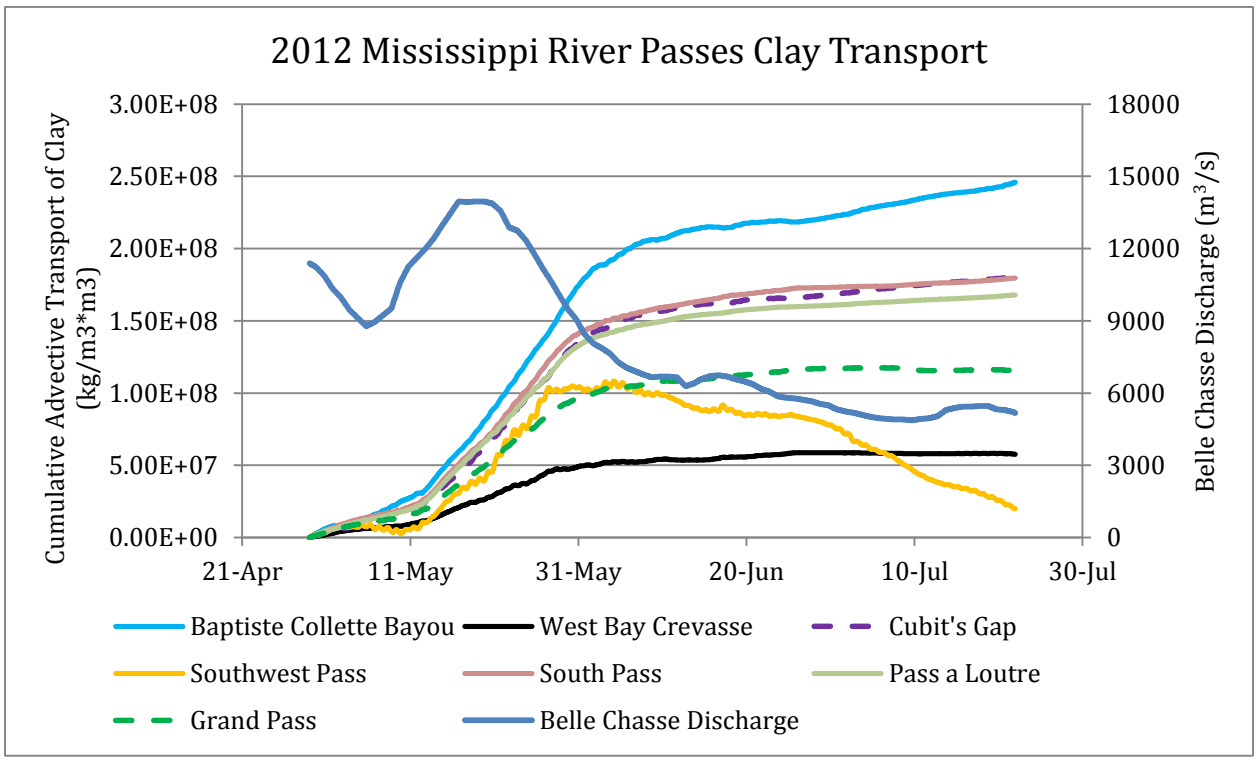

Figure 9-54 Cumulative clay transport in the Mississippi River passes from 29 April 2012 through 21 July 2012

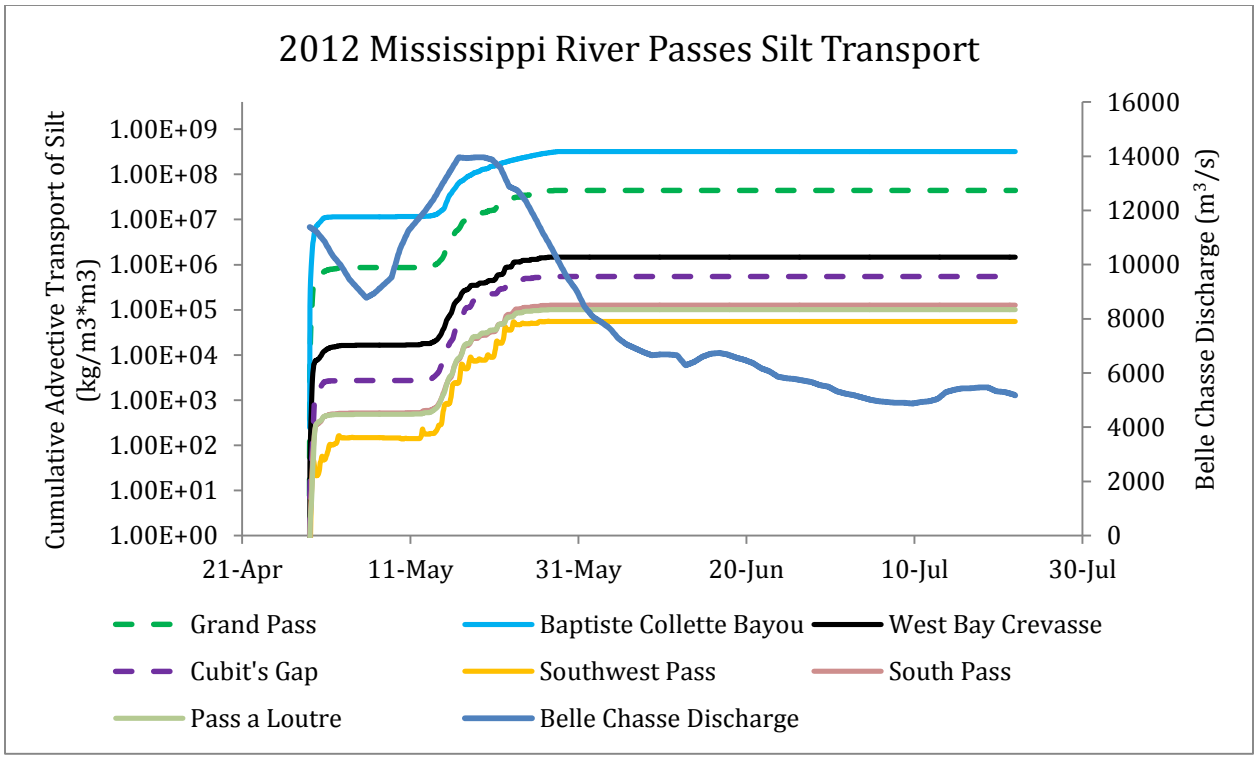

Figure 9-55 Cumulative clay transport in the Mississippi River passes from 29 April 2012 through 21 July 2012 (note logarithmic y-axis used for visualization of relatively small values)

The impact of the salinity wedge on the transport of fine sediment in the delta can be evaluated through a summary of weekly water volume and sediment constituent mass fluxes as summarized in Table 9-2, Table 9-3, and Table 9-4. In these tables, a number in parentheses indicates a flux in the opposite direction of the assumed positive direction which is seaward for the river cross sections and out of the river channel for the distributary cross sections. Corresponding bar charts are displayed for the Mississippi River cross sections in Figure 9-56, Figure 9-57, and Figure 9-58.

The density current conveys clay upstream towards the front of the advancing salt mass as evidenced in Table 9-3 showing a net flux of clay out of Southwest Pass and into the lower Mississippi River channel for the weeks of 9 June 2012 - 21 July 2012. This upstream flux of sediment conveyed in the turbidity current combined with the well mixed load of clay conveyed downstream by the fresh river water converge in the salt wedge resulting in a zone of mud deposition. This zone of elevated sediment deposition may

contribute to seasonal sediment deposition occurring at sensitive areas such as the Pilottown anchorage area.

Table 9-2 Weekly Delft3D water volume flux in cubic hectometers (hm^3)

2012 Week ending	Miss. River at Venice	Miss. River at West Bay	Miss. River at Pilottown	Southwest Pass	Baptiste Collette Bayou	Grand Pass	West Bay Crevasse	Cubit's Gap	South Pass	Pass a Loutre
	hm^3	hm^3	hm^3	hm^3	hm^3	hm^3	hm^3	hm^3	hm^3	hm^3
5 May	4,310	3,193	2,282	774	518	482	318	505	751	665
12 May	3,946	2,789	1,802	443	646	346	211	658	585	606
19 May	5,521	3,939	2,720	835	846	562	302	780	857	880
26 May	5,443	3,888	2,806	1,129	894	529	266	720	831	724
2 June	3,817	2,580	1,679	284	782	360	152	679	631	634
9 June	2,696	1,856	1,173	216	537	215	114	508	421	409
16 June	2,733	2,029	1,508	437	384	249	101	371	553	457
23 June	1,983	1,397	843	45	253	205	165	309	393	352
30 June	1,551	889	254	(332)	310	226	120	428	263	251
7 July	1,233	444	(206)	(849)	675	21	(56)	652	128	345
14 July	1,440	706	45	(737)	618	33	11	596	278	350
21 July	1,760	1,171	690	(111)	528	(10)	(40)	479	356	354

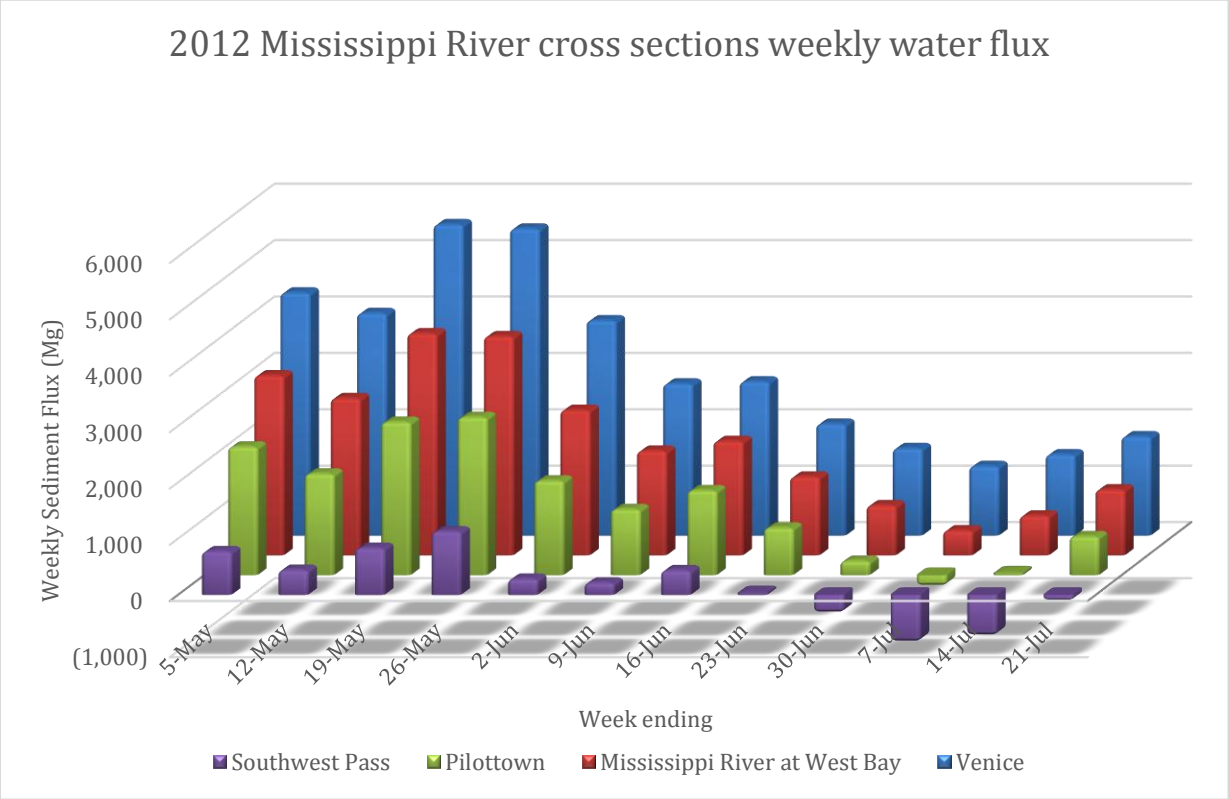

Figure 9-56 Mississippi River weekly Delft3D water volume flux in cubic hectometers (hm^3)

Table 9-3 Weekly Delft3D clay flux in metric tons (Mg)

2012 Week ending	Miss. River at Venice	Miss. River at West Bay	Miss. River at Pilottown	Southwest Pass	Baptiste Collette Bayou	Grand Pass	West Bay Crevasse	Cubit's Gap	South Pass	Pass a Loutre
	Mg	Mg	Mg	Mg	Mg	Mg	Mg	Mg	Mg	Mg
5 May	78,312	52,859	36,011	8,280	13,984	10,422	6,344	9,854	14,076	12,245
12 May	99,650	61,547	34,559	2,187	20,259	9,691	5,273	15,507	13,628	13,768
19 May	270,404	182,448	120,523	31,268	47,484	30,000	15,319	38,741	40,560	40,884
26 May	330,009	229,369	157,155	54,735	56,355	32,970	17,131	45,438	50,122	42,855
2 June	182,480	112,945	73,399	9,299	50,537	19,440	7,637	34,878	30,799	30,645
9 June	52,838	28,590	14,009	(7,435)	18,471	5,604	2,452	12,506	9,944	9,226
16 June	24,253	12,831	5,578	(7,990)	7,412	3,544	1,148	4,802	7,008	5,632
23 June	15,686	7,607	2,510	(6,567)	4,859	3,055	2,162	3,987	4,901	4,182
30 June	8,930	1,479	(3,748)	(8,231)	3,424	2,457	1,240	3,030	2,320	1,553
7 July	(4,213)	(13,181)	(17,668)	(22,245)	8,552	30	(523)	4,469	989	2,395
14 July	(4,122)	(10,177)	(13,556)	(18,029)	7,160	(1,442)	(47)	3,732	2,220	1,998
21 July	4,555	(3,607)	(8,360)	(15,371)	7,305	(770)	(433)	3,948	3,113	2,584

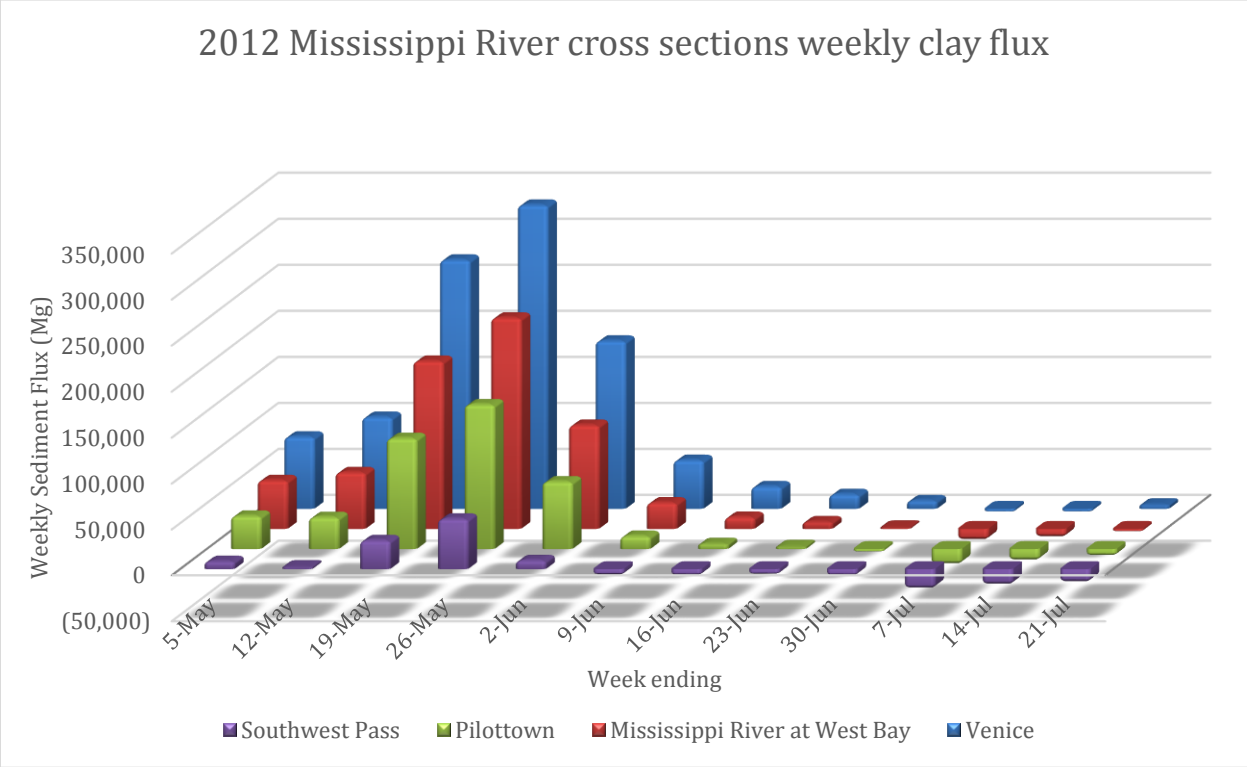

Figure 9-57 Mississippi River weekly Delft3D clay flux in metric tons (Mg)

Table 9-4 Weekly Delft3D silt flux in metric tons (Mg)

2012 Week ending	Miss. River at Venice	Miss. River at West Bay	Miss. River at Pilottown	Southwest Pass	Baptiste Collette Bayou	Grand Pass	West Bay Crevasse	Cubit's Gap	South Pass	Pass a Loutre
	Mg	Mg	Mg	Mg	Mg	Mg	Mg	Mg	Mg	Mg
5 May	30,445	347	8	0	11,540	862	16	3	1	0
12 May	1,217	26	1	0	316	28	1	0	0	0
19 May	370,533	12,428	328	8	120,642	13,598	384	194	27	30
26 May	532,743	45,887	1,366	47	160,274	27,058	1,025	334	97	69
2 June	65,808	2,682	35	1	28,067	2,565	47	12	2	2
9 June	(20)	0	0	0	12	0	0	0	0	0
16 June	(38)	0	0	0	3	1	0	0	0	0
23 June	(129)	(3)	0	0	12	1	0	0	0	0
30 June	0	0	0	0	0	0	0	0	0	0
7 July	0	0	0	0	0	0	0	0	0	0
14 July	0	0	0	0	0	0	0	0	0	0
21 July	0	0	0	0	0	0	0	0	0	0

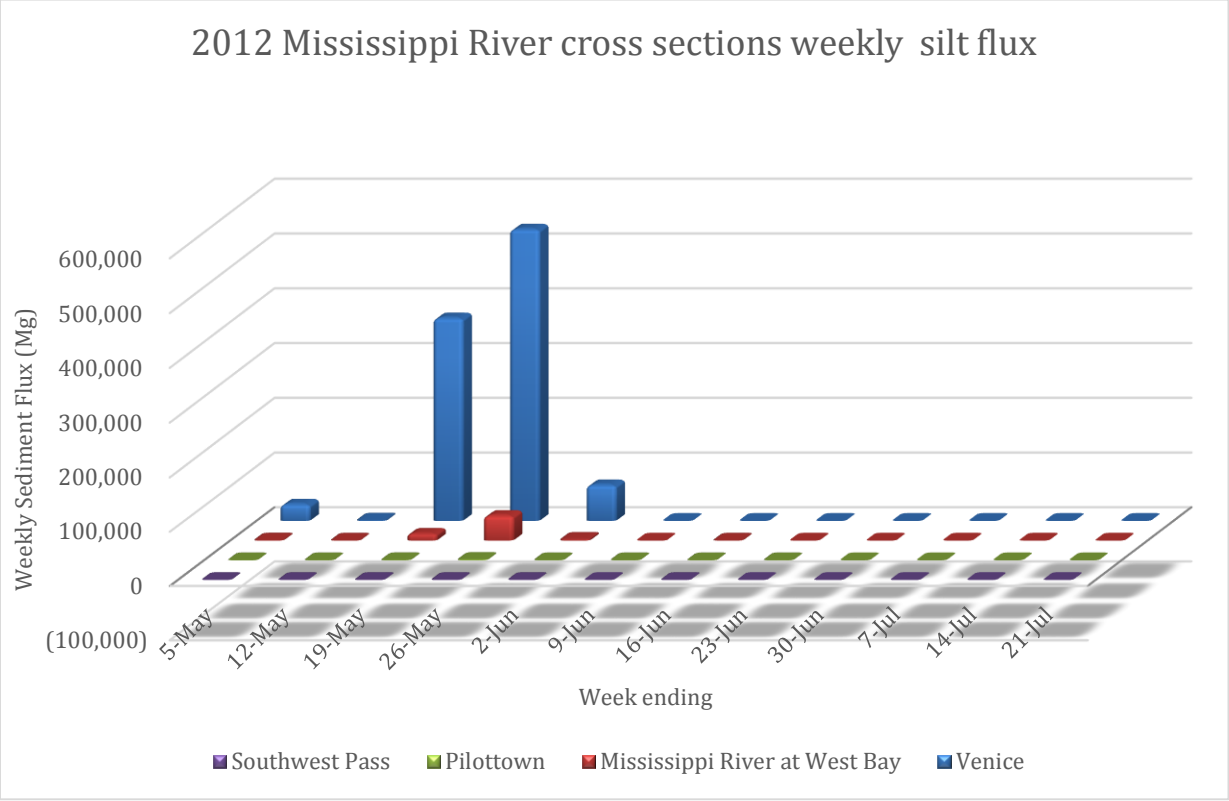

Figure 9-58 Mississippi River weekly Delft3D silt flux in metric tons (Mg)

The accumulation or loss of fine sediment in the bed may be obtained by performing a mass balance of the weekly cross section fluxes in the three channel zones bounded by the three river cross sections and the Southwest Pass cross section. For example, to determine the accumulation of clay in the channel between the Venice and Mississippi River at West Bay cross sections, the accounting would be: Venice clay flux – Mississippi River at West Bay clay flux – Baptiste Collette Bayou clay flux – Grand Pass clay flux = accumulation (or degradation) of clay. The results of the mass balance analyses are shown in Table 9-5 and corresponding bar charts in Figure 9-59, Figure 9-60, and Figure 9-61.

Table 9-5 Fine sediment weekly channel bed flux under 2012 drought conditions

2012 Week ending	Channel bed weekly clay flux between Venice and Mississippi River at West Bay	Channel bed weekly silt flux between Venice and Mississippi River at West Bay	Channel bed weekly clay flux between Mississippi River at West Bay and Pilottown	Channel bed weekly silt flux between Mississippi River at West Bay and Pilottown	Channel bed weekly clay flux between Pilottown and Southwest Pass	Channel bed weekly silt flux between Pilottown and Southwest Pass
	Mg	Mg	Mg	Mg	Mg	Mg
5 May	1,046	17,696	650	320	1,410	7
12 May	8,154	847	6,208	23	4,976	1
19 May	10,473	223,864	7,865	11,522	7,811	263
26 May	11,315	299,525	9,645	43,162	9,443	1,153
2 June	(442)	32,494	(2,968)	2,589	2,656	31
9 June	173	(32)	(376)	0	2,273	0
16 June	466	(42)	1,303	0	928	0
23 June	165	(139)	(1,051)	(4)	(6)	0
30 June	1,571	0	957	0	611	0
7 July	385	0	541	0	1,192	0
14 July	336	0	(306)	0	255	0
21 July	1,627	0	1,239	0	1,313	0

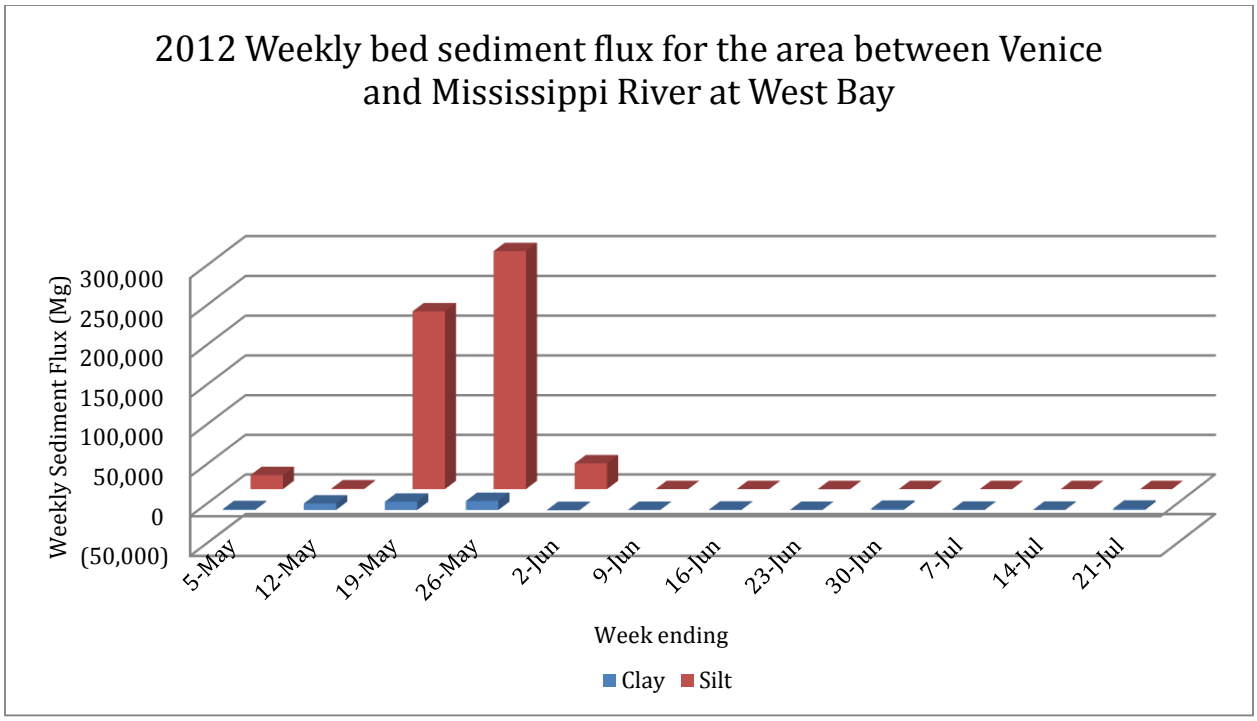

Figure 9-59 Fine sediment weekly channel bed flux for the area between Venice and Mississippi River at West Bay

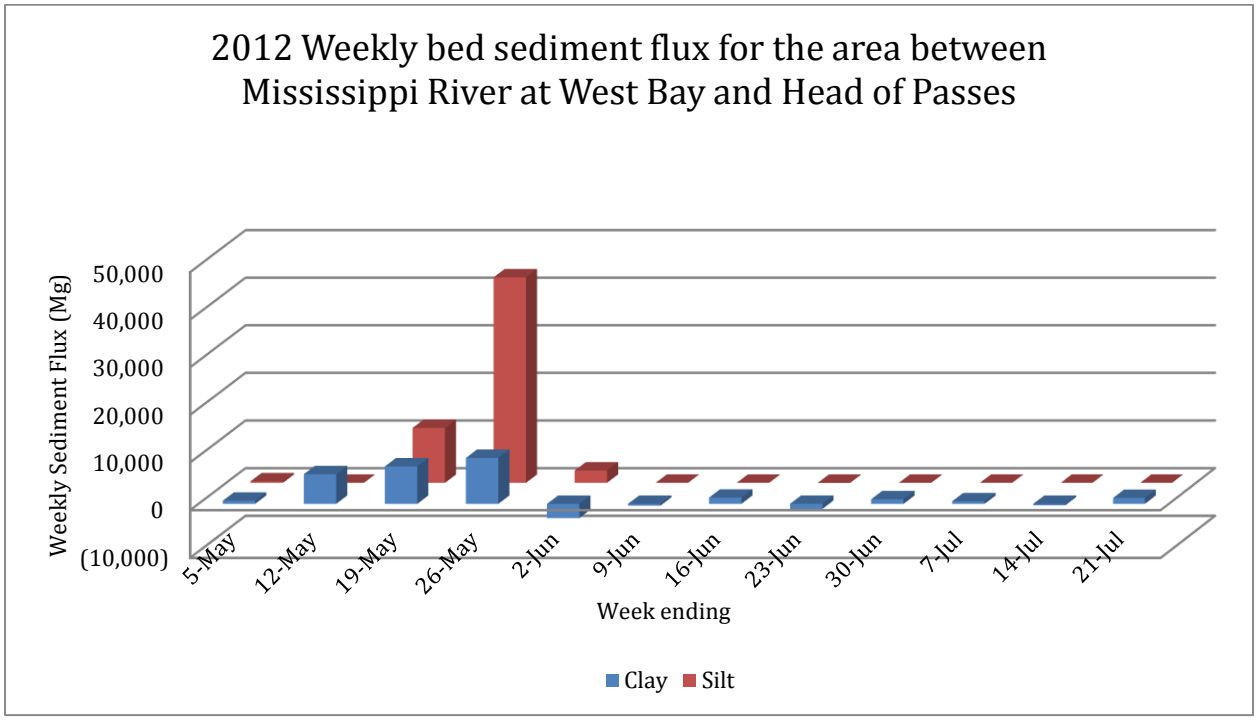

Figure 9-60 Fine sediment weekly channel bed flux for the area between Mississippi River at West Bay and Head of Passes

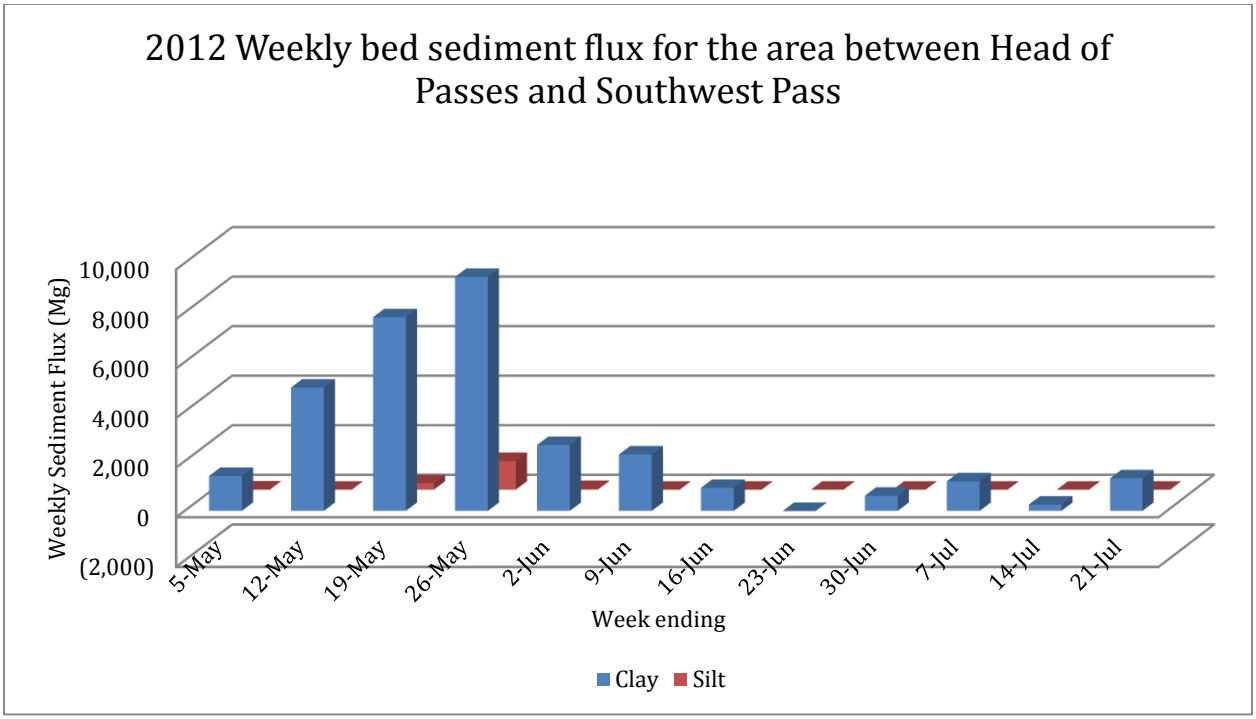

Figure 9-61 Fine sediment weekly channel bed flux for the area between Head of Passes and Southwest Pass

The results of the mass balance indicate that the Head of Passes area becomes a net depositional area of clay during these low flow periods when a salt wedge is present in the lower river channel. Much of the deposition may be attributed to the presence of the turbidity maxima in this area.

The bulk of the silt load which passes Venice is deposited in the area immediately downstream of Venice during these low flow periods. This is largely due to the energy loss in the river channel resulting from the diversion of flow through Baptiste Collette Bayou, Grand Pass, Cubit's Gap and the West Bay crevasse.

9.7 Model limitations

Models are necessarily limited in their approximations of the prototype whereby open boundaries must be imposed to restrict the model domain. In a numerical model, wave reflections may occur at open boundaries where in reality the wave passes unhindered. These wave reflections may affect the solution at the open boundaries appearing as spurious velocity plumes, node to node oscillations, and flow recirculation.

Some of these effects can be seen manifested in the horizontal velocity plot shown in Figure 9-62, especially at the open water boundary in the Southwest portion of the model domain. These effects were experienced throughout this model study but were not severe enough to cause model instability issues. It is believed that the open boundaries for this model were selected at a far enough distance from the area of interest so as not to influence model results. In other words, the Southwest Pass and lower Mississippi River channels are believed to be un-influenced by wave reflection issues at the open boundaries.

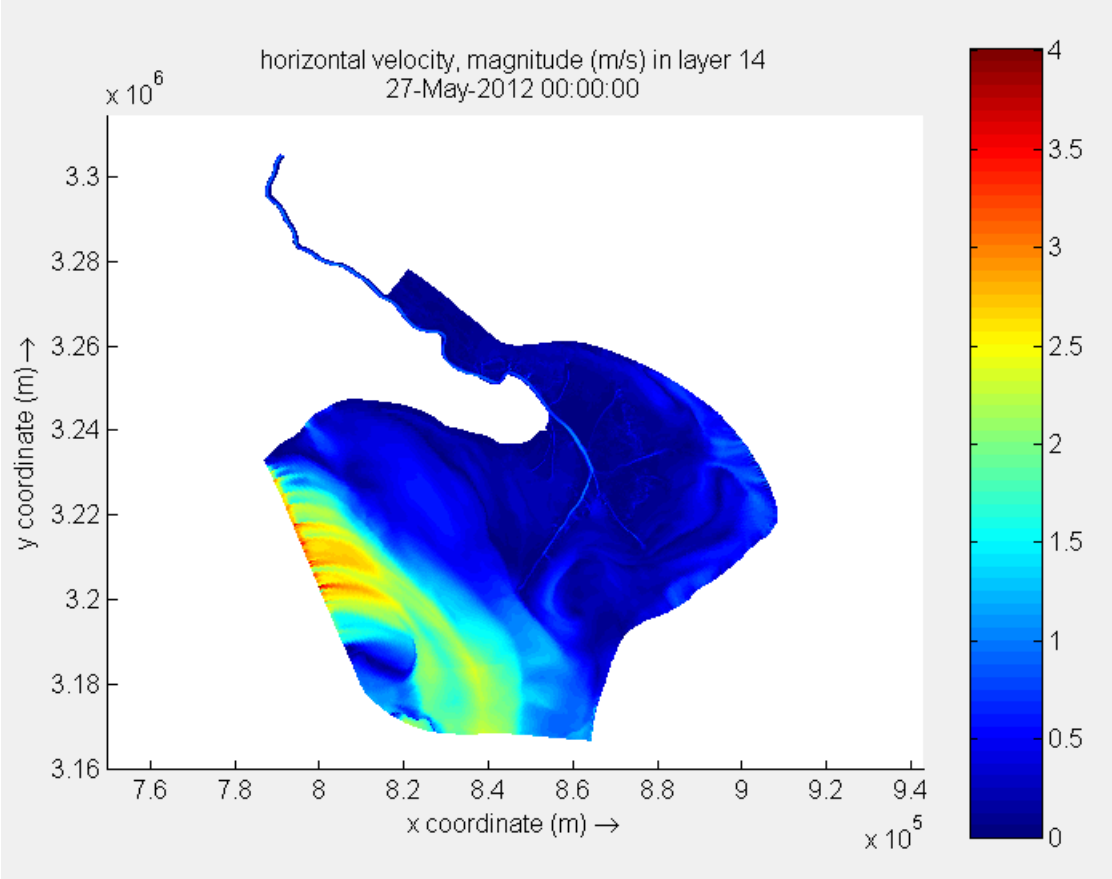

Figure 9-62 Open water wave reflection effects

Physical properties at the open water boundaries are defined from a limited number of data sources and the available data is assumed to be applicable to the boundary nodes. The definition of physical properties at the open water boundaries is further limited to the surface and bottom of the endpoints of a few boundary segments. This was done to make

boundary data easily manageable and allow for testing of vertical layering schemes without redefinition of boundary data. Linear interpolation both horizontally and vertically is used to define properties at intermediate nodes. This interpolation may introduce errors at the boundary if the tidal phase along the boundary segment or distribution of physical properties is non-linear.

Another necessary physical model limitation includes the representation of the bottom topography and the internal land/water boundaries. In the *Z*-model, the bottom topography takes the form of a stair step appearance; this form of discretization will impose errors and artificial mixing in the solution. The land/water boundaries in a curvilinear grid will have a zig-zag appearance where the curvilinear aspect is not able to compensate for a channel that does not follow grid line directions. This limitation will also impose error in the solution of the discretized equations.

There are a limited number of physical processes that can be reasonably evaluated due to computational limitations and our ability to represent natural processes with mathematical methods. For example, the sediment load which is made up of a continuous spectrum of grain sizes and shapes must be divided into a limited number of size classes and modeled with a limited number of physical qualities for each size class. The interaction between grain classes and the bed is limited by our understanding of the physical processes of a completely integrated environment and the ability to represent these processes with mathematical expressions. Turbulence modeling is hampered by the need to quantify a very complex process into a simple set of equations with parameters that may have been derived from laboratory studies. Wave-current interactions were not evaluated for this model study, but can influence sediment transport and mixing.

The use of the depth integrated shallow water equations is limited by the assumption of long waves in a computational environment where the horizontal length scale is much greater than the vertical length scale. When the gravitational waves can no longer be considered as "long" (i.e. when the water depth is equal to the wave length), the assumption of a two dimensional flow becomes invalid and vertical accelerations may

become important. In particular, breaking waves near the shoreline and vertical accelerations at steep side slopes cannot be realistically captured by this model.

The computational time step is necessarily limited to allow reasonable simulation run times but may introduce wave propagation errors if too large a value is selected. A 6-second time step was used for the simulations performed for this study. The assumption is made that the free surface waves are propagated correctly with the selected time step.

9.8 Model uncertainty

Uncertainty in the model results may be introduced from various sources. The finite difference method is simply a means to approximate partial differential equations whose exact solution may be too complicated to solve otherwise. This approximation process introduces numerical uncertainty in the model solution. Another source of numerical uncertainty may be introduced through computer truncation and rounding errors.

The lack of knowledge of the underlying physics of many physical processes and resultant inability to capture the processes with exact mathematical expressions will introduce uncertainty in the model results. Parameter uncertainty exists in a model when exact values are unknown to experimentalists. For example, the parameters used in the k-ε turbulence closure model as discussed in section 4.8 were derived through data fitting from experimental results of a range of physical conditions which may or may not be applicable to the situation evaluated in this study. Another example is the default wind stress parameters used in this model study due to a lack of available information to better inform the model parameters.

The limited representation of the physical space introduces model inadequacy through the discretization of the topography. Furthermore, a finite difference grid is unable to capture sub-grid features which may impact flow patterns and resultant transport characteristics of constituents in the prototype.

A limitation of the data sources available to define model boundary conditions will introduce uncertainty in model results. For example three water level data sources were

used to define the entire open water Gulf of Mexico boundary. Phase and amplitude errors are introduced through translation of the water level data to the boundary. The water level data records are also subject to vertical datum errors. Periods of missing data when linear interpolation was used to complete the data record are additional sources of error and uncertainty in the model results.

Data uncertainty exists in the source of data used to define the open water salinity and temperature boundary conditions, since the AMSEAS model itself is an approximation of the physical space. Data to define the suspended sediment boundary conditions at the open water boundaries other than the Belle Chasse boundary was not readily available and as previously discussed, the lack of a breakdown of the fine sediment classes at Belle Chasse will introduce error at that boundary and uncertainty in the model results.

10 CONCLUSIONS

A curvilinear grid was constructed representative of the modern Mississippi River digitate delta. Boundary conditions were developed for the drought year of 2012 and the grid was tested in order to evaluate the salinity intrusion and sedimentation abilities of the Cartesian *Z*-coordinate three-dimensional Delft3D code. The effect of salinity on fine sediment transport is evaluated by manipulation of the settling velocity through a cosine function.

The *Z*-model proved to have the ability to propagate the saline density current that regularly appears during low water conditions. Although the Cartesian *Z*-coordinate vertical discretization scheme proved to be subject to artificial mathematical diffusion that plagues all discretization schemes, the artificial diffusion did not overwhelm the density current and thus prevent upstream migration of the current. In fact, additional mixing was introduced in order to simulate the interfacial mixing that naturally occurs due to breaking internal gravity waves. Otherwise, the modeled density current would propagate too far upstream as compared to the prototype.

The model capably reproduced the fine sediment concentration profiles in a fully turbulent shear flow environment as evidenced by comparison of model results to the April 2012 sediment samples. Manipulation of the fine sediment fall velocity by means of the cosine function provided in the model code was an effective means to simulate the re-circulation of flocculated sediments in the saline wedge turbidity maxima. As a result the model was able to account for the contribution of fine sediment to the density gradient and the resultant increase in strength of the stratification through the buoyancy terms. A mass balance analysis of the lower river channel indicated that model predicted deposition patterns are consistent with literature describing high mud deposition in the leading edge of a salt wedge.

With the ability to reproduce the seasonal saline density current and its effect on sedimentation within the turbidity maxima as well as sedimentation characteristics in a fully turbulent shear flow, a model capable of analyzing all of the major processes affecting

fine sediment transport within the Mississippi River salt wedge estuary has been developed.

11 RECOMMENDATIONS

During the course of the model investigation, several shortcomings of the model were made apparent. During the drought of 2012, the salinity wedge advanced as far as the crossing located at RK 145 before the USACE constructed the barrier sill to halt further wedge progression. With the upstream boundary of the model grid placed at Belle Chasse (RK 121) the model was incapable of reproducing the prototype wedge dynamics during the period the wedge had progressed upstream past this physical boundary. Historically, the wedge has progressed as far upstream as the crossing at RK 225, however, this is an extreme example. The crossing located at RK 187, referred to as the Fairview Crossing may provide a more practical upstream grid limit to evaluate wedge progression without the barrier sill in place and has proven to be a difficult obstacle for the wedge to overcome. Existing records indicate it has only been overtopped by the wedge during the 1939 and 1940 low water periods. The Fairview Crossing stopped wedge progression during the 1952, 1953 and 1956 low water periods. Evaluations of wedge penetrations without the barrier sill in place are necessary to properly evaluate impacts of proposed altered channel configurations for deep draft navigation purposes. Although the addition of the river channel between RK 121 and RK 187 would not be expected to significantly increase the computation times in a parallel computational environment, the model solution files would increase in proportion to the grid area added to the existing grid.

The model results presented in Chapter 8 indicate that the model depths at some of the observation locations are not representative of the prototype during the model simulation periods in 2012. Therefore, the channel depths should be further evaluated in an effort to better match those observed in the prototype. Multi-beam data were collected in 2012 which may be processed into a depth sample set that could be utilized in the model. A more representative bathymetry set should further improve the reproduction of channel hydrodynamics and resultant suspended sediment profiles in the model.

Further evaluation of the water level data from 2012 during extreme low water periods is warranted. Investigation into the influence of the salinity wedge on water level

either through buoyancy effects or contamination of the pressure sensors at specific gages may provide guidance on the need to re-calibrate the September simulation to match water level data or examine other sources of error.

Further model evaluation of the four lateral outlets in Southwest Pass is recommended. Although this study utilized the bathymetric data collected in 2014 as shown in Figure 7-3 Southwest Pass lateral outlets multi-beam extent, ADCP data in Southwest Pass and the four outlets were also collected in 2014 as documented in "Southwest Pass Outlets Bathymetry and Flow Distribution Assessment" (Ayres, 2015). Thirty ADCP transects were collected at each outlet site to capture the flow budget under a range of tidal conditions as shown in Figure 11-1. This ADCP data could be used to verify the flow budget in Southwest Pass and the four lateral outlets. Such an evaluation would require construction of boundary conditions representing conditions in May 2014 and analysis of model response with adjustment of friction parameters and grid refinement as necessary.

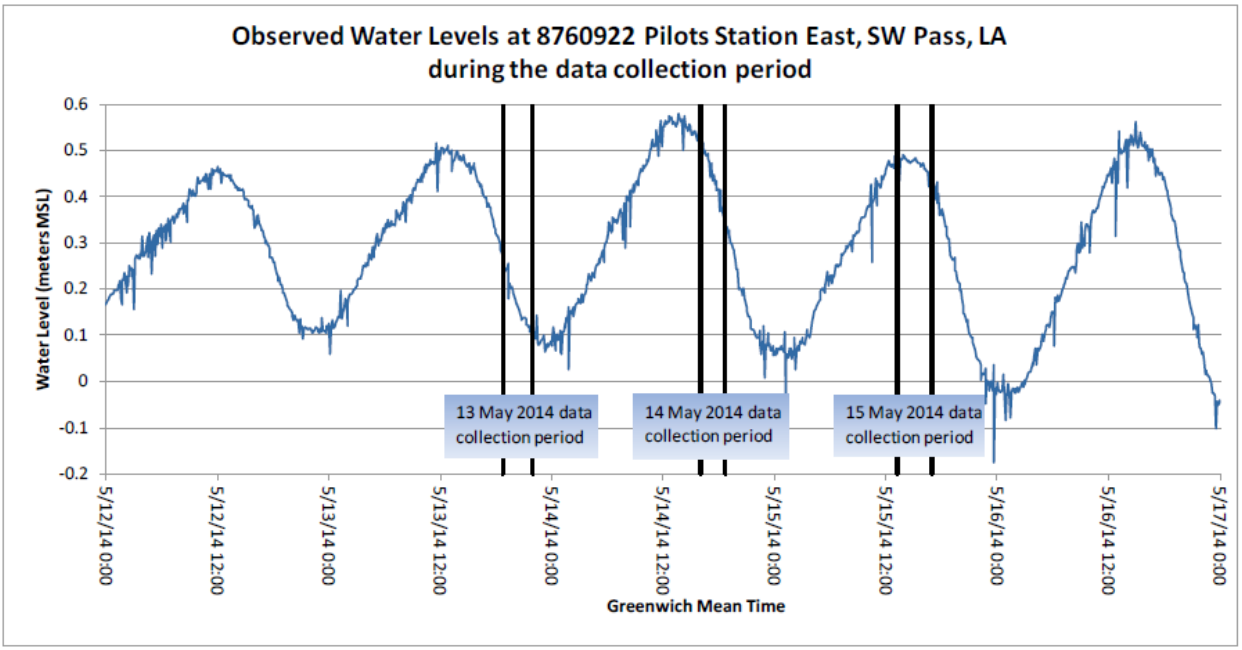

Figure 11-1 2014 ADCP data collection periods in Southwest Pass (from Ayres, 2015)

The gradation of the suspended sediment at Belle Chasse was limited to a split between fine sediment and sand during the simulation periods. Therefore, in order to evaluate the silt and clay classes in the model, a gradation based on Tarbert Landing was used. However during periods of very low river discharge, the suspended sediment records at Tarbert Landing, Baton Rouge and Belle Chasse indicate a drop in fine sediment concentration in the downstream direction. This implies that under very low river discharge conditions, the heavier silt classes would most likely drop out of the water column prior to reaching the Belle Chasse observation site. Efforts are being made to improve the evaluation of suspended sediment samples at Belle Chasse and this improved gradation information will be available to better inform model sediment boundary conditions at Belle Chasse. In the past, the sampling frequency decreased during periods of low river discharge. However, given the apparent drop in fine sediment concentration in the seaward direction during drought conditions, the recommendation is made to evaluate sufficient sample sets during these periods to provide a good understanding of sedimentation consequences under drought conditions which will then improve model boundary conditions.

A problem with the bottom layer re-mapping feature in the *Z*-level model as conceptualized in Figure 5-2 was made apparent during the model investigation. This shortcoming was reported to the model developers and appears to be limited to the Linux platform. Therefore, this feature was not evaluated. Although the model was still able to provide satisfactory results, any improvement in shear stress calculations provided by this feature would only prove to be beneficial to sediment investigations. Further testing of this feature is recommended once the developers resolve the situation in the model code.

Activation of the bottom layer re-mapping feature in combination with improved suspended sediment gradation information at Belle Chasse would make non-cohesive sediment analyses more feasible with the model and thus provide a model that could evaluate the complete range of sediment dynamics in the Mississippi delta from flood periods to drought periods. Therefore, model testing is recommended of flood conditions with non-cohesive sediment classes when these issues are resolved. The addition of non-

cohesive sediment classes and bed morphology to the model would also make this model a useful tool for estimation of future dredging needs considering river management changes as a result of sea level rise and flow diversions.

A means to reduce numerical diffusion of scalars due to the discretization scheme may be implemented through the use of iterative correction methods such as the multidimensional positive definite advection transport algorithm (MPDATA). The MPDATA method utilizes a successive application of a first-order accurate and positive definite upwind transport algorithm. Numerical diffusion generated by the first-order truncation error is minimized with a correction to the first-order truncation error through re-application of the upwind algorithm using an "anti-diffusion" velocity that is based on the local first-order truncation error. This corrective step may be applied numerous times depending on the level of accuracy desired at the cost of computational overhead. The MPDATA method is second-order accurate and positive definite (Smolarkiewicz, 1984 : Smolarkiewicz and Clark, 1986).

The MPI algorithm is automated in such a way as to sub-divide the computational grid along the longest dimension. When the purpose of the grid is to represent a fresh water source such as a river discharging into a delta or bay, this usually results in long sub-grid strips in the delta or bay portion of the grid (Figure 6-6 for an example). The computation times continued to decrease as more processors were added, however, the limitation of the grid sub-division algorithm prevented determination of the optimum number of compute cores to minimize simulation run times. Manual sub-division of the grid could provide a more efficient distribution of compute load to the cores by not only sub-dividing the grid along the longest dimension but also by the cross channel direction in the wider portion of the grid in the delta. Further investigation of a means to manually sub-divide the grid and implementation of the procedure would not only reduce compute times for the model developed for this study but would allow finer grid resolution in the delta and improved model response. A finer vertical resolution would also become more practical as well as the analysis of additional sediment constituent classes.

12 LITERATURE CITED

Allison, M.A., 2014. *Mississippi Hydrodynamic and Delta Management Study, Salt Wedge Dynamics Surveys, Water and Sediment Surveys of the Mississippi River Channel in April, June, and September 2012 and September-October 2013*. A report to the State of Louisiana Office of Coastal Protection and Restoration.

Arakawa, A. and Lamb, V.R., 1977. Computational design of the basic dynamical processes of the UCLA general circulation model. *Methods of Computational Physics* **17**. New York: Academic Press. pp. 173–265.

Ariathurai, R., 1974. *A finite element model for sediment transport in estuaries.* Ph.D. Thesis, University of California, Davis, CA.

Arita, M. and Jirka, G.H., 1987. Two-layer model of saline wedge. II. Prediction of mean properties. *Journal of Hydraulic Engineering*, ASCE, 113(10), 1249-1263.

Ayres, S.K., 2015. *Southwest Pass Outlets Bathymetry and Flow Distribution Assessment, Data Collection Summary and Analysis*. MRG&P Report No. 5, U. S. Army Corps of Engineers, New Orleans, LA 42 p.

Balloffet, A. and Borah, D.K., 1985. Lower Mississippi salinity analysis. *Journal of Hydraulic Engineering*, ASCE, 111(2), 300-315.

Blumberg, A.F. and Mellor, G.L., 1987. A Description of a Three-Dimensional Coastal Ocean Circulation Model. *In:* Heaps, N.S. (ed.), *Three-Dimensional Coastal Ocean Models*. American Geophysical Union, pp. 1-16.

Brown, G.; Callegan, C.; Heath, R.; Hubbard, L.; Little, C.; Luong, P.; Martin, K.; McKinney, P.; Perky, D.; Pinkard, F.; Pratt, T.; Sharp, J.; and Tubman, M.; 2009. *ERDC Workplan Report – Draft, West Bay Sediment Diversion Effects.* U. S. Army Corps of Engineers, ERDC/CHL.

Bunya, S.; Dietrich, J.C.; Westerink, J.J.; Ebersole, B.A.; Smith, J.M.; Atkinson, J.H.; Jensen, R.; Resio, D.T.; Luettich, R.A.; Dawson, C.; Cardone, V.J.; Cox, A.T.; Powell, M.D.; Westerink, H.J., and Roberts, H.J., 2010. A High-Resolution Coupled Riverine Flow, Tide, Wind, Wind Wave, and Storm Surge Model for Southern Louisiana and Mississippi: Part 1: Model Development and Validation. *Monthly Weather Review,* 138(2), 345-377.

Chen, C.; Beardsley, R.C.; Cowles, G.; Qi, J.; Lai, Z.; Gao, G.; Stuebe, D.; Xu, Q.; Xue, P.; Ge, J.; Ji, R.; Hu, S.; Tian, R.; Huang, H.; Wu, L.; and Lin, H., 2011. *An Unstructured Grid, Finite-Volume Coastal Ocean Model, FVCOM User Manual*.

Chien, N. and Zhaohui, W., 1999. *Mechanics of Sediment Transport*. ASCE Press, 932p.

Coleman, J.M., 1988. Dynamic Changes and Processes in the Mississippi River Delta. *Geological Society of America Bulletin*, 100(7), 999-1015.

Courant, R.; Friedrichs, K.; Lewy, H., 1967. On the partial difference equations of mathematical physics. *IBM Journal of Research and Development,* 11(2), 215–234, translated from Courant, R.; Friedrichs, K.; Lewy, H., 1928. Über die partiellen Differenzengleichungen der mathematischen Physik, *Mathematische Annalen* (in German), 100 (1), 32–74.

Cowdrey, A.E., 1977. *Land's end: A history of the New Orleans District, U. S. Army Corps of Engineers, and its lifelong battle with the lower Mississippi and other rivers wending their way to the sea.* Unknown Binding.

Crank, J. and Nicolson P., 1947. A practical method for numerical evaluation of solutions of partial differential equations of the heat-conduction type. *Proc. Cambridge Philos. Soc.* , 43 (1947) 50–67.

Deltares, 2014. *Delft3D Hydro-Morphodynamics User Manual* (28 May 2014). Published and Printed by Deltares, The Netherlands.

Einstein, H.A., 1950. *The bed load function for sediment transportation in open channel flows*. Technical Bulletin No 1026, U. S. Department of Agriculture, Washington, D. C.

Ellison, T.H., 1961. Turbulent transport of heat and momentum from an infinite rough plane. *Journal of Fluid Mechanics,* 2(5), 456-466.

Graf, W.H., 1971. *Hydraulics of Sediment Transport*. McGraw-Hill, New York, NY

Harleman, D.R.F., 1961. Stratified flow. *In:* Streeter, V.L. (ed.), *Handbook of Fluid Dynamics,* McGraw-Hill Book Co., New York, N.Y.

Harleman, D.R.F., 1990. Keulegan Legacy: Saline Wedges. ASCE *Journal of Hydraulic Engineering,* 117(12), 1616-1625.

Ippen, A.T., 1966. Sedimentation in Estuaries. *In:* Ippen, A.T. (ed.), *Estuary and coastline hydrodynamics*, McGraw Hill Book Co., New York, N. Y., pp. 648-672.

Johnson, B.H.; Boyd, M.B.; and Keulegan, G.H., 1987. *A mathematical study of the impact on salinity intrusion of deepening the lower Mississippi River navigation channel*. TR. HL-86-1, Dept. of the Army, Waterways Experiment Station, Corps of Engr., Vicksburg, MS.

Johnson, B.H.; Boyd, M.B.; and Copeland, R., 1987. Lower Mississippi River Salt Intrusion Modeling. *In:* Ragan, R.M. (ed.), *Proceedings of the ASCE National Conference on Hydraulic Engineering* (Williamsburg, Virginia), pp. 439-444.

Kay, D.J. and Jay, D.A., 2003. Interfacial mixing in a highly stratified estuary 1. Characteristics of mixing. *Journal of Geophysical Research,* 108(C3). doi: 10.1029/2000JC000252

Keulegan, G.H., 1966. The mechanism of an arrested saline wedge. *In:* Ippen, A.T. (ed.), *Estuary and coastline hydrodynamics*, McGraw Hill Book Co., New York, N. Y., pp. 546-574.

Krone, R.B., 1962. *Flume studies of the transport of sediment in estuarial shoaling processes*. Final report, Hydraulic Engineering lab and Sanitary Engineering lab, University of California, Berkeley.

Krone, R.B., 1972. Aggregation of suspended particles in estuaries. *In:* Kjerfve, B. (ed.), *Estuarine Transport Processes*, University of South Carolina Press, Columbia, pp. 177-190.

Kolb, C.R. and van Lopik, J.R., 1958. *Geology of the Mississippi River deltaic plain, southeastern Louisiana*. Technical Report 3-483. Vicksburg, MS: U. S. Army Corps of Engineers Waterways Experiment Station.

Launder, B.E. and Spalding, D.B., 1974. The numerical computation of turbulent flows. *Computer Methods in Applied Mechanics and Engineering,* 3(2), 269–289. doi:10.1016/0045-7825(74)90029-2.

McDonald M.G. and Harbaugh, A.W., 2003. The History of MODFLOW. *Ground Water,* 41(2): 280–283. doi:10.1111/j.1745-6584.2003.tb02591.x. PMID 1265629

Mehta, A.J. and Li, Y., 1996. Fine-grained sediment transport engineering. *Proc., Coastal and Oceanographic Engineering Dept. Course*, Univ. of Florida, Gainesville, Fla.

Migniot, C., 1968. Study on Physical Properties of Various Silt and Its Properties under Flow Dynamics. *La Houille Blanche*, No. 7 (in French).

Ozmidov, R.V., 1965. On the turbulent exchange in a stably stratified ocean., *Izv. Acad. Sci. USSR Atmos. Oceanic Phys.,* 1(8), 853-860.

Partheniades, E., 1962. *A study of erosion and deposition of cohesive soils in salt water*. Ph.D. Thesis, University of California, Berkeley, June, 1962.

Partheniades, E., 1965. Erosion and Deposition of cohesive soils. *Journal of the Hydraulics Division*, ASCE, 91(HY1), Proc. Paper 4204, 105-139.

Partheniades, E., 2007. *Engineering Properties and Hydraulic Behavior of Cohesive Sediments.* CRC Press, Boca Raton, FL.

Peaceman, D.W. and Rachford, H.H., 1955. The numerical solution of parabolic and elliptic differential equations. *Journal of the Society for Industrial and Applied Mathematics*, 3(1), 28-41.

Phillips, N.A., 1957. A co-ordinate system having some special advantage for numerical forecasting. *Journal of Meteorology*. 14:184-185.

Platzek, F.W.; Stelling, G.S.; Jankowski, J.A., and Pietrzak, J.D., 2014. Accurate vertical profiles of turbulent flow in z-layer models. *Water Resources Research*, 50,doi:10.1002/2013WR014411.

Portela, L.I;, Ramos, S., and Trigo-Teixeira, A., 2013. Effect of salinity on the settling velocity of fine sediments of a harbour basin. *In:* Conley, D.C., Masselink, G., Russell, P.E. and O'Hare, T.J. (eds.), *Proceedings 12th International Coastal Symposium* (Plymouth, England), *Journal of Coastal Research*, Special Issue No. 65, pp. 1188-1193, ISSN 0749-0208.

Postma H., 1967. Sediment transport and sedimentation in the estuarine environment. *In:* Lauff, G.H. (ed.), *Estuaries*. AAAS, Washington, pp. 158-179.

Prandtl, L., 1926. *Proc. second int. Congr. appl. Mech.*, Zurich (1926); translation quoted from Aeronautical Research Council paper, Ae. Techl. 341 (1927).

Prasuhn, A. L., 1980. *Fundamentals of Fluid Mechanics*. Prentice-Hall, Inc.

Putra, S.S.; v. d. Wegen, M.;, Reyns, J.; v. Dam, A.; Solomatine, D.P., and Roelvink, J.A., 2015. Multi station calibration of 3D flexible mesh model: a case study of the Columbia Estuary. *Procedia Environmental Sciences* 28 (2015) 297-306.

Richardson, L.F., 1920. The supply of energy from and to atmospheric eddies. *Proceedings of the Royal Society London* A97: 345-373.

Rodi, W., 1984. *Turbulence Models and Their Application in Hydraulics*. Int. Assoc. for Hydraulic Res., Delft, Netherlands, 104p.

Savant, G.; Berger, R.C., and McAlpin, T.O., 2014. *Three-dimensional shallow-water adaptive hydraulics (ADH-SW3): Hydrodynamic Verification and Validation*. U. S. Army Corps of Engineers, Engineer Research and Development Center, ERDC TR-14-7.

Schijf, J.B. and Schönfeld, J.C., 1953. Theoretical Considerations on the Motion of Salt and Fresh Water. *In: Proceedings of the Minnesota International Hydraulics Convention*, (Minneapolis, Minnesota), 321p.

Simmons, H. B., 1966. Field Experience in Estuaries. *In:* Ippen, A.T. (ed.), *Estuary and coastline hydrodynamics.* McGraw Hill Book Co., New York, N. Y., pp. 673-690.

Smolarkiewicz, P.K. and Clark, T.L., 1986. The Multidimensional Positive Definite Advection Transport Algorithm: Further Development and Applications. *J. Comp. Phys*., 67:396-438.

Smolarkiewicz, P.K., 1984. A Fully Multidimensional Positive Definite Advection Transport Algorithm with Small Implicit Diffusion*. J. Comp. Phys*., 54:325-362.

Spasojevic, M., and Holly Jr., F.M., 1993. Three-dimensional numerical simulation of mobile-bed hydrodynamics. *Technical Report No. 367*. Iowa Institute of Hydraulic Research, The University of Iowa, Iowa City, Iowa; also as Contract *Report HL-94-2.* Waterways Experiment Station, Vicksburg, Miss., 1994.

Spasojevic, M. and Holly Jr., F.M., 2008. Two- and Three-Dimensional Numerical Simulation of Mobile-Bed Hydrodynamics and Sedimentation. *In:* Garcia, M.H. (ed.), *Sedimentation Engineering, Processes, Measurements, Modeling, and Practice*. ASCE Manuals and Reports on Engineering Practice No. 110, pp. 683-761.

Uittenbogaard, R.E.; van Kester, J.A.T.M., and Stelling, G.S., 1992. *Implementation of three turbulence models in 3D-TRISULA for rectangular grids*. Tech. Rep. Z81, WL | Delft Hydraulics, Delft, The Netherlands.

UNESCO, 1981a. *Background papers and supporting data on the international equation of state 1980*. Tech. Rep. 38, UNESCO.

UNESCO, 1981b. *The practical salinity scale 1978 and the international equation of state of seawater 1980.* Tech. Rep. 36, UNESCO. Tenth report of the Joint Panel on Oceanographic Tables and Standards (1981), (JPOTS), Sidney, B.C., Canada.

van Leussen, W., 1988. Aggregation of particles, settling velocity of mud flocs: a review. *In:* Dronkers, J. and van Leussen, W., (eds.), *Physical Processes of Estuaries.* Berlin: Springer, pp. 347-403.

Wright, L.D., 1985. River deltas. *In:* Davis, R.A. (ed.), *Coastal Sedimentary Environments*. Springer-Verlag, New York, pp. 1-76.

VITA

The author was born in Tyler, Texas. After completing his work at Midland Lee High School, he entered Texas Tech University and received his Bachelor of Science in Civil Engineering in 1986. He completed work for a Master's of Science in Civil Engineering at Texas Tech in 1991. He entered the Graduate School at the University of New Orleans in 2007.